BULGARIAN CHEMICAL COMMUNICATIONS

2012 Volume 44/ Number 4

Journal of the Chemical Institutes
of the Bulgarian Academy of Sciences
and of the Union of Chemists in Bulgaria

Bulgarian Chemical Communications, Volume 44, Number 4 (pp. 283 - 288) 2012

Pressure drop of high performance random Intalox Metal Tower Packing

Sv. Ts. Nakov[1], D. B. Dzhonova-Atanasova, N. N. Kolev

Institute of Chemical Engineering, Bulgarian Academy of Sciences, Acad. G. Bonchev Str., Bl. 103, 1113 Sofia, Bulgaria

Received: October 31, 2011; Accepted: November 7, 2011

INTALOX Metal Tower Packing (IMTP) is one of the best random packings designed especially for use in distillation operations. The advantages realized in distillation have been abundantly applied in absorption, liquid-liquid extraction and direct contact heat transfer operations as well. There is no universal methodology for calculating the performance characteristics of this packing. The constants of the existing equations for practical calculations are obtained for each separate packing size. The present work presents and generalizes own experimental data for the pressure drop of 4 sizes of IMTP packing with nominal diameters of 25, 40, 50, and 70 mm. The experimental data for dry packing pressure drop are described by an equation with a mean deviation of 5.1%. Equations for determination of pressure drop of irrigated packing, up to the loading point and above it, are also obtained. These equations reflect not only the influence of the packing geometry, but also the column redumping.

Keywords: Packed columns; Random packings; Packing pressure drop; Equations for dry and irrigated IMTP.

INTRODUCTION

Packed bed columns are apparatuses with long history of exploitation for heat and mass transfer processes in gas-liquid systems. The actual level of technological development and the increasing number of international regulations which deal with environmental protection further expand the application field of packed columns. The main advantages of the random packings are their easy production using highly effective technology and easy dumping in the apparatus. Their great disadvantages are the higher pressure drop in comparison to the structured packings and the not very good distribution properties.

INTALOX Metal Tower Packing (IMTP) is a modern high capacity random packing characterized by high void fraction, low pressure drop [1, 2] and high mass transfer efficiency [3, 4]. IMTP is widely used in distillation towers: from deep vacuum towers, where low pressure drop is crucial, to high-pressure towers, where capacity easily surpasses that of conventional trays. Many absorption and stripping towers, especially those aiming at high capacity or close approach to equilibrium, rely on IMTP packing. The low pressure drop, high specific heat-transfer coefficient, as well as the fouling resistance of IMTP packing contributes to its success in heat transfer towers [1]. It was shown in [2], on the basis of a comparison of specific pressure drop, capacity, height equivalent to a theoretical stage, and pressure drop per theoretical stage between corresponding sizes of random packings, that the third generation random packings IMTP offer a noticeable advantage in comparison to the second generation Pall-Rings. However, the Raschig Super-Ring packing (RSR) offers a further evident benefit in comparison to the third generation random packings–this is why it is called 'fourth generation' [2]. The effective area, a_e, of IMTP can be much higher than the specific area [4, 5]. But at comparable values of the specific area and the liquid superficial velocities, RSR juxtaposed to IMTP [4], have about 15% higher effective area and over 35 % lower pressure drop versus effective area, at the same gas velocity.

The present paper aims at deriving more precise equations for evaluation of the pressure drop, taking into account such very important quantities as specific surface area and void fraction which carry the influence of the packing construction and dimensions,-as well as the dumping of the packing in the column [6].

EXPERIMENTAL DETAILS

The geometric characteristics of the investigated packings are given in Table 1. A photograph of one of them – IMTP 70 is presented in Fig.1. The packing elements are built of three types of lamellas, Fig.1: 1- main narrow lamellas, 2- lamellas specially bent at 90º, and 3- wide lamellas.

* To whom all correspondence should be sent: E-mail: svnakov@bas.bg

© 2012 Bulgarian Academy of Sciences, Union of Chemists in Bulgaria

The geometrical characteristic denotes the minimal width of lamellas 2 in their narrowest part, Fig. 1. The nominal diameter d_n is the diameter of the inscribed circle in the packing element. All other geometrical characteristics are defined as averages obtained from triplicate redumping of the packing in a single column section.

Table 1. Geometrical characteristics of the investigated types of IMTP packing

Name	Surface area a m^2/m^3	Free volume ε %	Size of lamellas 2 shown in Fig.1 s mm	Nominal Diameter d_n mm	Hydraulic Diameter d_h mm
IMTP 25	242.8	97.1	2.0	18.6	16.0
IMTP 40	171.6	96.7	3.1	26.5	22.5
IMTP 50	107.1	97.8	4.1	37.5	36.5
IMTP 70	66.1	98.5	4.1	61.0	59.6

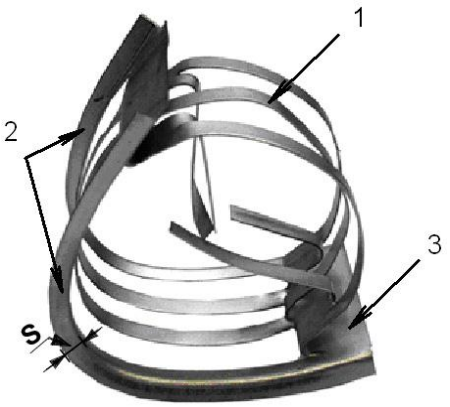

Fig.1. IMTP 70 packing

All experiments were carried out in a column with a diameter D=470 mm and a packing height of 2400 mm**.** The liquid phase distributor ensured 923 drip points per m^2. For the pressure drop investigation the liquid superficial velocity varied between L=10 and 120 $m^3/(m^2\ h)$ in an air – water system. The packing pressure drop was measured by means of a special optical differential manometer with an accuracy of 0.1 Pa. At a pressure drop higher than 200 Pa, a conventional U-tube differential manometer was used.

The data for all investigated packings at different liquid superficial velocities *versus* the gas velocity factor are presented in Figs. 2 to 5. The lines obtained are similar to those already established for the well-known random packings,

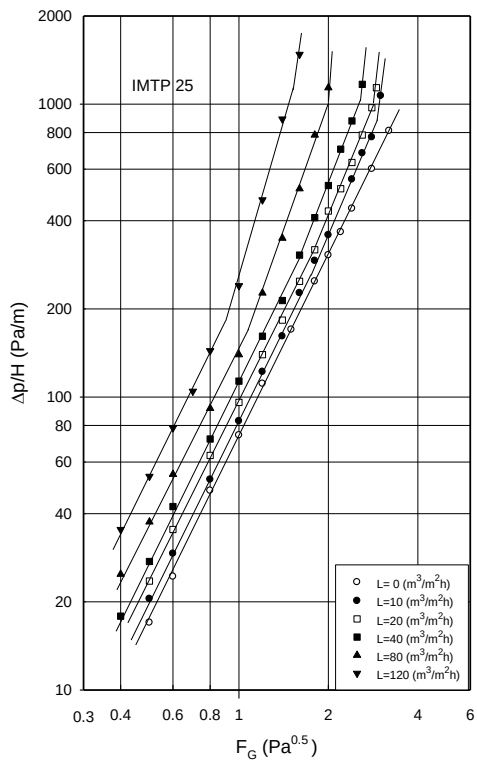

Fig.2. Pressure drop of IMTP 25 at various superficial liquid velocities vs. gas velocity factor.

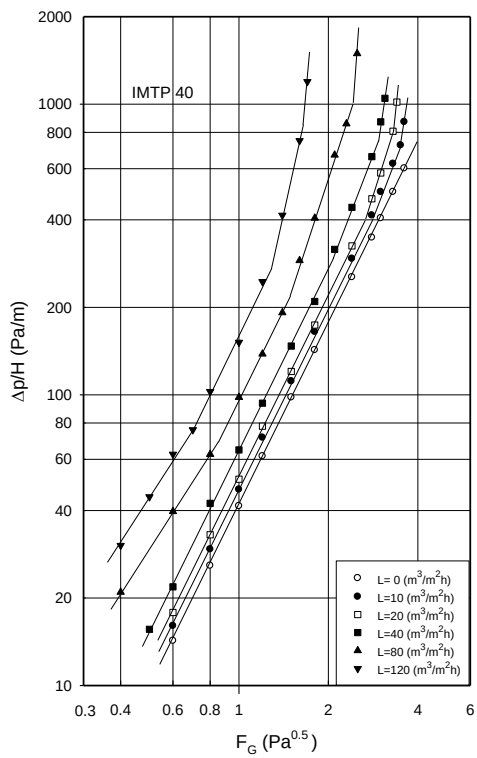

Fig.3. Pressure drop of IMTP 40 at various superficial liquid velocities vs. gas velocity factor.

but the measured lower pressure drop shows improved performance parameters and higher loading and flooding points.

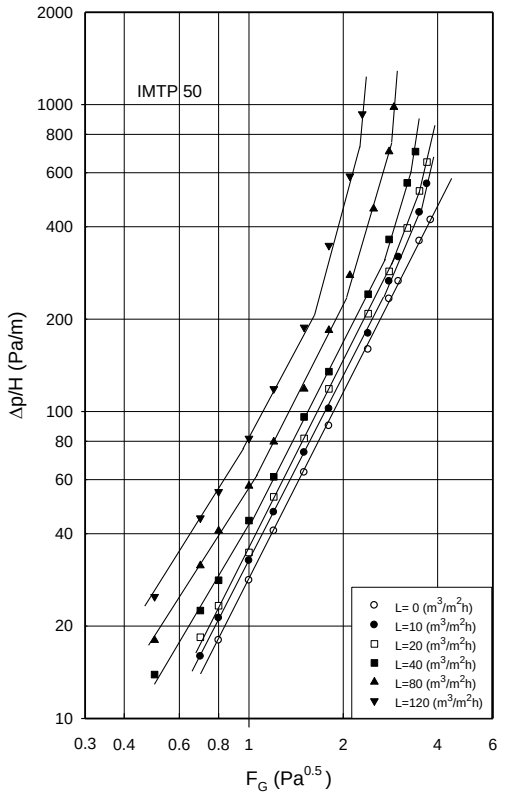

Fig.4. Pressure drop of IMTP 50 at various superficial liquid velocities vs. gas velocity factor

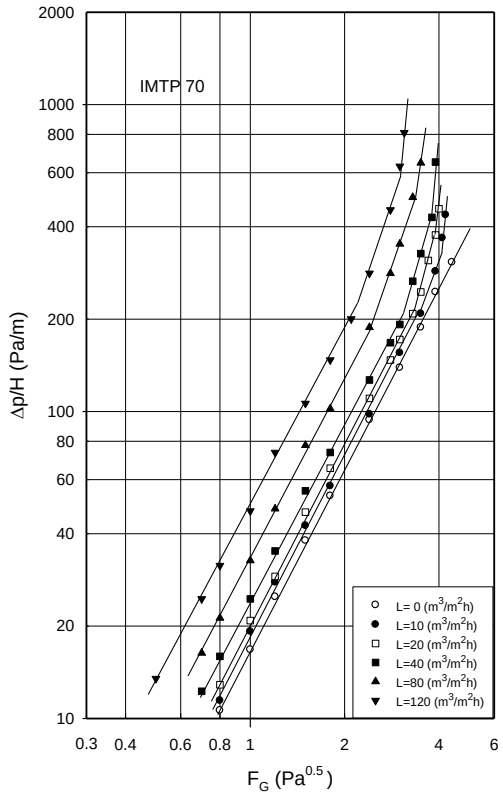

Fig.5. Pressure drop of IMTP 70 at various superficial liquid velocities vs. gas velocity factor.

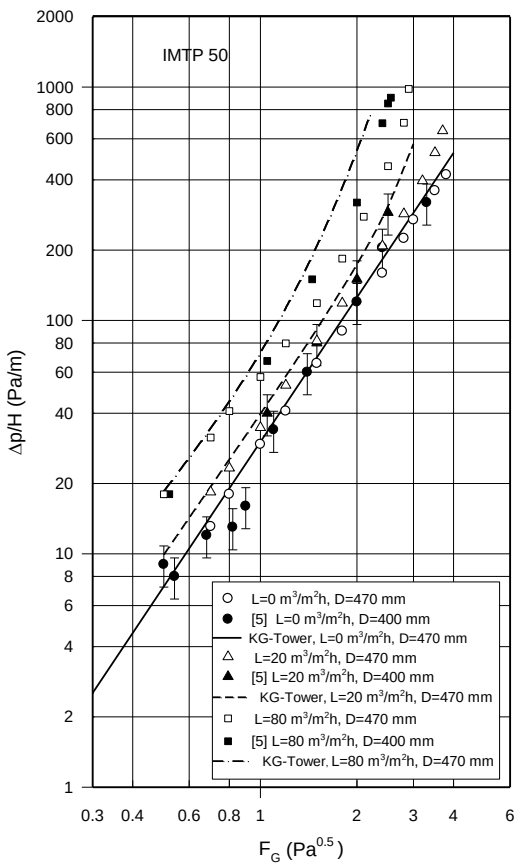

Fig.6. Pressure drop of dry and wetted IMTP 50 vs. gas velocity factor. Comparison with data from [5] and the manufacturer software KG- Tower 3.2.

DATA CORRELATION

Most of the equations for calculation of the pressure drop of irrigated packing need relation for the pressure drop of a dry one.

For practical calculation of the pressure drop of a dry packing Billet [7] proposed the equation

$$\frac{\Delta P_0}{H} = C_d F_G^e, \qquad (1)$$

where ΔP_0 is packing pressure drop in Pa; H denotes packing height in m; $F_G = w_o\sqrt{\rho_G}$ is the factor of vapour (gas) velocity in $Pa^{0.5}$; w_o is gas velocity related to the entire column cross section in m/s and ρ_G is gas density in kg/m^3. The experimental constants C_d and e take into account the influence of the packing dimensions and especially of the void fraction ε and are determined not only for each packing type, but also for each element size. Their values are given in [7] for a number of modern highly effective packings, but not for IMTP.

Fig. 6 presents a comparison of experimental and calculated data for the pressure drop of dry and irrigated IMTP 50 in the system air-water, at two liquid loads L = 20 and 80 $m^3/(m^2\ h)$. In all

experiments the column operates at atmospheric pressure and room temperature. In [5] the column diameter is 400 mm and the height of the packing bed is 1500 mm. The figure shows that the pressure drop data obtained in the present investigation, the data from [5] and the values predicted with the manufacturer software KG-Tower 3.2 are in good agreement for dry packing and under the loading point in wetted conditions. Over the loading point the pressure drop in [5] grows more rapidly with the increase of F_G, reaching over 30 % deviation and KG-Tower gives higher values reaching over 50% deviation from our experimental results. For the present generalization of the experimental data the dimensionless pressure drop of dry packing ψ is used [8, 9],

where $\psi = \dfrac{\Delta P_0 d_h}{2H\rho_G (w_0/\varepsilon)^2}$ is the dimensionless pressure drop equivalent to Euler number; $d_h = \dfrac{4\varepsilon}{a}$ is the packing hydraulic diameter, m; ε is the packing void fraction, m^3/m^3 and a - the packing specific surface area, m^2/m^3.

By using dimensional analysis and processing all data for the dry packings by the least squares technique, the following equation was obtained:

$$\psi = 0.96\left(\frac{s}{d_n}\right)^{0.27} \tag{2}$$

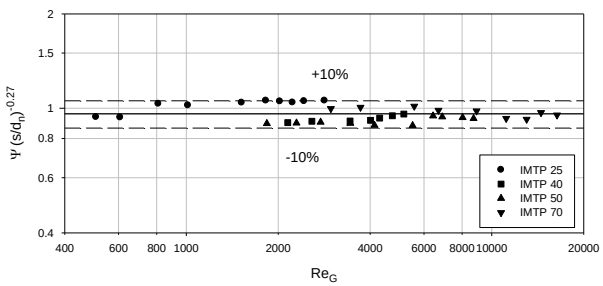

Fig.7. Comparison of experimental data for dry packings with results calculated by Eq. (2).

Fig. 7 presents a comparison of equation (2) with the data obtained for all studied packings, where $Re_G = \dfrac{w_0 d_h}{\nu_G . \varepsilon}$ is the Reynolds number for the gas phase and ν_G is the gas phase kinematic viscosity in m^2/s . The mean deviation of equation (2) is 5.1%. The precision of the obtained experimental constants at 95% statistical reliability is given below:

$$0.96 \pm 0.094;\ 0.27 \pm 0.052.$$

To determine the pressure drop of the wetted packing ΔP, the well known relationship proposed by Zhavoronkov *et al*. [10], was used:

$$\Delta P = \frac{\Delta P_0}{(1-A)^3}, \tag{3}$$

where A is a dimensionless value related to the liquid holdup which accounts for the effect of the part of free column cross section occupied by the liquid. To determine this value, the following additive relationship [10, 11] was used:

$$A = A_0 + \Delta A \tag{4}$$

where A_0 indicates the A value under the loading point, and ΔA is the increasing of A over this point.

Applying the dimensional analysis to the experimental data for packings pressure drop below the loading point the following expression was obtained:

$$A_0 = 2.5\,\mathrm{Re}_L^{-0.1}\, Fr_L^{0.44}\, Eo^{0.21} \tag{5}$$

where $Re_L = \dfrac{4L}{a\nu_L}$ is the Reynolds number for the liquid phase; L - liquid phase superficial velocity, m/s; $Fr_L = \dfrac{L^2.a}{g}$ - Froude number for the liquid phase; $Eo = \dfrac{\rho_L . g}{a^2 \sigma}$ - Eötvos number and σ is liquid surface tension, N/m.

The mean deviation of equation (5) regarding $\Delta P/\Delta P_0$ is 2.6%. The precision of the obtained experimental constants at 95% statistical reliability is given below:

$$2.5 \pm 0.14;\ -0.1 \pm 0.061;$$
$$0.44 \pm 0.012;\ 0.21 \pm 0.014.$$

For the experimental data for packing pressure drop over the loading point the following equation was obtained:

$$\Delta A = 7.10^{-4}\, Fr_L^{-0.16} \left(\frac{L\rho_L}{w_o \rho_G}\right)^{1.02} Eo^{0.14} \tag{6}$$

The mean deviation of equation (6) regarding $\Delta P/\Delta P_0$ is 3.8%. The precision of the obtained experimental constants at 95% statistical reliability is given below:

$$7.10^{-4} \pm 5.10^{-4};\quad -0.16 \pm 0.020;$$
$$1.02 \pm 0.047;\quad 0.14 \pm 0.021$$

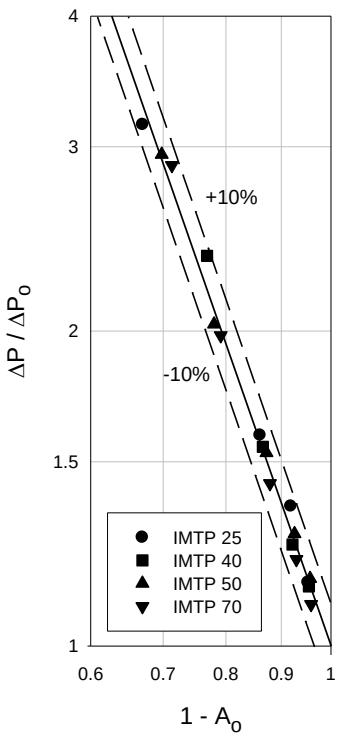

Fig.8. Comparison of experimental data for the pressure drop of the wetted packings below the loading point with results calculated by Eqs. (3) and (5).

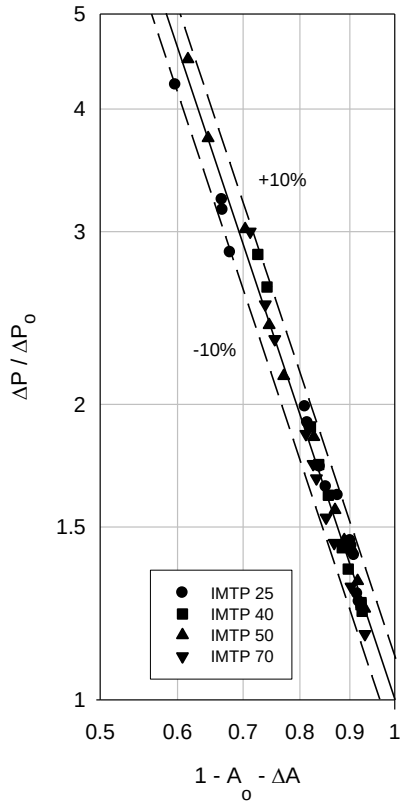

Fig.9. Comparison of experimental data for the pressure drop of the wetted packings above the loading point with results calculated by Eqs. (3), (4) and (6).

Figs. 8 and 9 present the comparison of the lines calculated with the proposed equations and the experimental data for gas velocities below and above the loading point for all investigated packings.

CONCLUSION

The pressure drop of four sizes of high effective IMTP packing is determined and summarized. The results confirmed the good performance of the investigated packings. More precise equations for prediction of the pressure drop at dry and wetted conditions are derived. They fit the experimental results with accuracy acceptable for practical use.

REFERENCES

1 IMTP High Performance Packing, Bulletin KGIMTP-2. Rev. 3-2010, Koch-Glitsch, LP (2010).
2 M. Schultes, *Trans. IChemE.*, **81, Part A**, 48, (2003).
3 N. Kolev, Sv. Nakov, L. Ljutzkanov, D. Kolev, *Chem. Eng. and Process.*, **45**, 429, (2006).
4 Sv. Nakov, N. Kolev, L. Ljutzkanov, D. Kolev, *Chem. Eng. and Process.*, **46**, **No 12**, 1385, (2007).
5 P. Alix, L. Raynal, *Energy Procedia* **1**, 845 (2009)
6 N. Kolev, Packed bed columns for absorption, desorption, rectification and direct heat transfer, Elsevier, 149, (2006).
7 R. Billet, Packed column analysis and design, Monograph, Ruhr University Bochum, 31 (1989).
8 V. M. Ramm, A. Y. Zakgeim, Proc. Inst. Chem. Technol. Kazan (in Russian), 223, (1961).
9 N. Kolev, Verfahrenstechnik, **6**, 241, (1969).
10 N. M. Zhavoronkov, M. E. Aerov, N. N. Umnik, *Chim. Prom*. **10**, 294, (1948).
11 N. Kolev, *Chem., Ing. Technik.*, **46**, 1105, (1976).

ХИДРАВЛИЧНО СЪПРОТИВЛЕНИЕ НА ВИСОКОЕФЕКТИВНИЯ МЕТАЛЕН INTALOX ПЪЛНЕЖ ЗА КОЛОННИ АПАРАТИ

Св. Ц. Наков, Д. Б. Джонова-Атанасова, Н. Н. Колев

Институт по инженерна химия, Българска академия на науките,Ул. "Акад. Г. Бончев" бл. 103, 1113 София

Постъпила на 31 октомври, 2011 г.; приета на 7 ноември, 2011 г.

(Резюме)

Пълнежът IMTP е един от най-добрите пълнежи, специално създаден за провеждане на дестилационни процеси. Предимствата, които е показал в този тип процеси, са разширили неговото приложение и при случаите на абсорбция, течно-течна екстракция и директен топлообмен. Все още не съществува универсална методика за изчисляване на работните характеристики на този тип пълнеж, като константите в съществуващите и използвани в практиката уравнения са получени за всеки отделен типоразмер пълнеж. В настоящата работа са показани и обобщени собствени експериментални данни за хидравличното съпротивление на 4 IMTP пълнежа с номинални диаметри 25, 40, 50 и 70 mm. Експерименталните данни за сухия пълнеж се описват с уравнение със средно отклонение от 5.1%. Получени са уравнения за определяне на съпротивлението и на умокрения пълнеж под и над точката на задържане. В предложените уравнения се отчита не само геометрията на пълнежа, но е взето предвид и влиянието на презареждането на колоната.

Bulgarian Chemical Communications, Volume 44, Number 4 (pp. 289 - 298) 2012

Dissymmetric tetradentate salicylaldimine Cu(II) and Co(II) complexes derived from 1,8-naphthalene and different salicylaldehydes

A. Kilic[1], E. Tas[2], B. Deveci[1], M. Durgun[1]

[1]*Department of Chemistry, University of Harran, 63190, Sanliurfa, Turkey*

[2]*Department of Chemistry, University of Siirt, 56100, Siirt, Turkey*

Received: June 17, 2011; Accepted: January 9, 2012

The synthesis, structure and spectroscopic properties of salicylaldimine Schiff base ligands (L_nH_2) (n = 1, 2, 3 and 4) (L_1H_2=*N, N'*-[1,8-naphthalene]-3-methylsalicylaldimine, L_2H_2 = *N,N'*-[1,8-naphthalene]-5-methylsalicylaldimine, L_3H_2 = *N,N'*-[1,8-naphthalene]-3-methoxy-salicylaldimine and L_4H_2= *N,N'*-[1,8-naphthalene]- 5-methoxysalicyl-aldimine), respectively and their mononuclear Cu(II) and Co(II) complexes [ML_n] are described. Four new dissymmetric tetradentate salicylaldimine ligands containing a donor set of N_2O_2 were prepared by reaction of 1,8-naphthalene with different salicylaldehydes. Tetradentate Cu(II) and Co(II) complexes were obtained by reacting the ligands with $Cu(Ac)_2.H_2O$ and $Co(Ac)_2.4H_2O$ in a 1:1 mole ratio. The ligands and their Cu(II) and Co(II) complexes were characterized by ^{1}H-NMR, FT-IR, UV-Vis, elemental analysis, molar conductivity, magnetic susceptibility, X-ray powder analysis, and their morphology was studied by SEM measurements.

Keywords: salicylaldimine, Cu(II) and Co(II) complexes, spectroscopy, X-ray powder, SEM analyses

1. INTRODUCTION

Since the first report of the Schiff reaction [1], the synthesis of symmetric tetradentate Schiff bases as ligands, and of their metal complexes, has been widely described. Some of them may be used as catalysts in various chemical processes [2, 3], or as models for a better understanding of some biological systems [4-6]. However, the unsymmetric tetradentate Schiff base metal complexes were less studied than the symmetric ones [7]. The investigation of Schiff base metal complexes has been of interest for many years to help understanding the interactions between metal ions and proteins or as other biological references. Recent years have witnessed a great deal of interest in the synthesis and characterization of transition metal complexes containing Schiff bases as ligands due to their applications as catalysts for many reactions [8-10], relation to synthetic and natural oxygen carriers [11] and use as new structural probes in nucleic acids chemistry and therapeutic agents [12-15]. Schiff base metal complexes containing different metal ions such as Ni, Co and Cu have been studied in great details for their various crystallographic features, structure-redox relationships, enzymatic reactions, mesogenic characteristics and catalytic properties [16-18]. Although the magnetic, spectroscopic and catalytic properties of these Schiff base complexes are well documented [19, 20], new and specific applications for such a unique class of compounds could be found. A considerable number of Schiff base complexes are of potential biological interest, being used as more or less successful models of biological compounds [21]. In addition, they are convenient model compounds for studying theoretical aspects of photochemistry and designing molecular architecture by means of molecular motifs capable of H-bond formation [22]. Their photochromic behavior suggests the possibility of using these

* To whom all correspondence should be sent:

E-mail: mustafadurgun@harran.edu.tr

© 2012 Bulgarian Academy of Sciences, Union of Chemists in Bulgaria

compounds as elements for constructing optical switches or optical memory devices [23].

In the present study, we report the synthesis and characterization of four new Schiff base ligands (L_1H_2, L_2H_2, L_3H_2 and L_4H_2, where L_1H_2 = *N,N'*-[1,8-naphthalene]-3-methylsalicylaldimine, L_2H_2 = *N,N'*-[1,8-naphthalene]- 5-methylsalicylaldimine, L_3H_2 = *N, N'*-[1,8-naphthalene]-3-methoxysalicylaldimine and L_4H_2 = *N,N'*-[1,8-naphthalene]- 5-methoxysalicylaldimine) involving N_2O_2 donor sites and their mononuclear Cu(II) and Co(II) complexes.

2. EXPERIMENTAL

All reagents and solvents were of reagent-grade quality and were purchased from commercial suppliers. The elemental analyses were carried out in the Laboratory of the Scientific and Technical Research Council of Turkey (TUBITAK). NMR spectra were recorded at 297 K on a Varian Mercury AS 400 NMR instrument at 400 MHz, FT-IR spectra were recorded on a Perkin Elmer Spectrum RXI FT-IR Spectrometer in KBr pellets. Infrared spectra of the ligands and their metal complexes were recorded in KBr pellets in the range from 4000 to 400 cm^{-1}. Magnetic susceptibilities were determined on a Model MK1 Sherwood Scientific Magnetic Susceptibility Balance at room temperature (20°C) using $Hg[Co(SCN)_4]$ as a calibrant; diamagnetic corrections were calculated from Pascal's constants [24]. Electronic spectral studies were conducted on a Perkin Elmer model Lambda 25 UV-Vis spectrophotometer in the wavelength range of 200-1100 nm. Molar conductivities (Λ_M) were recorded on an Inolab Terminal 740 WTW Series instrument. X-ray powder spectra were recorded on a Rigaku Ultima III Series spectrograph. The scanning electron microscopy (SEM) measurements were carried out on a Zeiss Evo 50 Series instrument. The samples were sputter coated with carbon using a Balzers Med 010 device to prevent charging when analyzed by the electron beam.

Synthesis of Ligands (L_1H_2, L_2H_2, L_3H_2 and L_4H_2):

N,N'-[1,8-naphthalene]-3-methylsalicylaldimine (L_1H_2), *N,N'*-[1,8-naphthalene]-5-methylsalicylaldimine (L_2H_2), *N,N'*-[1,8-naphthalene]-3-methoxysalicylaldimine (L_3H_2) and *N, N'*-[1,8-naphthalene]-5-methoxysalicylaldimine (L_4H_2) ligands were synthesized by the reaction of 5.0 mmol 1,8-diamino naphthalene in 40 ml absolute ethanol with 10.0 mmol 3-methylsalicylaldehyde for L_1H_2, 10.0 mmol 5-methylsalicylaldehyde for L_2H_2, 10.0 mmol 3-methoxysalicylaldehyde for L_3H_2 and 10 mmol 5-methoxysalicylaldehyde for L_4H_2, in 50 ml ethanol. 3-4 drops of formic acid were added as a catalyst. The mixtures were refluxed for 3-4 h and were cooled to room temperature. The crystals were filtered in vacuum. Then the products were recrystallized from $MeOH-CHCl_3$.

Synthesis of the Cu(II) and Co(II) complexes

1.0 mmol of the ligands (L_1H_2, L_2H_2, L_3H_2 or L_4H_2) were dissolved in absolute ethanol (60 ml). A solution of 1.0 mmol of the metal salt [$Cu(Ac)_2.H_2O$ or $Co(Ac)_2.4H_2O$] in absolute ethanol (35 ml), was dropwise added under continuous stirring in a N_2 atmosphere. The stirred mixture was heated to the reflux temperature and was maintained at this temperature for 5 hours. Then, the mixture was evaporated to a volume of 10-15 ml in vacuum and left to cool to room temperature. The compounds were precipitated after adding 5 ml of ethanol. The products were filtered in vacuum and washed with a small amount of ethanol and water. The products were recrystallized from ethanol and dried at 100 ^{o}C.

3. RESULTS AND DISCUSSION

The reaction steps for the synthesis of the ligands and their mononuclear Cu(II) and Co(II) complexes are shown in Schemes 1 and 2. In the first step, the ligands (L_1H_2, L_2H_2, L_3H_2 and L_4H_2) were

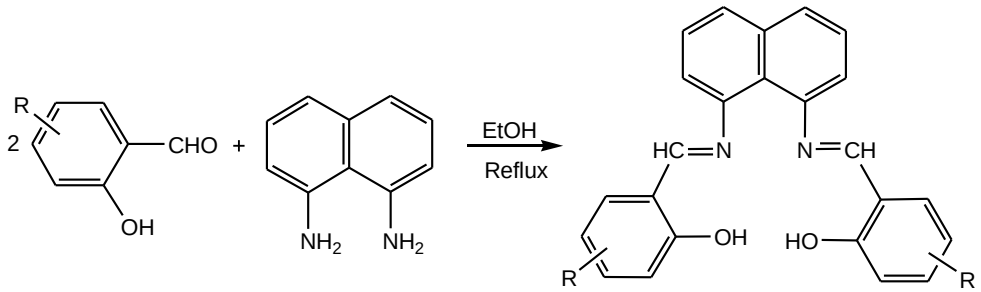

R= 3-CH_3 (L_1H_2), 5-CH_3 (L_2H_2), 3-OCH_3 (L_3H_2), 5-OCH_3 (L_4H_2)

Scheme 1 Synthetic route for preparation of the ligands (L_nH_2).

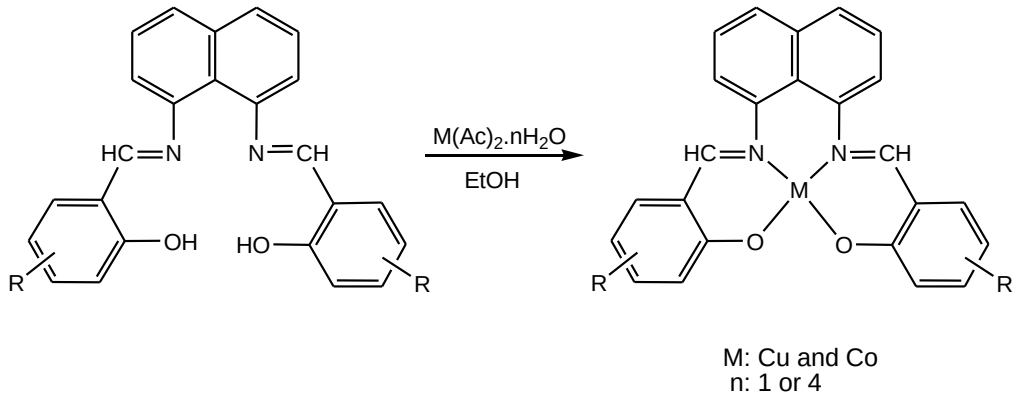

R= 3-CH_3 (L_1H_2), 5-CH_3 (L_2H_2), 3-OCH_3 (L_3H_2), 5-OCH_3 (L_4H_2)

Scheme 2 Synthetic route for preparation of mononuclear Cu(II) and Co(II) complexes

Table 1. Formula, color, melting point, yield, magnetic susceptibility and elemental analysis data for the ligands and their Cu(II) and Co(II) complexes.

Compound	*Color*	*M.p.* ^oC*(dec.)*	*Yield (%)*	μ_{eff} *[B.M]*	Λ_M $\Omega^{-1}cm^2$ mol^{-1}	*Elemental analyses Calcd (Found) %* *C*	*H*	*N*
L_1H_2	Dirty					79.18	5.58	7.16
$C_{26}H_{22}N_2O_2$	White	219	57	-	-	(79.40)	(5.56)	(7.13)
CuL_1	Dark					68.49	4.39	6.14
$C_{26}H_{20}N_2O_2Cu$	Green	>300	48	1.50	8.6	(68.90)	(4.41)	(6.16)
L_2H_2						79.18	5.58	7.16
$C_{26}H_{22}N_2O_2$	Orange	233	62	-	-	(78.60)	(5.55)	(7.06)
CuL_2	Dark					68.49	4.39	6.14
$C_{26}H_{20}N_2O_2Cu$	Brown	>300	56	1.41	10.2	(68.10)	(4.36)	(6.10)
CoL_2	Dark					69.19	4.45	6.26
$C_{26}H_{20}N_2O_2Co$	Brown	>300	73	2.15	12.8	(68.80)	(4.42)	(6.18)
L_3H_2						73.24	5.16	6.57
$C_{22}H_{22}N_2O_4$	Pink	186	68	-	-	(73.70)	(5.20)	(6.62)
CuL_3	Dark					64.92	4.10	5.74
$C_{26}H_{20}N_2O_4Cu$	Green	>300	44	1.67	10.8	(65.30)	(4.13)	(5.79)
CoL_3						63.60	4.14	5.79
$C_{26}H_{20}N_2O_4Co$	Brown	226	76	2.18	9.6	(63.3)	(4.12)	(5.77)
L_4H_2						73.24	5.16	6.57
$C_{26}H_{22}N_2O_4$	Orange	181	80	-	-	(72.80)	(5.14)	(6.54)
CuL_4						64.00	4.10	5.74
$C_{26}H_{20}N_2O_4Cu$	Green	>300	88	1.47	13.7	(63.78)	(4.08)	(5.71)
CoL_4	Dark					81.35	8.47	4.75
$C_{26}H_{20}N_2O_4Co$	Brown	238	67	2.27	9.2	(79.70)	(8.43)	(4.73)

Table 2. Characteristic ^{1}H-NMR spectra of the ligands

Compound	*Solvent*	*^{1}H NMR (TMS, δ ppm)*
L_1H_2	$CHCl_3$	13.02 (2H, s, -OH), 8.38 (2H, s, CH=N), 7.72 (2H, s, Ar-CH), 7.31-7.26 (6H, m, Ar-CH), 6.91 (2H, s, Ar-CH), 6.75 (2H, s, Ar-CH) and 2.24 (6H, s, C-CH_3)
L_2H_2	$CHCl_3$	13.18 (2H, s, -OH), 8.42 (2H, s, CH=N), 7.80 (2H, s, Ar-CH), 7.30-7.26 (6H, m, Ar-CH), 6.92 (2H, s, Ar-CH), 6.64 (2H, d, Ar-CH) and 2.35 (6H, s, C-CH_3)
L_3H_2	$CHCl_3$	12.98 (2H, s, -OH), 8.39 (2H, s, CH=N), 7.72 (2H, s, Ar-CH), 7.28 (4H, s, Ar-CH), 6.75 (2H, s, Ar-CH), 6.74-6.65 (4H, m, Ar-CH), and 3.68 (6H, s, O-CH_3)
L_4H_2	$CHCl_3$	13.04 (2H, s, -OH), 8.40 (2H, s, CH=N), 7.76 (2H, s, Ar-CH), 7.32 (4H, s, Ar-CH), 6.96 (2H, s, Ar-CH), 6.65-6.63 (4H, m, Ar-CH) and 3.73 (6H, s, O-CH_3)

synthesized by condensation of 1,8-diamino naphthalene with different salicylaldehydes. In the second step, the mononuclear Cu(II) and Co(II) complexes were synthesized by condensation of the ligands with the metal acetate salt. The Co(II) complex of the L_1H_2 ligand was not formed under these conditions. For the structural characterization of the ligands and their mononuclear Cu(II) and Co(II) complexes, elemental analysis, ^{1}H-NMR, FT-IR spectra, UV-Vis spectra, magnetic susceptibility measurements, molar conductivity, X-ray powder analyses and SEM measurements were used and the corresponding data are given in Tables 1-3. The metal-to-ligand ratio in the mononuclear Cu(II) and Co(II) complexes was found to be 1:1. The interaction of the ligands (L_1H_2, L_2H_2, L_3H_2 and L_4H_2) with Cu(II) and Co(II) salt yielded complexes corresponding to the general formula [Cu(L_n)] and [Co(L_n)].

Table 3. Characteristic FT-IR bands (cm^{-1}) of the ligands and their Cu(II) and Co(II) complexes in KBr pellets.

Compound	*O-H*	*Ar-CH*	*Aliph-CH*	*C-O*	*C=N*	*M-O*	*M-N*
L_1H_2	3275	3050	2967-2843	1229	1627	-	-
CuL_1	-	3054	2956-2852	1232	1602	490	512
L_2H_2	3296	3022	2917-2861	1257	1602	-	-
CuL_2	-	3016	2920-2861	1240	1586	492	516
CoL_2	-	3018	2924-2857	1258	1577	501	546
L_3H_2	3312	3044	2964-2835	1242	1612	-	-
CuL_3	-	3048	2934-2834	1241	1603	498	525
CoL_3	-	3057	2927-2831	1246	1604	502	548
L_4H_2	3341	3045	2953-2830	1239	1604	-	-
CuL_4	-	3046	2934-2831	1232	1587	496	528
CoL_4	-	3055	2955-2831	1236	1598	503	537

3. 1. NMR Spectra

The ^{1}H-NMR spectral data obtained for the ligands in $CDCl_3$, together with the assignments are given in Table 2. The ^{1}H-NMR spectra of L_1H_2, L_2H_2, L_3H_2 and L_4H_2 in $CDCl_3$ do not give any signal corresponding to 1,8-diamino naphthalene protons and different salicylaldehyde protons. The ^{1}H-NMR spectra of the free ligands show a peak at 13.02 ppm for L_1H_2, at 13.18 ppm for L_2H_2, at 12.98 ppm for L_3H_2 and at 13.04 ppm for L_4H_2, characteristic of intramolecular hydrogen bonded OH proton. The peaks in the range 7.72-6.75 ppm for L_1H_2, 7.80-6.64 ppm for L_2H_2, 7.72-6.65 ppm for L_3H_2 and 7.76-6.63 ppm for L_4H_2 are assignable to the protons of Ar-CH. In the ^{1}H-NMR spectra of the ligands, the chemical shift observed at δ=8.38 for L_1H_2, δ=8.42 for L_2H_2, δ=8.39 for L_3H_2 and δ=8.40 for L_4H_2 is assigned to the proton of azomethine (CH=N) as a singlet [25]. The protons of the methyl groups of the ligands exhibit a singlet peak at δ=2.24 for L_1H_2 and 2.35 ppm for L_2H_2. Also, the peaks in the range 3.68-3.73 ppm for the L_3H_2 and L_4H_2 ligands are assignable to the protons of O-CH_3 groups as singlet peaks.

3. 2. IR Spectra

The main stretching frequencies of the FT-IR spectra of the ligands L_1H_2, L_2H_2 L_3H_2 and L_4H_2 and of their mononuclear Cu(II) and Co(II) complexes are given in Table 3. The FT-IR spectra of the ligands and of their corresponding Cu(II) and Co(II) complexes are found to be very similar to each other. Hence, significant frequencies are selected by comparing the FT-IR spectra of the ligands with those of the mononuclear Cu(II) and Co(II) complexes. Coordination of the Schiff base ligands to Cu(II) and Co(II) through the nitrogen atom is expected to reduce the electron density in the

Table 4. Characteristic UV-Vis bands of the ligands and their Cu(II) and Co(II) complexes.

Compound	*Solvents*	*Wavelength [λmax. (nm)(logε)]*
L_1H_2	EtOH	236*(5.33), 281*(4.67), 330*(5.093), 343*(5.09)
	MeOH	281(4.86), 291(4.79), 331(5.26)
CuL_1	$CHCl_3$	273(1.79), 299(1.78), 405*, 692(1.98), 774*, 890*
	DMF	289(3.64), 343*, 415*, 715(2.6), 798(2.67),
	DMSO	305, 308, 387*, 399*, 403*, 563, 799
L_2H_2	EtOH	350(5.09), 413*(2.7), 438*(2.64), 467*(2.5), 495*(2.19)
	MeOH	279(6.34), 347(6.55), 348(4.33), 410*(2.82), 433*(2.76), 463*(2.6)
CuL_2	DMF	333*(0.59), 410(0.89), 450*(0.99), 775*(1.87)
	DMSO	305(4.89), 345(5.25), 355(4.8), 400*(5.1), 455*(4.14), 685*(3.1)
CoL_2	DMF	346(2.89), 470*
	DMSO	307, 308, 346, 350, 418*, 563*, 745*
L_3H_2	EtOH	233*(5.71), 237(5.18), 285*(4.48), 332(4.9), 344*(4.91)
	MeOH	285(3.95), 344(4.38)
CuL_3	$CHCl_3$	423, 457*, 570, 710*, 795*
	DMF	275(4.6), 344(4.44), 450*, 604(3.3), 655*, 800*
	DMSO	346(4.87), 387*(4.37), 410*(4.07), 572*(3.2), 667*(3.14)
CoL_3	$CHCl_3$	267*(4.15), 268*(4.39), 340(4.47)
	DMF	321(4.13), 600*, 858(2.41)
	DMSO	352(4.8), 398*(4.48), 460*(3.9), 600*(3.36), 886*(2.52)
L_4H_2	EtOH	235*(5.07), 238(5.24), 302*(4.48), 350(4.69),
	MeOH	304(4.13), 348(4.37), 429*(2.76), 466*(2.58), 490(2.23)
CuL_4	$CHCl_3$	354(2.03), 363(1.94), 450*
	DMF	287(2.56), 335*, 420*, 480*
	DMSO	305, 388*, 675*
CoL_4	$CHCl_3$	350(4.97), 351(5.38), 411*(3.69)
	DMF	325(3.23), 590*, 640*, 800*
	DMSO	305(5.02), 354(5.04), 473*(4.18), 480*(4.46), 863*(2.83)

* = shoulder peak

azomethine link and lower the υ(C=N) absorption frequency. The very strong and sharp υ(C=N) bands in the FT-IR spectrum of the free ligands are observed in the region 1627-1602 cm^{-1}. These bands are, however, shifted to 1603-1586 cm^{-1} in the spectra of the Cu(II) complexes and to 1604-1577 cm^{-1} in the spectra of the Co(II) complexes, which points to the coordination of the υ(C=N) nitrogen to the Cu(II) and the Co(II) ion [26-28]. The FT-IR spectra of the free ligands are characterized by the appearance of a band at 3275 cm^{-1} for L_1H_2, 3296 cm^{-1} for L_2H_2, 3312 cm^{-1} for L_3H_2, and 3341 cm^{-1} for L_4H_2, due to the υ(O-H) groups. In the FT-IR spectra of Cu(II) and Co(II) complexes, these bands disappear. The coordination is further confirmed by the shift in the υ(C-O) stretching vibration of the phenoxy group from the region 1257-1229 cm^{-1} to a different frequency range which indicates υ(M-O) coordination [29, 30]. The coordination of the azomethine nitrogen and the phenolic oxygen is further supported by the appearance of two peaks at 548-512 cm^{-1} for phenolic υ(M-N) and at 503-490 cm^{-1} due to υ(M-O) stretching vibrations that are not observed in the FT-IR spectra of the ligands [25]. Thus, it is clear that the free ligands are bonded to the Cu(II) and Co(II) ion in a N_2O_2 fashion through the deprotonated phenolate oxygen and the azomethine nitrogen.

3. 3. UV-Vis Spectra

Electronic spectra of the ligands and their mononuclear Cu(II) and Co(II) complexes were recorded in the 200-1100 nm range in different solutions at room temperature and the obtained data are given in Table 4. The electronic spectra of the ligands and their mononuclear Cu(II) and Co(II) complexes in the different solvents consist of very intense bands due to intraligand $\pi\rightarrow\pi^*$ and $n\rightarrow\pi^*$ transitions, metal-to-ligand or ligand-to-metal charge-transfer and d-d transitions, respectively. The absorption bands below 299 nm in different solvents are practically identical and can be attributed to $\pi\rightarrow\pi^*$ transitions in the benzene ring or azomethine (C=N) groups. The absorption bands observed below 399 nm in different solvents are most probably due to the $n\rightarrow\pi^*$ transition in the imine group corresponding to the ligands or the Cu(II) and Co(II) complexes [31, 32]. In the spectra of the corresponding mononuclear Cu(II) and Co(II) complexes, position and intensity of the bands, characteristic of the ligands appeared to be modified with respect to those of the free ligands. In addition, these spectra also presented new absorption bands in the range 400-886 nm that were characteristic of the formed mononuclear Cu(II) and Co(II) complexes. These bands were attributed to the $d\rightarrow\pi^*$ charge-transfer transitions, which overlap with the $\pi\rightarrow\pi^*$ or $n\rightarrow\pi^*$ transitions of the free ligands. These modifications in shifts and intensity for the absorption bands supported the coordination of the ligand to the central Cu(II) and Co(II) ion [33]. Also, the absorption bands in the range 400-495 nm in the different solvents are assigned to M→L charge transfer (MLCT) or L→M charge transfer (LMCT) and $^1A_{1g}\rightarrow{}^1B_{1g}$ transitions [34], respectively. The electronic spectra of Cu(II) and Co(II) in various solvents show broad bands in the range 563-886 nm, assigned to d-d transitions ($d_{xy}\rightarrow d_{x^2-y^2}$ and $d_z2\rightarrow d_{x^2-y^2}$) characteristic for tetragonal, elongated octahedral or square planar geometry [35, 36].

3. 4. Magnetic Moments

Magnetic susceptibility measurements provide sufficient data to characterize the structure of the Cu(II) and Co(II) complexes. Since the Cu(II) and Co(II) complexes are paramagnetic, their NMR spectra could be not obtained. The magnetic moments of the Cu(II) complexes at room temperature are found between 1.67-1.41 B.M., which are typical for mononuclear Cu(II) complexes with a S=1/2 spin-state and probably indicate antiferromagnetic coupling of spins at this

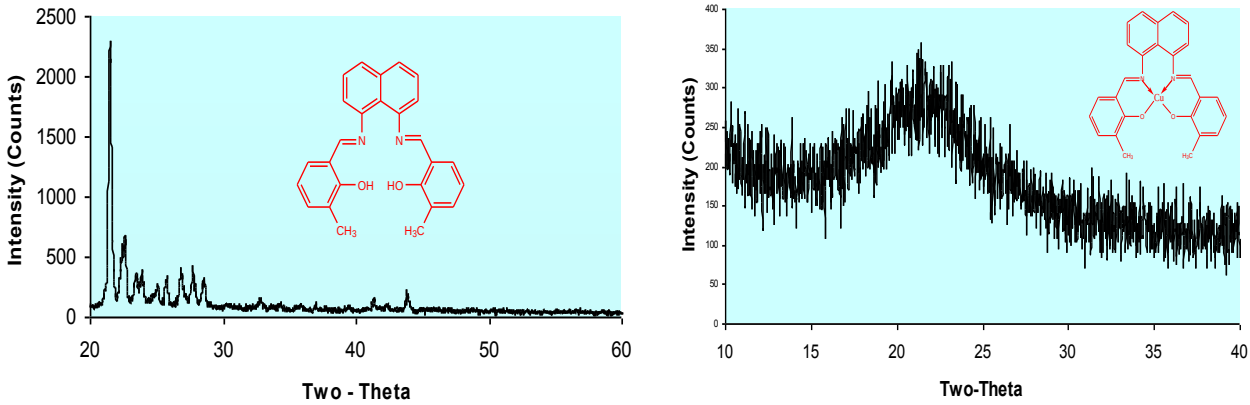

(a) **(b)**

Fig. 1. X-ray powder diffractograms of **(a)** L_1H_2 and **(b)** $[CuL_1]$

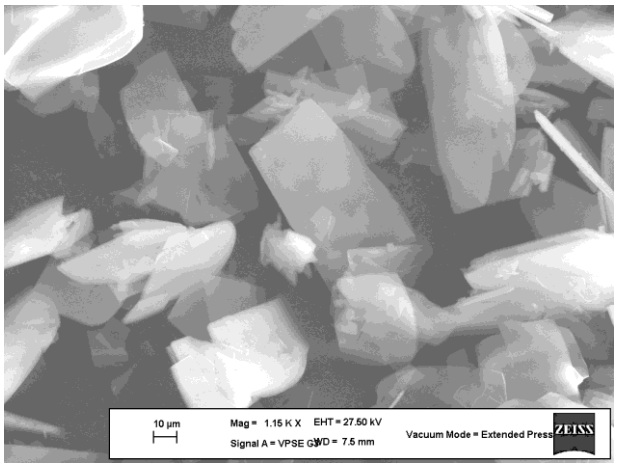

(a)

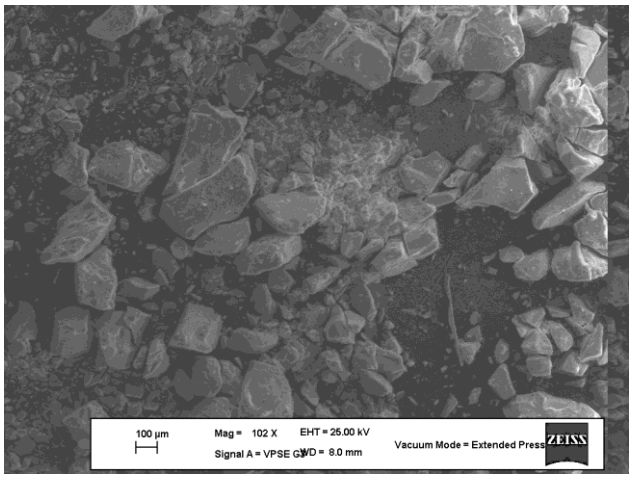

(b)

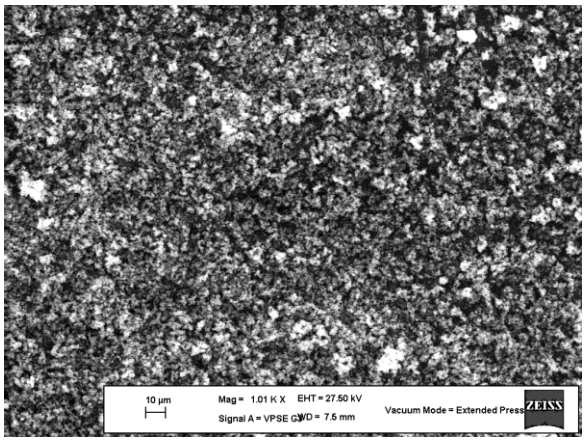

(c)

Fig. 2. SEM micrographs of **(a)** L_2H_2, **(b)** $[CuL_2]$ and **(c)** $[CoL_2]$

temperature. The magnetic moments of the d^7 Co(II) complexes at room temperature are also found between 2.27-2.15 B.M. (low-spin), which are close to the spin-only magnetic moments for one unpaired electron.

3. 5. Solubility and Molar Conductivity

The ligands L_1H_2, L_2H_2 L_3H_2 and L_4H_2 are soluble in EtOH, MeOH, DMSO and DMF solvents, while their mononuclear Cu(II) and Co(II) complexes are slightly soluble in common solvents. All complexes are stable at room temperature in the solvents reported in this study. With a view to studying the electrolytic nature of the mononuclear Cu(II) and Co(II) complexes, their molar conductivities were measured in DMF (dimethyl formamide) at 10^{-3} M. The molar conductivity (Λ_M) values of these Cu(II)

complexes are in the range of 13.7-8.6 and those of the Co(II) complexes are in the range of 12.8-9.2 $\Omega^{-1}cm^2$ mol^{-1} at room temperature, indicating their almost non-electrolytic nature (Scheme 2) [20, 37]. Due to the lack of free ions in the Cu(II) and Co(II) complexes, the results indicate that these metal complexes are very poor in molar conductivity. Probably, due to a different electron behavior, the electrical conductivity of the Cu(II) complexes differs from that of the Co(II) complexes. Conductivity measurements have frequently been used in structural elucidation of metal chelates within the limits of their solubility. They provide a method of testing the degree of ionization of the complexes, the molecular ions that a complex liberates in solution (if anions are present outside the coordination sphere), the higher will be its molar conductivity and vice versa. The molar conductivity values indicate that the anions may be present outside the coordination sphere or inside or absent [38].

3. 6. Crystallography and SEM analyses

We did not succeed in preparing single crystals of the ligands and their Cu(II) and Co(II) complexes in different solvents. However, the crystalline nature of the ligands can be readily evidenced from their X-ray powder patterns. The ligands exhibit sharp reflections and all diffractograms are nearly identical, indicating the isostructural nature of the ligands. Also, the large number of reflections, as well as their positions indicate a low crystal symmetry [39, 40]. These results point to the crystalline and not amorphous nature of the ligands. The X-ray powder patterns of the Cu(II) and Co(II) complexes exhibited, however, only broad humps, not typical for a crystalline nature (Figure 1).

The morphology of the compounds was illustrated by scanning electron micrography (SEM). Figures 2a, 2b, and 2c depict the SEM photographs of the ligand (L_2H_2), the [CuL_2] and [CoL_2] complexes. We noted that there is a uniform matrix of the synthesized complexes in the pictograph. This leads us to believe that we are dealing with a homogeneous phase material. The crystalline shape is observed in the ligand (L_2H_2). The amorphous shape is observed in the [CuL_2] and [CoL_2] complexes.

CONCLUSIONS

The synthesis, structure and spectroscopic properties of Schiff base ligands (L_nH_2) (n = 1, 2, 3 and 4) (L_1H_2 = *N,N'*-[1,8-naphthalene]-3-methylsalicylaldimine, L_2H_2= *N,N'*-[1,8-naphthalene]-5-methylsalicylaldimine, L_3H_2 = *N,N'*-[1,8-naphthalene]-3-methoxysalicyl-aldimine and L_4H_2 = *N,N'*-[1,8-naphthalene] -5-methoxysalicylaldimine), respectively and their mononuclear Cu(II) and Co(II) complexes [ML_n] are described. Classical methods such as ^{1}H-NMR, FT-IR, UV-Vis, elemental analysis, X-ray powder analysis, magnetic susceptibility and molar conductivity used for structural characterization and the SEM measurements for their morphology determination provided a powerful tool to reveal the complementary nature of the molecular structure of the new Schiff bases and their mononuclear Cu(II) and Co(II) complexes. This result agrees with the expected structure given in Scheme 2. Due to the lack of free ions in the Cu(II) and Co(II) complexes, the results indicate that these metal complexes are very poor in molar conductivity. These results show that the ligands are of crystalline and not amorphous nature, whereas the X-ray powder patterns of the Cu(II) and Co(II) complexes exhibited only broad humps, not typical for a crystalline nature.

Acknowledgements. *This work was supported, in part, by the HUBAK Fund of Harran University, Sanliurfa, Turkey.*

REFERENCES

1. H.S. Schiff, *Ann. Chim*. (Paris) **131,** 118 (1864**)**.
2. R.A. Sheldon, J.K. Kochi, Metal Catalyzed Oxidation of Organic Compounds, Academic Press, New York. (1981). p. 350.
3. T.G. Traylor, Y.S. Byun, P.S. Traylor, P. Battioni, D. Mansuy, *J. Am. Chem. Soc*. **113,** 7821 (1991).

4. J.P. Costes, G. Gros, M.H. Darbieu, Y.P. Laurent, *Trans. Met. Chem*. **7,** 219(1982).
5. D. Mansuy, *Pure Appl. Chem*. **59,** 759 (1987).
6. J.E. Kovacic, *Spectrochim. Acta* **23A,** 183 (1987).
7. A. Ourari, K. Ourari, W. Moumeni, L. Sibous, G.M. Bouet, M.A. Khan, *Trans. Met. Chem*. **31,** 169 (2006).
8. N.S. Enikolopyan, K.A. Bogdanova, K.A. Askarov, *Russ. Chem. Rev*., **52,** 25 (1983).
9. W.H. Leung, C.M. Che, *Inorg. Chem.*, **28,** 4116 (1989).
10. A.M. El-Hendawy, A.H. Alkubaisi, A. El-Ghany, K. El-Korashy, M.N. Sharab, *Polyhedron*, **12,** 2343 (1993).
11. P.J. McCarthy, R.J. Hovey, K. Veno, A.E. Martell, *J. Am. Chem. Soc*., **77,** 5820 (1955).
12. J.K. Barton, Science **233,** 727 (1986).
13. C.J. Burrows, J.G. Muller, *Chem. Rev*., **99**, 2777 (1998).
14. S. Delaney, M. Pascaly, P.K. Bhattacharya, K. Han, J.K. Barton, *Inorg. Chem*., **41,** 1966 (2002).
15. M. Odabasoglu, F. Arslan, H. Olmaz, O. Buyukgungor, *Dyes and Pigments*, **75**, 507 (2007).
16. E.J. Cambel, S.T. Nguyen, *Tetrahedron*, **42**, 1221 (2001).
17. A.J. Stemmler, C.T. Burrows, *J. Am. Chem. Soc*. **121**, 6956 (1999).
18. R. Klement, F. Stock, H. Elias, H. Paulus, M. Valko, M. Mazur, *Polyhedron*, **18**, 3617 (1999).
19. E. Gallo, C. Floriani, H. Miyasaka, N. Matsumoto, *Inorg. Chem.*, **35**, 5964 (1996).
20. Kilic, E. Tas, B. Deveci, I. Yilmaz, *Polyhedron*, **26**, 4009 (2007).
21. K.S. Suslick, T.J. Reinert, J. Chem. Educ., **62**, 974 (1988).
22. E. Hadjoudis, M. Vittoakis, I. Moustaki- Mavridis, *Tetrahedron*, **43,** 1345 (1987).
23. G.M.J. Schmidt, in: Solid State Photochemistry, Verlag Chemie, Weinheim, NewYork, 1976.
24. A. Earnshaw, Introduction to Magnetochemistry, Academic Press, London, 1968. pp. 4.
25. E. Tas, M. Aslanoglu, A. Kilic, O. Kaplan and H. Temel, *J. Chem. Res*. (S), **4,** 242 (2006).
26. E. Tas, A. Kilic, N. Konak, I. Yilmaz, *Polyhedron*, **27**, 1024 (2008).
27. O. Pouralimardin, A.C. Chamayou, C. Janiak, H.H. Monfared, *Inorg. Chim. Acta*, **360,** 1599 (2007).
28. J. L. Wyk, S. F. Mapolie, A. Lennartson, M. Hakanson, S. Jagner, *Inorg. Chim. Acta*, **361**, 2094 (2008).
29. R.B. Coles, C.M. Harris, E. Sinn, *Inorg. Chem*., **8**, 2607 (1969).
30. E. Schon, D.A. Plattner, P. Chen, *Inorg. Chem*., **43,** 3164 (2004).
31. C. Fraser, B. Bosnich, *Inorg. Chem*., **33**, 338 (1994).
32. S. Ilhan, H. Temel, I. Yilmaz, A. Kilic, *Trans. Met. Chem.*, **32**, 344 (2007).
33. A. Pui, J.P. Mahy, *Polyhedron*, **26,** 3143 (2007).
34. A.B.P. Lever, Inorganic Electronic Spectroscopy, Elsevier, Amsterdam. (1984). pp. 863.
35. J. F. Larrow, E. N. Jacobsen, Y. Gao, Y. Hong, X. Nie, C. M. Zepp, *J. Org. Chem*., **59** (1994) 1939.
36. H. Gary, C. J. Ballhausen, *J. Am. Chem. Soc*., **85**, 260 (1963).
37. R. L. Dutta, Inorganic Chemistry, Part II, 2nd Ed., The New Book Stall, Calcutta, (1981) p.386.
38. M. S J. Refat, *J. Mol. Struct*., **742**, 24 (2007).
39. B. R. Srinivasan, N. S. Dhuri, C. Nathar, W. Bensch, *Trans. Met. Chem*., **32,** 64 (2007).
40. A. Kilic, E. Tas, I. Yilmaz, *J. Chem. Sci*., **121,** 43 (2009).

АСИМЕТРИЧНИ ТЕТРАДЕНТАТ САЛИЦИЛАЛДИМИНОВИ CU(II) И CO(II) КОМПЛЕКСИ, ПОЛУЧЕНИ ОТ 1,8-НАФТАЛИН И РАЗЛИЧНИ САЛИЦИЛАЛДЕХИДИ

А. Килич[1], Е. Тас[2], Б. Девичи[1], М. Дургун[1]*

[1]*Департамент по химия, Университет в Харан, 63190 Санлиурфа, Турция*

[2]*Департамент по химия, Университет в Сиирт, 56100, Сиирт, Турция*

Постъпила на 17 юни 2011, Приета на 9 януари 2012

(Резюме)

Описани са синтезът, структурата и спектроскопските свойства на лиганди на салицилалдиминови Шифови бази (L_nH_2) (n = 1, 2, 3 и 4) (L_1H_2=*N, N'*-[1,8-нафталин]-3-метилсалицилалдимин, L_2H_2 = *N,N'*-[1,8-нафталин]-5- метилсалицилалдимин, L_3H_2 = *N,N'*-[1,8- нафталин]-3-метокси-салицилалдимин и L_4H_2= *N,N'*-[1,8-нафталин]- 5-метоксисалицил- алдимин), съответно и техните мононуклеарни Cu(II) и Co(II) комплекси [ML_n]. Четири нови асиметрични тетрадентат салицилалдиминови лиганди, съдържащи донорни групи N_2O_2, са получени чрез реакция на 1,8- нафталин с различни салицилалдехиди. Тетрадентатни Cu(II) и Co(II) комплекси са получени чрез реакция на лигандите с $Cu(Ac)_2.H_2O$ и $Co(Ac)_2.4H_2O$ в моларно съотношение 1:1. Лигандите и техните Cu(II) и Co(II) комплекси бяха характеризирани чрез ^{1}H-NMR, FT-IR, UV-Vis, елементен анализ, моларна проводност, магнитна чувствителност, Рентгенов прахов анализ и беше изследвана тяхната морфология чрез SEM измервания.

Bulgarian Chemical Communications, Volume 44, Number 4 (pp. 299 - 306) 2012

Field sampling, speciation and determination of dissolved iron (II) and iron (III) in waters

S. Arpadjan[1*], K. Tsekova[2], P. Petrova[3], J. Knutsson[3],

[1]*Faculty of Chemistry, University of Sofia, 1164 Sofia, bld. J. Bourchier 1*
[2]*Institute of Microbiology, Microbial Ecology Dept., Bulgarian Academy of Sciences, Acad. G. Bonchev Str., bl. 26, 1113 Sofia, Bulgaria*
[3]*Chalmers University, Fysikgränd 3, 41296 Gothenburg, Sweden*

Received: October 31, 2011; Revised: January 12, 2012

A simple and rapid field sampling procedure was developed for the speciation of dissolved Fe(II) and Fe(III) in waters. The determination of iron species was possible by selective batch solid phase extraction of Fe(III) using chelating resin Chelex-100 in H^+ form, sample acidity range of pH 1.5–2.5, elution with 0.03 mol L^{-1} NH_4-EDTA, and detection of Fe(III) by flame or electrothermal atomic absorption spectrometry (ETAAS). The concentration of Fe(II) was determined in the solution above the resin by direct ETAAS or after adsorption on Chelex-100 in NH_4^+ form without the need for preoxidation of Fe(II) to Fe(III). Water samples were collected *in situ* and filtered by passing them through a syringe filter (0.45 μm). The batch procedure was performed at the field and then, the tubes containing the resins with the loaded analytes were returned to the laboratory where the iron species were eluted and determined. Field sampling prevents changes in the oxidation state of iron. The effect of humic acid was also investigated. The results obtained indicated that the method was not affected by the presence of up to 0.01% humic acid. The limit of detection (3*s*) was 0.8 μg L^{-1} Fe (ETAAS detection). The relative standard deviation (*n*=10) ranged from 2% at the 1 mg L^{-1} Fe up to 20% at the 1 μg L^{-1} Fe(III) level. Recoveries of spiked Fe(II) and Fe(III) in river, lake, tap and groundwater samples ranged from 93 to 105%.

Key words: Iron speciation, Chelex-100, ETAAS, Humic acids, Water analysis

INTRODUCTION

Iron has an essential role for many metabolic functions and is one of the most important elements in environmental and biological systems. In fresh waters, iron is also an important nutrient for phytoplankton and other organisms. It is known that the biological activity in certain ocean regions is affected by iron [1]. Iron is not normally considered a toxic element, but it becomes toxic when accumulated, especially when present as free ion [2–4]. The question about the comparative toxicity of ferrous and ferric ions has not been clarified. In general, Fe(II) is considered to be more toxic than Fe(III) because it may cause cell degeneration [5–7]. The probable mechanism of this process involves iron catalysed auto-oxidation reactions, which generate hydroxyl-free radicals. The environmental and biological effects of iron depend on its oxidation state, solubility and the degree of complex formation. The ratio between the oxidation states Fe(III)/Fe(II) in waters depends on redox, light and flow conditions, pH, and the amount and type of dissolved organic matter. The main fraction of dissolved iron(III) is strongly complexed by organic ligands [8–10] as humic acids or organic substances produced by phytoplankton [11] or bacteria [12]. This organic complexation prevents the formation of insoluble oxyhydroxides. Iron(II) is thermodynamically unstable and is rapidly oxidized to iron(III). This oxidation is accelerated by some micro-organisms, trace metals, phosphate and fluoride ions and particles, including autocatalysis by fresh Fe oxides. However, dissolved or colloidal organic ligands, sulfate, nitrate and chloride ions may stabilize Fe(II) and retard its oxidation [13]. Further, Fe(III) complexed with organic compounds can be readily photoreduced by UV light to Fe(II) [14]. Accurate and precise measurements of iron redox species are important in the study of aqueous environmental chemistry and oceanic biogeochemistry. It will be beneficial to clarify the role of the two oxidation states of this element, and the essentiality and toxicity of both Fe(II) and Fe(III). Critical reviews of historical and current analytical methods for the determination of

* To whom all correspondence should be sent:
E-mail:sganeva@chem.uni-sofia.bg

© 2012 Bulgarian Academy of Sciences, Union of Chemists in Bulgaria

total dissolved iron and iron speciation in waters were presented by Pehkonen [15], Achterberg et al. [16] and Pohl and Prusisz [17]. Very low concentrations of iron species in non polluted waters and high reactivity of iron species poses a major challenge for redox speciation measurements. The ideal analytical strategy would be the direct *in situ* determination of Fe(III) and Fe(II) with minimal manipulation, use of minimal reagent amounts and minimal laboratory or research equipment. Flow injection techniques using resin-based column chromatography were developed to fulfill most of these requirements [17, 18]. A main drawback of these methods is that the selective complexing agents used can shift the iron redox speciation [17, 19, 20] and the necessity of preliminary oxidation or reduction of iron species. Some of the procedures require adjustment of pH higher than 4 [18] which changes the concentration of labile iron species. In addition, the flow injection systems are laboratory made and commercially not available constructions. Atomic absorption spectrometry and inductively coupled plasma mass spectrometry techniques applied for dissolved iron speciation require laboratory performance [21, 22]. In this case, the risk of changing of the oxidation state of iron during sample preservation and transportation always exists [23]. On the other hand, methods for *in situ* field sampling of several elements, allowing the final species determination in the laboratory, have been already published [22–25]. In this paper, the analytical potential of Chelex-100 resin in H^+ form for solid phase extraction separation/preconcentration of dissolved iron species and their *in situ* field sampling using batch process is investigated. The method involves final elution of Fe(III) species from the Chelex-100 in the laboratory using NH_4-EDTA as eluent and final detection of iron species using flame or electrothermal atomic absorption spectrometry.

EXPERIMENTAL

Instrumentation. The flame AAS technique used was AA400 (Perkin-Elmer) in an air acetylene flame. The light source was a hollow cathode lamp for Fe, wavelength 283.3 nm. The instrumental parameters were set up to obtain maximum signal to noise ratio. The ETAAS measurements were carried out using a Perkin-Elmer (Norwalk, CT, USA) Zeeman 3030 spectrometer with an HGA-600 graphite furnace. The spectral bandpass was 0.2 nm. Pyrolytic coated graphite tubes were used as atomiser. Autosampler AS-60 was used for injections of 20 µL sample solutions into the graphite tube. Only peak areas were used for quantification. The graphite furnace operating parameters for modifier-free ETAAS measurements of Fe were: drying at 120 ºC, pretreatment at 1100 ºC, atomization at 2100 ºC, cleaning at 2500 ºC.

Reagents and materials. All reagents used were of analytical reagent grade. Milli-Q water was used throughout. The stock standard solution of 1 g L^{-1} Fe(III) was prepared from Titrisol (Merck, Darmstadt, Germany) in 0.5 mol L^{-1} hydrochloric acid (p.a. Merck). The standard solution of 1g L^{-1} Fe(II) was prepared by dissolving 3.5111 g of ferrous ammonium sulfate hexahydrate (Sigma-Aldrich) in 500 mL of 0.5 mol L^{-1} HCl. The exact concentration of Fe(II) in the stock solution was checked by titration with standardized potassium permanganate. Working standard solutions for calibration were prepared by appropriate stepwise dilution of their stock solutions just before use. The hydrochloric acid was preliminary purified by isothermal distillation. Ethylenediaminetetraacetic acid diammonium salt (NH_4-EDTA) was prepared from EDTA-disodium salt (p.a. Merck) after precipitation as ethylenediaminetetraacetic acid with 6 mol L^{-1} HCl and subsequent dissolution of the precipitate in NH_4OH (p.a. Merck, additionally purified by isothermal distillation). Humic acid was supplied by Fluka, Switzerland. The chelating resin Chelex-100 (50–100 mesh, sodium form, Bio-Rad, UK) was previously NH_4-EDTA and water washed. The resin was converted to the H^+ form by stirring with 0.02 mol L^{-1} HCl for 20 min, followed by several water washes (till neutral reaction). Sterile polyethylene centrifuge tubes (15 and 50 mL), pasteur pipettes and syringe filters (0.45 µm) were NH_4-EDTA and Milli-Q water washed before use.

Water samples. For laboratory experiments and method development distilled water, river water from the local river (Perlovska), local tap water and groundwater (collected from 12.8 m depth) were used. River and ground waters were filtered through 0.45 µm pore size Millipore cellulose acetate membrane filters. The optimized procedure was further applied for *in situ* sampling/separation of dissolved Fe(II) and Fe(III) species (free ions and their labile complexes) in several rivers in Bulgaria (Danube, Iskar, Mariza, Ropotamo, Veleka, Struma, Mesta, Vladajska) and in lake Pancharevo situated near to Sofia city. The standard reference materials, SLRS-5 (river water) and a mineral water sample (Devin: pH 9.5, 62 mg L^{-1} Na^+, 18 mg L^{-1} SO_4^{2-}, 4 mg L^{-1} F^-, 2.3 mg L^{-1} Cl^-) from national proficiency testing procedure were

analysed to check the accuracy of the developed method for determination of total iron in water.

Procedure for iron speciation. The sample was acidified with 6 mol L^{-1} HCl to pH 2–2.5. The polyethylene centrifuge tube (15 mL) was rinsed with about 2 mL of the sample. Then 14 mL of the sample and 0.5 g of the sorbent Chelex-100 in H^+ form were placed in the tube. The tube was closed and the sample with the resin was shaken manually for 2 min. During this process, Fe(III) was removed from the water sample onto the chelating resin, Fe(II) remained in the aqueous solution above the resin. This aqueous solution was transferred to a second 15 mL polypropylene centrifuge tube using pasteur pipettes. For elution of the sorbed Fe(III) 3 mL of 0.03 mol L^{-1} NH_4-EDTA were added to the chelating resin, the tube was closed and the resin with the eluent was shaken manually for 3 min. The concentration of eluted Fe(III) was determined by flame AAS or ETAAS. Three blank samples were prepared in parallel. The concentration of Fe(II) can be determined direct or after the same preconcentration/elution procedure as for Fe(III), using the chelating resin Chelex-100 in ammonium form.

For preconcentration and determination of total dissolved iron a second aliquot (14 mL) of the same sample (acidified to pH 2–2.5) was placed in a new pre-rinsed polyethylene centrifuge tube. Then 0.5 g of the sorbent Chelex-100 in NH_4^+ form was placed in the tube. The tube was closed and the sample with the resin was shaken manually for 2 min. During this process both Fe(II)+Fe(III) were retained by the resin. The aqueous phase above the resin was removed using pasteur pipettes. The sorbent with the loaded total iron was two times water washed. Then 3 mL of 0.03 mol L^{-1} NH_4-EDTA were added to the sorbent, the tube was closed and the resin with the eluent was shaken manually for 3 min. The concentration of eluted Fe(II) + Fe(III) was determined by flame AAS or ETAAS. Two blank samples were prepared in parallel.

RESULTS AND DISCUSSION

Optimization of the batch procedure. The most important factor which affects the speciation, preconcentration and determination of iron species was the acidity of the samples. The range of pH investigated was between 1 and 8. The recovery values obtained using the proposed method for the Fe(II) and Fe(III) species as a function of pH are shown in Fig. 1. The results showed that the sorption of Fe(III) onto the Chelex-100 in H^+ form

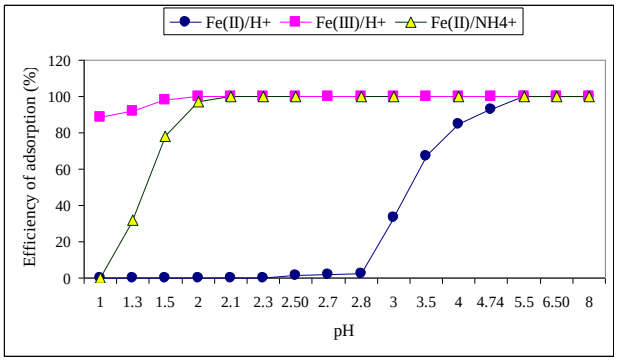

Fig.1. Influence of pH on adsorption of iron species on Chelex-100 in H^+ form (sample volume 10 mL, 5 mg L^{-1} Fe(II, III), contact time 5 min).

was quantitative between pH values of 1.5 and 8. In the pH range 1.5–2.5 the ferrous ions were not retained on the sorbent at all. This means that at pH 1.5–2.5 the Chelex-100 in H^+ form selectively retains Fe(III), making possible to quantitatively separate Fe(II) and Fe(III). The reason for this high selectivity is the big difference in the stability of chelate complexes formed between iron species and ligands containing iminodiacetic functional groups. The high recovery values for Fe(III) even at low pH values using Chelex-100 in H^+ form can be explained with the high conditional formation constant (β′) of Fe(III)-IDA complex at pH 2 (log β′= 10.7–11.1) [26, 27]. Chemosorption for Fe(II) under this conditions is not possible (log β′ (Fe(II)-IDA) < 0.6). Retention on Chelex-100 in H^+ form due to ion exchange is also not possible in acidic media because the equilibrium

$$\text{-R-N-}(CH_2COOH)_2 + Fe(II) \leftrightarrow \text{-R-N-}(CH_2COOFe/2)_2 + 2H^+$$

(Chelex-100 in H^+ form)

is shifted to the left and the protons on the sorbent functional groups cannot be exchanged with iron ions at pH 1.5–2.5. These are the reasons for the non-adsorptivity of Fe(II) ions which allows the subsequent quantitative separation of Fe(II) and Fe(III). The sorption recoveries obtained for both iron species at pH values between 2 and 2.5 were higher than 95% when the chelating resin Chelex-100 was in its ammonium form (Fig. 1). This allows to achieve quantitative separation using the chelating resin Chelex-100 in H^+ form for selective sorption of Fe(III) at pH 1.5–2.5 and in NH_4^+ form for sorption of total Fe(III)+Fe(II) at pH 2–2.5. The proposed procedure allows to estimate the content of the free Fe(II) and Fe(III) species released in this acidic medium and their labile complexes with inorganic or organic ligands.

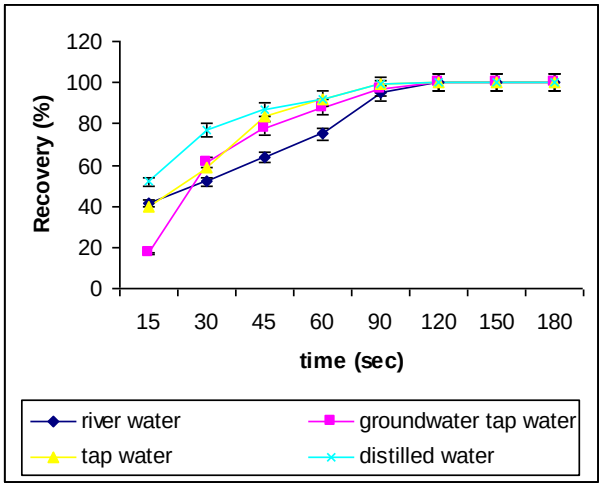

Fig.2. Kinetics of adsorption of Fe(III) on Chelex-100 in H^+ form (sample volume 10 mL, 5 mg L^{-1} Fe(III), pH 1.8–2.2).

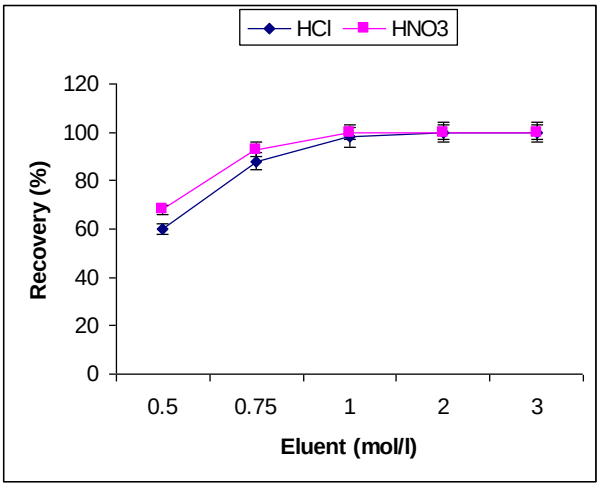

Fig. 3. Recoveries for elution of Fe(III) from Chelex-100 by the use of different concentrations of HCl and HNO_3 (volume of eluent 3 mL, elution time 5 min).

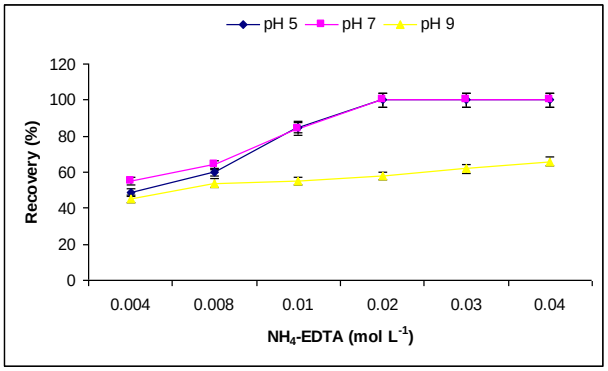

Fig. 4. Recoveries for elution of Fe(III) from Chelex-100 by the use of different concentrations of NH_4–EDTA (volume of eluent 3 mL, elution time 5 min).

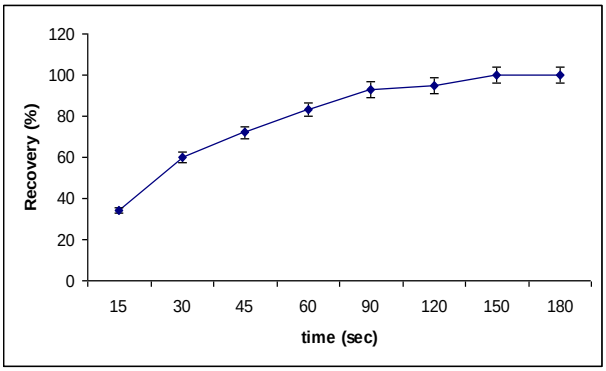

Fig. 5. Recoveries for elution of Fe(III) from Chelex-100 by the use of 3 mL of 0.03 mol L^{-1} NH_4–EDTA at pH 5 as a function of elution time.

To optimize the adsorption procedure, the kinetics of the retention of Fe(III) was investigated using 5 mg L^{-1} Fe(III) spikes in distilled, river, tap and groundwater. The contact time was varied between 15 sec and 5 min. The concentration of the non-sorbed Fe was measured in the aqueous layer above the Chelex-100 resin using flame AAS. The results are presented in Fig. 2. Obviously independent of the sample type, 2 min shaking time are sufficient for quantitative sorption of Fe(III). The experiment was repeated with spike concentrations of 100 µg L^{-1} Fe(III) to distilled water and ETAAS measurement of the concentration of the non-retained Fe. The same sorption behavior of Fe(III) was registered. Hence, 2 min sorption time can be considered as optimal.

Important step in the optimization of a solid phase extraction procedure is the choice of appropriate eluent. Quantitative elution of iron adsorbed on Chelex-100 was achieved with 3 mL of 1–3 mol L^{-1} HCl or HNO_3 or with 3 mL of 0.02–0.05 mol L^{-1} NH_4-EDTA (pH 5–7), as can be seen from Figs. 3 and 4. The use of NH_4-EDTA as eluent is preferable because in this case the same resin can be reused at least ten times for separation/preconcentration purposes. Hydrochloric and nitric acids destroy the resin and it cannot be used again. In addition, the ammonium salt of EDTA does not cause any interference during the analytical measurement by AAS. In all further experiments 0.03 mol L^{-1} NH_4-EDTA was used as eluent. The results for the kinetics of elution are presented in Fig. 5. Three minutes elution time were accepted as optimal.

It was found that the sorption recovery depends on the sample volume. In the investigated concentration range 0.1–5 mg L^{-1} the retention of Fe(III) is quantitative up to 14 ml sample for all studied waters. For 20 ml sample volume the recoveries varied between 74 and 80% in dependence on the water type. When the procedure was performed with 25 ml sample, the recoveries were between 60 and 65%.

Table 1. Efficiency of sorption (%) of Fe(III) in dependence on the water temperature (10 mL sample (pH 2), 2 min contact time; number of parallel determinations *n*=2–3

Temperature (^oC)	Chelex-100 in H^+ form 5 mg L^{-1} Fe(III)	0.5 mg L^{-1} Fe(III)	0.05 mg L^{-1} Fe(III)	Chelex-100 in NH_4^+ form 0.5 mg L^{-1} Fe(III)	0.05 mg L^{-1} Fe(III)
6 ± 2	72 ± 5	78 ± 5	82 ± 6	95 ± 3	96 ± 3
10 ± 2	88 ± 2	92 ± 4	91 ± 5	98 ± 2	97 ± 1
14 ± 2	95 ± 3	96 ± 2	96 ± 3	98 ± 3	97 ± 3
16 ± 2	98 ± 4	97 ± 2	98 ± 3	97 ± 2	99 ± 1
20 ± 2	99 ± 2	100 ± 1	99 ± 1	99 ± 2	98 ± 3

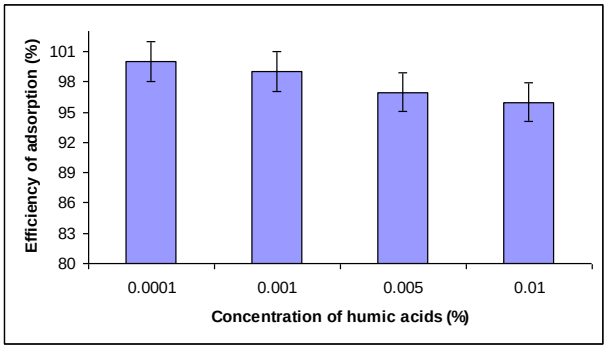

Fig. 6. Efficiency of adsorption of 5 mg L^{-1} Fe(III) on Chelex-100 in H^+ form (sample volume 10 mL, contact time 2 min).

For an in situ experiment it was also important to investigate the influence of the water temperature on the sorption of Fe(III). The results from these investigations are presented in Table 1. The effect of the water temperature on the adsorption efficiency depends on the chelating resin form and does not depend on the iron concentration in the range 0.05–5 mg L^{-1} Fe. At pH 2 the Chelex-100 in H^+ form is sufficiently effective at temperatures above 10°C. The chelating resin in NH_4^+ form is not so temperature sensitive. The DGT devices for passive sampling contain Chelex-100 chelating resin beads in ammonium or sodium form and at pH values of the natural waters the low temperatures are not expected to hinder the adsorption of free ions.

The effect of humic acid. Humic acids form relatively stable complexes with metal ions in natural systems. This was the reason to investigate their effect on the sorption of Fe(III) on Chelex-100 in H^+ form. The concentration range studied was 0.0001–0.01% humic acid, the pH range was 1.5–2.5. The results obtained (Fig. 6) indicated that the quantitative retention of Fe(III) is not affected by the presence of up to 0.01% humic acid.

Preconcentration of other ions. It was expected that other ions which could be quantitatively retained by Chelex-100 in H^+ form at low pH values, are ions producing complexes with EDTA with very high formation constants. Experiments were conducted to investigate the sorption of Bi(III), Tl(III), Sb(III), Sb(V), Sn(II) and Sn(IV) on Chelex-100 in H^+ form at pH 2 using batch procedure for 2 min contact time, i.e. at the optimal conditions for retention of Fe(III) and separation from Fe(II). The results showed that Bi(III), Tl(III), Sb(III) and Sn(II) were totally retained on the sorbent (> 97% retention). The sorption degree of Sn(IV) was around 82% and that of Sb(V) – around 34%. At the same experimental conditions Cu(II) was totally sorbed, while 60% of Pb(II), 40% of Ni, 25% of Cd, 20% of Co and Mn were sorbed. The adsorption of Fe(III) was not interfered by the presence of up to 1 mg L^{-1} Bi(III)+Tl(III)+Sb(III,V)+Sn(IV) as well as of up to 10 mg L^{-1} Cu(II) and of 20 mg L^{-1} Cd(II)+Co(II)+Ni(II)+Mn(II)+Pb(II). Tin(II) could change the oxidation state of iron by reducing the concentration of Fe(III) species if present in concentrations equal or higher to that of iron.

Analytical performance. Quantification has been performed based on calibration using aqueous standards for Fe(III) prepared in 0.3 mol L^{-1} HNO_3. The correlation coefficient R^2 of the calibration curves was 0.9996 for flame AAS (number of points 5) and 0.9991 for ETAAS (number of points 7). The detection limit was 0.8 μg L^{-1} Fe (ETAAS detection) and was evaluated as the concentration corresponding to three times the standard deviation of ten replicate measurements of a blank sample. The accurate determination of trace iron species requires low and reproducible blanks. The procedural blank based on 10 mL sample volume was (2.6±0.4) ng (analysis of five separate aliquots), provided: i) pre-cleaning of tubes, pipettes and syringe filters with 0.01 mol L^{-1} EDTA, followed by several Milli-Q water washes; ii) use of sterile disposable polyethylene centrifuge tubes; iii) preliminary check (ETAAS) for Fe content of the Milli-Q water and of all reagents and sorbents used. The relative standard deviation (*n*=10) ranged from 2% at the 1 mg L^{-1} Fe up to 20% at the 1 μg L^{-1} Fe(III) level.

To examine potential interference effects and to prove the accuracy of the proposed method in case of real samples, spike experiments were performed with river water, tap water and groundwater. The

Table 2. Determination of iron species in waters (mean ± *s*, number of parallel determinations *n* = 3)

Samples	Added (μg L^{-1})		Found (μg L^{-1})		Mean recovery (%)	
	Fe(II)	Fe(III)	Fe(II)	Fe(III)	Fe(II)	Fe(III)
SLRS-5*	0	0	< 0.8	101±3		101.0
Mineral water**	0	0	< 0.8	9.3±0.6		93.0
River water	0	0	19±1	57±3		
	20	50	37±3	108±6	94.9	100.9
	50	20	65±4	80±3	94.2	103.9
Tap water	0	0	< 0.8	39±3		
	10	50	10.5±0.8	88±7	105.0	98.9
Lake water	0	0	< 0.8	11±1		
	10	10	10.2±0.8	20 ± 2	102.0	95.2
	20	0	18.9±1.3	10.7±0.8	94.5	
Groundwater	0	0	57±4	29±2		
	50	50	111±5	72±6	103.7	91.1

*certified value: (100 ± 2) μg L^{-1} Fe
**accepted value: 10 μg L^{-1} Fe

Table 3. Iron species in waters (*n*–number of parallel determinations).

Sample	Fe_{total} (direct ETAAS) (μg L-1)	Fe(III)	Fe(II) (separation/ preconcentration)* (μg L-1)	$Fe_{tot.}$calculated / measured	Fe(III)/ Fe_{total} (%)
River Danube (n=3)	23 ± 2	17 ± 2	7 ± 1	1.04	72 ± 4
River Iskar (n=3)	34 ± 2	27 ± 2	6.8 ± 0.8	0.99	79 ± 5
River Mesta (n=3)	84 ± 3	60 ± 3	25 ± 2	1.01	71 ± 5
River Struma (n=3)	16 ± 1	11 ± 1	4.3 ± 0.7	0.96	67 ± 4
River Maritsa (n=3)	21 ± 1	13 ± 2	6.4 ± 0.8	0.97	62 ± 3
River Ropotamo(n=2)	182 ± 8	126 ± 6	58 ± 2	1.01	69 ± 3
River Veleka (n=3)	12 ± 1	7.7 ± 0.8	4.3 ± 0.6	1.02	64 ± 4
River Perlovska (n=5)	76 ± 2	57 ± 3	19 ± 2	1.00	75 ± 3
River Vladajska (n=4)	56 ± 2	43 ± 3	14 ± 1	1.02	77 ± 4
Tap water (n=5)	39 ± 2	40 ± 3	< 0.8	1.03	> 98
Lake water (n=3)	11 ± 1	10.6 ±0.8	< 0.8	0.96	> 98
Groundwater (n=4)	83 ± 6	29 ± 2	57 ± 4	1.04	34 ± 5

* Inorganic Fe(III) and Fe(II) species measured after separation/preconcentration on Chelex-100 in H^+ (for quantification of Fe(III) species) and NH_4^+ form (for quantification of Fe(II) species) at pH 2.

river water reference material SLRS-5 was 10 fold diluted and analysed according to the described procedure. Mineral water sample from national proficiency testing experiment was analysed according to the described procedure. All results of the accuracy tests are summarized in Table 2. The evaluated recoveries for Fe(II) and Fe(III) were in the range 93–105%, i.e. within the accepted range (90–110%) for the examined concentration levels [28]. In addition, the accuracy of the proposed procedure was validated by comparing the sum of the concentrations of individual iron species with that of total iron concentration. The ratio between the sum of the values for Fe(II) and Fe(III) determined individually and total iron concentration measured by direct ETAAS or after preconcentration (*Procedure for iron speciation*) was in the range 0.96–1.04 (Table 3).

The main advantages of the described batch procedure consist in: simplicity; possibility to

separate the species within 10–15 minutes after sampling thus preventing any redox changes due to transportation and storage [23]; use of commercially available chelating resin; possibility to determine both inorganic iron species separately at the same sample pH value using the chelating resin either in H^+ form or in ammonium form; separation/preconcentration without preliminary oxidation or reduction of analytes; no use of complexing agents. The chelating resin itself is not expected to change the iron redox state because it is known that aminocarboxylic acids are used to preserve the elements oxidation state due to fast formation of stable complexes. At pH 2 (applied for separation /preconcentration in the proposed procedure) it could be expected that all iron species in the studied water exist as free hydrated ions or labile iron complexes. At the pH values of most environmental waters (pH around 6 for tap water and pH > 7 for river and lake water) iron exists in form of stable complexes with some naturally occurring ligands as humic acids and fluorides. These complexes almost completely dissociate at pH 2. In this way, with the described procedure we determine the oxidation state of iron included in stable complexes with naturally existing ligands. At pH 2 the chelating resin gel swells, but this does not present any problem for batch procedure performance.

In situ field sampling, separation/preconcentration and sample analysis.

The sampling and speciation steps were performed off-line and *in situ* on the field. The sampling was performed on the coast of the river and the lake. The samples were taken using disposable syringes (20 mL). The syringes were at least three times rinsed with the examined sample. After sampling the sample was filtered through 0.45 μm syringe filter and the filtrate was collected in a 50 mL polyethylene centrifuge tube. To 50 mL of filtrate 100 μL of 6 mol L^{-1} HCl was added by Eppendorf pipette to adjust pH around 2 and then two aliquots of 14 mL were analysed for iron species as described in

Procedure for iron speciation.

The results obtained for the distribution of iron species in environmental waters are given in Table 4. Inorganic Fe(II) species and their labile complexes were not detected in tap and lake waters. These results agree with the results of Yan et al.[21] for tap water and disagree with the data reported by Pehlivan and Kara (27% Fe(II) in tap water) [22]. The tap water in Sofia is used as drinking water and is usually chemically treated before use, which explains the absence of Fe(II) species in our case. In river waters the Fe(III) species and their labile complexes were found as the predominant iron oxidation form representing 64–78 % of total iron concentration. Similar results for river waters were reported by Yan et al. (69% Fe(III)) [21], Pehlivan and Kara (74% Fe(III)) [22] and Bağ et al. (67% Fe(III)) [29]. In groundwater, the Fe(II) species represented 59–66 % of the total iron.

CONCLUSION

The batch solid phase extraction procedure using chelating resin Chelex-100 in hydrogen form as sorbent allows *in situ* field sampling and separation/preconcentration of dissolved Fe(II) and Fe(III) in waters. The developed method is simple, fast, reliable and cost effective. The use of the chelating resin in both H^+ form (for Fe(III)) and ammonium form (for Fe(II) or total iron) allows to separate/preconcentrate the iron species at the same sample acidity without preliminary oxidation or reduction. The contents of inorganic Fe(II) and Fe(III) species can be determined separately. The separation/preconcentration proceeds at pH of 2–2.5, which ensures high degree of dissociation of iron-natural ligands complexes. The method was used for the speciation of iron in river, tap, ground and lake waters with satisfactory precision and accuracy. It was found that the predominant form in all waters except groundwater is Fe(III).

Acknowledgements: *The authors gratefully acknowledge the financial support provided by Bulgarian Ministry of Education (Grants BY-X-207/06 and DOO2-185/2008).*

REFERENCES

1 J.H. Martin, S.B. Fitzwater, *Nature*, **331**, 341 (1988).
2 D.L. Tsalev, Z.K. Zaprianov, *Atomic Absorption Spectrometry in Occupational and Environmental Health Practice*, CRC Press, Florida, Vol. 1, 1983, p. 132.
3 P. Ponka, M. Tenenbein and J. Eaton, *Iron*, in *Handbook on the Toxicology of Metals*, G. Nordberg, B. Fowler, M. Nordberg, L. Friberg (eds.), Elsevier, 2007.
4 K.-M. Vuori, *Ann. Zool. Fennici*, **32**, 317 (1995).
5 B. Halliwell, J.M. Gutteridge, *Biochem. J.*, **219**, 1 (1984).
6 R.G. Stevens, D.R. Kalkwarf, *Environ. Health Persp.*, **87**, 291 (1990).

7 T. Obata, H. Hosokawa, Y. Yamanaka, *Comp. Biochem. Physiol*., **106C**, 629 (1993).
8 M. Gledhill, C.M.G van den Berg, *Mar. Chem*., **47**, 41 (1994).
9 E.L. Rue, K.W. Bruland, *Mar. Chem*., **50**, 117 (1995).
10 R.F. Nolting, L.A. Gerringa, M.W. Swagerman, K.R. Timmermans, H.J.W. de Baar, *Mar. Chem*., **62**, 335 (1998).
11 E.L. Rue, K.W. Bruland, *Limnol. Oceanogr*., **42**, 901 (1997).
12 J. Granger, N.M. Price, *Limnol. Oceanogr*., **44**, 541 (1999).].
13 T.L. Theis, P.C. Singer, *Environ. Sci. Technol*., **8**, 569 (1974).
14 B. Sulzberger, J.L. Schnoor, R. Giovanoli, J.G. Hering, J. Zobrist, *Aquatic Sci*., **52**, 56 (1990).
15 S. Pehkonen, *Analyst*, **120**, 2655 (1995).
16 E.P. Achterberg, T.W. Holland, A.R.Bowie, R.F.C. Mantoura, P.J. Worsfold, *Anal. Chim. Acta*, **442**, 1 (2001).
17 P. Pohl, B. Prusisz, *TrAC Trends in Analytical Chemistry*, **25**, 909 (2006).
18 K. Jitmanee, S.K. Hartwell, J. Jakmunee, S. Jayasvasti, J. Ruzicka, K. Grudpan, *Talanta*, **57**, 187 (2002).
19 H.S. Hong, D.R. Kester, *Limnol. Oceanogr*., **31**, 512 (1986).
20 R.J.M. Hudson, D.T. Covault, F.M.M. Morel, *Mar. Chem*., **38**, 209 (1992).
21 X.-P. Yan, M.J. Hendry, R. Kerrich, *Anal. Chem*., **72**, 1879 (2000).
22 E. Pehlivan, D. Kara, *Microchim. Acta*, **158**, 137 (2007).
23 P. L. Croot, P. Laan, *Anal. Chim. Acta*, **466**, 261 (2002).
24 B. Fairman, A. Sanz-Medel, *J. Anal. At. Spectrom*., **10**, 281 (1995).
25 W. Jiang, M.I. Mena, C.W. McLeod, J. Rollins, *J. Environ. Anal. Chem*., **57**, 99 (1994).
26 G. Anderegg, *Inorg. Chim. Acta*, **121**, 229 (1986).
27 J. Sanchiz, P. Esparza, S. Domínguez, F. Brito, A. Mederos, *Inorg. Chim. Acta*, **291**, 158 (1999).
28 M. Thompson, S.L.R. Ellison, A. Fajgelj, P. Willets, R. Wood, *HarmonisedGuidelines for the use of recovery information in analytical measurement* (IUPAC/ISO/AOAC International/EURACHEM, Technical Report, 1996).
29 29. H. Bağ, A.R. Türker, A. Tunçeli, M. Lale, *Anal. Sci*., **17**, 901 (2001).

ПОЛЕВО ПРОБОВЗЕМАНЕ, ОПРЕДЕЛЯНЕ НА РАЗТВОРЕНИТЕ ХИМИЧНИ ФОРМИ НА ЖЕЛЯЗО (II) И ЖЕЛЯЗО (III) ВЪВ ВОДИ

С. Арпаджян[1*], К. Цекова[2], П. Петрова-Кнутсон[3], Й. Кнутсон[3],

[1]*Химически Факултет, Софийски университет, 1164 София, бул .Дж. Буршиер1*
[2]*Институт по Микробиология, Българска академия на науките, ул. "Акад.Г.Бончев" бл. 26, 1113 София, България*
[3]*Чалмерс университет, ул. Физикгранд 3, 41296 Гьотеборг, Швеция*

Постъпила на 31 октомври, 2011 г.; преработена на 12 януари, 2012г.

(Резюме)

Разработена е проста и бърза процедура за определяне на разтворените химични форми на Fe(II) и Fe(III) във води. Определянето на химичните форми на желязо е възможно след селективна твърдофазна екстракция на Fe(III) върху хелатираща смола Chelex-100 в H^+ форма, киселинност на пробата в областта pH 1.5–2.5, елуиране с 0.03 mol L^{-1} NH_4-EDTA и определяне на Fe(III) с пламъкова или електротермична атомноабсорбционна спектрометрия (ETAAS). Концентрацията на Fe(II) в разтвора над сорбента се определя директно с или след сорбция върху Chelex-100 в NH_4^+ форма без необходимост от предварително окисление на Fe(II) до Fe(III). Взетите за изследване водни проби се филтруват на място през филтър спринцовки (0.45 μm). Сорбционната процедура се провежда при полеви условия и епруветките със сорбираните проби се пренасят до лабораторията, където формите на желязото се елуират и определят. Полевото пробовземане предотвратява промени в окислителното състояние на желязото. Установено е, че присъствието на хуминови киселини във водните проби до 0.01% не оказва влияние върху метода. Границата на откриване (3*s*) е 0.8 μg L^{-1} Fe (ETAAS). Относителното стандартно отклонение (*n*=10) е от 2% за съдържания около 1 mg L^{-1} Fe до 20% за съдържания около 1 μg L^{-1} Fe(III). Извличането на Fe(II) и Fe(III) от речна, езерна, питейна и подпочвена вода е в рамките на 93 –105%.

Bulgarian Chemical Communications, Volume 44, Number 4 (pp. 307 – 309) 2012

Computing PI index of micelle-like chiral dendrimers

H.Yousefi-Azari[1]*, A.R. Ashrafi[2]

[1]*School of Mathematics, Statistics and Computer Science, University of Tehran, Tehran, I. R. Iran*
[2]*Institute of Nanoscience and Nanotechnology, University of Kashan, Kashan 87317-51167, I. R. Iran*

Received: November 9, 2011; Accepted: February 1, 2012

A map taking graphs as arguments is called a graph invariant or topological index if it assigns equal values to isomorphic graphs. A dendrimer is an artificially manufactured or synthesized molecule built up from branched units called monomers. In this paper, the PI index of the micelle-like chiral dendrimers is computed.

Keywords: Micelle-like chiral dendrimer, molecular graph, PI index.

1 INTRODUCTION

The basic assumption for all molecule based hypotheses is that similar molecules have similar activities. This principle is also called structure-activity relationship (SAR). Quantitative structure-activity relationship, QSAR, is the process by which chemical structure is quantitatively correlated with a well defined process, such as biological activity or chemical reactivity.

A molecular graph is a simple graph in which vertices are the atoms and edge are bonds between them. A topological index for a molecular graph G is a numerical value for correlation of chemical structure with various physical properties, chemical reactivity or biological activity [1]. The Wiener index [2] is the first topological index introduced by chemist Harold Wiener. This index is defined as the sum of all topological distances between the pair of vertices. Khadikar *et al*. [3] defined a new topological index, named PI index. It is defined as $PI(G) = \sum_{e=uv\in G}[m_u(e) + m_v(e)]$, where $m_u(e)$ is the number of edges of G lying closer to u than to v and $m_v(e)$ is the number of edges of G lying closer to v than to u. Edges equidistant from both ends of the edge uv are not counted.

It is worthy to mention here that Khadikar and his co-workers [4-11] examined variety of cases in that the PI index was found more useful than many of the other distance-based topological indices in QSAR/QSTR analysis. They established the success of PI index with rigorous examples. Khadikar and his team observed that in many cases the biological activity is well correlated with PI index.

The PI index has more and more applications in nanoscience. Khadikar [12] established the

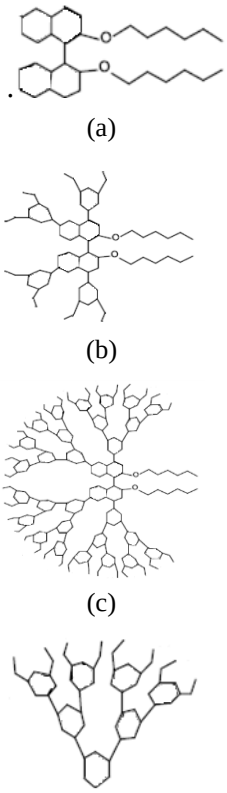

Fig. 1. a) The Core of Micelle-Like Chiral Dendrimer G[n];
b) The Molecular Graph of G[0];
c) The Molecular Graph of G[2];
d) A Branch of G[2].

importance of PI index in nanotechnology. The present article is an extension of our earlier work in demonstrating the applicability of PI index to model dendrimers and to investigate relative

* To whom all correspondence should be sent:
E-mail: Ashrafi@kashanu.ac.ir

© 2012 Bulgarian Academy of Sciences, Union of Chemists in Bulgaria

potential of PI index in such studies. We encourage the readers to consult paper [13-18] for background material as well as basic computational techniques. Our calculations are done with the help of GAP System.

2 PI Index of Micelle-Like Chiral Dendrimers

Nanobiotechnology is a rapidly advancing area of scientific and technological opportunity that applies the tools and processes of nanofabrication to build devices for studying biosystems. Dendrimers are one of the main objects of this new area of science. Here a dendrimer is a synthetic 3-dimensional macromolecule that is prepared in a step-wise fashion from simple branched monomer units, the nature and functionality of which can be easily controlled and varied. The aim of this article is mathematical study of this class of nano-materials.

Consider the molecular graph of micelle-like chiral dendrimer G[3] depicted in Figure 1. We extend this molecular graph to the case that there exists a maximal chain of length n from the core to the end hexagon and denote its molecular graph by G[n].

Suppose e is an edge of G[n] and N(e) denotes the number of parallel edges to e. Then $N(e) = M - (m_u(e) + m_v(e))$, where M is the number of edges in G[n]. We first notice that $PI(G) = M^2 - \sum_{e\in E(G)} N(e)$. From the molecular graph of this dendrimer, Figure 1, we can see that the core of G[n] has exactly 37 edges and by considering its branches we have:

$$M = 4 \times [1 + 10 + 2 \times (5 + 4) + 2^2 \times (5 + 4) + \ldots + 2^{n-1}(5 + 4)] + 37 = 9 \times 2^{n+2} + 9.$$

From Figure 1, one can see that there are three types of edges as follows: the edges with N(e) = 1, the edges satisfy N(e) = 2 and the edges with N(e) = 3. To compute the PI index of this dendrimer, it is enough to compute the number of edges in each case. Suppose m_i, denote the number of edge e such that $N(e) = i$, $1 \le i \le 3$. Then we have $m_1 = 3 \times 2^{n+2} + 7$, $m_2 = 3 \times 2^{n+3} - 8$ and $m_3 = 6$. By these calculations, $PI(G[n]) = 81\times 2^{2n+4} + 72\times 2^{n+3} - 1$.

3 CONCLUSIONS

In this paper a method for computing PI index of a dendrimer is presented by which it is possible to calculate this topological index for dendrimer molecules, in general. Our method is efficient for dendrimers and we apply on micelle-like chiral dendrimer.

Acknowledgement: *This research is partially supported by Iran National Science Foundation (INSF) (Grant No 86043/17).*

REFERENCES

1. Hansch, C.; Leo, L. Exploring QSAR Fundamentals and Applicability in Chemistry and Biology; American Chemical Society, Washington DC, 1996.
2. Wiener, H. J. Am. Chem. Soc. **1947**, 69, 17-20.
3. Khadikar, P. V.; Karmarkar, S.; Agrawal, V. K. J. Chem. Inf. Comput. Sci. **2001**, 41, 934-949.
4. Khadikar, P. V.; Karmarkar, S.; Varma, R. G. Acta. Chem. Slov. **2002**, 49, 755-771.
5. Khadikar, P. V.; Kale, P. P.; Deshpande, N. V.; Karmarkar, S.; Agrawal, V. K. J. Math. Chem. **2001**, 29, 143-150.
6. Khadikar, P. V.; Singh, S.; Mandloi, D.; Joshi, S.; Bajaj, A. V. Bioorg. Med. Chem. **2003**, 11, 5045-5050.
7. Khadikar, P. V.; Mandloi, D.; Bajaj, A. V.; Joshi, S. Bioorg. Med. Chem. Lett. **2003**, 13, 419-422.
8. Khadikar, P. V.; Singh, S.; Shrivastava, A. Bioorg. Med. Chem. Lett. **2002**, 12, 1125-1128.
9. Khadikar, P. V.; Bajaj, A. V.; Mandloi, D. Indian. J. Chem. **2002**, 41A, 2065-2067.
10. Balaban, A. T.; Khadikar, P. V.; Aziz, S. Iranian J. Math. Chem. **2010**, 1, 43-60.
11. Aziz, S.; Manikpuri, A. D.; John, P. E.; Khadikar, P. V. Iranian J. Math. Chem. **2010**, 1, 79-90.
12. Khadikar, P. V. Iranian J. Math. Chem. **2010**, 1, 7-42.
13. Diudea, M. V.; Vizitiu, A. E.; Mirzagar, M.; Ashrafi, A. R. Carpathian J. Math. **2010**, 26, 59-66.
14. Karbasioun, A.; Ashrafi, A. R.; Diudea, M. V. MATCH Commun. Math. Comput. Chem. **2010**, 63, 239-246.
15. Karbasioun, A.; Ashrafi, A. R. Macedonian J. Chem. Chem. Eng. **2009**, 28, 49-54.
16. Khalifeh, M. H.; Yousefi-Azari, H.; Ashrafi, A. R. Indian J. Chem. **2008**, 47A, 1503-1507.
17. Ashrafi, A. R.; Saati, H. J. Comput. Theor. Nanosci. **2008**, 5, 681-684.
18. Ashrafi, A. R.; Mirzargar, M. Indian J. Chem. **2008**, 47A, 538-541.

ИЗЧИСЛЯВАНЕ НА PI ИНДЕКС НА МИЦЕЛОПОДОБНИ ХИРАЛНИ ДЕНДРИМЕРИ

Х. Юсефи-Азари[1]*, А.Р. Ашрафи[2]

[1] *Училище по математика,статистика и компютърни науки, Университет в Техеран, Техеран, I.R., Иран*

[2] *Институт по нанонауки и нанотехнологии, Университет в Кашан, Кашан 87317-51167, I.R., Иран*

Постъпила на 9 ноември 2011, Приета на 1 февруари 2012

(Резюме)

Матрица с графи за параметри се нарича графова инварианта или топологичен индекс ако присвоява равни стойности на изоморфен граф. Дендримерът е изкуствено получена или синтезирана молекула, изградена от разклоняващи се структури, наречени мономери. В настоящата статия се изчислява PI индексът на мицелоподобни хирални дендримери.

Bulgarian Chemical Communications, Volume 44, Number 4 (pp. 310 – 313) 2012

Efficient approach to the synthesis of *i*-propylbenzonitriles by selective ammoxidation

Guangyong Xie[*,1,2,3], Aiqing Zhang[2]

[1]*Key Laboratory of Rubber-Plastics of Ministry of Education/Shandong Provincial Key Laboratory of Rubber -Plastics, Qingdao University of Science & Technology, Qingdao 266042, China*
[2]*Key Laboratory of Catalysis and Materials Science of Hubei Province, College of Chemistry and Materials Science, South-Central University for Nationalities, Wuhan 430074, China.*
[3]*Ministry of Education Key Laboratory for the Green Preparation and Application of Functional Materials, Hubei University, Wuhan 430062, China*

Received: October 26, 2011; Revised: January 31, 2012

Abstract *i*-Propylbenzonitriles were prepared for the first time by direct selective ammoxidation of *i*-propylbenzyl chlorides obtained by chloromethylation of *i*-propylbenzene with high yields and nearly 100% selectivity at a relatively low temperature of *ca.* 200 ºC.

Key words: ammoxidation · *i*-propylbenzonitrile · *i*-propylbenzene · cymene · chloromethylation

INTRODUCTION

Aromatic nitriles are important industrial chemicals and valuable synthetic intermediates [1–5]. As one type of important aromatic nitriles, *i*-propylbenzonitriles can easily be converted to corresponding amides, acids, esters, amines, etc., which are commercially interesting and valuable intermediates for the synthesis of pharmaceuticals, pesticides, dyestuffs, fluorescence whiteners, and so on.

The basic assumption for all molecule based hypotheses is that similar molecules have similar activities. This principle is also called structure-activity relationship (SAR). Quantitative structure-activity relationship, QSAR, is the process by which chemical structure is quantitatively correlated with a well defined process, such as biological activity or chemical reactivity. Similar to other aromatic nitriles, *i*-propylbenzonitriles can generally be synthesized by dehydration of amides [6], cyanation of aromatic bromides [7], diazotization of propylaniline [8], etc. These methods usually need expensive materials or lead to serious pollution and are not suitable for industrial production on a large scale. In general, the heterogeneous catalytic ammoxidation of methyl aromatics is the most simple and economically most profitable route for the production of aromatic nitriles [1–5]. However, *i*-propylbenzonitriles cannot be synthesized by direct catalytic ammoxidation of cymenes, which would mainly produce dinitriles with a little tolunitriles, due to the lower dissociation energy of the hydrogen at the α-C and the higher catalytic activity of the isopropyl group compared to the methyl group under gas phase ammoxidation conditions, as shown in Scheme **1**.

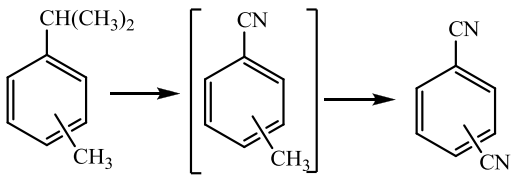

Scheme 1. Direct ammoxidation of cymenes

We have synthesized tolunitriles by selective ammoxidation of methylbenzyl chlorides prepared by chlorination of xylenes [9]. However, this reaction needs poisonous chlorine. Moreover, it is very difficult to controllably produce only alkylbenzyl chlorides by direct chlorination of methylaromatics, often along with the multi-chlorinated by-products. Here we report an efficient approach to the synthesis of *i*-propylbenzonitriles by selective ammoxidation of *i*-propylbenzyl chlorides prepared by chloromethylation of *i*-propylbenzene, as shown in Scheme **2**. To the best of our knowledge, this is the first case to synthesize *i*-propylbenzonitriles by catalytic gas phase ammoxidation. Furthermore, this approach provides a new synthetic path to obtain alkylbenzonitriles and other aromatic nitriles, especially those having heat-sensitive

* To whom all correspondence should be sent:
E-mail: xxgyy@hotmail.com
© 2010 Bulgarian Academy of Sciences, Union of Chemists in Bulgaria

groups and not being prepared by direct ammoxidation.

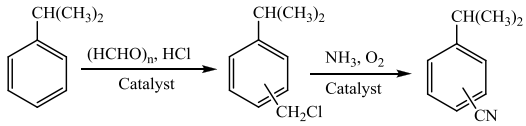

Scheme 2. Synthesis of *i*-propylbenzonitriles by selective ammoxidation

EXPERIMENTAL

General

The reagents for the preparation of catalysts and *i*-propylbenzene were analytically or chemically pure. The $VCrO/SiO_2$ catalysts were prepared according to our previous works [10, 11]. The products were characterized by ^1H NMR, IR spectroscopy and elemental analysis. The ^1H NMR spectra were recorded on a Bruker AM–300 MHz spectrometer with tetramethylsilane as an internal standard. The IR spectra were measured on a Nicolet Nexus470 FT-IR spectrometer. Elemental analyses were carried out using Vario EL 111. The purity of the products was determined on a Shimadzu GC-17A gas chromatograph.

CHLOROMETHYLATION OF *I*-PROPYLBENZENE

The procedure for chloromethylation of *i*-propylbenzene was referred to our previous work [12]. The mixture of *i*-propylbenzyl chlorides was obtained by vacuum distillation in 93 % yields, b.p. 118 – 120ºC / 35 mmHg.

SELECTIVE AMMOXIDATION OF *I*-PROPYLBENZYL CHLORIDES

The selective ammoxidation of *i*-propylbenzyl chlorides was carried out in a 30 mm-inside-diameter quartz tube fixed-bed reactor [10, 11, 13] loaded with 10 g catalyst. The *i*-propylbenzyl chlorides were fed by a micropump, vaporized and mixed in a preheated vessel with ammonia and air after having passed gas flowmeters with suitable molar ratios. The preheated gas flow was then fed directly into the reactor. The temperature was maintained at 220 ± 2ºC. *i*-Propylbenzyl chlorides (PBCs) were introduced at a rate of 0.6 mL h^{-1} and the molar ratios of air / PBCs and NH_3 / PBCs were 15 and 3, respectively. After the reaction, the outlet stream was cooled and the products were condensed in a condensing apparatus in 96 % yields. Pure *ortho*-*i*-propylbenzonitrile and *para*- *i*-propylbenzonitrile could be obtained by fractional distillation with 21 % (b.p. 72 – 75 ºC / 5 mmHg) and 75 % (b.p. 88 – 90 ºC / 5 mmHg) yields, respectively, and the purities were 98 % and 99 % by GC. Characterization data for *ortho*- *i*-propylbenzonitrile: ^1H NMR (300 MHz, $CDCl_3$): δ 7.45–7.63(m, 4H, Ph-*H*), 2.87(m, 1H, -C*H*$(CH_3)_2$), 1.23(d, 6H, -CH(C*H*$_3)_2$). IR(KBr, cm^{-1}): 2226 (–CN). Calcd for $C_{10}H_{11}N$: C, 82.72; H, 7.64; N, 9.65. Found: C, 82.36; H, 7.85; N, 9.79. Characterization data for *para*-*i*-propylbenzonitrile: ^1H NMR (300 MHz, $CDCl_3$): δ 7.46–7.58 (m, 4H, Ph-*H*), 2.85(m, 1H, -C*H*$(CH_3)_2$), 1.20(d, 6H, -CH(C*H*$_3)_2$). IR(KBr, cm^{-1}): 2224 (-CN). Calcd for $C_{10}H_{11}N$: C, 82.72; H, 7.64; N, 9.65. Found: C, 82.98; H, 7.71; N, 9.31.

RESULTS AND DISCUSSION

In ammoxidation of methylaromatics, the hydrogen extraction from the methyl group to generate the benzyl species is generally considered to be the rate-determining step of the reaction. Similar to the methyl group, the alkyl groups can also be converted to cyano groups under gas-phase ammoxidation conditions (*ca.* 400 ºC), so alkylaromatics can also be ammoxidized to aromatic nitriles. Because the dissociation energies of the α-C-H bonds in different alkyl groups are different, the different alkyl groups existing on one benzene ring would have different reactivities. In the ammoxidation of cymene, the methyl and isopropyl groups are generally ammoxidized to cyano groups, but due to the lower dissociation energy of the hydrogen at α-C of the isopropyl group (350 kJ/mol) compared with the methyl group (370 kJ/mol) [14], the isopropyl group is more active and would thus more easily be ammoxidized to the cyano group. So, besides dinitriles, considerable amounts of tolunitriles would exist in the products [15]. *i*-Propylbenzonitriles cannot be prepared by direct ammoxidation of cymenes. We have previously prepared tolunitriles by selective ammoxidation of methylbenzyl chlorides [9]. Considering the lower C-Cl bond energy (290 kJ/mol) and the higher reactivity of the chloromethyl group, here we report a new route to prepare *i*-propylbenzonitriles from the inexpensive *i*-propylbenzene by chloromethylation to *i*-propylbenzyl chlorides, which could then be selectively ammoxidized to *i*-propylbenzonitriles at a relatively low temperature of *ca.* 200 ºC (Scheme 2). The ammoxidation temperature of *i*-propylbenzyl chlorides is reduced by more than 100 ºC compared with that of ordinary methylaromatics. At such a low temperature, the *i*-propyl group could not be

ammoxidized, so the selectivity for *i*-propylbenzonitriles is very high, and the total molar yields of *i*-propylbenzonitriles can reach 89 % calculated with respect to *i*-propylbenzene. The possible catalytic mechanism for ammoxidation of *i*-propylbenzyl chlorides is shown in Scheme 3.

Chloromethylation of *i*-propylbenzene can give *ortho*-*i*-propylbenzyl chloride and *para*- *i*-propylbenzyl chloride [12]. Because of the very close boiling points and similar reactivities under the ammoxidation conditions, *i*-propylbenzyl chlorides could not be separated but reacted as a mixture to afford the *i*-propylbenzonitrile isomers, which can be separated by fractional distillation.

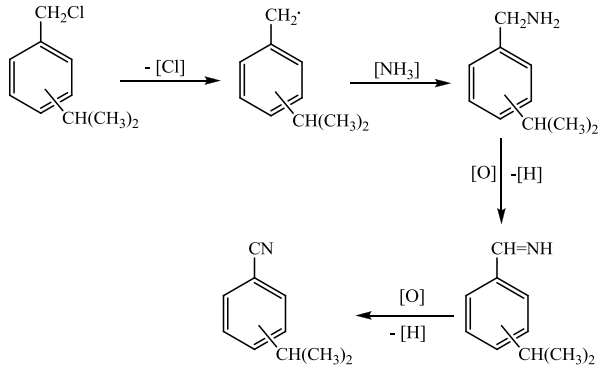

Scheme 3. Possible mechanism for ammoxidation of *i*-propylbenzyl chlorides.

The vanadium-containing mixed oxides are generally the most active and selective catalysts used for ammoxidation of methylaromatics. We have found that silica supported vanadium-chromium oxides [10, 11] show higher catalytic activity and selectivity at a lower reaction temperature than the corresponding unsupported vanadium-containing oxides for ammoxidation of methylaromatics. They could also be used for ammoxidation of *i*-propylbenzyl chlorides at very low temperature. The silica supported vanadium-chromium oxides were prepared according to our previous reports [10, 11]. With 10 wt.% of V-Cr loaded in the catalysts, highest catalytic activity and selectivity for ammoxidation of methylaromatics were registered. The X-ray diffraction (XRD) data show that V-Cr oxides exist as an amorphous phase in the 10 wt.% loadings [10]. With a V/Cr molar ratio of 1, the $VCrO/SiO_2$ catalyst shows best catalytic performance with 96% of yield and 98% of selectivity.

CONCLUSIONS

i-Propylbenzonitriles were synthesized by selective ammoxidation of *i*-propylbenzyl chlorides prepared by chloromethylation of *i*-propylbenzene at low temperature in high yields and nearly 100% selectivity. This approach provides a new path to obtain alkylbenzonitriles and other aromatic nitriles, especially for those having heat-sensitive groups and not being prepared by direct ammoxidation.

Acknowledgments *This work was financially supported by the National Natural Science Foundation of China (40830852, 21172269), the Open Fund of Ministry of Education Key Laboratory for the Green Preparation and Application of Functional Materials, the Open Fund of Key Laboratory of Rubber-Plastics of Ministry of Education /Shandong Provincial Key Laboratory of Rubber-plastics (KF2010001) and the Natural Sciences Foundation of South-Central University for Nationalities (YZZ10005).*

REFERENCES

1. A. Martin, B. Lücke, Catalysis Today, 57, 61 (2000).
2. B. Lücke, K.V. Narayana, A. Martin, K. Jähnisch, Adv. Synth. Catal., 346, 1407 (2004).
3. C. Hong, Y. Li, Chinese J. Chem. Eng., 14, 670 (2006).
4. F. Chen, Y. Wang, X. Zhan, Chinese J. Chem. Eng., 13, 615 (2005).
5. Q. Zheng, C. Huang, G. Xie, C. Xu, Y. Chen, Synth Commun., 29, 2349 (1999).
6. C.S. Rao, M. Rambabu, P. S. Srinivasan, Synth. Commun., 19, 1431 (1989).
7. S. Ushijima, K. Moriyama, H. Togo, Tetrahedron, 67, 958 (2011).
8. H. Gilman, A.H. Blatt, Org. Synth., 2, 514 (1956).
9. G. Xie, Q. Zheng, C. Huang, Y. Chen, Synth. Commun., 33, 1103 (2003).
10. G. Xie, Q. Zheng, C. Huang, Y. Chen, Indian J. Chem. A., 41, 963 (2002).
11. G. Xie, C. Huang, Fine Chemicals (in Chinese), 24, 790 (2007).
12. G. Xie, N. Liu, L. Lei, H. Ai, Journal of South Central University for Nationalities (Nat. Sci. Edition), 28, 8 (2009).
13. G. Xie, C. Huang, Indian J. Chem. Technol., 14, 371 (2007).
14. Y. Luo, The Data Handbook of Chemical Bond Energies, Science Press, Beijing, 2005.
15. B.V. Suvorov, S.R. Rafikov, B. A. Zhubanov, Zh. Prikl. Khim., 36, 1837 (1963)

ЕФЕКТИВЕН ПОДХОД ЗА СИНТЕЗИРАНЕ НА ИЗО-ПРОПИЛБЕНЗОНИТРИЛИ, ЧРЕЗ СЕЛЕКТИВНО АМОКСИДИРАНЕ

Гуангйонг Ксие*[,1,2,3], Аикинг Чанг[2]

[1] *Централна лаборатория по каучук и пластмаса към Министерството на образованието/ Централна лаборатория в провинция Шандонг по каучук и пластмаса, Университет по наука и технология Кингдао, Кингдао 266042, Китай*

[2] *Централна лаборатория по катализ и материалознание в провинция Хубеи, Колеж по химия и материалознание, Южноцентрален Университет за националностите, Ухан 430074, Китай*

[3] *Централна лаборатория за зелено производство и приложение на функционални материали на Министерството на образованието, Университет Хубей, Ухан 430062, Китай*

Постъпила на 26 октомври, 2011, преработена на 31 януари 2012

(Резюме)

Синтезирани са за първи път изо-пропилбензонитрили чрез директно селективно амоксидиране от i-пропилбензилни хлориди, получени чрез хлорметилиране на i-пропилбензен с висок добив и почти 100% селективност при сравнително ниска температура от около 200ºC.

Bulgarian Chemical Communications, Volume 44, Number 4 (pp. 314 – 317) 2012

Unexpected formation of novel oxazolidine and tetrahydrooxazine derivatives by condensation of 2-(hydroxymethy) or 2-(2-hydroxyethyl) piperidine, and ketones

S. Nishikawa,* M. Okimoto, T. Yoshida, M. Hoshi, K. Ohashi

Department of Biotechnology and Environmental Chemistry, Kitami Institute of Technology, Koen-cho 165, Kitami, Hokkaido 090-8507, Japan

Received: December 14, 2011; revised: February 28, 2012

Several novel oxazolidine and tetrahydrooxazine derivatives, which possess a spiro carbon, were unexpectedly obtained during our attempts to prepare enamines that possess a hydroxy group by condensation between a piperidine alcohol and a ketone in the presence of an acidic catalyst. The reaction times under reflux conditions were significantly influenced by the structure of the starting substrates.

Key words: Enamine, Oxazolidine, Tetrahydrooxazine, Spiro carbon, Three ring compounds.

INTRODUCTION

As shown in Scheme 1, enamine **1** is often utilized as a precursor for the preparation of α-substituted ketone **3**. In such reactions, electrophiles (E) such as alkyl or acyl halides attacks **1** at the β-position of the nitrogen atom to give substituted enamine **2** (X=E), which readily undergoes hydrolytic cleavage to yield **3** (X=E) [1, 2].

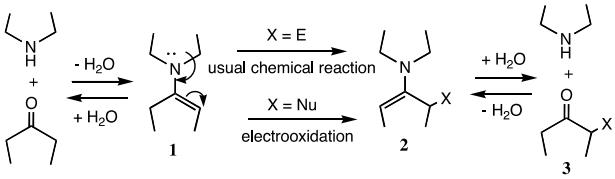

Scheme 1. Preparation of α-substituted ketone via enamine

In contrast, Shono et al. [3] and Chiba et al. [4] have previously reported that **1** can instead be attacked by a nucleophile (Nu), such as a methoxide ion or organic anions derived from β-dicarbonyl compounds, via electrooxidation to give **2** (X=Nu), which then hydrolyzes to **3** (X=Nu). Consequently, we were naturally interest in the electrooxidative behavior of enamines, such as compound **6** that possess a hydroxyl group. We attempt to prepare **6** by refluxing a mixture of **4** and **5** in toluene in the presence of catalytic amount of an acidic catalyst. However the reaction resulted in unexpected formation of three ring compounds, probably via autoxidation by ambient oxygen in the open dehydration apparatus. [5]

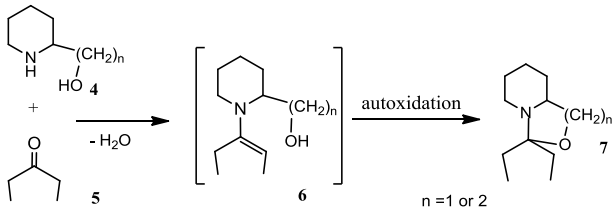

Scheme 2. Unexpected formation of three rings compound **7.**

EXPERIMENTAL

The oxazolidine (**7**, n=1) and tetrahydrooxazine (**7**, n=2) derivatives were prepared as follow: in a 200-mL round bottomed flask equipped with a water trap condenser was added hydroxy piperidine **4** (50 mmol), symmetrical ketone **5** (55 mmol), and *p*-toluenesulfonic acid (PTSA 0.1 g) in toluene (50 mL). The reaction mixture was refluxed until water was completely removed using the water trap (Table 1). After removal of the toluene under vacuum, the resulting residue was purified by distillation under reduced pressure. Structures of the isolated products were confirmed by IR and NMR and High resolution mass spectra. Infrared spectra (IR) were recorded on a Perkin Elmer Spectrum One FT-IR spectrometer. NMR spectra were obtained on a JEOL JNM-ECX 400 spectrometer. High resolution mass spectra were measured on a JEOL JMS-100GCV gas chromatography time-of-flight mass spectrometer.

- compound **7a**. Colorless viscous oily liquid, bp : 108–110ºC/19 mmHg. R_f : 0.90(Silica gel TLC, Et_2O). IR (neat) : 2934, 2861, 2805, 1463, 1441, 1347, 1153, 1144, 1079, 1032 cm^{-1}. ^1H

* To whom all correspondence should be sent:
E-mail: nishikawa@chem.kitami-it.ac.jp

© 2010 Bulgarian Academy of Sciences, Union of Chemists in Bulgaria

NMR ($CDCl_3$) :δ= 0.84(t, J= 12Hz, 3H), 0.90(t, J=12Hz, 3H), 1.1–1.2(m, 2H), 1.3–1.8(m, 8H), 2.4–2.5(m, 1H), 2.7–2.8(m, 2H), 3.3–3.4(m, 1H), 3.9–4.0(m, 1H). ^{13}C NMR ($CDCl_3$) :δ= 7.30(CH_3), 8.85(CH_3), 23.89(CH_2), 25.88(CH_2), 27.15(CH_2), 27.89(CH_2), 28.45(CH_2), 44.67(CH_2), 58.57(CH), 71.62(CH_2), 96.86(C). MS m/z (relative intensity, %) : 183(2) [M^+], 156(14), 155(33), 154(100), 98(48), 70(10), 57(17), 56(14), 41(18), 29(15). HRMS : m/z calcd. for $C_{11}H_{21}NO$: 183.1623 ;found : 183.1614[M^+].

- compound **7b**. Colorless viscous oily liquid, bp : 143–145˚C/45 mmHg. R_f : 0.56(Silica gel TLC, Et_2O). IR (neat) : 2935, 2867, 2798, 1440, 1323, 1280, 1226, 1141, 1057, 1030 cm^{-1}. ^{1}H NMR ($CDCl_3$) :δ= 1.2–1.4(m, 2H), 1.5–1.9(m, 11H), 2.2-2.3 (m, 1H), 2.5–2.7(m, 1H), 2.8-2.9(m, 1H), 3.4-3.5(m, 2H), 3.8–4.0(m, 1H). ^{13}C NMR ($CDCl_3$) :δ= 23.01(CH_2), 23.25(CH_2), 24.48(CH_2), 25.29(CH_2), 27.78(CH_2), 29.55(CH_2), 35.35(CH_2), 45.35(CH_2), 59.87(CH), 69.31(CH_2), 105.58(C). MS m/z (relative intensity, %) : 181(20) [M^+], 153(36), 152(100), 139(21), 98(33), 97(36), 82(28), 57(25), 55(28), 41(25). HRMS : m/z calcd. for $C_{11}H_{19}NO$: 181.1467 ;found : 181.1470[M^+].

- compound **7c**. [6, 7] Slightly yellowish viscous oily liquid, bp : 143-145˚C/19 mmHg. R_f : 0.23 (Silica gel TLC, Et_2O). IR (neat) : 2933, 2858, 2796, 1442, 1373, 1244, 1229, 1200, 1123, 1080 cm^{-1}. ^{1}H NMR ($CDCl_3$) :δ= 1.1–1.2(m, 1H), 1.3–1.4(m, 2H), 1.5–1.8(m, 10H), 1.9–2.3(m, 4H), 2.7–3.0(m, 2H), 3.7–3.8(m, 2H). ^{13}C NMR ($CDCl_3$) :δ=22.39(CH_2), 23.59(CH_2), 24.83(CH_2), 26.26(CH_2), 26.68(CH_2), 28.70(CH_2), 32.88(CH_2), 38.73(CH_2), 45.16(CH_2), 53.55(CH_2), 60.65(CH), 100.10(C). MS m/z (relative intensity, %) : 195(41) [M^+], 166(100), 151(55), 150(72), 138(64), 122(86), 84(54), 83(57), 55(51), 41(52). HRMS : m/z calcd. for $C_{12}H_{21}NO$: 195.1623 ; found : 195.1648[M^+].

- compound **7d**. Colorless viscous oily liquid, bp : 132–134ºC/16 mmHg. R_f : 0.85(Silica gel TLC, Et_2O). IR (neat) : 2933, 2860, 2804, 1448, 1365, 1291, 1203, 1155, 1130, 1037 cm^{-1}. ^{1}H NMR ($CDCl_3$) :δ= 1.0-1.3(m, 4H), 1.4–1.9(m, 12H), 2.2-2.4(m, 1H), 2.6–2.9(m, 2H), 3.3–3.5(m, 1H), 3.8–4.0(m, 1H). ^{13}C NMR ($CDCl_3$) :δ=22.86(CH_2), 23.77(CH_2), 23.83(CH_2), 25.73(CH_2), 25.81(CH_2), 28.14(CH_2), 29.93(CH_2), 35.78(CH_2), 45.43(CH_2), 58.72(CH), 70.08(CH_2), 94.93(C). MS m/z (relative intensity, %) : 195(26) [M^+], 166(17), 153(35), 152(100), 139(25), 98(26), 96(23), 82(18), 55(21), 41(23). HRMS : m/z calcd. for $C_{12}H_{21}NO$:195.1623 ;found : 195.1638[M^+].

- compound **7e**. [6, 7] Slightly yellowish viscous oily liquid, bp : 153–155ºC/19 mmHg. R_f : 0.47(Silica gel TLC, Et_2O). IR (neat) : 2932, 2857, 2796, 1445, 1375, 1289, 1258, 1227, 1117, 1084 cm^{-1}. ^{1}H NMR ($CDCl_3$) :δ= 1.0–1.2(m, 1H), 1.2–1.4(m, 4H), 1.4–1.8(m, 12H), 2.1–2.2(m, 1H), 2.2-2.3(m, 1H), 2.6–2.8(m, 1H), 2.9–3.0(m, 1H), 3.6-3.8(m, 2H). ^{13}C NMR ($CDCl_3$) :δ= 21.84(CH_2), 22.41(CH_2), 22.66(CH_2), 23.72(CH_2), 26.10(CH_2), 26.74(CH_2), 31.85(CH_2), 34.24(CH_2), 36.10(CH_2), 45.84(CH_2), 52.04(CH_2), 58.80(CH), 87.39(C). MS m/z (relative intensity, %) : 209(20) [M^+], 166(70), 165(49), 164(34), 138(29), 123(34), 122(100), 82(36), 55(36), 41(35). HRMS : m/z calcd. for $C_{13}H_{23}NO$: 209.1780 ;found : 209.1764[M^+].

- compound **7f**. Colorless viscous oily liquid, bp : 125-127˚C/2 mmHg. R_f : 0.87(Silica gel TLC, Et_2O), IR (neat) : 2938, 2865, 2804, 1442, 1365, 1289, 1203, 1154, 1130, 1030 cm^{-1}. ^{1}H NMR ($CDCl_3$) :δ= 0.86(s, 9H, 3 × CH_3), 0.8–1.0(m, 2H), 1.1-1.8(m, 13H), 2.2–2.3(m, 1H), 2.7–2.8(m, 1H), 2.8-2.9(m, 1H), 3.3–3.4(m, 1H), 3.9–4.0(m, 1H). ^{13}C NMR ($CDCl_3$) :δ= 23.64(CH_2), 23.82(CH_2), 24.58(CH_2), 25.70(CH_2), 27.71(CH_3), 28.13(CH_2), 29.82(CH_2), 32.39(C), 35.93(CH_2), 45.45(CH_2), 47.82(CH), 58.87(CH), 70.12(CH_2), 94.23(C). MS m/z (relative intensity, %) : 251 (14) [M^+], 236(18), 194(38), 153(40), 152(100), 139(29), 98(28), 97(28), 55(25), 41(25). HRMS : m/z calcd. for $C_{16}H_{29}NO$: 251.2249 ;found : 251.2260[M^+].

- compound **7g**. Colorless viscous oily liquid, bp : 150-152˚C/19 mmHg. R_f : 0.96(Silica gel TLC, Et_2O), IR (neat): 2931, 2857, 2799, 1455, 1441, 1275, 1221, 1126, 1074, 1032 cm^{-1}. ^{1}H NMR ($CDCl_3$) :δ= 1.1–1.3(m, 2H), 1.3-1.9(m, 16H), 2.2-2.3(m, 1H), 2.5–2.6(m, 1H), 2.9-3.0(m, 1H), 3.3-3.4(m, 1H), 3.8-3.9(m, 1H). ^{13}C NMR ($CDCl_3$) :δ= 22.86(CH_2), 23.29(CH_2), 23.72(CH_2), 25.71(CH_2), 27.88(CH_2), 30.08(CH_2), 30.75(CH_2), 32.82(CH_2), 40.55(CH_2), 45.14(CH_2), 58.54(CH), 69.91(CH_2), 98.21(C). MS m/z (relative intensity, %) : 209(24) [M^+], 166(37), 153(36), 152(100), 139(30), 98(27), 97(28), 82(21), 55(27), 41(25). HRMS : m/z calcd. for $C_{13}H_{23}NO$:209.1780 ;found : 209.1792[M^+].

- compound **7h**. Colorless viscous oily liquid, bp : 162–164ºC/17 mmHg. R_f : 0.72(Silica gel TLC, Ethyl ether), IR (neat) :2930, 2854, 2800, 1443, 1278, 1195, 1142, 1124, 1075, 1037 cm^{-1}. ^{1}H NMR ($CDCl_3$)δ= 1.1–1.3(m, 2H), 1.4–1.9(m, 18H), 2.2-2.3(m, 1H), 2.6–2.7(m, 1H), 2.9-3.1(m, 1H), 3.3-3.4(m, 1H), 3.8-3.9(m, 1H). ^{13}C NMR

($CDCl_3$) :δ= 22.15(CH_2), 22.64(CH_2), 23.78(CH_2), 24.80(CH_2), 25.92(CH_2), 27.65(CH_2), 28.16(CH_2), 28.70(CH_2), 29.47(CH_2), 36.83(CH_2), 45.91(CH_2), 59.15(CH), 70.11(CH_2), 97.08(C). MS m/z (relative intensity, %) : 223(23) [M^+], 194(26), 192(26), 166(32), 153(45), 152(100), 139(87), 98(44), 97(59), 55(34). HRMS : m/z calcd. for $C_{14}H_{25}NO$:223.1936 ;found : 223.1933[M^+].

RESULTS AND DISCUSSION

Beginning of the study, we examined preparation of **6** by refluxing 2-(hydroxymethy) piperidine (**4d**, n=1) (Entry 4 in Table 1) or 2-(2-hydroxyethyl) piperidine (**4e**, n=2) (Entry 5), and several symmetrical ketones (**5a**–**h)**. Although after theoretical amount of water could be removed from the reaction mixture, unexpected oxazolidine (**7d**, n=1**)** and tetrahydrooxazine (**7e**, n=2**)** derivatives were formed dominantly via a probable formation of the corresponding **6** (n=1 or 2) as the intermediates in good yield.

Interestingly, to the best of our knowledge, there are only very few reports regarding the preparation of compound type **7**, and most of the unique products consisting of three condensed rings obtained here are novel compounds. [6–11]

Table 1. Formation of oxazolidine and tetrahydrooxazine derivatives [a)]

Entry	**4**, **5**, **7**	n	R_1	R_2	r. time (h)	Yield of **7** (%) [b)]
1	a	1	Et	Et	70	75
2	b	1	$-(CH_2)_4-$		2	93
3	c	2	$-(CH_2)_4-$		3	95
4	d	1	$-(CH_2)_5-$		2	88
5	e	2	$-(CH_2)_5-$		26	87
6	f	1	$-(CH_2)_2CH(t\text{-}Bu)(CH_2)_2-$		7	95
7	g	1	$-(CH_2)_6-$		7	85
8	h	1	$-(CH_2)_7-$		9	64

[a)] **4**: 50 mmol, **5** : 55 mmol, PTSA : 0.1 g. Refluxing in toluene : 50 mL.
[b)] Isolated yields.

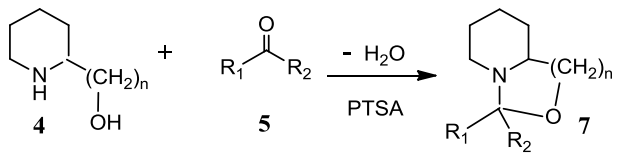

Scheme 3.

Table 1 shows relationship among the type of piperidine **4**, ketone **5**, reaction time, and the yields of the corresponding cyclic compound **7**. Refluxing times (see experimental section) required to complete the reaction were significantly depended on the structure of not only **4** but also **5** moiety. For example cyclopentanone **5b** (Entry 2), **5c** (Entry 3) and cyclohexanone **5d** (Entry 4) react readily with **4** (n=1 and 2) to give the corresponding cyclic compounds **7b**, **7c** and **7d** in high yields (88~95%), however much more long reaction times were needed in the cases of 3-pentanone **5a** (Entry 1, 70h) and cyclohexanone **5e** (Entry 5, 26h). Long refluxing time decreased the yield of **7h** (r. time 20hr, 55%) in the case of Entry 8. Further investigations of reactivity between **4** and **5**, and into the stereo-specificity of the products are currently underway in our laboratories.

REFERENCES

1. G. Cook, Enamine, Marcel Dekker, New York, 1969.
2. G. Stork, A. Brizzolara, H. Landesman, R. Terrell, *J. Am. Chem. Soc*., **85,** 207 (1963).
3. T. Shono, Y. Matsumura, H. Hamaguchi, K. Imanishi, T. Yoshida, *Bull. Chem. Soc. Jpn*., **51**, 2179 (1978).
4. T. Chiba, M. Okimoto, H. Nagai, Y. Takata, *J. Org. Chem.*, 44, 3519 (1979).
5. V.T. Angelova, N.G. Vassilev, A-S. Chauvin, A. H. Koedjikov, P.M. Ivanov, I.G. Pojarlieff, ARKIVOC, (xi), 11 (2008).
6. A.G. Cook, C.A. Schering, P.A. Campbell, S.S. Hayes, *Tetrahedron Lett*., **46**, 5451 (2005).
7. S. Ohki, H. Shimada, K. Sugimoto, *Yakugaku Zasshi*, **87,** 1359 (1967).
8. C.H. Tilford, Jr., M.G.V. Campen, *J. Am. Chem. Soc*., **76**, 2431 (1954).
9. F.J. McCary, C.H. Tilford, Jr., M.G. Van Campen, *J. Am. Chem. Soc*., **79**, 472 (1957).
10. L.H. Goodson, H. Christopher, *J. Am. Chem. Soc*., **72**, 358 (1950).
11. H.C. Beyeman, L. Maat, A.V. Veen, A. Zweistra, W.V. Philipsborn, *Rec. Trav. Chim*., **84**, 1367 (1965).

НЕОЧАКВАНО ОБРАЗУВАНЕ НА НОВИ ПРОИЗВОДНИ НА ОКСАЗОЛИДИН И ТЕТРАХИДРООКСАЗИН ПРИ КОНДЕНЗАЦИЯ НА 2-(ХИДРОКСИМЕТИЛ) ИЛИ 2- (2-ХИДРОКСИЕТИЛ) ПИПЕРИДИН И КЕТОНИ

Н. Нишикава*, М. Окимото, Т. Йошида, М. Хоши, К. Онаши

Департамент по биотехнология и химия на околната среда, Технологичен Университет Китами, Коен-чо 165, Китами, Хокайдо 090-8507, Япония

Постъпила на 14 февруари, 2011, преработена на 28 февруари 2012

(Резюме)

Няколко нови производни на оксазолидин и тетрахидрооксазин, притежаващи спиро-въглерод, бяха получени неочаквано при опитите да се получат енамини, които притежават хидроксилна група, при кондензация на пиперидинов алкохол и кетон в присъствието на киселинен катализатор. Реакционните времена при нагряване с обратен хладник се влияят значително от структурата на изходните субстрати.

Bulgarian Chemical Communications, Volume 44, Number 4 (pp. 318 – 323) 2012

Conducting polyanilline based paints on hot dip galvanized low carbon steel for corrosion protection

P. Deshpande*[1], S. Vagge[1], S. Jagtap[2], R. Khiarnar[3], S. Kelkar[4], M. More [5]

1 Department of Metallurgy and Materials Science, College of Engineering, Shivajinagar, Pune- 411005 (M.S.), India
[2] Sinhgad Institute of Technology, Lonavala, Pune- 411 001 (M.S.), India
[3] Department of Physics, Swami Ramanand Teerth, Marathwada University, Nanded - 431 606 (M.S), India
[4] National Chemical Laboratory, Pune- 411008 (M.S.), India
[5] Department of Physics, University of Pune, Pune - 411 007 (M.S), India

Received February 20, 2012; Accepted February 20, 2012

Conducting polyaniline based paints have been applied on hot dip galvanized low carbon steel samples. The corrosion protection performance of these paint coatings was evaluated by using Tafel plots and impedance spectroscopy. It was found that the paint coatings offered significant corrosion protection to hot dip galvanized low carbon steel in aqueous 3.5 wt % NaCl solution.

***Key words**:* Conducting polyaniline based paints; hot dip galvanized low carbon steel; corrosion prevention

INTRODUCTION

The use of conducting polymers for the corrosion protection of metals and alloys has received substantial attention recently [1–3]. Within the class of conducting polymers, polyaniline occupies a unique place due to its stability, low cost and ease of synthesis [4]. However, the extent of using this conducting polymer family is limited due to the exclusivity of the monomers that are required for synthesis [5, 6]. Presently three methodologies are being used to overcome this situation.

The first approach is concerned with the use of substituted conducting polyanilines on metals and alloys. Dimitra Sazou reported the electrochemical polymerization of several ring substituted anilines such as o-toluidine, m-toluidine, o- nisidine and o-chloroaniline on iron samples from aqueous oxalic acid. It was found that the anticorrosion ability of the conducting polymer increases in the order: polyaniline>poly (o-toluidine) ≈ poly(m- toluidine) >poly(o-anisidine)>poly(o-chloroaniline) [7]. P. Patil et al. carried out electrochemical synthesis of conducting poly(o-toluidine) and conducting poly(o-anisidine) flims on low carbon steel substrates from aqueous solutions of sodium tartrate and sodium salicylate respectively, and evaluated their corrosion protection performance in 3 % NaCl. A reduction in the corrosion rate by a factor of 50 and 15 was noted in case of conducting poly (o-toluidine) and conducting poly (o-anisidine) respectively in these works [8, 9]. Aziz Yagan et al. reported conducting poly (N-methylaniline) electrodeposited coating on iron from aqueous solution of oxalic acid and found that PNMA coating provides corrosion protection to iron in 0.5 M NaCl and 0.1 M HCl [10].

The second method is based on the copolymerization of two conducting polymers. Gozen Bereket et al. carried out the electrochemical deposition of poly(aniline-co-2-anisidine) films on stainless steel in tetrabutylammonium perchlorate/acetone solution containing perchloric acid. They found that the polyaniline, poly(2-anisidine) and poly(aniline-co-2- anisidine) films have corrosion protection effect for 304-stainless steel in 0.5 M HCl. However, the conducting poly(aniline-co-2-anisidine) coating was unstable and its durability was maintained up to 3 hrs [11]. A. Ozyilmaz et al. used aqueous sodium oxalate solutions both with and without p-toluenesulfonic acid to synthesize conducting poly(aniline-co-o-anisidine) film on mild steel. These conducting copolymer coatings provided significant corrosion protection in 3.5 % NaCl for longer periods [12].

The third technique involves the formation of bi layer coatings which consist either of a top coat of conducting polyaniline on the layer of the other conducting polymer such as polypyrrole, or a top coat of conducting polyaniline on the metallic coating such as nickel. R. Rajagopalan et al. electrodeposited conducting polyaniline-

© 2012 Bulgarian Academy of Sciences, Union of Chemists in Bulgaria

* To whom all correspondence should be sent:
E-mail: pravinpd@hotmail.com

polypyrrole composite coatings on low carbon steel. It was shown that the composite coating shows better corrosion resistant properties than the homo polymeric coatings [13]. Recently S. Ananda Kumar et al. reported corrosion resistant behavior of polyaniline-nickel, nickel-polyaniline, polyaniline-zinc and zinc-polyaniline coating on mild steel substrates. PANI-Zn coating was found to offer the maximum protection compared to other coatings [14]. However, it will be difficult to electro-deposit a zinc layer on the conducting polyaniline film commercially. In addition, in most of the reported investigations electrochemical techniques such as cyclic voltammetry were used for synthesis of conducting polymer coating on the metals and alloys. Cyclic voltammetry is not suitable for practical applications. Hot-dip galvanized coatings are used to protect steel against corrosion due to their low cost and ease of application. It is beneficial to improve the corrosion resistance of such coatings to enhance their service life [15]. Since hot dip galvanizing is a commercially established technique, it was thought that conducting polyaniline based paint on hot dip galvanized steel might provide an alternative to conventional toxic paint formulations. This technology is being used for applying coatings on electrical poles, fencing, domestic roofs, refrigerator panels, etc. It will also be possible to prepare conducting polyaniline based paints on a commercial scale and to apply these paints on massive engineering structures such as poles and fencing. To the best of our knowledge, there are no reports in the literature regarding application of conducting polyniline based paint coating on hot dip galvanized steel for corrosion prevention. Therefore, in the present work we have prepared conducting polyaniline based paints and subsequently applied on hot dip galvanized low carbon steel samples. Hot dip galvanized coating was obtained on low carbon steel samples by immersing these samples in molten zinc. The corrosion resistance of the painted steel samples was subsequently evaluated using potentiodynamic techniques and impedance spectroscopy and reported in this work.

EXPERIMENTAL

Materials

Aniline (AR grade supplied by Loba Chemicals, Colaba, Mumbai – 400 005, India) was double distilled prior to use. Chemicals - hydrochloric acid, ammonium persulphate and ammonia solution (AR grade supplied by Loba Chemicals, Colaba, Mumbai – 400 005, India) were used without further purification. Ingredients - Xylene, titanium dioxide (TiO_2), and dioctyl phthalate (DOP) (R grade supplied by Loba Chemicals, Colaba, Mumbai - 400 005, India) were used as received. Standard epoxy resin (GY 250 supplied by Huntsman Advanced Materials, India) Pvt Ltd. Andheri (East), Mumbai – 400 093, India) was used as received. Low carbon steel samples (AISI 1015) and zinc ingots were purchased from a local supplier.

Conducting polyaniline based paints preparation and its application

Conducting polyaniline was synthesized from aniline in aqueous HCl solution using ammonium persulphate as catalyst by following the method of Chaing and MacDiarmid [16]. Conducting polyaniline based paints were prepared by adopting a technique developed by P. Deb et al. [17] and elaborated below. The ingredients listed in the Table 1 were added after filtering to the solution of epoxy resin and the mixture was ball milled for 16 hrs (Drive motor: Crompton Make - 2 HP, 1440 rpm 415 V, 50 Hz, FLP foot mounted motor along with gearbox U 287, 25:1 Shanthi Make: Ball Mill supplied by Indo German Industries, Daman, India). The purpose of adding TiO_2 and Di-octyl phthalate (DOP) in the epoxy resin is to improve viscosity and elastic properties of the paints. Xylene was used as a solvent for paint formulation. The paints were filtered through fine cotton and applied on the low carbon steel samples. Hot dip galvanizing coating was obtained on low carbon steel samples by following the procedure adopted by S. Vagge and V. Raja [18]. Conducting paint formulations were subsequently applied on hot dip galvanized low carbon steel samples.

Table1. Conducting polyaniline based paint ingredients.

Ingredients	wt %
Epoxy Resin (GY 250)	100 gm
PANI-HCl	0.1 gm to 1.5 gm
TiO_2	10 gm
DOP	10 gm
Xylene	10 gm

Characterization

Conducting polyaniline powder was characterized by using UV-Vis spectrometry. The UV-Vis absorption study was carried out ex situ in the wave length range 200-1200 nm using micro processor controlled double beam UV-vis spectrophotometer (Model U 2000, Hitachi, Japan).

Corrosion studies

A corrosion cell with three electrode geometry of a paint coated sample as working electrode (8 cm^2), platinum as counter electrode, and a saturated calomel electrode (SCE) as a reference electrode was used. The cell was coupled with a Gamry Reference system 600 (Wilmington, USA) for corrosion studies.

RESULTS AND DISCUSSION

UV – Vis Analysis

The optical absorption spectrum of the conducting polyaniline powder in DMSO is shown in Fig. 1.

This spectrum shows the characteristics peak at 327 nm and a weak broad peak at 580 nm. The first one corresponds to the $\pi - \pi^*$ transition and $n - \pi^*$ transition. The second one at 580 nm can be assigned to the excition transition, which is rather weak in these polymers [19].

Corrosion studies

The corrosion protection performance of unpainted hot dip galvanized low carbon steel and conducting polyaniline based paint coating was assessed by potentiodynamic polarization and EIS studies in aqueous 3.5 wt % NaCl solution.

The potentio dynamic polarization curves for unpainted hot dip galvanized low carbon steel and for conducting polyaniline based painted hot dip galvanized low carbon steel samples in 3.5 wt % NaCl solution are shown in Fig. 2. (curve **a** - unpainted hot dip galvanized low carbon steel, curve **b** – 1.5 wt % painted steel, curve **c** – 1 wt % painted steel and curve **d** – 0.1 wt % painted steel).

The values of the corrosion potential, corrosion current density and corrosion rate obtained from Fig. 2 are recorded in Table 2.

The positive shift in the E_{corr} and substantial reduction in the I_{corr} of the hot dip galvanized low carbon steel due to the conducting polyaniline based paint is observed, indicating that the conducting polyaniline based paint protects the underlying substrate from the corrosion in aqueous 3.5 wt % NaCl. The E_{corr} increases from – 1063 mV versus SCE for unpainted hot dip galvanized steel to – 1040 mV versus SCE for 1 wt % PANI - HCl painted steel. It is also observed that the I_{corr} decreases from 0.006 mA/cm^2 (for unpainted hot dip galvanized steel) to 10.4 μA/cm^2 for 1 wt% PANI-HCl painted steel respectively. The corrosion rate of 1 wt % PANI-HCl paint coated steel is found to be 1.769 mpy which is 3.5 times lower than that of unpainted hot dip galvanized steel.

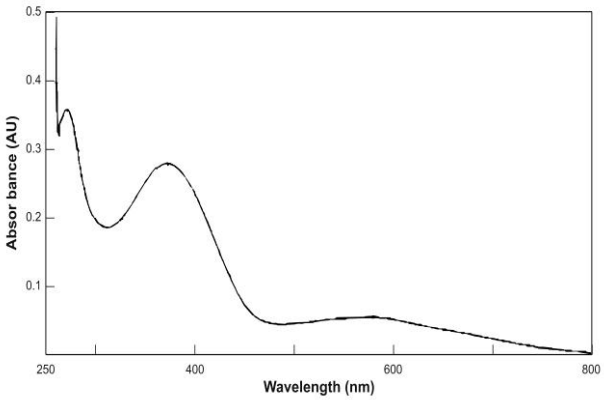

Fig. 1. UV Analysis of the conducting polyaniline powder in DMSO.

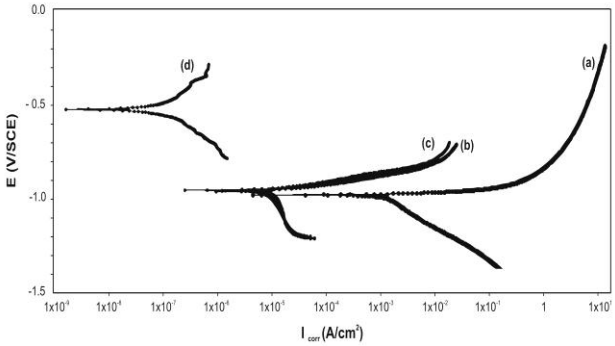

Fig. 2. Tafel plot for hot dip galvanized low carbon steel samples and paint coated carbon steel samples in 3.5 wt % NaCl (curve **a** - unpainted hot dip galvanized low carbon steel, curve **b** - 1.5 wt % painted steel, curve **c** - 1 wt % painted steel and curve **d** - 0.1 wt % painted steel).

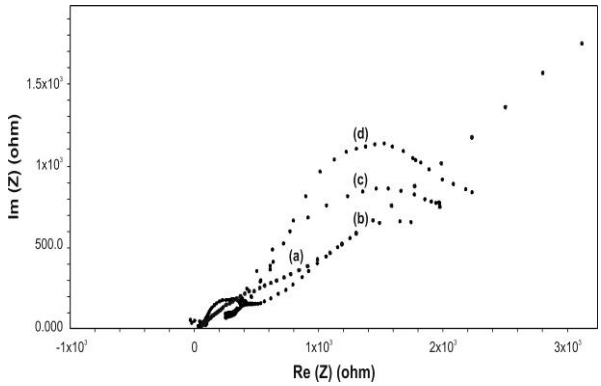

Fig. 3. Nyquist plot for hot dip galvanized low carbon steel sample and for paint coated carbon steel samples. (curve **a** - unpainted hot dip galvanized low carbon steel, curve **b** - 1.5 wt % painted steel, curve **c** - 1 wt % painted steel and curve **d** - 0.1 wt % painted steel).

Table 2. Comparison of corrosion rates for unpainted hot dip galvanized steel and paint coated hot dip galvanized steel.

Parameters	I_{corr}, A/cm ^{2}	E_{corr}, mV	B_A, V/dec	B_C, V/dec	Corrosion Rate, mpy
Unpainted hot dip galvanized steel	0.006×10^{-3}	-1063	1.4786	2.0209	6.1
0.1 wt% PANI- HCl painted steel	236×10^{-9}	-521	1.4824	2.0267	1.998
1 wt % PANI –HCl painted steel	10.40×10^{-6}	-1040	1.4886	2.1209	1.769
1.5 wt % PANI-HCl painted steel	17.30×10^{-6}	-1040	1.4856	2.0288	2.937

Table 3. Impedance parameters based on curve fitting and corrosion protection efficiency.

Parameters	**R_p**, ohms /cm ^{2}	**C_c**, μF	**R_f**, ohms/cm ^{2}	**C_f**, μF	**R_u**, ohms /cm ^{2}	**P_R**, ohms /cm ^{2}	**% P. E.**
Unpainted hot dip galvanized steel	323	45	2.0	231	56	381	-
0.1 wt % PANI-HCl painted steel	433	4.40	1.03	249.1	33.73	467.76	18.54
1 wt % PANI-HCl painted steel	213.7	17.51	1.27	556.8	322.5	537.47	29.11
1.5 wt % PANI-HCl painted steel	196	25.81	3.89	507.2	201.5	401.39	5.1

The Nyquist plots for hot dip galvanized low carbon steel sample and paint coated carbon steel samples in 3.5 wt % NaCl are shown in the Fig. 3.

The Nyquist impedance plots for hot dip galvanized low carbon steel and painted steel sample shown in the Fig. 3 are modeled by using the equivalent circuit depicted in the Fig. 4.

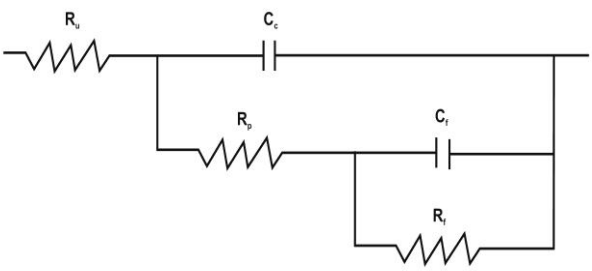

Fig. 4. Equivalent circuit used for modeling impedance curve.

It consists of the electrolyte resistance (R_u), the pore resistance (R_p), the coating capacitance (C_c), the charge transfer resistance (R_f) and double layer capacitance (C_f). The impedance plot of hot dip galvanized low carbon steel sample can be fitted with two semicircles, a smaller one at high frequency range followed by a larger one at lower frequencies. The first semicircle is attributed to the formation of the corrosion film and the second one to processes occcuring below the corrosion film. The Nyquist impedance plot of conducting polymer based paint coated sample is also modeled using the same circuit. However, the parameter values of the best fit to the impdence curve are different when compared to those for unpainted hot dip galvanized low carbon steel. It can be also fitted with two semicircles, a smaller one at high frequency range followed by a larger one at lower frequencies. The first capacitve loop can be attributed to the paint/steel interface. It is characterized by the pore resistance (Rp) and the coating capacitance (Cc). The second semicircle can be attribued to the processes occuring below the paint coating. It is characterized by charge transfer resistance (Rf) and double layer capacitance (Cf). The values of these impedance parameters obtained from the fitting of the experimental parameters are given in Table 3. The polarization resistance (P_R) was calculated by using following relation and recorded in Table 3.

$$P_R = R_p + R_f + R_u,$$

where Rp is the pore resistance, R_f is the charge transfer resistance and R_u is the electrolyte resistance. The protection efficiency based on EIS data was calculated by using following expression [20] and recorded in Table 3.

$$\%P.E. = \frac{P_c - P_R}{P_c}.100 ,$$

where P_R and P_c denote the polarization resistance of unpainted hot dip galvanized low carbon steel sample and painted hot dip galvanized low carbon steel sample respectively.

The R_f value for 1 wt % PANI-HCl painted steel is found to be to order of 537.47 ohms/cm^2, which is 71 % higher than that of unpainted steel. The higher value of the R_f can be attributed to the effective barrier property of the paint coating. The lower values of Cc for paint coated samples provide further support for the protection of steel by paint coating. The polarization resistance in the case of unpainted hot dip galvanized steel is of the order of 381 ohms per cm^2, which is close to the value reported by Vagge et al. [21]. It increases with the weight percentage of conducting polyaniline in paint formulation and reaches maximum i.e. 537.47 ohms per cm^2 for 1 wt % PANI-HCl painted hot dip galvanized steel and subsequently decreases. Thus EIS results support the Tafel investigations and it can be said that hot dip galvanized steel can be protected by applying conducting polyaniline based paint. It can be observed that the paints with lower loading of PANI- HCl offer good corrosion protection and the paint containing 1 wt % PANI-HCl is more effective in corrosion protection of hot dip galvanized steel in aqueous a 3.5 wt % NaCl solution. These results are in agreement with previous studies of conducting polyaniline based paints on low carbon steel [17].

CONCLUSIONS

Hot-dip galvanized coatings are used to protect steel against corrosion due to their low cost and ease of application. It is beneficial to improve the corrosion resistance of these coatings in order to prolong their service life. Conducting polyaniline based paints can be applied on hot dip galvanized low carbon steel. The paints containing a lower loading of PANI- HCl further enhance corrosion protection offered by hot dip galvanized coating to low carbon steel, and the paint containing 1 wt % PANI-HCl is more effective for corrosion prevention of hot dip galvanized steel in aqueous 3.5 wt % NaCl solution.

Acknowledgements: *The authors thank Prof. M. Rathod, Head, Department of Metallurgy and Materials Science, College of Engineering, Pune – 411005 (M.S.), India for providing facilities for the work and Prof. Anil Sahasrabudhe, Director, College of Engineering, Pune-411005 (M.S.), India for his encouragement.*

REFERENCES:

1. D.Tallman, G. Spiniks, A. Dominis, G. Wallace, *J. Sol. State Electrochem.* **6,** 73 (2002).
2. G. Spinks, A. Dominis, G. Wallace, D. Tallman, *J. Sol. State Electrochem*. **6,** 85 (2002).
3. S. Biallozor, A. Kupniewska, *Synth. Metals*, **155,** 443 (2005).
4. P. Deshpande, D. Peshwe, S. Pathak, *J. Institution of Engineers (India)* **82**, 33 (2001).
5. H. Nalwa, Hand Book of Organic Conductive Molecules and Polymers, John Wiley and Sons, New York, USA (1997).
6. T. Skotheim, R. Elsenbaumer and J. Reynolds, Handbook of Conducting Polymers, Marcel Dekkar, New York, USA (1997).
7. D. Sazou, *Synth. Metals* **118,** 133 (2001).
8. V. Shinde, S. Sainkar, P. Patil, *J. Appl. Polymer Sci*. **96,** 685 (2005).
9. M. Wankhede, A. Gaikwad, P. Patil, *Surf. Coat. Tech.* **01,** 2240 (2006).
10. A. Yagan, N. Pekmez, A. Yildiz , *Electrochim. Acta* **53,** 5242 (2008).
11. G. Bereket, E. Hur,Y. Sahin , *Prog. in Org. Coat.* **54,** 63 (2005).
12. A. Ozyilmaz, G. Ozyilmaz, N. Colak, *Sur. and Coat. Tech.* **201**, 2484 (2006).
13. R. Rajagopalan, J. Iroh, *Surf. Engin*. **18,** 59 (2002).
14. S. Ananda Kumar, K. Shree Meenakshi, T. Sankaranarayanan, S. Srikanth, *Prog. in Org. Coat.* **62,** 285 (2008).
15. S. Vagge, V. Raja, *Surf. and Coat. Tech.* **203,** 3092 (2009).
16. J. Chaing, A. MacDiarmid, *Synth. Metals* **13,** 193 (1986).
17. A. Samui, A. Patankar, J. Ragarajan, P. Deb, *Prog. in Org. Coat*. **47**, 1 (2003).
18. S. Vagge, V. Raja, *Surf. and Coat. Tech*. **201,** 2296 (2006).
19. C. Ozdemir, H. Can, N. Kolac, A. Guner, *J. App. Polymer Sci*. **99,** 2182 (2006).
20. S. Chaudhari, P. Patil, *Electro Chim. Acta* **53,** 927 (2007).
21. S. Vagge, V. Raja, *Appl. Surf. Sci.* **253,** 8415 (2007).

ПРОВОДЯЩИ БОИ НА ПОЛИАНИЛИНОВА ОСНОВА ЗА КОРОЗИОННА ЗАЩИТА НА ПОЦИНКОВАНА НА ГОРЕЩО НИСКОВЪГЛЕРОДНА СТОМАНА

П. Дешпанд*[1], С. Ваг[1], С. Джагтап[2], Р. Кхиарнар[3], С. Келкар[4], М. Мор[5]

[1] *Департамент по металургия и материалознание, Колеж по инженерство, Шиважинагар, Пун- 411005(М.С.), Индия*
[2]*Технологичен Институт Синхгад, Лонавала, Пун - 411001(М.С. Щат Махаращра), Индия*
[3] *Департамент по физика, Свами Рамананд Тиирт, Университет Маратвада, Нандед- 431 606 (М.С.), Индия*
[4]*Национална химична лаборатория, Пун - 411008(М.С.), Индия*
[5] *Департамент по физика, Университет Пун, Пун - 411007(М.С.), Индия*

Постъпила на 20 февруари, 2012 г; приета на 20 февруари, 2012 г

(Резюме)

Проводящи бои на полианилинова основа са приложени върху образци от поцинкована на горещо нисковъглеродна стомана. Корозионната защита на такива покрития е оценена с помощта на Тафелови зависимости и импедансна спектроскопия. Установено е, че покритията с боя осигуряват значителна защита от корозия на поцинкованата на горещо нисковъглеродна стомана в разтвори на 3.5 % (тегл.) NaCl.

Bulgarian Chemical Communications, Volume 44, Number 4 (pp. 324 – 332) 2012

The Integration of EIS parameters and bulk matrix characterization in studying reinforced cement-based materials

D.A. Koleva*, K. van Breugel

Delft University of Technology, Faculty of Civil Engineering & Geosciences, Department Materials & Environment, Stevinweg 1, 2628 CN, Delft, The Netherlands

Received February 20, 2012

Corrosion in reinforced concrete is a major and costly concern, arising from the higher complexity of involved phenomena on different levels of material science (e.g. electrochemistry, concrete material science) and material properties (macro/micro/ nano). Reinforced cement-based systems (e.g. reinforced mortar and concrete) are multi-phase composite materials at different levels of aggregation. Hence, multi-phase interfaces are involved in their structural performance and material behavior. Reinforced concrete has the potential to be durable and capable of withstanding a variety of adverse environmental conditions. One of the major difficulties in the engineering practice, however, is the multi-dimensional nature of reinforcement corrosion related issues. Nevertheless, materials and processes involved in the service life of a civil structure and their interaction are independently weighed and are seldom brought together. Very often the design of concrete mix proportions and the design of protective measures (such as the application of coatings or electrochemical techniques) are made in separate steps and (positive or negative) interactions among themselves are neglected.

This work reports on the integration of fundamental electrochemical techniques (as Electrochemical impedance spectroscopy) and concrete material science (bulk matrix properties) within monitoring and assessment of the corrosion performance of reinforced cement-based materials. Further, hereby discussed is the implementation of an eco-friendly approach of waste utilization for corrosion control and/or achieving superior properties and performance.

Key words: Reinforced concrete, Corrosion, EIS, Microstructure, Red mud

INTRODUCTION

The main objective of this study is to illustrate the synergy of electrochemistry (in terms of steel corrosion resistance) and concrete material science (mainly in terms of evaluation concrete bulk matrix properties) in studying reinforced cement-based systems. The paper briefly presents part of a comparative investigation of the corrosion behavior of reinforcing steel in concrete, using Ordinary Portland cement (OPC), Blast furnace slag cement (BFS) and Red Mud (RM) in chloride containing environment. The variables of main interest are: the corrosion parameters of the steel reinforcement and the alterations in the bulk cement-based matrix (porosity, pore size distribution). The investigation is performed as a comparative study of control (non-corroding) specimens from each group and corroding such (conditioned in 5% NaCl).

Steel corrosion, being a major problem in civil engineering, presents a huge cost (e.g. 30 to 50% of annual costs for infrastructure maintenance in EU are spent on corrosion-related issues). Dealing with steel corrosion in an eco-friendly manner, using wastes for example, is a sustainable way of solving corrosion problems. Additionally, the cement replacement by wastes in a reinforced concrete system would even further create sustainable solutions (less cement utilization, less CO_2 produced).

Recycling of waste materials in the construction industry is an eco-friendly and a technically successful option. However, major wastes (e.g. the bauxite residue – the highly alkaline red mud) are still not practically utilized and cause serious and alarming environmental issues: each tone of produced aluminum results in 0.5–2 tones waste; approximately 145 million tones of red mud are annually produced [1]. Red mud (RM) is reported to increase steel passivity in alkaline solutions [2]; RM additions to cement-based materials are also recently reported to result in mortars and concretes for shielding X-ray radiation [3], heavy metal (and other toxic substances) binding effects [4-6] while maintaining sufficient mechanical properties [7]. Practical applications are however extremely limited.

* To whom all correspondence should be sent:
E-mail: D.A.Koleva@tudelft.nl

© 2012 Bulgarian Academy of Sciences, Union of Chemists in Bulgaria

Table 1. Chemical composition, main compounds (dry cements (ENCI. NL) and red mud, as received)

Wt %	OPC (CEM I) (ENCI, NL)	BFS (CEM III B) (ENCI, NL)	RM (XRF)
CaO	61.0	48.0	3.5
SiO_2	19.0	29.0	20.2
Na_2O	Alkali	Alkali	14.3
K_2O	Equivalent: 1.12	Equivalent: 0.90	0.1
Al_2O_3	4.90	9.70	29.1
Fe_2O_3	3.50	1.48	24.9
MgO	1.80	52.0	0.1
SO_3	3.50	2.70	0.5
Cl	0.09	0.05	0.14

Blast furnace slag (BFS) is another largely generated waste (from the steel production); in contrast to RM, it is widely used in European countries; e.g. in The Netherlands it has a market share of more than 50%. A practical inconvenience however is the impeded cement hydration of BFS, compared to Portland cement (OPC) [8, 9], resulting in a coarser structure at earlier hydration ages. Further, BFS concrete requires proper and careful water curing at early ages and even then, reinforcing steel in BFS concrete exhibits reduced properties of the passive layer, due to: limited oxygen availability and thus a shift of the steel corrosion potential to a more negative state [10, 11]; lower calcium content and pH decrease [12]. Despite the higher chloride binding capacity of BFS, the passive layer on the steel surface is weakened as the Fe^{3+} species are reduced by the reducing agents from BFS cement itself; additionally BFS concrete is highly susceptible to carbonation and freeze-thaw durability issues [13].

To this end, the present contribution reports on the investigation of both BFS and RM containing reinforced mortar. Further, a mixture of RM and BFS as OPC cement replacement was also studied. A comparative investigation of control and corroding cells is presented for the period of approximately 250 days of conditioning (the test is still on-going).

EXPERIMENTAL

Materials

Reinforced mortar cylinders (d = 3.5 cm; h = 20cm) were cast from OPC CEM I 42.5 and CEM IIIB 42.5, cement/sand ratio of 1:3 and water/cement ratio of 0.6. The waste Red mud (RM) was added as 20% OPC or BFS replacement (chemical composition in Table 1). Eight groups (5 replicates per group) were monitored: four control groups (non-corroding) with (designation RM) and without red mud, denoted as OPC, RMOPC, BFS and RMBFS respectively, and four corroding groups, with and without red mud, denoted OPCn, RMOPCn, BFSn and RMBFSn. All specimens were cured for 7 days in fog room (20 ºC and 98% RH) and maintained in lab air further on. An external solution of 10 % NaCl was used as a chloride-induced accelerator for the corroding groups (the specimens were 1/3rd of height immersed in the solution; the control specimens were immersed in tap water). Red mud was added (after drying at 105ºC and grinding to cement finesse) for the RMOPC, RMOPCn, RMBFS and RMBFSn specimens.

The chemical and mineralogical composition of red mud depends on the processed bauxite, the aluminum production process itself and the geographical location. The red mud used in this study was supplied from Suriname (XRF analysis of the received supply gives major contributions of: Al_2O_3 29.1 wt.%, Fe_2O_3 24.9 wt.%, Na_2O 14.3 wt.%, SiO_2 20.2 wt.%, CaO 3.5 wt.%). The steel re-bars (construction steel FeB500 HKN, d=0.8cm, h=10cm, exposed surface of 21 cm^2, composition according NEN6008 (in wt.%): C < 0.12 wt.%, Si max 0.6, P max 0.05, S max 0.05, N max 0.012) were embedded “as received” i.e. there was no preliminary treatment of the bars before casting. Both ends of the steel bars were isolated (to avoid crevice corrosion) and the bar was positioned in the middle of the concrete specimens. Mixed Metal Oxide (MMO) titanium mesh served as a counter electrode; SCE electrode was used as a reference electrode. The experimental set-up and specimen’s

geometry are as previously used and reported in [14, 15].

Methods

With regard to the experimental results and discussion, which this paper briefly summarizes, the following methods and techniques are relevant.

- Scanning electron microscopy, coupled with EDX analysis (using ESEM Philips XL30);
- Open circuit potential (OCP), Electrochemical Impedance Spectroscopy (EIS) and Potentio-dynamic polarization (PDP), using EcoChemie Autolab.
- Microstructure and image analysis (for porosity and pore size distribution) ESEM for imaging and visualization of morphological and microstructure investigation; OPTIMAS software was used for image analysis (for image analysis, a set of ESEM images of the cement matrix was obtained in backscattered electron (BSE) mode with the magnification of 500x. The results are an average of 35 locations per sample (details about the sample preparation and procedures as reported in [16–20]).

RESULTS AND DISCUSSION

Electrochemical Impedance Spectroscopy (EIS)

EIS is a useful technique for obtaining knowledge of the steel/concrete system as it provides information for both the steel surface (electrochemical parameters) and the concrete bulk matrix (concrete bulk and pore network resistance) [21, 22]. Figure 1 depicts the equivalent electrical circuit, used for interpretation and data fitting of the experimental EIS response (the circuit is based on previously used and reported such for reinforced cement-based systems [14, 23], including additional parameters to account for bulk matrix properties [24], considering the frequency range hereby used of 1MHz to 10mHz.

The elements of the equivalent circuit present the following physical meaning: The first part of the circuit i.e. the high frequency domain (C1,R1 and C2, R2) is attributed to the properties of the concrete matrix in terms of pore network: solid phase and disconnected pore pathways and the resistance of the pore network in terms of continuous connected pores; The second part of the circuit i.e. middle and low frequency domains (time constants R3C3 and R4C4) deals with the electrochemical reaction on the steel surface including the contribution of redox processes, taking place in the product layers on the steel surface.

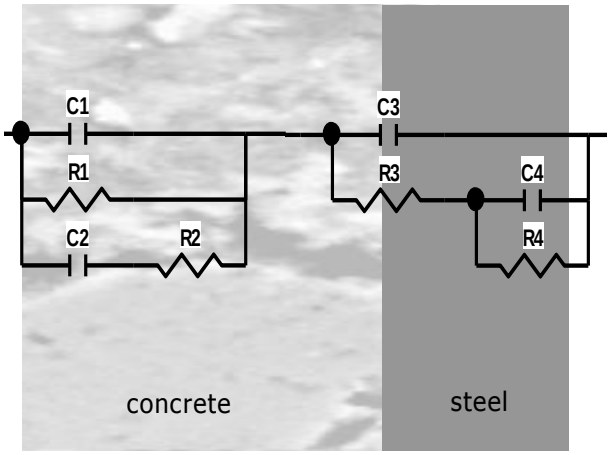

Fig. 1. Equivalent electrical circuit: C1R1 = capacitance and resistance of disconnected pore pathways incl. solid phase; C2R2 = capacitance and resistance of pore network (continuous conductive paths); C3R3 = charge transfer resistance and double layer capacitance (steel reinforcement); C4R4 = product layer characteristics

An overlay of the experimental EIS response for all groups is presented in Fig.2 relevant to the final so far recorded time interval of 250 days, which corresponds to the time interval of microstructural analysis. Summarized data for the best fit parameters are presented in Table 2.

The high frequency response corresponds to the concrete bulk resistance, including the contribution of electrolyte resistance (electrolyte resistance was in the range of 10 ohm for corroding cases to 30 for control cases). For deriving polarization resistance (R_p) from EIS measurements in reinforced concrete (R_{ct} and R_{red} respectively), the medium-low and low frequency limits of the impedance spectra are generally considered, as reported in [25–28], previously discussed and reported for reinforced mortar and concrete in [14, 23] and used in the present study as well.

At the stage of 250 days similar EIS response in terms of electrochemical behavior was recorded for all control cells, evidenced by the close to capacitive behavior at low frequencies (indicating situation of passivity). The corrosion resistance for BFS cells is lower, compared to OPC cells (Table 2, R_p values). The influence of RM as BFS replacement is well evident (Table 2, Fig.2, curves 2 and 3, top) and as previously reported for steel in simulated pore solutions of BFS and RM [29, 30]. The response for all OPC and BFS specimens

Table 2. Best fit parameters EIS response

Control cells

Cell type	R_1 Ohm	C_1 nF	$R_{p.netw.}$ (R2) Ohm	$C_{p.netw.}$ (C2) μF	$R_{ct.}$ (R3) Ohm.cm^2	C_f (C3) μF/cm^2	$R_{red.}$ (R4) Ohm.cm^2	C_{red} (C4) μF/cm^2	R_p (R3+R4) Ohm.cm^2	E mV SCE
OPC	230	2.3	170	350	127	26	2192	20	2300	-183
RMOPC	190	2.5	192	420	165	23	2846	17	3100	-170
BFS	2600	0.3	900	63	312	15	923	23	1200	-65
RMBFS	1090	0.6	1050	102	335	14	1719	15	1700	-120

Corroding cells

Cell type	R_1 Ohm	C_1 nF	$R_{p.netw.}$ (R2) Ohm	$C_{p.netw.}$ (C2) μF	$R_{ct.}$ (R3) Ohm.cm^2	C_f (C3) μF/cm^2	$R_{red.}$ (R4) Ohm.cm^2	C_{red} (C4) μF/cm^2	$Q_{red,}$ $Y_0 \times 10^{-3}$ $\Omega^{-1}s^n$	R_p (R3+R4) Ohm.cm^2	E mV SCE
OPCn	285	0.7	206	429	37	628	123	1.67, n=0.65		150	-470
RMOPCn	252	0.8	246	140	41	1125	115	1.69, n=0.62		160	-540
BFSn	1770	0.3	356	0.2	22	88	69	0.73, n=0.61		90	-480
RMBFSn	2630	0.2	430	0.1	79	30	1615	15		1700	-130

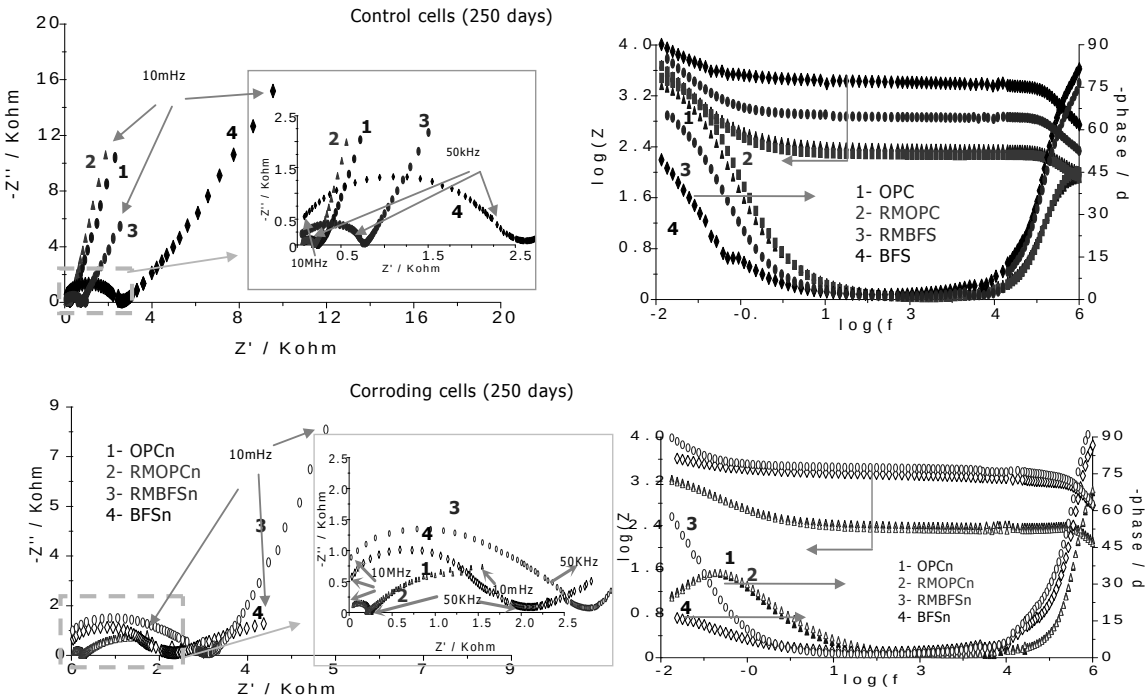

Fig. 2. EIS response for control (top) and corroding (bottom) cells after 350 days of conditioning (zoomed areas in the Nyquist plots give the high frequency response, and total response (very low magnitude of |Z|) for corroding cells OPC and RMOPC).

differs in the high frequency domain, denoted to the bulk properties of the cement-based matrix in BFS, compared to OPC. The former matrix is generally reported to be denser compared to the latter one [31–35], which gives the difference in bulk matrix resistance, Table 2. Figure 2 (bottom) presents the EIS response for the corroding cells at 250 days, reflecting still passive state for the corroding RMBFSn group and enhanced corrosion activity for the BFSn, OPCn and RMOPCn groups (reduced magnitude of |Z| and phase angle drop to below 40º). The bulk matrix resistance for all specimens (corroding and control groups) increases with time as a result of cement hydration (NaCl slightly influencing the electrical resistivity values), the major difference being denoted to the type of cement i.e. OPC cells (corroding and control) presenting bulk matrix resistance in the range of 400 – 480 Ohm, while for BFS cells, this range is 2126 – 3500 Ohm at 250 days.

The charge transfer resistance (R_{ct}) decreased for all corroding cells, compared to the control ones, the specimens RMBFSn, however, behave as control ones (E_{ocp}= –130 mV), exhibiting R_p values

in the range of the control cells (1.7 kOhm.cm2), capacitive behavior and higher phase angle (Table 2, Fig.2, specimen RMBFSn). As evident from the electrochemical measurements, 20% red mud as cement replacement, particularly for the BFS cells, results in a corrosion delay in the very aggressive environment of 10% NaCl. The presence of RM in reinforced mortar (and concrete respectively) will account for an increased corrosion resistance in the wastes-modified systems. In order to clarify the responsible mechanisms and related phenomena, microstructural analysis of the bulk cementitious matrix is performed and discussed in what follows.

Bulk matrix properties (microstructural parameters)

Relevant to morphological aspects of the pore structure and ion transport, the pore inter-connectivity (defined as the fraction of connected pores out of the total pore area) is used in terms of pore distribution density (PDD).

The electrolytic path in reinforced cementitious systems is dependent on the kinetics of ion transport mechanisms. These mechanisms, in addition to the cement hydration and the morphological alterations, are affected by the pore size distribution and the pore connectivity of the bulk concrete material. The critical pore size can be conceived as the diameter of the pore that completes the first interconnected pore pathway in a network, developed by a procedure of sequentially adding pores of diminishing size to this network. The critical pore size lc is a unique transport length scale of major significance for permeability properties and can be associated with the inflection point of the cumulative pore size distribution curve (Fig.3).

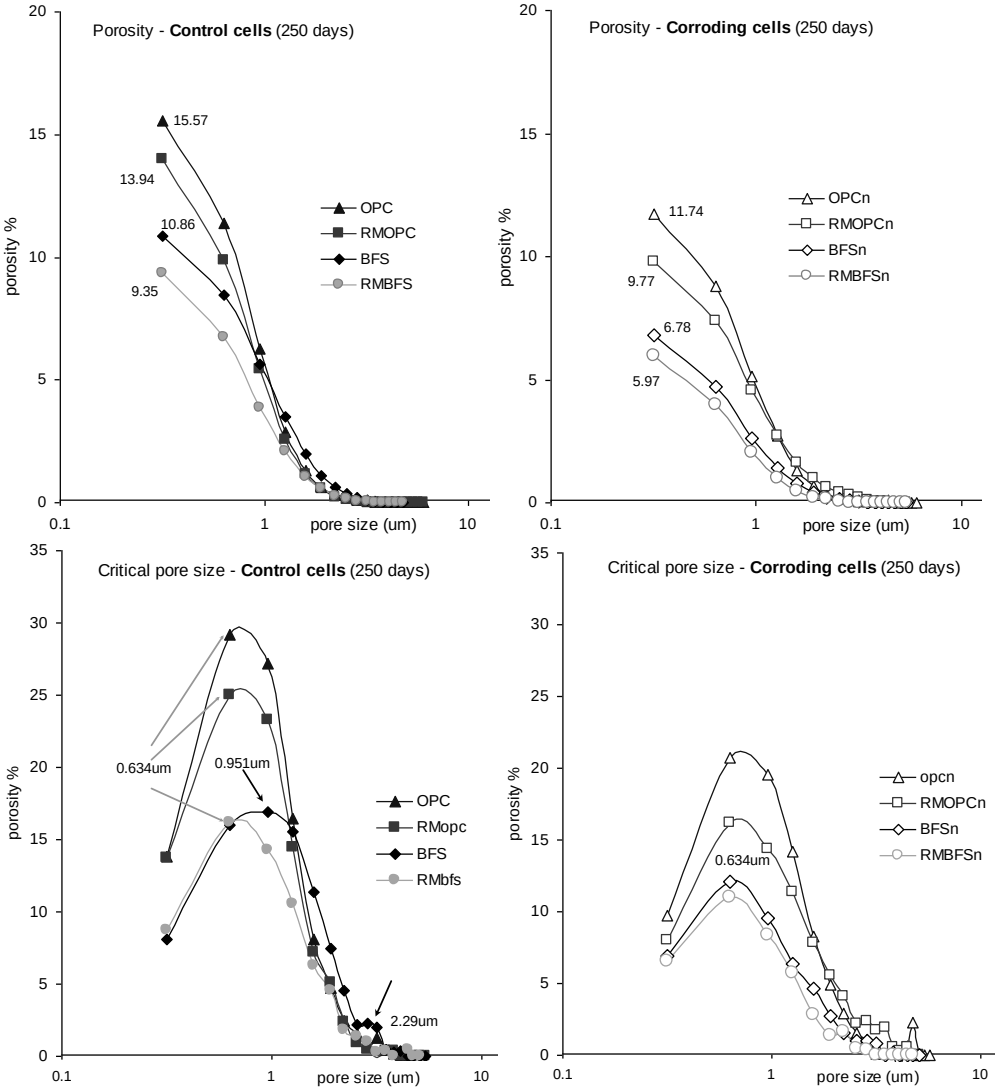

Fig. 3. Porosity and pore size distribution (bulk matrix) for control cells and corroding cells

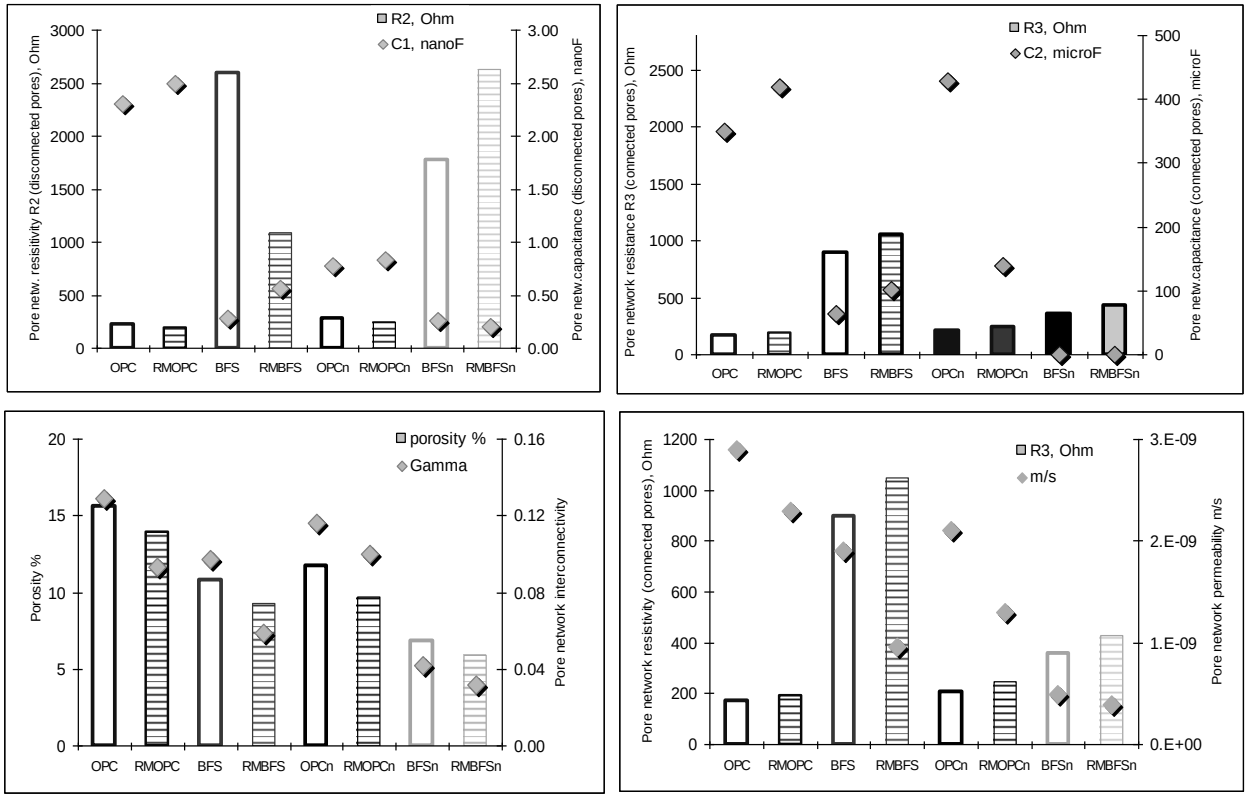

Fig. 4. Correlation of pore network capacitance and resistance (top) for disconnected (left) and connected (right) pore pathways; correlation of porosity and pore connectivity (bottom, left) and pore network resistance (connected pores) and permeability (m/s) – (bottom, right).

For more details on the fundamental aspects and image analysis of cement-based materials, including mortar, plain concrete and reinforced concrete, please see [16-18].

A set of SEM images on polished sections were made and were further subject to image analysis. The hereby discussed porosity and pore size distribution refer to the bulk matrix only. The structural parameters were averaged from at least 35 locations in the bulk matrix (sample of 2x2 cm). The final data were considered after performing a statistical evaluation in terms of frequency of occurrence (% distribution) vs class (porosity in %). The calculated pore size distribution and critical pore size are presented in Fig.3bottom) for the bulk matrix (> 250 μm away from the steel surface). Lower porosity was observed for the corroding cells, compared to the control cells, Fig.3 top (as a result from the influence of NaCl as accelerator of cement hydration at initial stages). Further, the influence of BFS and RM is well visible, the lowest recorded porosity being in the RM containing BFS cells. The critical pore size for all investigated groups is similar (approximately 0.634 μm), except for the control BFS cells (0.951 μm).

For the BFS control cells, carbonation of the mortar cover was specifically relevant (well known is the high susceptibility of BFS to carbonation), resulting in coarser structure of the mortar cover, higher pore network connectivity and therefore influence on critical pore size. Additionally, the difference in mortar cover porosity (not hereby presented) and internal bulk matrix porosity and connectivity respectively, for the BFS specimens, resulted in some discrepancies in the correlation of EIS and structural parameters.

The microstructural investigation reveals that the RMBFSn corroding specimens, which electrochemically behave as control ones (i.e. higher corrosion resistance compared to OPCn, BFSn and RMOPCn) exhibit the lowest porosity. In addition to the specific properties of RM in terms of inducing steel passivity, the combination of RM and BFS apparently exerts a significant positive effect (reduced permeability, increased chloride binding mechanisms) and thus is responsible for the

observed higher corrosion resistance in these specimens.

Porosity alone is, however, not a factor solely determining the significantly different electrochemical behavior. What has to be considered is the pore interconnectivity in the cement-based matrix and thus the matrix permeability. What will be further discussed is the correlation of these microstructural parameters with derived EIS parameters for the bulk matrix.

A correlation can be made between pore network parameters (Fig.3) and electrochemical (EIS) parameters (Table 2), mainly pore network capacitance ($C_{p.netw}$) and pore network resistance, $R_{p.netw}$ – Fig.4. The higher porosity (P%) and permeability (m/s) in OPC control and corroding cells (Fig.4. bottom right) corresponds to the highest $C_{p\cdot netw}$ and lowest $R_{p.netw}$, the values being lower for OPC corroding cells, compared to OPC control cells (Fig.4 top left). The lowest $C_{p.netw}$ (Fig.4top) corresponds to the lowest permeability values, derived for specimens BFS (both corroding and control groups). The result is very well in line with the derived global bulk electrical resistivity of the matrix in BFS as well (Table 2). Consequently, the BFS matrix (and especially in the presence of RM) in the corroding specimens would be characterized with a larger pore surface area but also increased portion of disconnected and isolated conductive pore pathways (increased pore network resistance). The capacitance values for BFS corroding cells are significantly lower than those for the OPC corroding cells, therefore a comparison of pore network permeability and interconnectivity between OPC and BFS specimens can be reliably derived on the basis of pore network capacitance and resistance.

Consequently (and moreover, after verification with microstructural analysis), it can be stated that EIS is a powerful, non-destructive technique for evaluation of pore network parameters. Combined with the electrochemical parameters, derived for the embedded steel, EIS allows a thorough evaluation of a reinforced concrete system.

CONCLUSIONS

Summarizing, this study discussed the corrosion behavior of reinforcing steel in OPC and BFS concrete with and without Red Mud replacement, subjected to chloride-induced corrosion (5% NaCl), in comparison with control cases for both concrete types. Additionally, the electrochemical parameters for the embedded steel were correlated with the microstructural parameters and properties of the bulk concrete matrix. After 250 days of conditioning, corrosion resistance is higher in the RM containing BFS corroding cells, whereas active behavior was observed for the Red mud free corroding cells and the RM containing OPC cells. The higher corrosion resistance in RMBFS reinforced mortar is denoted to decreased pore-network interconnectivity, evident from the significantly lower pore network capacitance and higher pore network resistance, as derived from EIS and verified on the basis of microstructural analysis. In that sense EIS appears to be a valuable tool for non-destructive and thorough evaluation of not only the electrochemical behavior of reinforcing steel, but also for detailed investigation of the bulk cement based matrix.

REFERENCES:

1 F. Kehagia, *Resources, Conservation and Recycling* **54,** 417, (2010).

2 M. I. Collazo, M. Izquierdo, X.R. Novoa, C. Perez, *Electrochim. Acta* **52,** 7513, (2007).

3 A. Anshul, S.S. Amritphale, N. Chandra, N. Ramakrishnan, A. Shrivastava, U.S.P. Verma, *Adv. App. Ceramics* **108,** 429, (2009).

4 S.S. Amritphale, A. Anshul, N. Chandra, N. Ramakrishnan, *J. Eur. Ceram. Soc.,* **27**, 1945, (2007).

5 Y. Cengeloglu, A. Tor, G. Arslan, M. Ersoz, S. Gezgin, *J. Hazard. Mater.,* **142,** 412, (2007).

6 Y. Liu, Ch. Lin, Y. Wu, *J. Hazard. Mater.,* **146,** 255, (2007).

7 P.E. Tsakiridis, S. Agatzini-Leonardou, P. Oustadakis, *J. Hazard. Mater.,* **116,** 103, (2004).

8 P.K. Mehta In: Malhotra VM, ed. Pozzolanic and cementitious by products as mineral admixtures for concrete – a critical review, vol. 1. ACI SP-79; 1983, 1.

9 P.K. Mehta In: Malhotra VM, ed. Pozzolanic and cementitious by products in concretes – another look, vol. 1. ACI SP-114; 1989, p. 1.

10 D.A. Koleva, K. van Breugel, J.M.C. Mol, J.H.W. de Wit, Monitoring chloride-induced corrosion in portland cement and blast furnace slag cement reinforced concrete. In s.n. (Ed.), Corrosion form the nanoscale to the plant (pp. 1–12). Nice: Eurocorr 2009.

11 C. Dehghanian, M. Arjemandi, *Cem. Concr. Res.* **27,** 937, (1997).

12 P. Dinakar, K.G. Babu, Santhanam, *Cem. Concr. Comp*. **29,** 136, (2007).

13 O. Çopuroğlu, A. Fraaij, J. Bijen, *Cem. Concr. Res*. **36**, 1475, (2006).

14 D.A. Koleva, J.H.W. de Wit, K. van van Breugel, E. van Westing, *J. Electrochem. Soc*. **154,** P52, (2007).

15 D.A. Koleva, J. Hu, A.L.A. Fraaij, K. van Breugel, J.H.W. de Wit, *Cem. Concr. Res.* **37**, 604, (2007).
16 J. Serra, Image analysis and mathematical morphology. London: Academic Press, 1982.
17 G. Ye, Experimental Study and Numerical Simulation of the Development of the Microstructure and Permeability of Cementitious Materials, PhD thesis, Delft University of Technology, Delft, 2003.
18 J. Hu, P. Stroeven, *Image Anal. Stereol.gy* **22,** 97, (2003).
19 D.A. Koleva, Z. Guo, K. van Breugel, J.H.W. de Wit, *Mater. & Corrosion* **61,** 561, (2010).
20 D.A. Koleva, Corrosion and Cathodic Protection in Reinforced concrete, PhD Thesis, Delft University of Technology, Delft ,(2007).
21 A.A. Sagüés, S.C. Kranc, E.I. Moreno, *Corr. Sci*. **37,** 1097, (1995).
22 V. Feliú, J.A. González and S. Feliú, *J. Electrochem. Soc*. **151,** B134, (2004).
23 D.A. Koleva, Z. Guo, K. van Breugel, J.H.W. de Wit, *Mater. Corrosion* **60**, 344, (2009).
24 M. Cabeza, P. Merino, A. Mirandab, X.R. Novoa, I. Sanchez, *Cem. Concr. Res*. **32,** 881, (2002).
25 M.F. Montemor, M.P. Cunha, M.G. Ferreira, A.M. Simões, *Cem. Concr. Comp*. **24,** 45, (2002).
26 V. Feliú, J.A. González, C. Andrade, S. Feliú, *Corr. Sci.* **40,** 975, (1998).
27 F. Wenger, J. Galland, *Electrochim. Acta* **35,** 1573, (1990).
28 L. Fedrizzi, F. Azzolini, P. L. Bonora, *Cem. Concr. Res.* **35,** 551, (2005).
29 D.A. Koleva, The significant delay of chloride-induced corrosion in reinforced mortar, containing red mud as cement replacement, Submitted to J. Electrochem. Soc. 2011.
30 D.A. Koleva, Jie Hu, K. van Breugel, J. H. W. de Wit, J. M. C. Mol, Steel corrosion resistance in model solutions, containing wastes, The European Corrosion Congress: EUROCORR 2010, Sept 13th – 17th, Moscow, proceedings CD; EFC event 324, Publisher: Dechema e.V. (2010)
31 A. Bouikni, R.N. Swamy, A. Bali, *Constr. Build. Mater*. **23**, 2836, (2009) .
32 O.E. Giorv, O. Vennesland, *Cem. Concr. Res*. **9**, 229, (1979).
33 D. Manmohan, P.K. Mehta, *Cem. Concr. Aggr*. **3**, 63, (1981).
34 A.D.M. Kumar In: Proc. 8th Conf. Chemistry of Cement, Brazil, 1986; p. 73.
35 R.D. Hooton In: Frohnsdorff G, ed. Blended cement, ASTM STP 897; 1986, 128.

ИЗСЛЕДВАНЕ НА ЖЕЛЕЗОБЕТОНИ ЧРЕЗ КОМПЛЕКСНОТО ПРИЛОЖЕНИЕ НА ЕЛЕКТРОХИМИЧНА ИМПЕДАНСНА СПЕКТРОСКОПИЯ И МЕТОДИ ЗА МИКРОСТРУКТУРНО ХАРАКТЕРИЗИРАНЕ

Д. А. Колева, К. ван Брьогел

Технологичен университет Делфт, Факултет по строителство и науки за Земята, катедра материали и околна среда, , Стевинвег 1, 2628 CN, Делфт, Холандия

Постъпила на 20 февруари, 2012 г.; приета на 20 февруари, 2012 г.

(Резюме)

Корозията на железобетона е значителен и скъпо струващ на икономиката проблем, произтичащ от комплексността на различните протичащи процеси, свързани с материалознанието (например електрохимия и материалознание в областта на бетоните), както и от свойствата на материалите на макро-, микро- и нано ниво. Железобетонът представлява многофазен композитен материал с различна степен на агрегация на отделните фази. Следователно, границите между последните също участват при характеризиране на структурата и поведението на материала. Железобетонът е дълготраен материал и е в състояние да издържа на най-различни въздействия на околната среда. Една от основните трудности в инженерната практика обаче е свързана с установяването на разнообразните прояви на протичащите корозионни процеси в този материал. Обикновено процесите и материалите, характеризиращи експлоатационния ресурс на дадена конструкция в строителното инженерство, както и тяхното взаимодействие се изследват поотделно, а не в тяхната комплексност. Много често подборът на състава на бетоновите смески и на мерките за защита (например прилагане на покрития или електрохимични техники) се реализират поотделно, а възможните взаимодействия между тях (позитивни или негативни) се пренебрегват.

Настоящата работа показва съвместното приложение на фундаментални електрохимични техники като Електрохимична импедансна спектроскопия и материалознание в областта на бетона (микроструктурно характеризиране) за мониторинг и оценка на корозионната устойчивост на железобетона. Дискутирана е също така възможността за екологичен подход, т.е. използване на отпадни продукти, при корозионния контрол и подобряване на механичните показатели на железобетона.

Bulgarian Chemical Communications, Volume 44, Number 4 (pp. 333 – 337) 2012

Dynamic impedance studies of ethanol oxidation at polycrystalline Pt

M-L Tremblay[1, 2], D. Guay[2], A. Lasia[1,*]

[1]*Université de Sherbrooke, Sherbrooke, Québec, Canada*
[2]*INRS-ET, Varennes, Québec, Canada*

Received February 20, 2012, accepted February 20, 2012

Ethanol oxidation in sulfuric acid solutions was studied at polycrystalline Pt electrode using cyclic voltammetry and dynamic electrochemical impedance spectroscopy (DEIS). It was found that negative resistances appear in the vicinity of the voltammetric peak causing instabilities (saddle-node bifurcation) and sharp peaks on the voltammograms. At the least positive potentials some H UPD takes place but the capacitance drops quickly at more positive potentials due to strong adsorption of EtOH fragments and CO. At the foot of the voltammetric peak log R_{ct} is a linear function of the potential with the slope of -0.143 V dec^{-1}.

Keywords: Ethanol oxidation, Platinum electrode, Dynamic electrochemical impedance spectroscopy, Instabilities in cyclic voltammetry, Negative charge transfer resistances, Double-layer capacitance

INTRODUCTION

Ethanol is considered as a potential fuel for the direct ethanol fuel cells (DEFC) [1]. Although many electrode materials were tested it is not possible to oxidize it completely to CO_2. Platinum is the reference material in electrochemistry. Mechanism of ethanol oxidation reaction at Pt was studied in the literature by cyclic voltammetry [2–5], FTIR based techniques [3, 6–9] and DEMS [6, 10]. Some authors obtained strange voltammograms with a very sharp peak during the backward sweep [3, 5, 8] and tried to explain it by assuming fast desorption. Very few studies of the EtOH oxidation reaction were carried out using electrochemical impedance spectroscopy (EIS). Some authors reported simple semicircles at the complex plane plots others observed inductive loops [5, 11] or negative resistances [12, 13].

The purpose of the present work was to explain the impedance spectra of EtOH oxidation in 0.5 M H_2SO_4 using dynamic electrochemical impedance spectroscopy (DEIS).

2. RESULTS AND DISCUSSION

2.1. Cyclic voltammetric studies

Our first goal was to explain the differences in cyclic voltammograms observed by different authors [2–5]. Comparisons of the cyclic voltammograms at Pt wire electrode in 0.5 M sulfuric acid and with addition of 1 M EtOH is shown in Fig. 1.

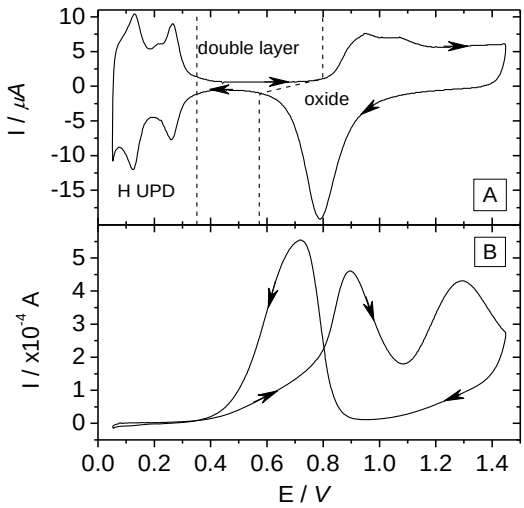

Fig. 1. Cyclic voltammograms of Pt wire electrode in 0.5 M H_2SO_4 in the absence (A) and presence (B) of 1 M EtOH.

Current observed in the presence of EtOH is two orders of magnitude larger that in its absence. There are two anodic peaks on the forward scan and one on the backward scan. By adding a resistor in series in the working electrode connection changes the form of backward peak to a sharp spike. The results are shown in Fig. 2. Such a behavior is characteristic of the systems with negative resistances [14–16]. Adding the resistance in series shifts the low frequency negative resistance to zero causing the saddle-node bifurcation [14]. Therefore, this peak is an artifact only. Similar behavior was

* To whom all correspondence should be sent:
E-mail: A.Lasia@USherbrooke.ca

© 2012 Bulgarian Academy of Sciences, Union of Chemists in Bulgaria

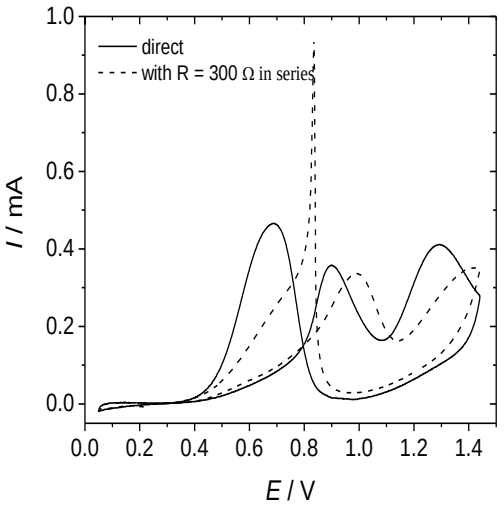

Fig. 2. Cyclic voltammograms of Pt in 1 M EtOH and 0.5 M H_2SO_4 measured directly and after adding a resistance of 300 Ω in the working electrode connection; sweep rate 50 mV s^{-1}.

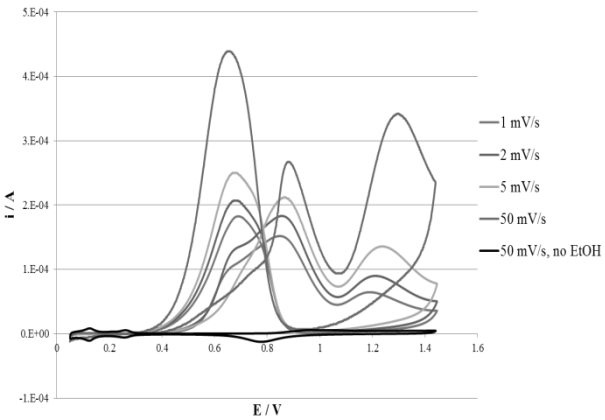

Fig. 3. Influence of the sweep rate on the voltammograms of Pt in EtOH.

observed for larger Pt electrodes when shifted further from the Luggin capillary where the larger solution resistance displaced the low frequency resistance to zero.

Cyclic voltammograms observed are strongly dependent on the sweep rate, cf. Fig. 3. With the decrease of the sweep rate the second anodic and the reverse peaks decrease relatively to the first anodic peak. It has been reported that CO_2 is formed only at the potentials of the first anodic peak [10]. The second peak only was observed during the oxidation of acetaldehyde [8] while fragments CH_3O^+ and CH_3^+ are produced proportionally to the current in cyclic voltammograms of EtOH [10]. The proposed mechanism is presented in ref. [9].

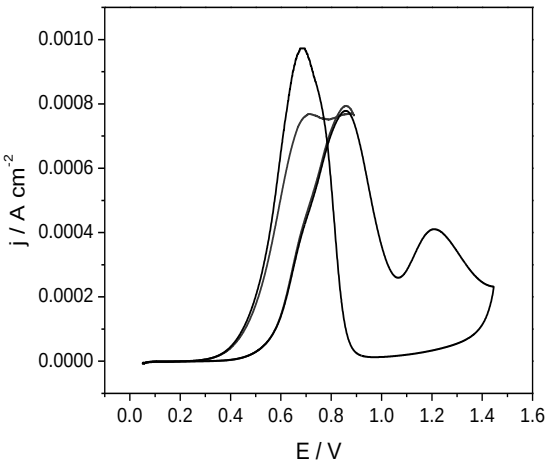

Fig. 4. Voltammograms at Pt electrode at the sweep rate of 2 mV s^{-1} at two potential zones.

2.2. DEIS measurements

The problems with the classical impedance measurements of EtOH oxidation are related to the fact that a steady state in not easily reached and, at some potentials it takes ~7 h to stabilize the current. This makes it difficult to measure impedance at a steady state at different potentials.

Sacci and Harrington [17] recently developed software for dynamic electrochemical impedance spectroscopy (DEIS) and applied it to study formic acid oxidation [16]. In this method multiple frequencies are applied simultaneously during a slow voltammetric sweep and the Fast Fourier Transform (FFT) is carried to analyze small segments of the data and calculate the dynamic impedance of the system. Our experiments were limited to the first anodic peak. Cyclic voltammograms and DEIS were recorded at v = 2 mV s^{-1}. Fig. 4 presents the voltammograms in a wide and a narrow potential zone; the forward currents are identical.

Depending on the potential zone different impedance curves were obtained. They can be divides in three groups:

1. Simple R_s-CPE blocking electrode circuit
2. R_s-(CPE-R_{ct}) circuit producing one semicircle
3. R_s-(C-CPE-R_{ct}) (in parallel) observed when negative resistances were obtained

Types of the equivalent circuits used are shown in Fig. 5. It is interesting to note that at the potentials around the voltammetric peak negative dynamic resistance is observed. All the obtained impedance data are Kramers-Kronig transformable. It should be stressed that in the case of negative resistances only the transformation of admittances

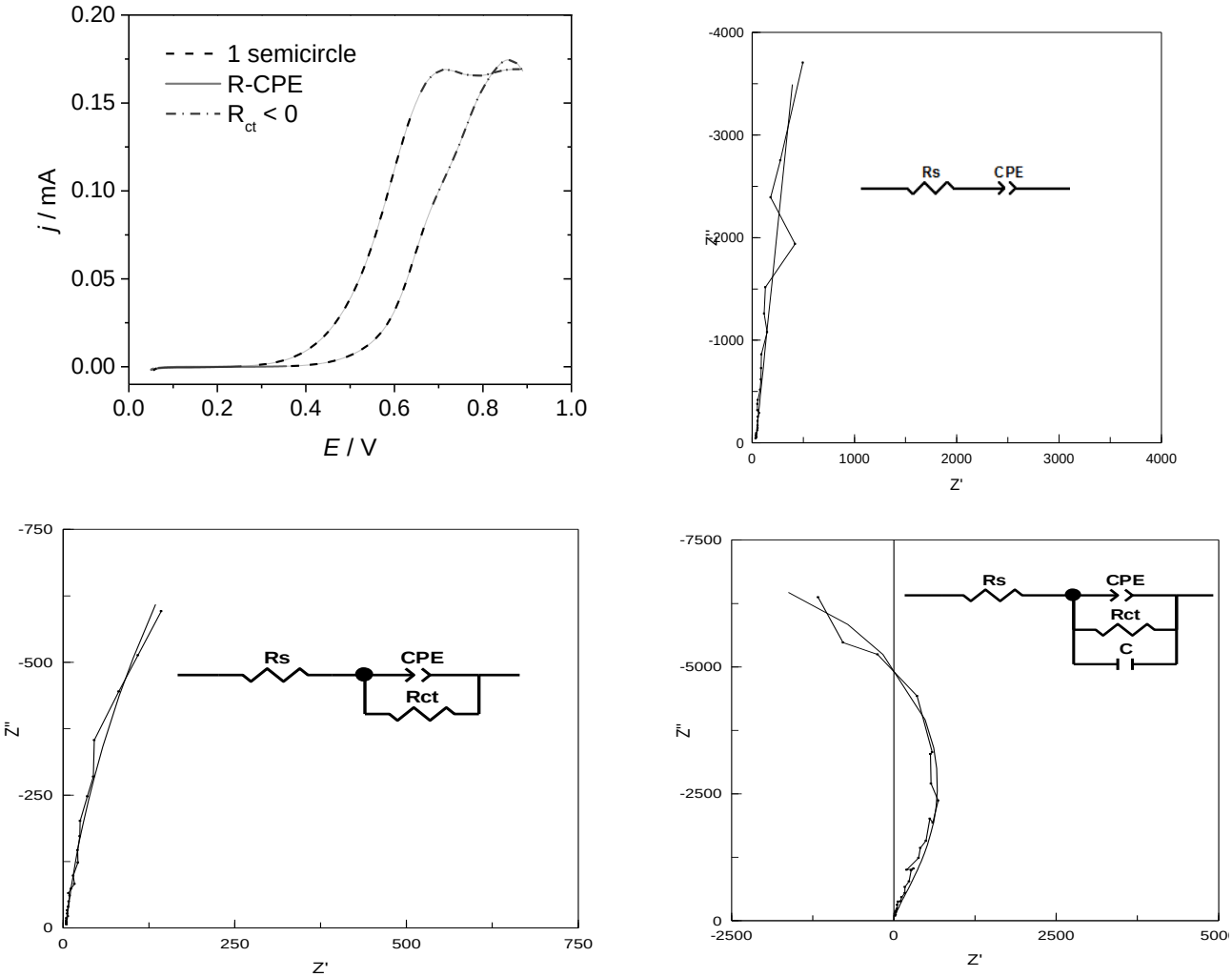

Fig. 5. Cyclic voltammogram and the types of the equivalent circuits used for the approximation of the impedances.

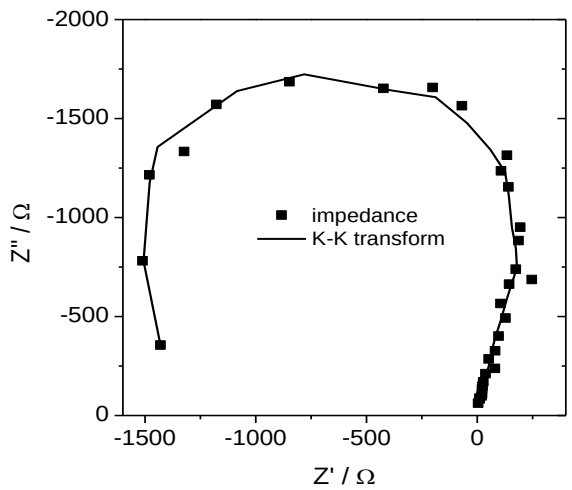

Fig. 6. Impedance and its Kramers-Kronig transform; the transform was carried out on the admittances.

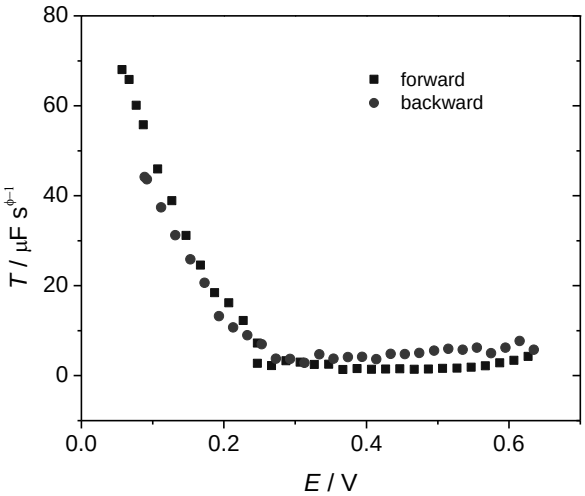

Fig. 7. Dependence of the CPE capacitance parameter *T* on potential.

leads to the correct results [18]. An example of the Kramers-Kronig transform of admittances in shown in Fig. 6 where data are displayed in the complex impedance plot.

Dependence of the double layer capacitance expressed here as the CPE capacitance parameter *T* is shown in Fig. 7. By sweeping to more positive potentials there is a strong decrease of

the capacitance due to adsorption of different organic fragments (CH_3, CH_3CO) and CO which block the electrode surface. This process is reversible. Dependence of the logarithm of the charge transfer resistances on potential is linear, Fig. 8, in the zone where current is increasing/decreasing with potential, the slopes are – 0.143 and – 0.198 V for the forward and backward sweeps.

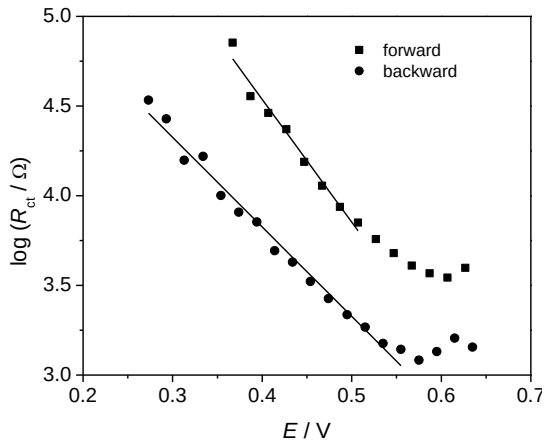

Fig. 8. Dependence of the logarithm of the charge transfer resistance on potential.

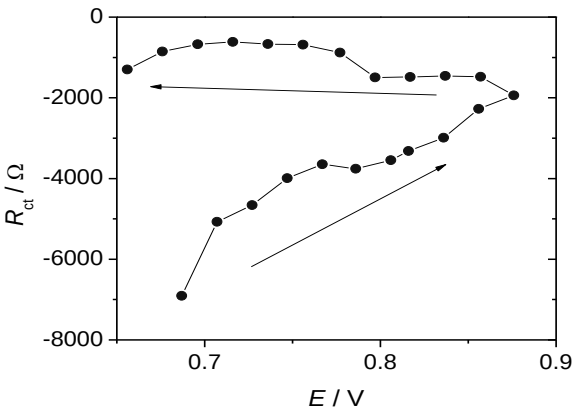

Fig. 9. Dependence of the negative R_{ct} on potential.

Negative values of the charge transfer resistances appear at potentials > 0.65 V, close to the current peak in Fig. 4. Their presence is not evident from the cyclic voltammograms. The plot of negative R_{ct} is shown in Fig. 9.

The dynamic impedance results shed new insight into the mechanism of EtOH oxidation at polycrystalline Pt and explain the behavior of cyclic voltammograms. Further studies at lower concentrations of EtOH and of acetaldehyde and acetic acid are planned.

REFERENCES

1. C. Coutanceau, S. Baranton, C. Lamy, *Modern Aspects of Electrochemistry,* **50,** 397, (2010).
2. K. D. Snell, A. G. Keenan, *Electrochim. Acta* **26,** 1339, (1981).
3. T. Iwasita, B. Rasch, E. Cattaneo, W. Vielstich, *Electrochim. Acta* **34,** 1073, (1989).
4. F. Cases, M. López-Atalaya, J. Vázquez, A. Aldaz, J. Clavilier, *J. Electroanal. Chem.* **278,** 433, (1990).
5. S. S. Mahapatra, A. Dutta, J. Datta, *Electrochim. Acta* **55,** 9097, (2010).
6. E. Pastor, T. Iwasita, *Electrochim. Acta* **39,** 547, (1994).
7. T. Iwasita, E. Pastor, *Electrochim. Acta* **39,** 531 (1994).
8. H. Hitmi, E. M. Belgsir, J. M. Léger, C. Lamy, R. O. Lezna, *Electrochim. Acta* **39,** 407, (1994).
9. F. C. Simoes, D. M. dos Anjos, F. Vigier, J. M. Leger, F. Hahn, C. Coutanceau, E. R. Gonzalez, G. Tremiliosi, A. R. de Andrade, P. Olivi, K. B. Kokoh, *J. Power Sourc.* **167,** 1, (2007).
10. H. Wang, Z. Jusys, R. J. Behm, *J. Phys. Chem. B* **108**, 19413, (2004).
11. S. Sen Gupta, J. Datta, *J. Electroanal. Chem.* **594**, 65, (2006).
12. Y. Bai, J. Wu, J. Xi, J. Wang, W. Zhu, L. Chen, X. Qiu, *Electrochem. Commun*. **7,** 1087, (2005).
13. P. Bommersbach, M. Mohamedi, D. Guay, *J. Electrochem. Soc*. 154 (2007) B876.
14. M.T.M. Koper, in *Advances in Chemical Physics*, I. Prigogine, S. A. Rice, Edts., Wiley, NY, 1996, vol. 92, p. 161.
15. F. Seland, R. Tunold, D. A. Harrington, *Electrochim. Acta* **51,** 3827, (2006).
16. F. Seland, R. Tunold, D. A. Harrington, *Electrochim. Acta* **53,** 6851, (2008).
17. R. L. Sacci, D. A. Harrington, *ECS Transactions* **19(20)**, 31, (2009).
18. D. D. Macdonald, *Electrochim. Acta* **51**, 1376, (2006).

ДИНАМИЧНО ИМПЕДАНСНО ИЗСЛЕДВАНЕ НА ОКИСЛЕНИЕТО НА ЕТАНОЛ ВЪРХУ ПОЛИКРИСТАЛНА ПЛАТИНА

М.-Л. Трамбле[1,2], Д. Ге[2], А. Лазиа[1,*]

[1] *Университет Шербрук, Шербрук, Квебек, Канада*
[2] *INRS-ET, Варен, Квебек, Канада*

Постъпила на 20 февруари, 2012 г.; приета на 20 февруари, 2012 г.

(Резюме)

Чрез циклична волтаметрия и динамична електрохимична импедансна спектроскопия (DEIS) е изследвано окислението на етанол в разтвор на сярна киселина върху поликристален платинов електрод. Установено е, че в близост до волтаметричния пик възникват отрицателни съпротивления, предизвикващи нестабилност (седловинно-възлова бифуркация) и остри пикове във волтамограмата. При най-малките положителни потециали се получава подпотенциално отлагане на водород , но капацитетът спада бързо при по-положителни потенциали поради силната адсорбция на части от EtOH и CO. В основата на волтаметричния пик, log R_{ct} е линейна функция на потенциала с наклон -0.143 V dec^{-1}.

Bulgarian Chemical Communications, Volume 44, Number 4 (pp. 338 – 345) 2012

Electrochemical impedance spectroscopy using exponentially-rising voltage steps. (I) Analysis of a model electrical circuit

P. Millet

Institut de Chimie Moléculaire et des Matériaux d'Orsay, UMR CNRS n° 8182, Université Paris Sud 11, 15 rue Georges Clémenceau, 91405 Orsay cedex France

Received February 20, 2012; accepted February 20, 2012

Electrochemical impedance spectroscopy (EIS) is commonly used by electrochemists to analyze multi-step reaction paths occurring at electrode/electrolyte interfaces. Since the kinetics of individual reaction steps is usually a function of electrode potential, the impedance of the interface is measured for different but constant potential values. In most cases, impedance diagrams are obtained from harmonic analysis: a surimposed low amplitude (typically 5-10 mV) ac potential modulations or alternatively, a low amplitude (typically a few mA) ac galvanostatic modulation, is used as perturbation. However, according to the theory of linear and time invariant systems, harmonic analysis should be restricted to the analysis of linear and reversible processes. To a certain extend, the problem of linearity can be circumvented by reducing the amplitude of the modulation. But that does not help to solve the problem of irreversibility. For example, a significantly large hysteresis is observed during the electro-insertion of hydrogen into palladium or palladium alloy electrodes. This is a clear indication that non-linear phenomena are taking place and therefore, the use of harmonic analysis should be prohibited because the system does not fulfill the requirements of linearity and time invariance imposed by the theory of systems. There is therefore a need to use non-alternating perturbations. The purpose of this paper is to report on the measurement of impedance spectra from exponentially-rising voltage-step excitations. This is a methodology-oriented communication. In the first part of the paper, an electrical circuit containing only electrical resistances and capacitances is used as a model system to explain how impedance diagrams can be obtained from such non-harmonic perturbations. In the second part of the paper, the methodology is extended to the electro-insertion of hydrogen in palladium foils.

Key words: Impedance spectroscopy, Voltage excitation, Electrical circuit

INTRODUCTION

In chemical science, the term "kinetics" is usually making reference to the rate (expressed in $mol.s^{-1}$ or in $mol.s^{-1}.cm^{-2}$ when the active surface is known) at which a given process is occurring. But raw kinetic data, when properly analyzed, carry detailed information on chemical or electrochemical multistep reaction mechanisms. From a practical viewpoint time domain analysis and modeling of raw data is not always trivial because kinetic features of individual steps are usually convoluted. Alternatively, frequency-domain (Fourier) analysis offers the possibility of measuring transfer functions which unambiguously characterize reaction mechanisms and gives access to the rate parameter associated with each reaction step. Electrochemical transfer functions measured at electrode/electrolyte interfaces relate potential perturbations to associated current responses. Such (complex) transfer functions are thus electrical impedances (or conversely, admittances). Harmonic analysis (using sine-wave perturbations) is certainly the most popular way of measuring electrochemical impedances [1] but miscellaneous signals (such as white noise [2], square-waves [3] or multiple sine waves [4]) have also been used as input potential or current perturbations. Other techniques such as current interrupt [5] and alternating current (ac) voltammetry, which was invented in the 1950s [6-9], can also be used for quantitative evaluation of the mechanisms of electrode processes. Conventionally, with the ac technique, a small amplitude sinusoidal potential with a frequency of 10 Hz-100 kHz is superimposed onto the triangular waveform used in dc cyclic voltammetry, and either the total ac response or the dc, fundamental, and higher harmonic are then measured as a function of dc potential and frequency. Garland *et al.* used the technique to study the UPD adsorption of Bi^{3+} at gold electrodes [10]. The technique has also been extended to the combination of cyclic voltametry and surimposed square waves, triangles, sawtooth waveforms or non-harmonically related sine components [11]. However, according to the theory of linear and time invariant systems, the use of wave (alternating) perturbations is restricted to the

* To whom all correspondence should be sent:
E-mail: pierre.millet@u-psud.fr

© 2012 Bulgarian Academy of Sciences, Union of Chemists in Bulgaria

characterization of linear systems and reversible transformations. To a certain extend, the problem of linearity can be circumvented by reducing the amplitude of the surimposed modulation. But that does not help to solve the problem of irreversibility. For example, a significantly large hysteresis is observed during the electro-insertion of hydrogen in palladium or palladium alloys. This is a clear indication that non-linear phenomena are taking place and therefore, the use of harmonic analysis should be prohibited because the system does not fulfill the requirements of linearity and time invariance imposed by the theory of systems. To investigate the dynamic features of such systems, there is therefore a need to use non-alternating perturbations. Potential steps are appropriate signals for the measurement of impedances at electrode/electrolyte interfaces where irreversible processes are taking place because their first time-derivative is strictly positive (rising up step) or negative (rising down step). Application of potential steps to such systems offers the possibility to study separately back and forth transformations. The concept has already been proposed to analyze the electrochemical hydriding reactions of palladium in two-phase domains [12] but few details were given concerning the methodology used for the measurements. A similar concept based on the application of "pressure steps" has also been used to analyze gas-phase reactions [13]. The purpose of this paper is to describe the measurement of impedance diagrams from potential steps. This is a methodology-oriented communication and we focus primarily on the constraints and criteria of measurements in the context of new data acquisition electronics that became available during the last few years. In the first part of the paper, an electrical circuit containing only electrical resistances and capacitances is used as a model system. This is a simple case because experiments are very brief (a few milliseconds long). As a result, sampling conditions and data treatment procedures are easy to manage and impedance diagrams easy to obtain. In the second part of the paper, the methodology is extended to the study of a more complicated case, the electro-insertion of hydrogen in palladium foils.

EXPERIMENTAL

Experimental setup

A computer-controlled Radiometer Analytical PGZ 402 potentiostat-galvanostat has been used to apply voltage excitations. In addition, an Agilent DSO 6032 A (2 channels, 300 MHz) oscilloscope has been used to sample the potential and current transients. Short (10 cm long) electric cables were used to minimize parasite impedance losses.

Electrical circuit

The model electrical circuit used for the experiments is pictured in Fig 1. Two parallel RC circuits (R_1, C_1 and R_2, C_2) are connected in series. The time constants of each sub-circuit ($\tau_1 = R_1.C_1 = 2.35\text{x}10^{-5}$ s and $\tau_2 = R_2.C_2 = 10^{-2}$ s) differ by a factor of $\tau_2/(\tau_1 = 425$, and each sub-circuit has quite different dynamic features. A third resistance R_0 is connected in series.

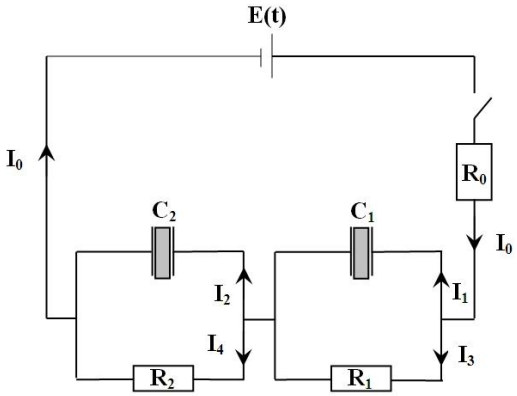

Fig. 1. Model electrical circuit. R_0 = 12100 Ω; R_1 = 4990 Ω; $C_1 = 4.7\text{x}10^{-9}$ F;R_2 = 10000 Ω; $C_2 = 1\text{x}10^{-6}$ F. E(t) = voltage excitation. I_0, I_1, I_2, I_3 and I: current responses.

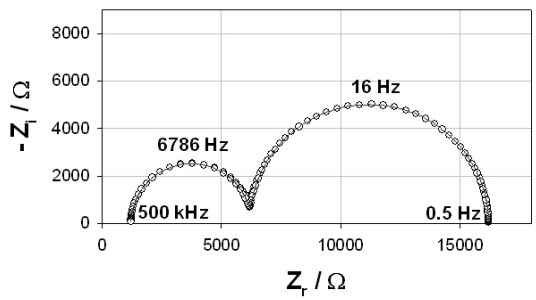

Fig. 2. Impedance diagram of the electrical circuit of Fig 1.(o) experimental (sine wave perturbation); (—) calculated from Eq. (1).

The analytical impedance of the electrical circuit of Fig. 1 is given by equation (1) where $\omega = 2\pi f$ is the pulsation in rad.s^{-1} and f is the frequency in Hz:

$$Z(\omega) = R_0 + \frac{1}{j\,\omega\,C_1 + \frac{1}{R_1}} + \frac{1}{j\,\omega\,C_2 + \frac{1}{R_2}} \qquad (1)$$

The experimental impedance diagram measured with the Radiometer potentiostat using sine wave potential perturbations is plotted in Nyquist coordinates in Fig. 2. The measure was made at a constant voltage of 0 V with a 5 mV sur-imposed ac perturbation. The model impedance diagram

obtained from Eq. (1) is also plotted for comparison. There is a good overall agreement over the entire frequency range, indicating that the values of R_0, R_1, R_2, C_1 and C_2 given in the caption of figure 1 are known with a sufficiently good accuracy and that the signal-to-noise ratio is appropriately high. The time constant of the two RC circuits are significantly different and the impedance of each sub-circuit (a semi circle along the real axis) are well separated in frequency. The impedance of the first sub-circuit (R_1, C_1) with the lowest time constant appears in the high frequency range and the impedance of the second sub-circuit (R_2, C_2) appears in the low frequency range. The characteristic pulsations ω_c (in rad.s^{-1}) at the top of each semi-circle is related to each time constant: $\omega_{ci} = 2\pi f_{ci} = 1/\tau_i$. where f_{ci} is the corresponding characteristic frequency (in Hz or s^{-1}). Practical conditions required for obtaining impedance diagrams from potential step excitations are discussed in the following sections.

THEORY

Linear and time invariant systems (LTIS)

In the followings, the implicit variable is time (t) throughout. System theory analyzes the relationships between any given input i(t) and the corresponding output o(t). A system is said to be linear and time invariant when the following conditions are satisfied:

(i) causality:

$$i(t), o(t) = 0 \quad \forall\, t < 0 \qquad (2)$$

(ii) linearity:

$$\alpha_1\, i_1(t) + \alpha_2\, i_2(t) \rightarrow \beta_1\, o_1(t) + \beta_2\, o_2(t) \qquad (3)$$

where α_1, α_2, β_1 and β_2 are scalars.

(iii) time invariance:

$$i(t-\tau) \rightarrow o(t-\tau) \qquad (4)$$

where τ is the time shift.

Let h(t) be the output obtained when the unit impulse (Dirac) function □(t) is applied as input. h(t) is called the impulse response :

$$\delta(t) \rightarrow h(t) \qquad (5)$$

The theory of LTIS demonstrates that for systems satisfying conditions (2), (3) and (4), the output o(t) is related to the convolution product of the input i(t) by h(t) :

$$o(t) = \int_{-\infty}^{+\infty} i(\tau)\, h(t-\tau)\, d\tau = i(t) * h(t) \qquad (6)$$

Complex exponentials remain frequency unaltered when passing through LTIS. Only amplitude modulations and phase shifts occur. i(t) and o(t) can thus be adequately expressed on the basis of complex exponentials. This operation is called Fourier transformation:

$$G(f) = FT[g(t)] = \int_{-\infty}^{+\infty} g(t)\, e^{-j\omega t}\, dt \qquad (7)$$

where f is the frequency in Hz, $\omega = 2\pi f$ is the pulsation in rad.s^{-1}, and FT[g(t)] is the Fourier transform of g(t).

An interesting property of the Fourier transformation is that the convolution product (6) in the time (direct) domain is simply an algebraic product in the Fourier (frequency) domain:

$$FT[i(t) * h(t)] = FT[i(t)] \bullet FT[h(t)] = FT[o(t)] \qquad (8)$$

The FT of the impulse response h(t) is called the transfer function of the system:

$$FT[h(t)] = H(f) = \int_{-\infty}^{+\infty} h(t)\, e^{-j\omega t}\, dt \qquad (9)$$

Thus, for a LTIS, the general relationship between input i(t) and output o(t) is a convolution product in the time-domain and an algebraic product in the Fourier domain. According to Eq. (8), the transfer function H(f) can be obtained in principle by taking the ratio of the FTs of any pair {i(t); o(t)}, *ie* : H(f) = FT{o(t)}/FT{i(t)}. This is possible as long as the denominator is non-zero at the frequencies of interest. It turns out that this is the case for electrical and electrochemical systems for which the input i(t) is the electric potential E(t) and the response o(t) is the current I(t). The associated transfer function is a complex impedance Z(ω):

$$Z(\omega) = \frac{E(\omega)}{I(\omega)} \qquad (10)$$

E(ω) is the Fourier Transform (FT) of the voltage excitation E(t) in Volt and I(□) is the FT of the current response in Amp.

Voltage excitations

Electrical potential steps E(t) generated by commercial potentiostats are not true Heaviside steps. In order to avoid dumping effects, E(t) has usually a finite rising-time and is, instead of a true step, an exponential function rising to a maximum value (Fig. 3), the analytical expression of which is:

$$E(t) = a.\,[1 - \exp(-\,b.t)] \qquad (11)$$

where a is the amplitude in V and b = 1/τ in s^{-1} (τ is a time constant in s). This is why in this paper, such signals are called "exponentially-rising voltage-step excitations". Results were obtained using a PGZ402 potentiostat from Radiometer, with a mean time constant τ = 1/b = 6.424x10^{-5} s (when no filter is used). Experimental voltage excitations generated by the potentiostat were found to be reproducible

within ± 0.05 % from one experiment to the other. The frequency content of such voltage excitations can be determined by taking the Fourier transform (FT) of Eq. (11). A convenient way to do that is to calculate the Laplace transform (LT) and then explicit the transformation variable $s = j\omega$:

$$LT\{E(t)\} = a\int_0^{+\infty}\left(1-e^{-bt}\right)e^{-pt}\,dt = a\left[\frac{1}{p}-\frac{1}{p+b}\right] = \frac{ab}{p^2+bp} \quad (12)$$

$$FT\{E(t)\} = LT\{E(t), p = j\omega\} = \frac{ab+j0}{-\omega^2+j\omega b} \quad (13)$$

Eq. (13) is the general solution except for ω = 0 for which (δ (t) is the Dirac function):

$$FT\{E(t), \omega = 0\} = \delta(t)\frac{a}{2} \quad (14)$$

In conventional harmonic analysis, sine wave functions of similar amplitudes are used to measure the impedance of the system over the entire frequency range of interest on a frequency-to-frequency basis. As can be seen from Eqs. (13) and (14), the energy content of an exponentially-rising voltage-step excitations is inversely proportional to the frequency. This is a limitation of the technique because the energy of the signal decreases as the frequency increases. Therefore, the amplitude of the excitation must be sufficiently large and the apparatus used to measure the current response must be sufficiently sensitive to accurately sample the signals.

RESULTS AND DISCUSSION

Experimentally, the problem to solve consists in the measurement of the impedance of a given system of interest by using such smooth voltage excitations as perturbation. In the first part of this paper, the system under consideration is the electrical circuit of Figure 1. This is a low noise system and equilibrium is reached within a few tens of milliseconds. In the second part of the paper, the system will be a noisier electrode/electrolyte interface for which equilibrium is reached within only a few seconds. The same methodology is used to characterize both systems. In a typical experiment, two transient signals are sampled : the rising voltage excitation E(t) and the associated current response I(t). To determine the unknown impedance of the electrical circuit there are two options: (i) frequency-domain analysis : the Fourier transform of both E(t) and I(t) are calculated and the ratio of the two FTs is taken as shown in Eq. (10), yielding the impedance Z(ω) of the circuit; this is the most straightforward method; (ii) time-domain analysis: a model circuit impedance Z(ω) is postulated; then, I(ω), the FT of the current response to the voltage excitation is calculated from Eq. (10): I(ω) = E(ω) / Z(ω); then, model I(t) is calculated from I(ω) by inverse Fourier transformation and used to fit transient experimental current I(t); parameters of the model impedance Z(ω) are iteratively adjusted to minimize the difference between model and experimental I(t) in order to determine the exact characteristic of circuit components. This second approach is more difficult to implement than the first one but can sometimes be more efficient and even more accurate. It can also be automated. The two approaches are detailed in the followings. The circuit of Fig. 1 of known impedance is used as a model system to describe the methodology and to evaluate the role of data sampling and data filtering on the quality of the resulting impedance.

Frequency-domain analysis

Solution to the convolution equation in the frequency domain. The impedance diagram of the circuit of Fig. 1 can be obtained directly from frequency-domain analysis of experimental data using Eq. (15):

$$Z(\omega) = \frac{E(\omega)}{I_0(\omega)} \quad (15)$$

where E is the voltage excitation in Volt, I_0 is the current response of the cell in A, and ω is the pulsation in rad.s^{-1}. E(ω) denotes the Fourier transform of the voltage excitation E(t), and $I_0(\omega)$ denotes the Fourier transform of the current response I(t).

Sampling conditions and data treatment. In order to calculate the impedance diagram, there is a need to sample both transient signals : voltage excitation and current response. The Fourier transform of the discrete transients can then be calculated and the ratio yields the desired impedance diagram. The sampling rate must respect the Nyquist criterion which states that the signal must be sampled more than twice as fast as the highest waveform frequency (f_c). If not, it turns out that all of the power spectral density (PSD) which lies outside of the frequency range $-f_c < f < f_c$ is spuriously moved into that range and the spectrum is corrupted. This phenomenon is called aliasing [14]. According to Fig. 2, the impedance of the circuit reaches the real axis at a frequency value of ≈ 500,000 Hz. Therefore, a sampling rate of one sample every 1 μs (or less) is required. The sampling rate must be maintained until the end of the experiment (20 millisec in the present case). As

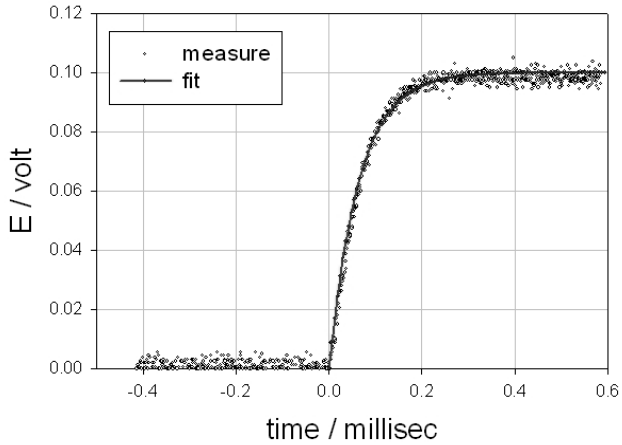

Fig. 3. (o) experimental voltage excitation and (+) best fit using Eq. (11).

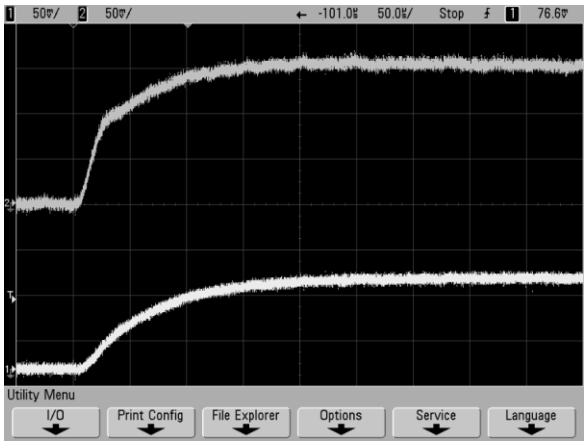

Fig. 4. Experimental voltage excitation (bottom) and current response (top) of the electrical circuit of Fig. 1.

a result, 20,000 datapoints will be collected for each signal, corresponding to a file of only *ca.* 4 Mbytes of floats. The signals displayed on the screen of the oscilloscope at the onset of the step during a typical experiment are shown in Fig. 4 (time scale 0-500 μsec).

Raw data cannot always be used directly. Electronic or numerical filtering using low-pass filters is required prior to Fourier transformation in order to get rid of the polluted high frequency content of raw data [14]. Different filters (available on most potentiostats) can be used for that purpose although they also change the time constant of the step functions. In order to improve the signal-to-noise ratio, a first approach is to use the analytical expression of E(ω) (taken from Eq. (13)) in Eq. (15) instead of sampling the true experimental voltage step. This is justified by the fact that exponentially-rising voltage steps delivered by potentiostat are highly reproducible. Thus, the sampled current response is the only source of noise for the impedance diagram. It should also be noted that, according to Eq. (13), the PSD =

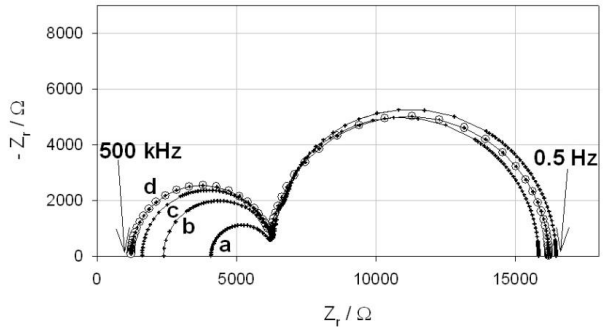

Fig. 5. Impedance diagrams of the circuit of Fig. 1; (o) calculated from Eq. (1); (+) experimental from exponentially-rising voltage-step excitations: (a) Δt = 50 μs; (b) Δt = 20 μs; (c) Δt = 10 μs; (d) Δt = 5 μs.

$\sqrt{\mathrm{Re}^2\{E(\omega)\}+\mathrm{Im}^2\{E(\omega)\}}$ of the exponentially-rising voltage steps decreases exponentially with frequency. Therefore, a highly sensitive amperemeter and low-pass filtering should be used to obtain well-defined impedance diagrams in the potentially noisiest high-frequency region where widely scattered data-points are obtained otherwise [5].

*Comparison of model and experimental impedance values.*Impedance diagrams obtained from exponentially-rising voltage-step excitations are plotted in Fig. 5. The theoretical impedance diagram obtained from Eq. (1) is also plotted for comparison. There is a good agreement between both techniques, both in terms of impedance values and frequency content. However, the sampling rate of current responses plays a critical role. A sampling rate of at least one data-point every 5 μs is required to obtain a satisfactory fit (curve d). At 5 μs, a data file of 400 kbytes is obtained and the impedance is calculated within only a few seconds. Therefore, this is achievable using conventional personal computers. If lower sampling rates are used (curves a, b, c), then significant distortions appear in the high frequency range.

Time-domain analysis

Solution to the convolution equation in the time domain. Circuit impedance parameters can also be determined from a time-domain analysis of experimental data. In a typical experiment, the electrical circuit of Fig. 1 is excited by a voltage transient E(t) of any shape. $E_{R0}(t)$ (the voltage of the resistance R_0), $E_{R1}(t)$ (the voltage of the resistance R_1), $E_{C1}(t)$ (the voltage of the capacitance C_1), $E_{R2}(t)$ (the voltage of the resistance R_2), and $E_{C2}(t)$ (the voltage of the capacitance C_2) are the five unknown transient voltages. $I_0(t)$ (the main transient current across the circuit), $I_1(t)$ (the current across capacitance C_1), $I_3(t)$ (the current across

resistance R_1), $I_2(t)$ (the current across capacitance C_2) and $I_4(t)$ (the current across resistance R_2) are the five unknown transient currents. By applying Kirchhoff's laws (conservation of charge and) to the circuit of Fig. 1, the following set of five equations is obtained:

$$\frac{1}{C_1}\int_0^t I_1(t)\,dt = R_1\left[I_0(t)-I_1(t)\right] \quad (16)$$

$$\frac{1}{C_2}\int_0^t I_2(t)\,dt = R_2\left[I_0(t)-I_1(t)\right] \quad (17)$$

$$E(t)=R_0\,I_0(t)+\frac{1}{C_1}\int_0^t I_1(t)\,dt+\frac{1}{C_2}\int_0^t I_2(t)\,dt \quad (18)$$

$$I_0(t)=I_1(t)+I_3(t) \quad (19)$$

$$I_0(t)=I_2(t)+I_4(t) \quad (20)$$

The system can be solved by use of Laplace transformation. Solutions for the five voltage transients are:

$$E_{R0}(s)=R_0\,I_0(s) \quad (21)$$

$$E_{R1}(s)=R_1\left[I_0(s)-I_1(s)\right] \quad (22)$$

$$E_{C1}(s)=\frac{I_1(s)}{s\,C_1} \quad (23)$$

$$E_{R2}(s)=R_2\left[I_0(s)-I_2(s)\right] \quad (24)$$

$$E_{C2}(s)=\frac{I_2(s)}{s\,C_2} \quad (25)$$

Solutions for the five current transients are:

$$I_0(s)=E(s)\left[R_0+\frac{1}{s\,C_1}\left[\frac{R_1}{R_1+\frac{1}{s\,C_1}}\right]+\frac{1}{s\,C_2}\left[\frac{R_2}{R_2+\frac{1}{s\,C_2}}\right]\right]^{-1} \quad (26)$$

$$I_1(s)=I_0(s)\left[\frac{R_1}{R_1+\frac{1}{s\,C_1}}\right] \quad (27)$$

$$I_2(s)=I_0(s)\left[\frac{R_2}{R_2+\frac{1}{s\,C_2}}\right] \quad (28)$$

$$I_3(s)=I_0(s)-I_1(s) \quad (29)$$

$$I_4(s)=I_0(s)-I_2(s) \quad (30)$$

Time domain solutions to Eqs. (20-29) can be obtained analytically (this is not always possible, especially as the complexity of the circuit increases) by choosing the shape of the perturbation E(t). Alternatively, solutions can also be conveniently obtained numerically by computing the inverse discrete Fourier transform (IDFT) of Eq. (20-29) for s = jω. The IDFT h(t) of a signal with a frequency content H(f) is given by:

$$h(t)=\int_{-\infty}^{+\infty} H(f)e^{2\pi j f t}\,df \quad (31)$$

The discrete expression of Eq. (31) is :

$$h(t)=\sum_{-\infty}^{+\infty} H(f)\left[\cos(2\pi f t)-j\sin(2\pi f t)\right]\Delta f \quad (32)$$

Transient voltage values. Numerical voltage responses of circuit components (Fig. 1) to E(t) = exponentially-rising voltage-step excitation are plotted in Fig. 6. Data have been obtained numerically by solving Eqs. (21-25) using the circuit impedance of Eq. (1).

The time axis is in logarithmic scale to facilitate the differentiation of the different voltages. The rising voltage excitation E(t) has an amplitude of 0.1 V and reaches its plateau value in less than 0.5 milliseconds. Stationary signals are obtained after *ca.* 2×10^{-2} seconds. At that time, capacitances C_1 and C_2 are charged and their impedance is infinite. A stationary current flows across the series-connected resistances: $\sum_i R_i = R_0 + R_1 + R_2$ = 16200 Ω. Therefore, the stationary current for t > 10^{-2} s is $I_0=\frac{A}{\sum_i R_i}$=0.1/16200 = 6.17 μA.

Individual stationary voltages are:

$$E(t)=\lim_{t\to\infty} a\left(1-e^{-\frac{t}{\tau}}\right)=a=100\ mV$$

$E_{R0}=R_0\,I_0$=7.5mV; $E_{R1}=E_{C1}=R_1\,I_0$ = 30.8 mV;

$E_{R2}=E_{C2}=R_2\,I_0$ = 61.7 mV.

According to Kirchhoff's law: E(t) = $E_{R0}(t)$ + $E_{R1}(t)$ + $E_{R2}(t)$.

Therefore, experimental transient voltages of individual circuit components can be fitted with model values. The difference between experimental and model values can be minimized by iteration and the impedance of each circuit component can be adjusted until a complete agreement is obtained between both sets of data.

Transient current values. Numerical current responses of the electrical circuit of Fig. 1 to a exponentially-rising voltage-step excitation E(t) are plotted in Fig. 7. Data have been obtained by solving Eqs. (26-30). Again, the time axis is in logarithmic scale to facilitate the differentiation of the different signals.

For t > 10^{-2} s, the stationary currents are:

$I_0(t\to\infty)=I_3(t\to\infty)=I_4(t\to\infty)$ = 6.17 μA and $I_1(t\to\infty)=I_2(t\to\infty)=0$.

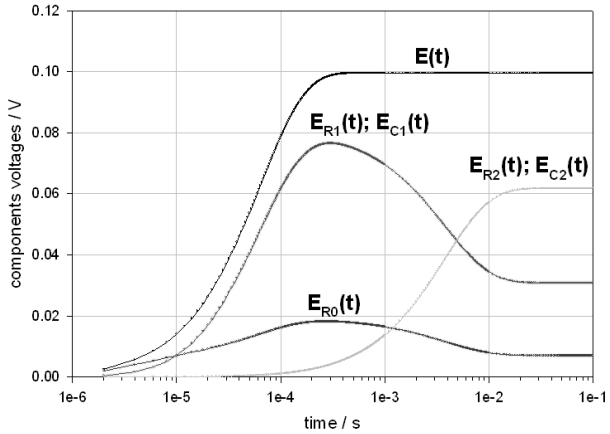

Fig. 6. Transient voltages responses of the electrical circuit of figure 1 when E(t) = a [1 – exp (-t/τ)]. a= 100 mV. τ = 1/b = 6.424x10^{-5} s.

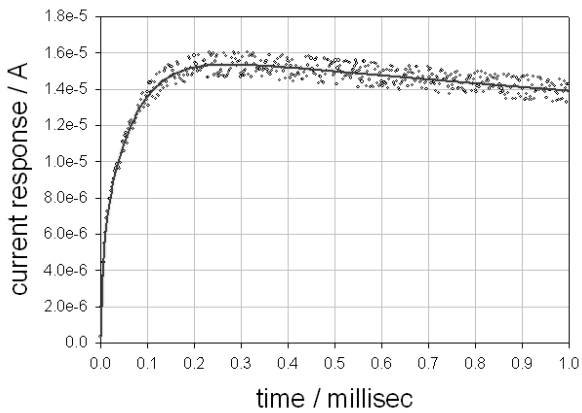

Fig. 8. Experimental (o) and model (—) current responses $I_0(t)$ of the circuit of Fig. 1 when a smooth voltage excitation is applied

Model current responses can be used to fit experimental current values, as discussed in the next section.

Comparison of experimental and model values. The experimental current response $I_0(t)$ has been fitted as follows. First, I(ω) has been calculated from Eq. (10): I(ω) = Z(ω) / E(ω). Z(ω) was taken from Eq. (1) and E(ω) was taken from Eq. (13). Second, I(t) was calculated from I(ω) by discrete inverse Fourier transformation. Results obtained for the first millisecond of the experiment are plotted in Fig. 8. There is a good agreement between experimental and calculated transients. Therefore, time-domain analysis of the current response of the interface to a smooth voltage excitation can also be used to determine the impedance of an unknown circuit.

CONCLUSIONS

The work reported here describes a methodology used to determine the impedance of

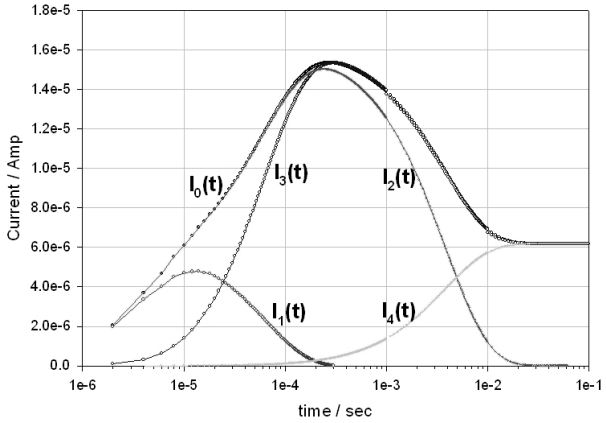

Fig. 7. Transient current responses of the electrical circuit of figure 1 when E(t) = a [1 – exp (-t/τ)]. a= 100 mV. τ = 1/b = 6.424x10^{-5} s.

electrical circuits from exponentially-rising voltage-step excitations. When such experiment is carried out, two transient signals are synchronously sampled: the potential excitation E(t) and the current response I(t). To determine the unknown impedance of the electrical circuit there are two options: (i) frequency-domain analysis : the Fourier transform of both E(t) and I(t) are calculated and the ratio of the two FTs is taken using Eq. ω (10), yielding the impedance Z(ω) of the circuit; this is the most straightforward method; (ii) time-domain analysis: a model circuit impedance Z(ω) is postulated; then, the FT I(w) of the current response to a exponentially-rising voltage-step excitation is

calculated from Eq. (10) : I(ω) = E(ω) / Z(ω); then, model I(t) is calculated from I(ω) by inverse Fourier transformation and used to fit transient experimental current I(t); parameters of the model impedance Z(ω) are iteratively adjusted to minimize the difference between model and experimental I(t) in order to determine the exact characteristic of circuit components. There are two critical problems. First, an appropriate sampling rate must be used. Second, data filtering is required. When these problems are appropriately handled, then correct impedance diagrams are obtained. Therefore, it can be concluded that exponentially-rising voltage-step excitations can be used to measure impedance diagrams of electrical circuits.

***Acknowledgements**: Financial support from the French Agence Nationale de la Recherche, within the frame of the Plan d'Action National sur l'Hydrogène (EolHy project ANR-06-PANH—008-06 and AP'H project ANR-05-PANH—011-04), is acknowledged.*

REFERENCES

1. L. Schlapbach, A. Züttel, Nature, **414**, 353 (2001).
2. P. Millet, R. Ngameni, Electrochimica Acta 2011, doi: 10.1016/j.electacta.2010.12.106.
3. G. Tsirlina, S. Baronov, F. Spiridonov, M. Rusanova, T. Safonova, O. Petrii, Russ. J. Electrochem., **36**, 1179 (2000).
4. J. Chen, R. Durand, C. Montella, *J. Chem. Phys.*, **91,** 383 (1994).
5. P. Millet, *Electrochem. Commun.*, **7,** 40 (2005).
6. A. Frumkin, in: P. Delahay (Ed.), Advances in Electrochemistry and Electro-chemical Engineering, Vol. 3, Interscience, NewYork, 1963.
7. J. Bockris, J. McBreen, L. Nanis, *J. Electrochem. Soc.*, **112,** 1025 (1965).
8. L. Jacobsen, K. West, *Electrochimica Acta*, **40,** 255 (1995).
9. C. Lim, S. Pyum, *Electrochimica Acta*, **38,** 2645 (1993).
10. E. Barsoukov, J. R. Mac Donald, Impedance Spectroscopy, Theory, Experiment, and Applications, Wiley, 2005.
11. R. Bucur, E. Indren, *Acta Met*., **35,** 1325, (1987).
12. W. Press, in *Numerical Recipes, the Art of Scientific Computing*, Cambridge University Press: Cambridge, 1986.
13. H. Wiese, K. Weil, IEEE Transactions on Acoustics, Speech, and Signal Processing, **36**(7) July 1988.
14. E. Barsoukov, S. Ryu, H. Lee, *J. Electroanal. Chem.*, **536,** 109 (2002).

ЕЛЕКТРОХИМИЧНА ИМПЕДАНСНА СПЕКТРОСКОПИЯ С ЕКСПОНЕНЦИАЛНО НАРАСТВАЩИ СТЪПКИ НА НАПРЕЖЕНИЕТО (I) АНАЛИЗ НА МОДЕЛНА ЕЛЕКТРИЧЕСКА СХЕМА

П. Мийе

Институт по молекулярна химия и материали в Орсе, UMR CNRS n° 8182, Университет Париж Юг, ул. Жорж Клемансо 11, 15, 91405 Орсе седекс, Франция

Постъпила на 20 февруари, 2012 г.; приета на 20 февруари, 2012 г.

(Резюме)

Електрохимичната импедансна спектроскопия (IES) обикновено се използва от електрохимиците за анализиране на многостепенни реакции, протичащи на фазовата граница електрод/електролит. Понеже кинетиката на отделните стъпки на реакцията обикновено е функция на електродния потенциал, импедансът на фазовата граница се измерва при различни, но постоянни стойности на потенциала. В повечето случаи импедансните диаграми се получават чрез хармоничен анализ: за възбуждане се използва наложена променливотокова модулация на потенциала с ниска амплитуда (типично 5-10 мВ) или галваностатична променливотокова модулация с ниска амплитуда (типично няколко мА). Според теорията на линейните и непроменливи във времето системи обаче, хармоничният анализ следва да бъде ограничен до анализа на линейни и обратими процеси. Проблемът с линейността може да бъде преодолян до известна степен чрез намаляване амплитудата на модулацията. Но това не помага да се разреши проблема с необратимостта. Например, при електро-интеркалацията на водород в електроди от паладий или паладиеви сплави, се наблюдава значителен хистерезис. Това е ясно указание, че протичат нелинейни процеси и следователно хармоничният анализ не може да се използва, защото системата не изпълнява изискванията за линейност и неизменност във времето, наложени от системната теория. Значи трябва да се използва непроменливо възбуждане. Целта на настоящата работа е да се докладва за измерването на импедансни спектри при възбуждане с експоненциално нарастващи стъпки по напрежение. Това съобщение е ориентирано към методологията. В първата част на работата, електрическа схема съдържаща само електрическо съпротивление и капацитет се използва като моделна система, за да се обясни как от такова нехармонично възбуждане може да се получи импедансна диаграма. Във втората част на работата, методологията се разширява до електро-интеркалацията на водород в паладиево фолио.

Bulgarian Chemical Communications, Volume 44, Number 4 (pp. 346 – 355) 2012

Electrochemical impedance spectroscopy using exponentially-rising voltage steps. (II) Analysis of the hydrogen electro-insertion into palladium foils

P. Millet

Institut de Chimie Moléculaire et des Matériaux d'Orsay, UMR CNRS n° 8182, Université Paris Sud 11, 15 rue Georges Clémenceau, 91405 Orsay cedex France

Received February 20, 2012; accepted February 20, 2012

Electrochemical impedance spectroscopy (EIS) is commonly used by electrochemists to analyze multi-step reaction paths occurring at electrode/electrolyte interfaces. Since the kinetics of individual reaction steps is usually a function of electrode potential, the impedance of the interface is measured for different but constant potential values. In most cases, impedance diagrams are obtained from harmonic analysis: a surimposed low amplitude (typically 5-10 mV) ac potential modulations or alternatively, a low amplitude (typically a few mA) ac galvanostatic modulation, is used as perturbation. However, according to the theory of linear and time invariant systems, harmonic analysis should be restricted to the analysis of linear and reversible processes. To a certain extend, the problem of linearity can be circumvented by reducing the amplitude of the modulation. But that does not help to solve the problem of irreversibility. For example, a significantly large hysteresis is observed during the electro-insertion of hydrogen into palladium or palladium alloy electrodes. This is a clear indication that non-linear phenomena are taking place and therefore, the use of harmonic analysis should be prohibited because the system does not fulfill the requirements of linearity and time invariance imposed by the theory of systems. There is therefore a need to use non-alternating perturbations. The purpose of this paper is to report on the measurement of impedance spectra from exponentially-rising voltage steps. This is a methodology-oriented communication. In the first part of the paper, an electrical circuit containing only electrical resistances and capacitances is used as a model system to explain how impedance diagrams can be obtained from such non-harmonic perturbations. In the second part of the paper, the methodology is extended to the electro-insertion of hydrogen in palladium foils.

Key words: Impedance spectroscopy, Palladium, Hydriding kinetics, Voltage step

INTRODUCTION

The advantages of exponentially-rising voltage steps over voltage sine waves for the measurement of chemical or electrochemical impedances have been exposed in the first part of this part. The purpose of this second part is to report on the determination of the impedance of a palladium electrode during hydrogen insertion using an exponentially-rising voltage step as electrical perturbation. Analysis of phase transformation processes observed in most hydrogen-absorbing materials (pure metals, alloys or compounds) is still a matter of active research, in view of electrochemical or chemical hydrogen storage applications. Metal-hydride forming materials (some elemental metals, some alloys and some intermetallic compounds) are of great practical interest for miscellaneous industrial applications such as H_2(g) storage and purification, NiMH batteries, heat pumps or hydrogen isotopic separation. The current status of metal hydride technology is such that new materials with enhanced thermodynamic and kinetic properties are still required, in particular for the storage of gaseous hydrogen in the automotive industry, an application for which the energy density of current storage tanks is still a limiting factor [1]. The kinetics of hydrogen insertion can be analyzed through either electrochemical or chemical (gas-phase) experiments and both techniques provide complementary information [2]. One of the most striking characteristic of metal hydrogen systems is the presence of a large hysteresis which complicates the measurements of kinetic parameters. Hysteresis indicates that irreversible processes are taking place at the microscopic scale and therefore, sine waves perturbations commonly used in the popular electrochemical impedance

* To whom all correspondence should be sent:
E-mail: pierre.millet@u-psud.fr

© 2012 Bulgarian Academy of Sciences, Union of Chemists in Bulgaria

spectroscopy (EIS) are inappropriate. There is a need to use non-alternating perturbations. The purpose of this paper is to investigate the possibility of measuring electrochemical impedances from exponentially-rising voltage step experiments. This is a methodology-oriented communication. In the first part of the paper, an electrical circuit containing only electrical resistances and capacitances was used as a model system. The situation was simple because experiments are very brief (a few milliseconds long). As a result, sampling conditions and data treatment procedures are easy to manage and impedance diagrams are easy to obtain. In the second part of the paper, the methodology is extended to the study of a more complicated case, the electro-insertion of hydrogen into palladium foils.

EXPERIMENTAL

Chemicals

A palladium foil (99.9 %, 100 μm thick, 680.23 mg = 6393 Pd μmole, S ≈ 8 cm^2, Aldrich) has been used as working electrode. The roughness factor of the foil determined from cyclic voltammetry experiments by integrating the reduction peak of chemisorbed oxygen [3] and using a reference charge of 0.42 mC cm^{-2}, was found to be close to unity. Although the sample microstructure can potentially have a strong impact on hydrogen solubility and mobility, the Pd electrode was used "as-received" (a cold-rolled sample) without any preliminary treatment to adjust the microstructure to any reference state. 0.1 M H_2SO_4 solutions prepared from suprapur (Merck Co.) H_2SO_4 using 18 MΩ cm deionised water have been used as liquid electrolyte.

Experimental setup

Electrochemical experiments have been performed using a conventional one-compartment electrochemical cell. The Pd working electrode was connected to the external electric circuitry using a gold connector. Two large counter electrodes (Pt foils) were placed on each side of the Pd WE to warrant symmetrical loadings/un-loadings as described elsewhere [4]. Short (10 cm long) electric cables were used to minimize parasite impedance losses. A computer-controlled Radiometer Analytical PGZ 402 potentiostat-galvanostat was used to apply exponentially-rising voltage steps and collect transient current responses with sampling rates of a few kHZ. In addition, an Agilent DSO 6032 A (2 channels, 300 MHz) oscilloscope was also used to sample the transients during the first tens of milliseconds of the experiments, when the double layer capacitance is charged.

PdH isotherms

A typical electrochemical PdH isotherm measured at room temperature using galvanostatic pulses [5] is plotted in figure 1. The hydrogen content of the Pd foil is expressed in terms of H/Pd, the dimensionless ratio of mole numbers. At low hydrogen contents (H/Pd < 0.04), a homogeneous solid solution (α-PdH) of hydrogen in palladium is formed. In this composition range, the Pd-H system is bi-variant and the electrode potential rises with composition. After saturation, a sub-stoechiometric ($PdH_{0.6}$ at this temperature) hydride phase (β-PdH) starts to precipitate. The system becomes mono-variant and according to Gibbs' rule of phase, a potential plateau appears. Once the sample is fully hydrided (H/Pd ≈ 0.6), it is still possible to insert limited amounts of hydrogen to form a new solid solution of hydrogen in β-PdH. Since α-PdH is now totally transformed into β-PdH, the PdH system is again bi-variant and the electrode potential rises again sharply with composition. A symmetrical situation prevails during desorption. However, phase limits are slightly different because of hysteresis. As can be seen from Fig. 1, the potential plateau during electrochemical insertion is close to + 50 mV vs. RHE at 298 K and the amplitude of hysteresis is *ca.* 12 mV. Because of hysteresis, it is not possible to follow a reversible path during a displacement from one plateau to the other. Starting from one equilibrium point {electrode potential;composition point) along the absorption plateau, it is only possible to move along a closed loop (labels A and B in Fig. 1). The use of sine wave perturbations in this two-phase domain would change the composition at the measurement point during the experiment and would complicate the interpretation.

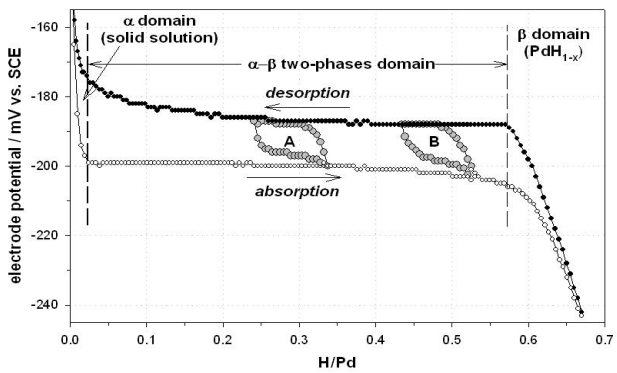

Fig. 1. Experimental PdH isotherm measured at 298K in H_2SO_4 1 M.

Results reported in this paper focus on the methodology. Data were obtained in the solid solution domain (α –PdH) were reversible hydriding phenomena are taking place. In such domains, both sine waves and exponentially-rising voltage steps can be used as perturbations and it is therefore possible to compare impedance diagrams obtained by both methods.

THEORY

The basic principles of impedance spectroscopy from exponentially-rising voltage steps have been described in the first part of the paper.

Hydrogen insertion mechanism

As discussed elsewhere [2], the electrochemical insertion of hydrogen in Pd is a multi-step process. In the low hydrogen concentration domain (where single-phased solid solutions are formed), each individual step of the multi-step process is reversible. In acidic media, the detailed reaction path is:

$H^+ + 1\,e^- + M \longleftrightarrow MH_{ad}^{surface}$ (step 1–a)

$2\,MH_{ad}^{surface} \longleftrightarrow H_2(g) + 2\,M$ (step 1–b)

$H^+ + 1\,e^- + MH_{ad}^{surface} \longleftrightarrow H_2(g) + M$ (step 1–b')

$MH_{ad}^{surface} \longleftrightarrow M + H_{ab}^{sub\text{-}surface}$ (step 1–c)

$H_{ab}^{sub\text{-}surface} \longleftrightarrow H_{bulk}$ (step 1–d)

where H_{ad} denotes a surface ad-atom, H_{ab} denotes a hydrogen atom absorbed in the metal sub-surface and H_{bulk} denotes a hydrogen atom in bulk regions. H_{ad} species are formed by the reduction of protons (Volmer step 1–a). From the viewpoint of H insertion, surface recombination of hydrogen ad-atoms (Tafel step 1–b) and electrochemical recombination (Heyrovsky step 1–b'), both leading to hydrogen evolution, are side-steps, the kinetics of which is an increasing function of electrode overvoltage. Surface ad-atoms can also cross the metal surface, reach sub-surface regions (step 1–c) and then bulk regions (step 1–d) by diffusion. According to Frumkin *et al.* [6], steps (1–a) and (1–c) form one single step whereas according to Bockris *et al.* [7], they are separated steps.

Model impedances

Impedances associated with reaction steps (1–a, 1–b, 1–b', 1–c) can be modeled by frequency-independent resistances. Analytical expressions of diffusion impedances (step 1–d) have been derived in the literature for various geometries including planar diffusion [8, 9] which is more specifically considered here. Electrochemical impedance diagrams can be modeled using the equivalent circuit shown in Fig. 2.

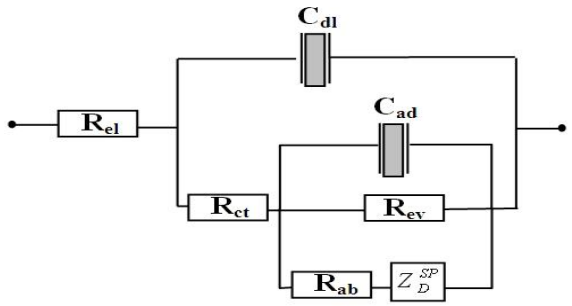

Fig. 2. Electrical equivalent circuit associated with the hydriding reaction

The corresponding impedance expression is given by Eq. (1):

$$Z(\omega) = R_{el} + \cfrac{1}{j\,\omega\,C_{dl} + \cfrac{1}{R_{ct} + \cfrac{1}{j\,\omega\,C_{ad} + \left(\cfrac{1}{R_3 + Z_D^{SP}}\right) + \cfrac{1}{R_{ev}}}}} \qquad (1)$$

where:

R_{el} in Ω cm^2 is the resistance of the electrolyte between working and reference electrodes

C_{dl} in F cm^{-2} is the double layer capacitance

R_{ct} in Ω cm^2 is the charge transfer resistance associated with step (1-a)

C_{ad} in F cm^{-2} is the adsorption capacitance associated with step (1-a)

R_{ab} in Ω cm^2 is the resistance associated with step (1–c)

R_{ev} in Ω cm^2 is the resistance associated with the hydrogen evolution step (1–b or 1–b')

$Z_D^{SP}(\omega)$ in Ω cm^2 is the diffusion impedance associated with hydrogen transport to bulk regions (step 1–d). An analytical expression is available from the literature [8,9] :

$$Z_D^{SP}(\omega) = R_D^{SP}\,\frac{\coth\left(u^p\right)}{u^p} \qquad (2)$$

where D stands for diffusion and SP for single phase domain.

$$R_D^{SP} = \frac{\delta}{F\,D_H}\left(-\frac{\partial E}{\partial C_H}\right)$$

is the diffusion resistance in Ω cm^2;

$$u = j\,\frac{\omega\,\delta^2}{D_H}\,.$$

j is the imaginary unit; 2δ is the thickness of the palladium foil in cm; D_H is the hydrogen diffusion coefficient in cm^2 s^{-1}; 0 < p < 1 is a dimensionless

factor used to model interfaces with distributed properties [10] (p = 0.5 for an ideal interface); $-\left(\frac{\partial E}{\partial C_H}\right)$ is the slope of the electrochemical isotherm at the measurement point in V mol^{-1} cm^3.

The graph of $Z_D^{SP}(\omega)$ is very typical. At high frequencies

$$\lim_{\omega\to\infty} \coth\left[u(\omega)\right] = \lim_{\omega\to\infty} \frac{e^u + e^{-u}}{e^u - e^{-u}} = \lim_{\omega\to\infty} \frac{e^u}{e^u} = 1 + j\,0$$

(the imaginary part is zero), since

$$\lim_{\omega\to\infty} Z_D^{SP}(\omega) \approx \frac{R_D}{u} = 0 + j\,0 = \{0;0\}.$$

In the intermediate frequency range (f in Hz), as long as ω is sufficiently high, coth(u) ≈ 1, and therefore,

$$Z_D^{SP}(\omega) \approx \frac{R_D}{u}.$$

Taking $u = \sqrt{\pi f \frac{\delta^2}{D}} + j\sqrt{\pi f \frac{\delta^2}{D}}$ (ω = 2.π.f).

$$Z_D^{SP}(\omega) = \frac{1}{2F\left(-\frac{\partial C}{\partial E}\right)\sqrt{D}\sqrt{\pi f}} - j\frac{1}{2F\left(-\frac{\partial C}{\partial E}\right)\sqrt{D}\sqrt{\pi f}} \quad (3)$$

This is the equation of a semi-line in the Nyquist plan.

In the low frequency range, $th(u) = \frac{e^u - e^{-u}}{e^u + e^{-u}}$.

The exponential function can be approximated by Taylor series:

$$e^u = \sum_{n=0}^{n=\infty} \frac{u^n}{n!} = 1 + u + \frac{u^2}{2!} + \ldots$$

By considering only fifth order terms, we obtain:

$$e^u = 1 + u + \frac{u^2}{2} + \frac{u^3}{6} + \frac{u^4}{24} + \frac{u^5}{120}$$

$$e^{-u} = 1 - u + \frac{u^2}{2} - \frac{u^3}{6} + \frac{u^4}{24} - \frac{u^5}{120}$$

Therefore:

$$th(u) \approx \frac{2u + \frac{u^3}{3} + \frac{u^5}{60}}{2 + u^2 + \frac{u^4}{12}} \approx \frac{u + \frac{u^3}{6} + \frac{u^5}{120}}{1 + \frac{u^2}{2} + \frac{u^4}{24}} \approx u\left[\frac{1 + \frac{u^2}{6} + \frac{u^4}{120}}{1 + \frac{u^2}{2} + \frac{u^4}{24}}\right] \approx u\left(1 - \frac{u^2}{3}\right)$$

since $u = \sqrt{\frac{j\omega\delta^2}{D}} \Rightarrow u^2 = \frac{j\omega\delta^2}{D} \Rightarrow u^4 = -\frac{\omega^2\delta^4}{D^2}$

therefore :

$$\frac{Z_D^{SP}(\omega)}{R_D^{SP}} \approx \frac{1}{u^2\left(1 - \frac{u^2}{3}\right)} \approx \frac{3}{3u^2 - u^4} \approx \frac{3 + j\,0}{\frac{\omega^2\delta^4}{D^2} + j\frac{3\omega\delta^2}{D}}$$

Neglecting fourth order terms, we obtain:

$$Z_D^{SP}(\omega) \approx \frac{R_D^{SP}}{3} - j\frac{D_H R_D^{SP}}{\omega\delta^2} = R_{in} - j\frac{1}{\omega C_{in}} \quad (4)$$

Eq. (4) is the equation of a vertical semi-line along the imaginary axis in Nyquist coordinates. R_{in} is the insertion resistance in Ω cm^2 :

$$R_{in} = \frac{R_D}{3} = \frac{\delta}{3F D_H}\left(-\frac{\partial E}{\partial C_H}\right) \quad \textbf{(5)}$$

C_{in} is the insertion capacitance per unit area of interface in F cm^{-2}:

$$C_{in} = \frac{\delta^2}{D_H R_D} = \frac{\delta F}{\left(-\frac{\partial E}{\partial C_H}\right)} \quad (6)$$

$\tau_{in} = R_{in}.C_{in}$ in seconds is the insertion time constant.

RESULTS AND DISCUSSION

From the experimental viewpoint, the problem is to determine the impedance of a given system of interest by using an exponentially-rising voltage step as perturbation. In the case considered here, the system is the electrode/electrolyte electrochemical interface represented by the circuit of Fig. 2. In a typical experiment, two transient signals are sampled synchronously: the exponentially-rising step E(t) and the current response I(t). To determine the unknown impedance of the interface there are two options: (i) frequency-domain analysis : the Fourier transform of both E(t) and I(t) are numerically calculated and the ratio of the two FTs is taken as shown by Eq. (10), yielding the impedance Z(ω) of the circuit; this is the most straightforward method; (ii) time-domain analysis: a model circuit impedance Z(ω) is postulated; then, I(ω), the FT of the current response to a voltage step is calculated from Eq. (10): I(ω) = E(ω) / Z(ω); then, model I(t) is calculated from I(ω) by inverse Fourier transformation and used to fit transient experimental current I(t); parameters of the model impedance Z(ω) are iteratively adjusted to minimize the difference between model and experimental I(t) in order to determine the exact

characteristic of circuit components. This second approach is more difficult to implement than the first one but can sometimes be more efficient and even more accurate. It can also be automated. The two approaches are detailed in the followings.

Frequency-domain analysis

Impedance diagram of the hydrogen insertion reaction

Interface impedance parameters can be determined from a frequency-domain analysis of experimental data. The equivalent electrical circuit of Fig. 2 can be simplified by considering that (i) the parasitic reaction of the HER is negligible (this assumption is justified because experiments considered here were made at high potential values where Pd-H solid solutions are formed; accordingly, resistance R_4 is infinite); (ii) the adsorption capacitance C_2 is small and its impedance is infinite. The simplified electrical circuit is pictured in Fig. 3.

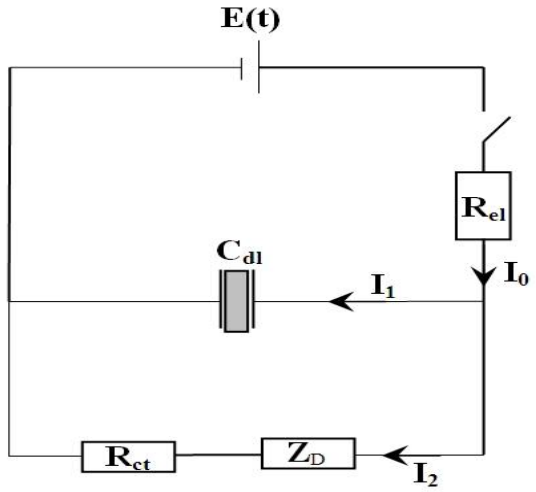

Fig. 3. Simplified equivalent circuit of the Pd-H interface

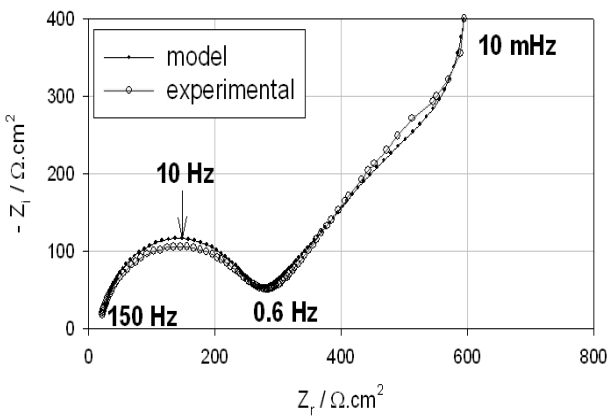

Fig. 4. (o) experimental impedance diagram measured at 298K on a PdH electrode in 0.1 M H_2SO_4 solution at + 60 mV RHE;(+) model impedance diagram from Eq. (7).

The analytical impedance of the electrical circuit of Fig. 3 is given by equation (7) where $\omega = 2\pi f$ is the pulsation in rad.s^{-1} and f is the normal frequency in Hz:

$$Z(\omega) = R_{el} + \frac{1}{j\,\omega\,C_{cl} + \dfrac{1}{R_{ct} + Z_D}} \tag{7}$$

The impedance diagram of the working electrode has been measured at a potential of + 60 mV (Fig. 4). The experimental impedance diagram has been fitted using Eq. (7) and the best fit is also plotted in Fig. 4.

At E = + 160 mV RHE, the slope of the isotherm is large (see Fig. 1) and the corresponding insertion capacitance C_{in} is rather low. The value of the hydrogen diffusion coefficient obtained from the fit is similar to values reported in the literature for palladium at 298 K [11]. The pulsation at the summit of the HF semi-circle is rather low, and this may be partly due to un-reduced surface oxides (the experiment was performed on the "as-received" sample) or to un-activated surface sites. On a fully activated sample, characteristic frequencies of several hundred Hz can sometimes be observed.

Solution to the convolution equation in the frequency domain

The impedance diagram of the circuit of Fig. 1 can be obtained directly from exponentially-rising voltage-step experiments. The impedance Z(ω) is obtained directly from Eq. (8):

$$Z(\omega) = \frac{E(\omega)}{I(\omega)} \tag{8}$$

where E is the voltage excitation in Volt, I_0 is the current response of the cell in A, and ω is the pulsation in rad.s^{-1}. E(ω) denotes the Fourier transform of the rising step E(t), and $I_0(\omega)$ denotes the Fourier transform of the current response I(t).

Sampling conditions and data treatment

A correct sampling rate is a key factor for obtaining experimental impedance diagrams. The sampling rate must respect the Nyquist criterion which states that the signal must be sampled more than twice as fast as the highest waveform frequency (f_c). If not, all of the power spectral density (PSD) which lies outside of the frequency range $-f_c < f < f_c$ is spuriously moved into that range and the spectrum is corrupted. In other words, high-frequency components of a time function can

impersonate lower frequencies if the sampling rate is too low. This phenomenon is called aliasing [12]. As discussed above, experiments have been made using exponentially-rising voltage steps. The typical current measured on the Pd electrode at E = + 60 mV RHE and T = 298K in response to a 10 mV rising step is reproduced in Fig. 5.

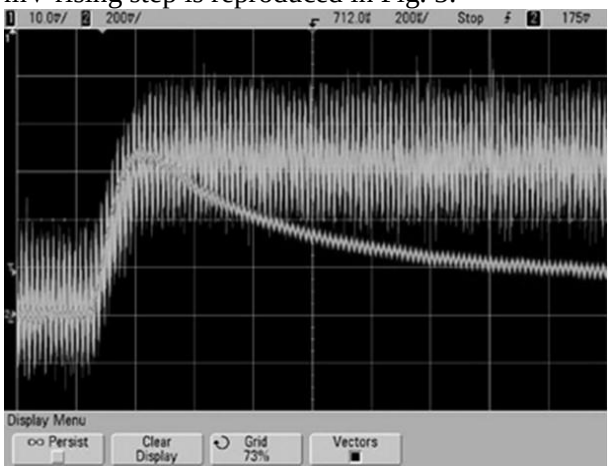

Fig. 5. Transient rising voltage step (top) and current response (bottom) measured on the Pd electrode at E = + 60 mV vs. RHE and T = 298K.

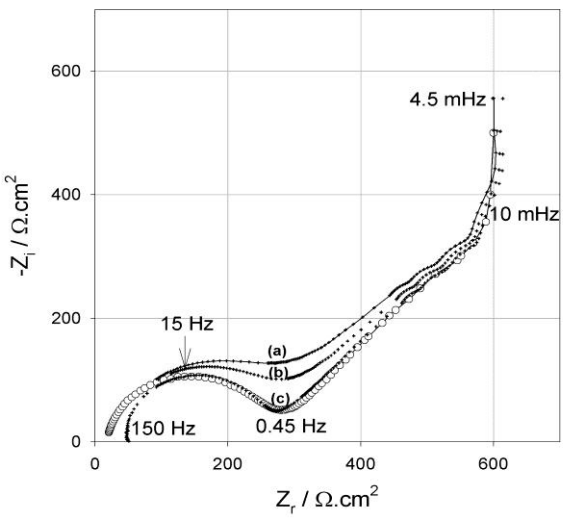

Fig. 6. Experimental electrochemical impedance diagrams measured on Pd-H at 298 K at E = +160 mV RHE. (o) theoretical from Eq. (7); (+) exponentially-rising voltage steps: (a) Δt = 50 ms (f_{max} = 10 Hz); (b) Δt = 25 ms (f_{max} = 20 Hz); (c) Δt = 2.5 ms (f_{max} = 200 Hz)

Considering the time constant of the exponentially-rising voltage step ($\tau = 1/b \approx 65$ μs), an appropriate sampling rate of one data-point every 10 μs (or less) corresponding to a maximum frequency of 50 kHz should be used to properly sample the peak current. Such a rate should be maintained until the end of the experiment (sometimes, depending on the electrode potential and hydrogen solubility, several tens of seconds are required) and this of course will yield large amounts of data points. However, the problem of data sampling can be simplified as discussed in the first part of this paper. First, there is no need to sample the exponentially-rising voltage step. Its shape was found sufficiently reproducible from one experiment to the other to allow the direct use of the analytical expression of E(ω) (Eqs. 13–14 in the first part of this paper) directly into Eq. (8). The amount of data is thus reduced by a factor of two. An additional advantage of this approach is that the voltage excitation does not introduce any noise in the impedance diagram. Second, the kinetics of surface (charge transfer step) and bulk (diffusion step) rate contributions usually differ significantly and appear at quite different frequencies (see Fig. 4 where the HF semi-circle is due to the parallel connection of the charge transfer resistance with the electrode/electrolyte capacitance and the MF 45º semi-line is due to bulk diffusion of atomic hydrogen). Therefore, the high frequency (HF) part of the impedance diagram associated with the surface step can be obtained with a good precision from the current response in the 0–0.5 ms time range. This is the period of time during which the double layer capacitance is charged and when a peak current is observed (Fig. 5). The medium (MF) and low (LF) frequency part of the impedance diagram can be obtained from the current response in the 0-10 s time range with a lower sampling rate of a few milliseconds. In the work reported here, the oscilloscope was used to record the transient at short times and the potentiostat was used to record the signal until equilibrium with a typical sampling rate of a few milliseconds. The oscilloscope was triggered by the rising potential on the first acquisition channel. The complete I(t) transient was finally obtained by adding the two signals, low-pass filtering and interpolating.

Comparison of model and experimental impedance values

The theoretical impedance diagram of the Pd foil polarized at E = + 160 mV RHE measured with sine wave perturbations is plotted in Fig. 6. Then, experimental electrochemical impedance diagrams have been obtained from rising voltage step experiments. Typically, the WE was first polarized at +160 mV RHE until equilibrium was reached and then a 10 mV amplitude step was applied and the resulting transient current was sampled. Impedance diagrams obtained with different sampling rates are also plotted in Fig. 6 for comparison. A sampling rate of one data-point every 2.5 ms is necessary to obtain a good agreement between theory and experiments in the

medium and low frequency regions (hydrogen diffusion). However, the HF semi-circle still remains distorted due to aliasing effects and higher sampling rates are required to obtain a better resolution of the HF semi-circle and extract the corresponding kinetics information.

From these results, it can be concluded that impedance diagrams can be obtained with a good accruracy from exponentially-rising voltage-step experiments. Although impedance diagrams can be computed easily within a few seconds, a disdavantage of the technique is that it requires the acquisition of large amounts of data (several Mbyte files) and data sampling is the most critical issue. To a certain extend, logarithmic sampling of data can be used to circumvent the problem. Although Fourier-transforms cannot be obtained directly from such sketch of data, some solutions have been described in the literature [13]. Another option would be to use Laplace transformation in place of Fourier transformation as discussed in Ref. [14].

Time-domain analysis

Solution to the convolution equation in the time domain

Electrode impedance parameters can also be obtained from time-domain analysis of experimental data. In a typical experiment, the circuit of Figure 3 is excited by a voltage transient E(t) of any shape. $E_{Rel}(t)$ (the voltage drop over the electrolyte resistance R_{el}), $E_{Cdl}(t)$ (the voltage of the double layer capacitance C_{dl}), $E_{Rct}(t)$ (the voltage of the charge transfer resistance R_{ct}) and $E_{ZD}(t)$ (the voltage drop due to hydrogen diffusion) are the four unknown transient voltages of the problem. $I_0(t)$ (the main transient current across the circuit), $I_1(t)$ (the current across capacitance C_{cdl}) and $I_2(t)$ (the current across resistance R_1) are the three unknown transient currents of the problem. By applying Kirchhoff's laws (conservation of charge and energy) to the circuit of Figure 3, the following set of three equations is obtained:

$$E(t) = R_{el}\, I_0(t) + \frac{1}{C_{dl}} \int_0^t I_1(t)\, dt \tag{9}$$

$$\frac{1}{C_{dl}} \int_0^t I_1(t)\, dt = R_{ct}\left[I_0(t) - I_1(t)\right] + Z_D\left[I_0(t) - I_1(t)\right] \tag{10}$$

$$I_0(t) = I_1(t) + I_2(t) \tag{11}$$

The system can be solved by use of Laplace transformation. Solutions for the five voltage transients are:

$$E_{Rel}(s) = R_{el}\, I_0(s) \tag{12}$$

$$E_{Cdl}(s) = \frac{I_1(s)}{s\, C_{dl}} \tag{13}$$

$$E_{Rct}(s) = R_{ct}\left[I_0(s) - I_1(s)\right] = R_{ct}\, I_2(s) \tag{14}$$

$$E_{ZD}(s) = Z_D(s)\left[I_0(s) - I_1(s)\right] = Z_D(s)\, I_2(s) \tag{15}$$

Solutions for the three current transients are:

$$I_1(s) = \frac{E(s)}{R_{el}}\left[R_{ct} + Z_D(s)\right]\left[\frac{1}{s\, C_{dl}}\left(1 + \frac{R_{ct}}{R_{el}} + \frac{Z_D(s)}{R_{el}}\right) + R_{ct} + Z_D(s)\right]^{-1} \tag{16}$$

$$I_0(s) = \frac{1}{R_{el}}\left[E(s) - \frac{I_1(s)}{s\, C_{dl}}\right] \tag{17}$$

$$I_2(s) = I_0(s) - I_1(s) \tag{18}$$

Time domain solutions to Eqs. (12–18) can be obtained numerically by computing the Fourier transforms (s = jω) and by taking the inverse discrete Fourier transform (IDFT), as discussed in the first part of this paper.

Transient voltage values

Numerical voltage responses of the circuit components (Fig. 3) to E(t) = exponentially-rising voltage step are plotted in Fig. 7. Data have been obtained by solving Eqs. (12–15) using parameters of Table 1. The time axis is in logarithmic scale to facilitate the differentiation of the different voltages. The rising voltage step E(t) has an amplitude of 10 mV and reaches its plateau value in less than 0.5 milliseconds. The main differences with the electrical circuit analyzed in the first part of the paper are (i) the total experiments extends over several tens of seconds; (ii) no stationary current is reached since $Z_D(_w)$, the impedance of the electrode because infinite when the ω → 0.

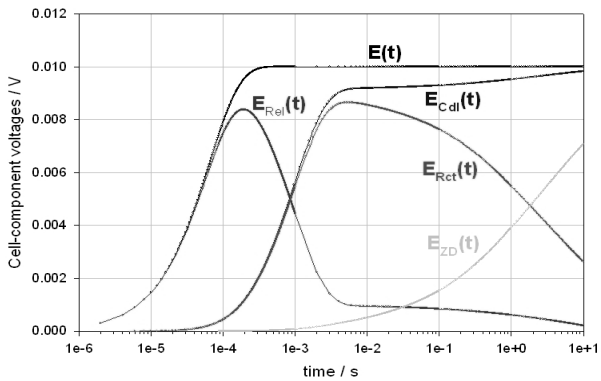

Fig. 7. Transient voltages responses of the electrical circuit of figure 1 when E(t) = a [1 –exp (-t/τ)]; a= 10 mV; τ = 1/b = 6.424×10^{-5} s

Table 1. Fit parameter values corresponding to the plot of Fig. 4.

R_{el}	τ_c	C_{dl}	R_{ct}	R_D	D_H	$-(\partial E/\partial C_H)$	R_{in}	C_{in}	τ_{in}	p
$\Omega.cm^2$	s	$\mu F.cm^{-2}$	$\Omega.cm^2$	$\Omega.cm^2$	$cm^2.s^{-1}$	$V.mol^{-1}.cm^3$	$\Omega.cm^2$	$F.cm^{-2}$	s	
24	1×10^{-2}	45	224	1194	2.8×10^{-7}	6484	398	0.074	29.5	0.52

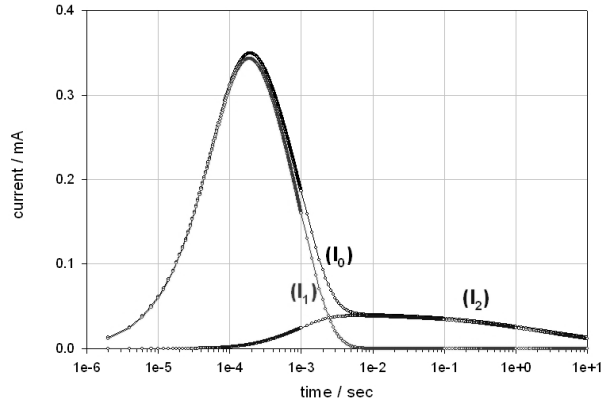

Fig. 8. Transient current responses of the interface (Fig. 3) when E(t) = a [1 – exp (-t/τ)] ; a = 10 mV ; τ = 1/b = 6.424×10^{-5} s.

At the onset of the voltage step (t < 0.2 ms) the main voltage drop is located across the electrolyte resistance. Then (0.1 –> 2 ms) the double layer capacitance charges and the charge transfer process begins, leading to the formation of hydrogen surface ad-atoms. Then hydrogen diffusion takes place for t > 10 ms until the end of the experiment.

Transient current values

Numerical current responses of the different components of the electrical circuit of figure 4 to an exponentially-rising voltage step E(t) are plotted in Fig. 8. Again, the time axis is in logarithmic scale to facilitate the differentiation of the different signals. The stationary currents are :

$$I_0(t\to\infty) = I_1(t\to\infty) = I_2(t\to\infty) = 0 .$$

Comparison of experimental and model values

Results were obtained using a PGZ402 potentiostat from Radiometer. Exponentially-rising voltage steps with a mean time constant τ = 6.424×10^{-5} s have been used as voltage excitation:

$$E(t) = a.\ [1 - \exp(-t/\tau)] \qquad (19)$$

Experimental step-functions generated by the potentiostat are reproducible within ± 0.05 % from one experiment to the other. The experimental voltage step has been fitted using Eq. (19). Results are plotted in Fig. 9.

Then, the experimental current response $I_0(t)$ has been fitted using a model equation. The model equation was obtained as follows. First, I(ω) was potential steps.calculated from I(ω) = Z(ω) / E(ω). Z(ω) was taken from Eq. (7) using the parameters of Table 1 and E(ω) was obtained by taking the FT of the exponentially-rising voltage step E(t). Second, I(t) was calculated from I(ω) by discrete inverse Fourier transformation. Results obtained for the first 2 milliseconds are plotted in Fig. 10. There is a good agreement between experimental and calculated transients, indicating that time-domain analysis of the current response of the electrochemical interface to an exponentially-rising voltage step can also be used to determine the impedance of an unknown circuit. Of course, the calculation is simple in the case presented here because Z(ω) was known accurately from sine wave experiments. Nevertheless, a similar methodology can be used when Z(ω) is unknown. In such cases, a model impedance is first postulated and then parameters are optimized iteratively by

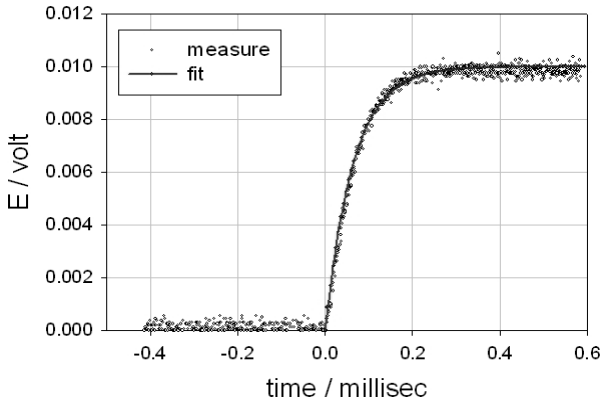

Fig. 9. Experimental (o) and model (—) potential steps..

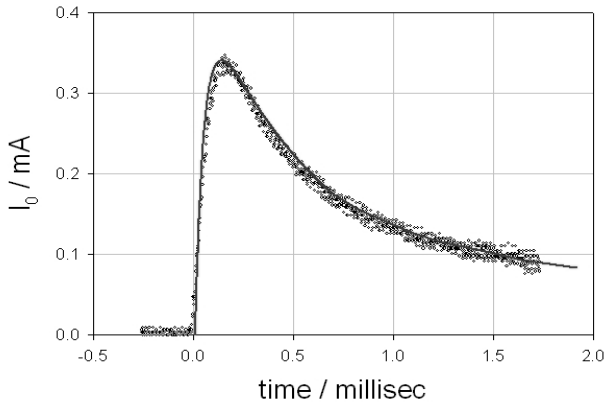

Fig. 10. Experimental (o) and model (–) current responses $I_0(t)$.

minimizing the difference between experimental and model $I_0(t)$.

CONCLUSIONS

The work reported here describes a methodology used to determine the impedance of palladium electrodes from exponentially-rising voltage step experiments. When a voltage step experiment is carried out, two transient signals are measured: the voltage step E(t) and the current response I(t). To determine the unknown impedance of the electrochemical circuit there are two options: (i) frequency-domain analysis: the Fourier transform of both E(t) and I(t) is taken and the ratio of the two FT is calculated, yielding the impedance of the circuit; (ii) time-domain analysis: a model impedance is postulated, the associated current transient I(t) obtained in response to the exponentially-rising voltage step is calculated and used to fit transient experimental current I(t); parameters of the model impedance circuit are iteratively adjusted to minimize the difference between calculated and experimental I(t) in order to determine the exact characteristic of circuit components. From a practical viewpoint, there are two main critical problems. First, an appropriate sampling rate must be used. Second, data filtering is required. When these problems are appropriately handled, then correct impedance diagrams are obtained. Therefore, it can be concluded that exponentially-rising voltage steps can be used to measure electrochemical impedance diagrams.

Acknowledgements: *Financial support from the French Agence Nationale de la Recherche, within the frame of the Plan d'Action National sur l'Hydrogène (EolHy project ANR-06-PANH—008-06 and AP'H project ANR-05-PANH—011-04), is acknowledged.*

REFERENCES:

1 L. Schlapbach, A. Züttel, Nature 414, 353-358, (2001).
2 P. Millet, R. Ngameni, Electrochimica Acta 2011, doi: 10.1016/j.electacta.2010.12.106.
3 G. Tsirlina, S. Baronov, F. Spiridonov, M. Rusanova, T. Safonova, O. Petrii, Russ. J. Electrochem. 36, 1179, (2000).
1 J. Chen, R. Durand, C. Montella, *J. Chem. Phys.* **91,** 383, (1994).
2 P. Millet, *Electrochem. Commun.* **7,** 40, (2005).
3 A. Frumkin, in: P. Delahay (Ed.), Advances in Electrochemistry and Electro-chemical Engineering, Vol. 3, Interscience, NewYork, 1963.
4 J. Bockris, J. McBreen, L. Nanis, *J. Electrochem. Soc.* **112,** 1025, (1965).
5 L. Jacobsen, K. West, *Electrochimica Acta* **40,** 255, (1995).
6 C. Lim, S. Pyum, *Electrochimica Acta* **38,** 2645, (1993).
7 E. Barsoukov, J. R. Mac Donald, Impedance Spectroscopy, Theory, Experiment, and Applications, Wiley, 2005.
8 R. Bucur, E. Indren, *Acta Met.* **35,** 1325, (1987).
9 W. Press, in *Numerical Recipes, the Art of Scientific Computing*, Cambridge University Press: Cambridge, 1986.
10 H. Wiese, K. Weil, IEEE Transactions on Acoustics, Speech, and Signal Processing, 36(7) July 1988.
11 E. Barsoukov, S. Ryu, H. Lee, *J. Electroanal. Chem.* **536,** 109,(2002).

ЕЛЕКТРОХИМИЧНА ИМПЕДАНСНА СПЕКТРОСКОПИЯ С ЕКСПОНЕНЦИАЛНО НАРАСТВАЩИ СТЪПКИ НА НАПРЕЖЕНИЕТО.

(II) АНАЛИЗ НА ИНТЕРКАЛАЦИЯТА НА ВОДОРОД В ПАЛДИЕВИ ФОЛИА.

П. Мийе

Институт по молекулярна химия и материали в Орсе, UMR CNRS n° 8182, Университет Париж Юг, ул. Жорж Клемансо 11, 15, 91405 Орсе седекс, Франция

Постъпила на 20 февруари, 2012 г.; приета на 20 февруари, 2012 г.

(Резюме)

Електрохимичната импедансна спектроскопия (IES) обикновено се използва от електрохимиците за анализиране на многостепенни реакции, протичащи на фазовата граница електрод/електролит. Понеже кинетиката на отделните стъпки на реакцията обикновено е функция на електродния потенциал, импедансът на фазовата граница се измерва при различни, но постоянни стойности на потенциала. В повечето случаи импедансните диаграми се получават чрез хармоничен анализ: за възбуждане се използва наложена променливотокова модулация на потенциала с ниска амплитуда (типично 5-10 мВ) или галваностатична променливотокова модулация с ниска амплитуда (типично няколко мА). Според теорията на линейните и непроменливи във времето системи обаче, хармоничният анализ следва да бъде ограничен до анализа на линейни и обратими процеси. Проблемът с линейността може да бъде преодолян до известна степен чрез намаляване амплитудата на модулацията. Но това не помага да се разреши проблема с необратимостта. Например, при електро-интеркалацията на водород в електроди от паладий или паладиеви сплави, се наблюдава значителен хистерезис. Това е ясно указание, че протичат нелинейни процеси и следователно хармоничният анализ не може да се използва, защото системата не изпълнява изискванията за линейност и неизменност във времето, наложени от системната теория. Значи трябва да се използва непроменливо възбуждане. Целта на настоящата работа е да се докладва за измерването на импедансни спектри при възбуждане с експоненциално нарастващи стъпки по напрежение. Това съобщение е ориентирано към методологията. В първата част на работата, електрическа схема съдържаща само електрическо съпротивление и капацитет се използва като моделна система, за да се обясни как от такова нехармонично възбуждане може да се получи импедансна диаграма. Във втората част на работата, методологията се разширява до електро-интеркалацията на водород в паладиево фолио.

Bulgarian Chemical Communications, Volume 44, Number 4 (pp. 356 – 363) 2012

Parametrization of impedance spectra of GC/H_2SO_4 electrode: trials and errors

V. Horvat-Radošević*, K. Magdić, K. Kvastek

Rudjer Bošković Institute, Bijenička c. 54, 10000 Zagreb, Croatia

Received February 20, 2012; accepted February 20, 2012

Impedance spectra of two differently prepared (polished and anodically oxidized) GC electrodes measured at +0.30 V *vs.* SCE in 0.5 mol dm^{-3} H_2SO_4 electrolyte have been analysed on the basis of presumed electrical equivalent circuit(s) and complex non-linear least square fitting procedure. Statistical analysis of model residuals and reliability of the estimated values of parameters were used as indicators for correct or incorrect modeling. In such a way, the polished GC electrode has been modeled using not-ideal capacitive element describing relatively flat surface, whereas anodically oxidized GC electrode has been modeled using not-ideal capacitive element loaded by transmision line element representing a porous surface structure.

Key words: GC electrodes, Electrochemical impedance spectroscopy, Electrical equivalent circuits, Parametrization

INTRODUCTION

It has already been shown that oxidized GC electrodes, like most of other carbon materials [1], exhibit high capacity values that become relevant even for advanced electrochemical double-layer capacitors [2, 3]. In that area, Electrochemical Impedance Spectroscopy, EIS, technique appears to be one of the principal methods for examining fundamental behaviour of electrode materials. This is primarily due to the possibility of EIS to estimate not only capacitance values, but also to follow charge transfer and transport related phenomena occurring at different time scales, what is essential for predictions of rate capabilities of capacitor devices [1, 4]. There are, however, only few studies available in the literature on the impedance analysis of GC electrodes. Although for a polarized carbon electrode, purely capacitive impedance response has generally been expected over broad potential region [1-4], more or less distributed capacitive response is found dominant for both: not activated and variously activated GC electrodes in different electrolyte solutions [2, 5-8]. Consequently, impedance models containing constant phase element(s), CPE, or transmission line, TL, have been discussed to account for roughness, including possible fractal geometry [5-8] or porosity of the GC surface [2].

The goal of the present paper was to find the optimum parameter set(s) of impedance spectra of not treated, *i.e. o*nly hand polished GC electrode, PGC, and anodically oxidized GC electrode, AGC, in H_2SO_4 electrolyte solution. Impedance analysis based on electrical equivalent circuits, EECs, involving lumped RC and/or distributed impedance elements [9] was applied and submitted to the statistical analysis of model residuals. The calculations were performed using the complex linear least square, CNLS, fitting procedure and modulus weighting mode [10, 11]. Improvements were made by replacement(s) and/or addition(s) of particular impedance(s) to the basic model and re-fitting this new model to the experimental data.

Criteria for finding the most reliable EEC were equal frequency distribution and small values of real and imaginary fitting residuals, Δ' and Δ'', defined as:

$$\Delta'_k = \frac{Z'_{k(\exp)} - Z'_{k(cal)}}{|Z_{k(\exp)}|} \qquad \Delta''_k = \frac{Z''_{k(\exp)} - Z''_{k(cal)}}{|Z_{k(\exp)}|} \quad (1)$$

In Eqn. (1), Z', Z'' and k are real and imaginary impedance and particular frequency of measurements, respectively. $|Z|$ is impedance magnitude, while by "*exp*" and "*cal*", experimentally measured and calculated quantities are denoted. A fit was considered good for fitting residuals, Δ' and Δ'', being below 0.01 and near equally distributed over the frequency region of impedance measurements.

EXPERIMENTAL IMPEDANCE SPECTRA

Bode plots (log of $|Z|$ and phase angle, φ *vs.* log ω, ($\omega = 2\pi f$) of PGC and AGC electrodes (0.028 cm^2

* To whom all correspondence should be sent:
E-mail: *vhorvat@irb.hr*

© 2010 Bulgarian Academy of Sciences, Union of Chemists in Bulgaria

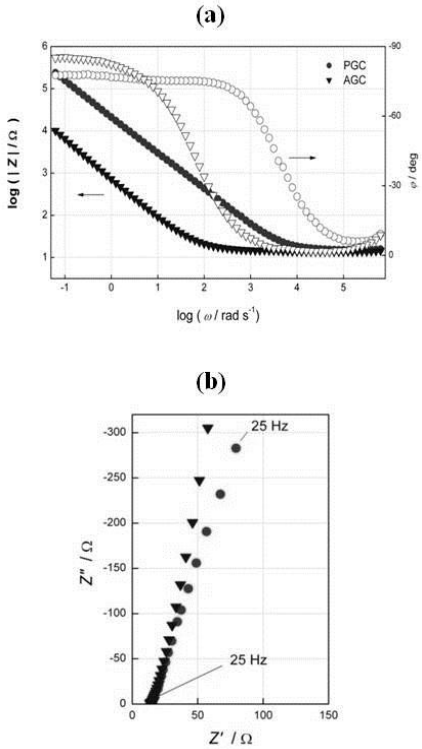

Fig. 1. Experimental IS of PGC and AGC electrodes in 0.5 mol dm^{-3} H_2SO_4 at +0.30 V *vs*. SCE: (a) Bode plots, (b) high to medium frequency parts of Z'' *vs*. Z' plots

of apparent area) measured at +0.30 V *vs*. SCE using three-electrode cell filled with 0.5 mol dm^{-3} H_2SO_4 electrolyte solution are together with high frequency parts of Z'' *vs*. Z' curves, presented in Fig. 1. Visual observation of experimental impedance spectra, IS, in Fig. 1a indicates two distinct domains, almost resistive response at higher and almost capacitive response at lower frequencies, respectively. Not prominent shifts of high frequency intercepts in Fig. 1b pointed to domination of the solution resistance, R_s = 13–15 Ω, over any contact and/or intrinsic resistance of GC electrodes. The values of $|Z|$ and degree of deviation from ideal capacitive response are higher for PGC than AGC electrode. The capacitance values, C_{IS}, calculated at f = 0.1 Hz using the relation $C_{IS} = -(\omega Z'')^{-1}$ are 5.15×10^{-5} F (1.8 mF cm^{-2}) for PGC and 1.90×10^{-3} F (68 mF cm^{-2}) for AGC electrode, respectively.

IMPEDANCE MODELING PROCEDURE

As is suggested by visual observation of IS in Fig. 1 and also by other authors [6-8], impedance response of GC electrodes can be associated with R_s and almost capacitive electrode impedance with frequency dispersed CPE having admittance, $Y_{CPE} = (Z_{CPE})^{-1}$, defined as:

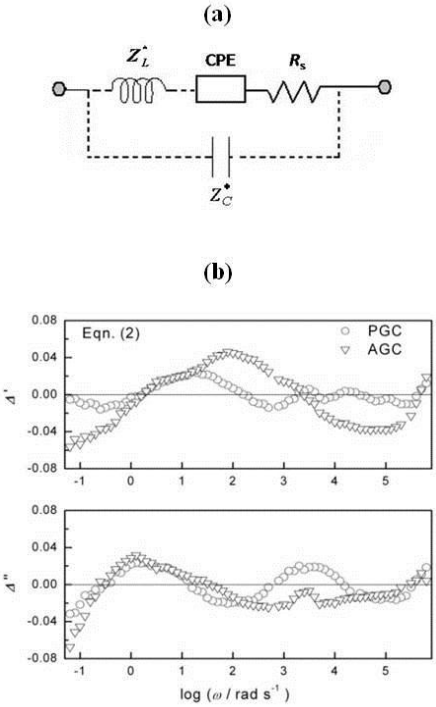

Fig. 2. (a) EEC with CPE defined by Eqn. (2) used for fittings to experimental IS of PGC and AGC electrodes in Fig. 1, (b) real and imaginary fitting residuals, Δ' and Δ'', *vs*. log ω

$$Y_{CPE}(i\omega) = Q(i\omega)^n \qquad (2)$$

This model in the form of EEC is drawn in Figure 2a, together with, Z_L* and Z_C* involved for correction of experimental artefacts manifested at high frequencies [12, 13]. In all present experiments, $L^* = 4.1–6.0 \times 10^{-6}$ H and $C^* = 4.2–5.7 \times 10^{-8}$ F. EEC in Fig. 2a defines 3+2* model parameter-case (R_s, Q, n, L^*, C^*). The mean values of the extracted impedance parameters Q and n are together with their standard deviations, listed in Table 1.

Although for both electrodes, the results of fitting procedure of the EEC in Fig. 2a to IS in Fig. 1 yielded reasonable values for Q and n with low standard deviations, Δ' and Δ'' were quite high and showed significant frequency dispersions (*cf*. Fig. 2b).

According to Figure 3, similar is obtained when CPE in Fig. 2a is replaced by the finite transmission line element, TL, with impedance defined as [9]:

$$Z_{TL}(i\omega) = \frac{R_0}{(i\omega\tau)^p}\coth(i\omega\tau)^p \qquad (3)$$

Generally, TL element with $Z_{TL}(i\omega)$ defined by Eqn. (3) can describe a situation within a porous

Table 1. The best fit main parameter values of the EEC in Fig. 2(a) with $Y_{CPE}(i\omega)$ defined by Eqn. (2).

	Parameter	PGC	AGC
3+2* parameter-case	104 × Q/Ω–1 sn	0.462 ± 0.001	17.42 ± 0.09
	n	0.856 ± 0.001	0.888 ± 0.002

Table 2. The best fit main parameter values of the EEC in Fig. 2(a) with CPE replaced by TL and $Z_{TL}(i\omega)$ defined by Eqn. (3).

	Parameter	PGC	AGC
4+2* parameter-case	R_0/Ω	3.8 ± 0.7	4.7 ± 0.4
	$10^3 \times \tau$/s	0.037 ± 0.009	4.6 ± 0.4
	p	0.4275 ± 0.0003	0.4464± 0.0007

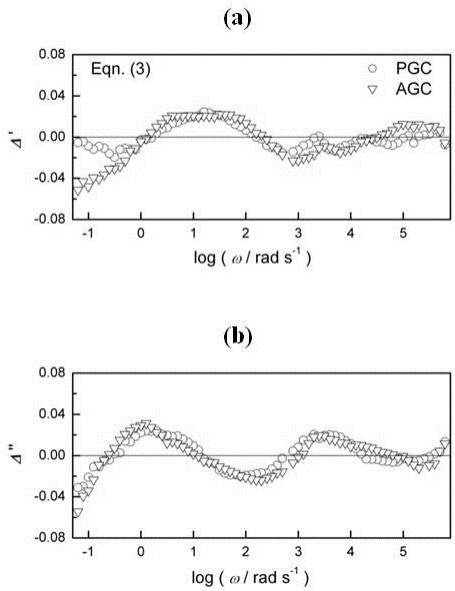

Fig. 3. Real and imaginary fitting residuals, Δ' and Δ'' obtained after fittings the EEC in Fig. 2(a) with CPE replaced by TL defined by Eqn. (3) to experimental IS of PGC and AGC electrodes in Fig. 1, *vs*. log ω.

electrode where the electrolyte resistance in pores is dependent not only on apparent conductivity of the electrolyte but also on a pore length [14]. This impedance/frequency function has already been applied in the impedance analysis of porous electrodes [14], including porous carbon [15] and anodically oxidized GC electrode [2]. In the ideal case of p = 0.5, impedance spectrum exhibits –45° inclined line at higher and –90° (capacitive) line at lower frequencies. Low frequency differential capacitance is defined here as $C_{LF} = \tau/R_0$, where τ is relaxation time, while R_0 represents resistance to ion transport.

By replacing CPE with TL having impedance defined by Eqn. (3), the model in Fig. 2a becomes 4+2* model parameter-case (R_s, R_0, τ, p, L^*, C^*). The mean values of the extracted parameters describing TL are, together with their standard deviations, listed in Table 2.

Although Eqn. (3) has already been proposed in impedance analysis of variously activated GC electrodes [2], use of TL instead of CPE in Fig. 2a did not improve results of fittings much. As is demonstrated in Fig. 3, fitting this model to the actual IS provided poor fits at large domain of measured frequencies. Therefore, for improving the results for GC electrodes, new impedance has to be added to the model. Generally, this can be done in two ways, what results with the well known problem of ambiguity in impedance data analysis [11, 16]. The first way is to add some new impedance that is capacitive at low frequency limit, in parallel connection to CPE (model P in Fig. 4a). The second is to add new impedance in a form of parallel *R*-CPE combination in series connection to CPE (model S in Fig. 4a).

For GC electrode, the P-type model has already been applied to account for some possible side reaction(s), including adsorption of electrolyte ions at the electrode surface [7,8]. On the other side, the S-type model is generally used to describe surface films with properties different than surrounding media (bulk electrode and electrolyte) [17]. For powdered carbon electrodes, the S-type model has also been proposed for accounting inhibition of charging/discharging of high carbon area surface caused by (bulk electrode/surface film or surface film/electrolyte) interfacial charge transfer [18, 19]. Somewhat modified S-type model, with two parallel CPEs, has already been proposed to account for different rates of charging/discharging at basal and edge planes of GC electroderespectively [5]. By replacing CPE with either P- or S-types of the models drawn in Fig. 4a, the EEC in

Fig. 2a becomes 6+2* model parameter-case (R_s, Q_1, n_1, R_1, Q_2, n_2, L^*, C^*). As is seen from decreased values of Δ' and Δ'' and their lower

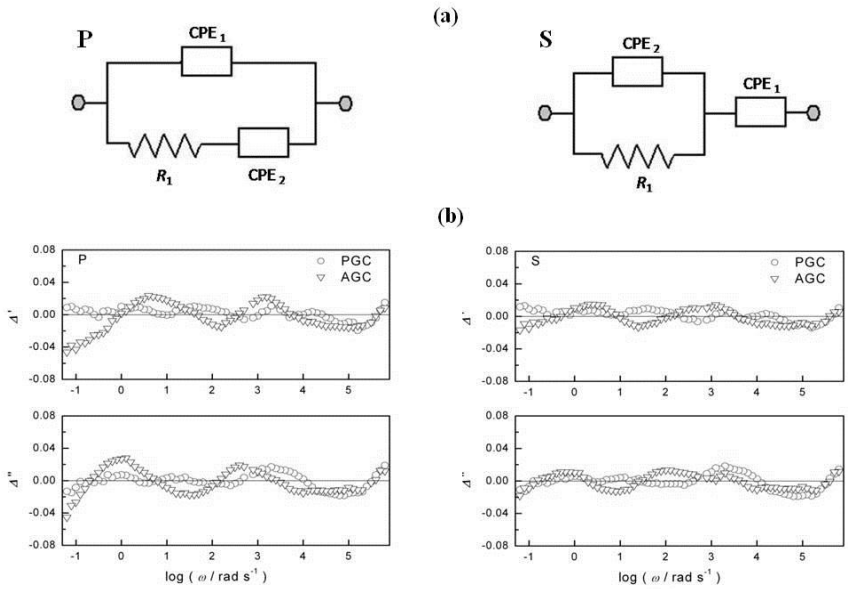

Fig. 4. (a) EECs used instead CPE in Fig. 2(a) for approximation of experimental IS of PGC and AGC electrodes in Fig. 1, (b) real and imaginary fitting residuals, Δ' and Δ'', *vs.* log ω

Table 3. The best fit main parameter values of the EEC in Fig. 2(a) with CPE replaced by the EECs in Fig. 4(a).

6+2* parameter-case	Parameter		PGC		AGC	
	P	S	P	S	P	S
$10^4 \times Q_1/\Omega^{-1}\,s^{n1}$	0.437 ± 0.003		0.474 ± 0.001		10.5 ± 0.5	
n_1	0.863 ± 0.001		0.869 ± 0.001		0.90 ± 0.06	
R_1/Ω	44152 ± 8274		373 ± 66		11 ± 9	
$10^4 \times Q_2/\Omega^{-1}\,s^{n2}$	0.0345 ± 0.003		4.9 ± 0.3		7 ± 5	
n_2	0.92 ± 0.03		0.82 ± 0.01		0.88 ± 0.08	
$10^4 \times Q_1/\Omega^{-1}\,s^{n1}$	0.437 ± 0.003		0.474 ± 0.001		10.5 ± 0.5	

frequency dispersions in Fig. 4b, these two models fit better to both experimentally measured IS in Fig. 1 when compared to the results obtained with previous models (*cf.* Figs. 2(b) and 3). Improvements of fits, however, are more pronounced after using the S-type model. The extracted main parameter values are together with their standard deviations summarized in Table 3. For either P- or S-type of the model, impedance of CPE_1 remained dominant impedance of each IS. For the PGC electrode, there are almost no differences between the values of parameters Q (n) in Table 1 and Q_1 (n_1) in Table 3, suggesting minor influence of additional impedance to the total electrode impedance. For the AGC electrode, however, additional impedance is found necessary for obtaining improvements in fitting results, suggesting thus more complex surface characteristics of this electrode. Although for the AGC electrode, the results using the S-type model yielded better fits with minor frequency dispersion (*cf.* Fig. 4b), unreasonable values for additional impedance were obtained (*cf.* Q_2 = 187 $\Omega^{-1}s^{n2}$ and n_2 = 0.59 in Table 3). This pointed to another type(s) of element(s) that should be used instead CPE_2 in the S-type of model. As has already been observed and discussed [1, 2], when carbon electrodes are polarized to high anodic potential, a porous surface with high content of oxygen containing species is formed. For that a reason, TL element, with impedance defined by Eqn. (4) and denoted here as TL_1, is included as additional element to either P or S-type of the model. These two new models that remain 6+2* model parameter-cases (R_s, Q_1, n_1, R_{01}, τ_1, p_1, L^*, C^*) are drawn in Fig. 5a and denoted as P-I and S-I.

Qualities of fittings are shown in Fig. 5b, whereas the main parameter values are, together

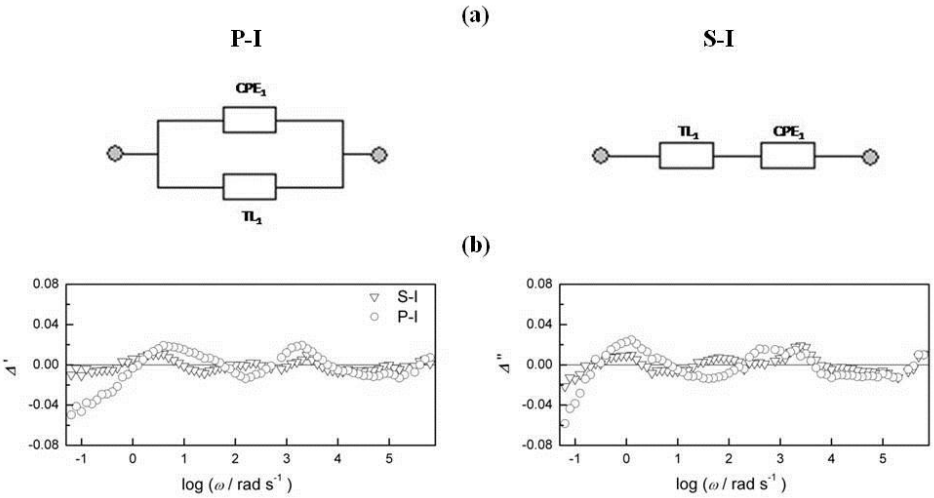

Fig. 5. (a) EECs used instead CPE in Fig. 2(a) for approximation of experimental IS of the AGC electrode in Fig. 1**,** (b) real and imaginary fitting residuals, Δ' and Δ'', *vs.* log ω.

Table 4. The best fit main parameter values of the EEC in Fig. 2(a) with CPE replaced by the EECs in Fig. 5(a)..

6+2*parameter- case	$10^4 \times Q_1/\Omega^{-1}\,s^{n1}$	n_1	R_{01}/Ω	τ_1 /s	p_1
P-I	8 ± 6	0.90 ± 0.09	20 ± 15	0.011 ± 0.004	0.44 ± 0.04
S-I	41 ± 5	0.68 ± 0.01	2.2 ± 0.2	0.006 ± 0.001	0.491 ± 0.006

with the corresponding standard deviations, listed in Table 4.

Again, high(er) quality of fitting for the S-I type model is observed in Fig. 5b. As a consequence of different ways of connection of two elements in P-I and S-I models respectively, contribution of CPE_1 to total electrode capacitance is higher for the P-I than for the S-I type of the model. This means that in the case of S-I type of the model, impedance due to CPE_1 becomes some sort of additional impedance to dominant impedance of TL_1.

High value of Q_1 and n_1 = 0.68 for the S-I type of the model in Table 4 suggests again that some element exhibiting "Warburg type" of frequency response (–45° sloped line) should be used as additional impedance to the dominant impedance of TL_1. It has already been shown [20] that deviations, frequently observed from medium to low frequencies after applying the Eqn. (3), can be corrected by adding a new TL element with impedance defined as [9]:

$$Z_{TL}(i\omega) = \frac{R_0}{(i\omega\tau)^p}\tanh(i\omega\tau)^p \qquad (4)$$

Series combination of Z_{TL} defined by Eqn. (4) and Z_{TL} defined by Eqn. (3) has already been applied in impedance analysis of thin conducting polymer films to account impedance of two mobile charge carriers [21-23]. Here, Z_{TL} defined by Eqn. (4) and denoted as TL_2 is added to Z_{TL} defined by Eqn. (3) and already denoted as TL_1, in both types of the model in Fig. 5a. For the P-I type of the model, however, over-parametrization becomes immediately evident by insensitivity of the calculation results on the impedance of CPE_1. Thus the P-I model becomes reduced to the series sum of two TL's (*cf.* Figure 6a), what is just the same situation obtained by substitution of CPE_1 with Z_{TL2} into S-I type of the model. By using the model in Fig. 6a instead CPE, the model in Fig. 2a becomes the 7+2* model parameter-case (R_s, R_{01}, τ_1, p_1, R_{02}, τ_2, p_2, L*, C*). Frequency dispersion of Δ' and Δ'' showing acceptable results of fittings are presented in Fig. 6c, while the values of extracted parameters are, together with their standard deviations, listed in the first raw of Table 5. The parameter values in Table 5 indicate that the total AGC electrode capacitance originates fully from TL_1. Due to relatively high τ_2, the contribution of the Warburg (–45° sloped line) part of TL_2 is prominent at mediate to low frequencies. What is observed not only here, but also elsewhere [22, 23], $\tau_1 \neq \tau_2$, what has not been predicted theoretically [21]. Interpretation, however, remains unclear, but full equivalence between impedance of the series sum of TL_1 and TL_2 and parallel sum of two TL_2 points toward possible interpretation in the terms of pores of unequal lengths [20]. Low τ_1 value makes TL_1 response almost capacitive, what could be a basis for decrease of the number of model parameters. In its reduced form, shown in Fig. 6b, the sum of TL_1 and TL_2 is reduced to the sum of

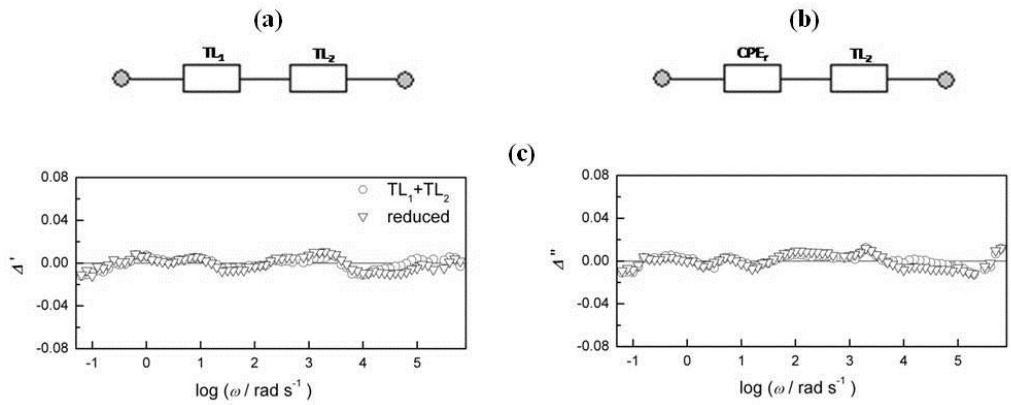

Fig. 6. (a-b) EECs used instead CPE in Fig. 2(a) for approximation of experimental IS of the AGC electrode in Fig. 1, (c) real and imaginary fitting residuals, Δ' and Δ'', *vs.* log ω.

Table 5. The best fit main parameter values of the EEC in Fig. 2(a) with CPE replaced by the EECs in Fig. 6a and b.

Parameters	R_{01}/Ω	$10^3 \times \tau_1$ /s	p_1	R_{02}/Ω	τ_2 /s	p_2
7+2* (Fig. 6a)	1.0 ± 0.1	1.0 ± 0.01	0.4594 ± 0.0005	22 ± 1	0.67 ± 0.05	0.50 ± 0.01
	--	$10^4 \times Q_r/\Omega^{-1}\,s^n$	n_r			
6+2* (Fig. 6b)	--	18.25 ± 0.02	0.921 ± 0.001	25 ± 1	0.75 ± 0.05	0.491 ± 0.008

CPE_r and TL_2. Now the model in Fig. 2a becomes reduced again to the 6+2* model parameter-case (R_s, C_r, n_r, R_{02}, τ_2, p_2, L^*, C^*). The results of fittings are also shown in Fig. 6c and the extracted parameter estimates are listed in Table 5. Very low residuals, randomly distributed over the range of measured frequencies and low standard deviation of each parameter value, point to the acceptable model used for fittings. This final model is checked through the potential dependence of measured IS of the AGC electrode, shown in Fig. 7 as the complex capacitance spectra, $Y'\omega^{-1}$ *vs.* $Y''\omega^{-1}$, that has already been found advantageous in visualization of not-ideal capacitive impedance responses of various origins [24].

Almost arc shaped curves in Fig. 7 exhibiting certain tails at lower frequencies, indicate a series connection of R_s and impedance of not ideal capacitive electrode. More or less prominent vertical lines observed at low frequencies for some potential values, indicate some additional and almost resistive contribution(s), probably due certain faradaic reaction(s) occurring at these potentials. The values of total electrode capacitances that can graphically be determined as the crossing points between the corresponding arcs and $Y''\omega^{-1}$ axis, show that the highest capacitance value is attained at +0.20 V, what is close to the redox potential of some oxygen containing, probably quinone-like surface groups, formed at carbon/H_2SO_4 (pH=0-3) electrodes [1,25]. Just the same is seen in Table 6, where the main parameter values estimates, including Q_1 (n_1) are listed. In such a way, the potential dependent contribution from the redox pseudocapacitance to the total electrode capacitance is approved. Changes of R_{02} and τ_2 values of TL_2 impedance in Table 6 show constant increase suggesting continuous change of the surface structure with increase of E. This, however, can have a detrimental effect when GC electrode is under conditions of continuous oxidation such as in capacitor devices.

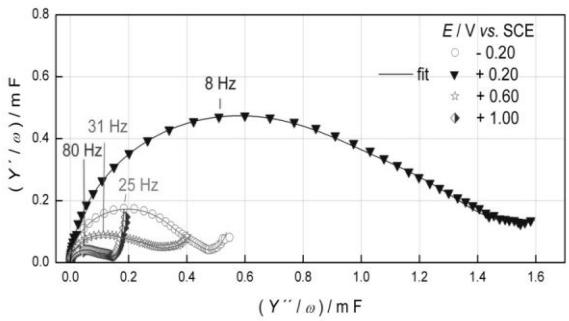

Fig. 7. Potential dependence of experimental complex capacitance spectra, $Y'\omega^{-1}$ *vs.* $Y''\omega^{-1}$, of the AGC electrode in 0.5 mol dm^{-3} H_2SO_4.

CONCLUSIONS

Experimental impedance spectra of polished, PGC and anodically oxidized, AGC, electrodes in H_2SO_4 electrolyte solution have been analysed using different EECs composed by gradual addition of different impedance elements. Statistical analysis of model residuals and

Table 6. The best fit main parameter values of the EEC in Fig. 2(a) with CPE replaced by the EEC in Fig. 6(b) to experimental IS of AGC electrode measured at various potentials

E/V *vs.* SCE	$10^4 \times Q_1/\Omega^{-1} s^n$	n_1	R_{02}/Ω	τ_2 /s	p_2
–0.20	4.76 ± 0.01	0.958 ± 0.001	14 ± 5	0.4 ± 0.3	0.39 ± 0.02
+0.20	13.99 ± 0.03	0.952 ± 0.001	25 ± 1	0.46 ± 0.04	0.431 ± 0.006
+0.60	3.322 ± 0.005	0.922 ± 0.001	23 ± 1	0.077 ± 0.007	0.450 ± 0.007
+1.00	1.55 ± 0.03	0.939 ± 0.001	49 ± 2	0.068 ± 0.004	0.492 ± 0.006

reliability of parameter estimates have been used as indicators for correct/incorrect modelling.

It has been shown that PGC electrode can be analysed as the 3+2* model parameter-case (not ideal capacitive element in series with electrolyte resistance), describing relatively flat electrode surface of PGC with some degree of roughness or fractal-scaled imperfections.

AGC electrode showed more complex behaviour and impedance analysis was based on more comprehensive model. While there was not a fundamental reason that one EEC is more significant than the other, several different types of EECs were applied and all were reduced to the 6+2* model parameter-case (not ideal capacitive element loaded by an impedance of distributive type). This model suggests a porous surface structure of AGC made by anodic oxidation and formation of high quantity of oxygen containing surface groups.

Acknowledgements. *Financial support from Ministry of Science, Education and Sports of the Republic of Croatia (Project 098-0982904-2905) is acknowledged.*

REFERENCES

1. B. E. Conway, Electrochemical Supercapacitors, Scientific, Fundamentals and Technological Applications, Kluwer Academic/Plenum Publ. New York (1999).
2. M. G. Sullivan, R. Kötz, O. Haas, J. *Electrochem. Soc.* **147** , 308, (2000).
3. Y. Wen, G. Cao, Y. Yang, *J. Power Sources* **148,** 121, (2005).
4. R. Kötz, M. Carlen, *Electrochim. Acta* **45,** 2483, (2000).
5. P. Heiduschka, A. Munz, W. Göpel, *Electrochim. Acta* **39,** 2207, (1994).
6. C.-H. Kim, S.-I. Pyun, J.-H. Kim, *Electrochim. Acta* **48,** 3455, (2003).
7. S. S. Moganty, R. E. Baltus, D. Roy, *Chem. Phys. Letters* **483,** 90, (2009).
8. J. P. Zheng, P. C. Goonetilleke, C. M. Pettit, D. Roy, *Talanta* **81,** 1045, (2010).
9. R. R. Macdonald (Ed.), Impedance Spectroscopy, Wiley, New York, 1987.
10. B. A. Boukamp, *Solid State Ionic*s **169,** 169, (2004).
11. P. Zoltowski, *Solid State Ionics* **176,** 1979, (2005).
12. S. Fletcher, *Electrochem. Commun*. **3,** 71, (2001).
13. V. Horvat-Radošević, K. Kvastek, *J. Electroanal. Chem.* **631,** 10, (2009).
14. R. De Levie, Adv. Electrochem. Electrochem. Eng., Vol. 6. Interscience, New York, 1967.
15. J. H. Jang, S. M. Oh, *J. Electrochem. Soc*. **151,** A751, (2004).
16. V. Freger, S. Bason, J. Membrane Sci. **302,** 1, (2007).
17. M. D. Levi, D. Aurbach, *J. Phys. Chem. B* **101**, 4630, (1997).
18. K. Sawai, T. Ohzuku, *J. Electrochem. Soc*. **144,** 988, (1997).
19. M. Toupin, D. Bélanger, I. Hill, D. Quinn, *J. Power Sources* **140,** 203, (2005).
20. M. D. Levi, C. Wang, D. Aurbach, *J. Electroanal. Chem.* **561,** 1, (2004).
21. M. A. Vorotyntsev, L. I. Daikhin, M. D. Levi, *J. Electroanal. Chem*. **364,** 37, (1994).
22. G. Láng, M. Ujvári, G. Inzelt, *J. Electroanal. Chem*. **572,** 283, (2004).
23. V. Horvat-Radošević, K. Kvastek, M. Kraljić-Roković, *Electrochim. Acta* **51,** 3417, (2006).
24. T. Pajkossy, D. M. Kolb, *Electrochim. Acta* **53,** 7403, (2008).
25. H. Andreas, B. E. Conway, *Electrochim. Acta* **51,** 6510, (2006).

ОПРЕДЕЛЯНЕ ПАРАМЕТРИТЕ НА ИМПЕДАНСНИТЕ СПЕКТРИ НА GC/H_2SO_4 ЕЛЕКТРОД: ПРОБИ И ГРЕШКИ

В. Хорват - Радошевич, К. Магдич, К. Квастек

Институт Руджер Бошкович, Биженичка 54, 10000 Загреб, Хърватска

Постъпила на 20 февруари, 2012 г.; приета на 20 февруари, 2012г.

(Резюме)

Импедансните спектри на два подготвени по различен начин (полиран и анодно оксидиран) стъкловъглеродни електрода, измерени при +0.30 V спрямо SCE в електролит от 0.5 mol dm^{-3} H_2SO_4 са анализирани въз основа на предполагаеми електрически еквивалентни схеми и комплексна процедура на нелинейно напасване по метода на най-малките квадрати. Като индикатори за правилното моделиране е използван статистически анализ на остатъците в модела и анализ на надеждността на оценените стойности на параметрите. По такъв начин, полираният стъкловъглероден електрод е моделиран чрез неидеален капацитивен елемент, описващ сравнително гладка повърхност, докато анодно оксидираният стъкловъглероден електрод е моделиран чрез неидеален капацитивен елемент, свързан с елемент на дълга линия, представящ пориста структура на повърхността.

Bulgarian Chemical Communications, Volume 44, Number 4 (pp. 364 – 370) 2012

Dual membrane fuel cell – impedance approach for proof of concept

D. Vladikova[1,*], Z. Stoynov[1], G. Raikova[1], M. Krapchanska[1], A. Thorel[2], A. Chesnaud[2]

[1]*Institute of Electrochemistry and Energy Systems (IEES – BAS), 10 Acad. G. Bonchev, 1113 Sofia, Bulgaria*
[2]*Centre Matériaux, Mines-ParisTech BP87 Evry Cedex 91003, Franc*

Received February 20, 2012, accepted February 20, 2012

The dual membrane fuel cell (DMFC) is an innovative SOFC architecture in which an oxygen compartment (cathode and oxide ion conducting electrolyte) is combined with a hydrogen compartment (anode and proton conducting electrolyte) through a porous mixed conducting central membrane (CM) where the two types of ions react and produce water which is evacuated through the pores. This concept is proved on a model cell via sets of investigations based on D.C. testing and Impedance Spectroscopy. For optimization of the three DMFC compartments (oxygen, hydrogen and CM) with regard to materials and technological conditions for the deposition of the functional layers, impedance studies were carried out on symmetrical half cells. Special attention was given to some new experiments elucidating the processes of water formation and propagation through the central membrane.

Key words: Dual membrane fuel cell, Impedance spectroscopy, Central membrane, LSCF48, BCY15, YDC15

INTRODUCTION

When compared to conventional PEM FC, solid oxide fuel cells (SOFC), including the proton conducting design (PCFC), offer several advantages, mainly concerning efficiently and multi-fuel operation. However, they also have some limitations that slow down their marketing. A weak point is the dilution of the reacting gases with the exhaust water at the anode side in SOFC and at the cathode side in PCFC and decrease of the electrodes catalytic activity. In order to overcome those limitations, innovative Dual Membrane Fuel Cell (DMFC) architecture was proposed [1] and is under development in an FP7 project [1–3]. The new concept combines the advantages and eliminates the disadvantages of both SOFC and PCFC. The main idea is the separation of the hydrogen and oxygen from the exhaust water. It is realized by the introduction of a junction layer between a SOFC electrolyte/cathode (cathode compartment) and a PCFC anode/electrolyte (anode compartment) with mixed (H^+ and O^{2-}) conducting porous structure. Thus protons produced at the anode progress toward the junction central membrane (CM) where they meet the oxide ions that are created at the cathode and produce water which is evacuated through the pores of the membrane. Therefore hydrogen, oxygen and exhaust water are located in three independent chambers (Fig. 1).

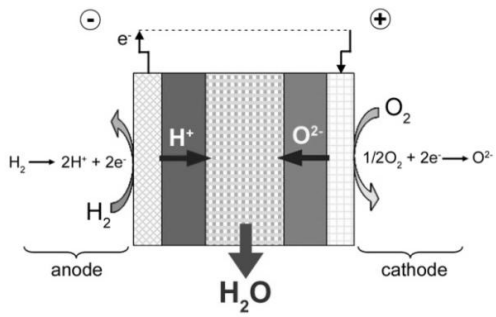

Fig. 1. Schematic representation of the dual membrane fuel cell concept.

The innovative concept (Fig. 1) avoids the gases dilution, the inhibition of the electrodes' charge/mass transfer by the water, and the corrosion by the oxygenized water at high temperatures [2, 3].

In order to prove the new concept and to understand and evaluate the processes taking place, impedance studies of the cell and its compartments were carried out and presented in this work.

EXPERIMENTAL

For investigations of the dual membrane fuel cell and its three compartments, the following materials appropriate for operating temperatures 700–600ºC were selected: LSCF48 ($La_{0.6}Sr_{0.4}Co_{0.2}Fe_{0.8}O_{3-\delta}$) as cathode, YDC15 ($Ce_{0.85}Y_{0.15}O_{1.925}$) as oxide ion conductor, BCY15 ($BaCe_{0.85}Y_{0.15}O_{2-\delta}$) as proton conductor and

* To whom all correspondence should be sent:
E-mail: d.vladikova@bas.bg

© 2012 Bulgarian Academy of Sciences, Union of Chemists in Bulgaria

BCY15-Ni cermet as anode. For elimination the influence of the electrodes quality on the electrolytes characterization, metal (Me = Pt, Ag) electrodes were also used. For electrochemical characterization of the selected materials and the technological procedures for the fabrication of the functional layers, impedance measurements were performed on 3 types of symmetrical half cells: electrolyte supported LSCF48/YDC15/LSCF48, electrolyte supported BCY15-Ni/BCY15/BCY15-Ni and central membrane supported Me/YDC15$_{porous}$BCY15$_{porous}$/Me with cell diameter about 2 cm and thickness about 1 mm. The measurements of the CM half cell were carried out in oxygen/air and in wet hydrogen, which ensured information about the conductivity of every component of the composite porous membrane. For the proof of the concept measurements at operating conditions were performed on a model button type cell (diameter / thickness = 20 / 1 mm) with Pt electrodes:

Pt/YDC15/ YDC15$_{porous}$BCY15$_{porous}$/BCY15/Pt.

From system theory point of view, SOFC are large statistical multivariable electrochemical systems with distributed parameters in macro- and micro-levels. Processes of charge and mass transfer are taking place, changing (at least partially) the behavior of the electrodes and that of the cell as an electrochemical system. Since a big number of external parameters (temperature, gases flows etc.) determine the intensity and the nature of the dominating processes, those parameters should be conditioned carefully. For improving the quality of the impedance data, a special furnace with D.C. galvanostatic current supply (100A, 15V) and a system for temperature regulation with two thermocouples was constructed. It ensures less noisy conditions for measurements in the range 20 – 900ºC with stability 0.2ºC and sensitivity 0.02ºC. The gases flows (air, N_2, Ar_2, O_2 and H_2 or mixtures of them) were regulated with flow-regulators ensuring stability exceeding 0.2 % in the full range of 140 NmL/min.

The impedance measurements were carried out on Solartron 1260 FRA. The D.C. conditioning/loading was ensured by the internal galvanostat or by external 100 mA galvanostat. The total control of the experiments was performed by a home made threefold computerized system for measurement, monitoring and registration of the impedance data, temperature and load. The D.C. control system is monitoring directly the current I, the voltage U, the power P and P_{max} of the cell. For low impedance measurements inductance errors correction procedure, based on carefully collected calibration measurements, was applied [4–6]. For the most interesting experiments the method of the Differential Impedance Analysis [5–6], which improves the model assessment and the parameters estimation, was performed.

The big volume of impedance data (more than 3000 records of experimental impedance diagrams together with their temperature profiles) was stored in Data Bank applying Large Structured Files (LSF) [6] as data exchange formats.

The impedance measurements were performed in a very large frequency range - from 10 MHz down to 1 mHz. Thus a big variety of phenomena (with very different time-constants) could be monitored, distinguished and evaluated: ionic conductivity, fast electrochemical kinetics, interface behaviour, diffusion and other types of transport limitations, accumulation of species, formation and growth of new (water-based) phase. The combination of impedance with mirco-structural analyses (Scanning Transmission Electron Microscopy - High Angle Annular Dark Field (STEM-HAADF) and X-ray diffraction) ensured the necessary completeness of the experimental information and its interpretation.

RESULTS AND DISCUSSION

Cathode compartment studies

The performance of the impedance measurements on symmetrical half cells LSCF48/YDC15/LSCF48 in temperature range 100–700ºC combined with the procedures for cell rig errors correction and DIA ensured evaluation of both the electrolyte resistance with its two components coming from the bulk and from the grain boundaries (Fig. 2a, c) and the polarization resistance (Fig. 2b, d) [3].

Due to the application of DIA, the charge transfer was separated from the dominating transport limitation of the charged species in the bulk of the electrode, identified as Bounded Constant Phase Element (BCP) [5–7] (Fig. 2b, d). It was strongly reduced by replacement of the pure LSCF with a composite LSCF/YDC15 (Fig. 3).

Anode compartment studies

For characterization of the anode compartment impedance measurements of symmetrical half cell BCY15-Ni/BCY15/BCY15-Ni (starting powders ratio: 71,4 vol.% NiO; 28,6 vol.% BCY15) were

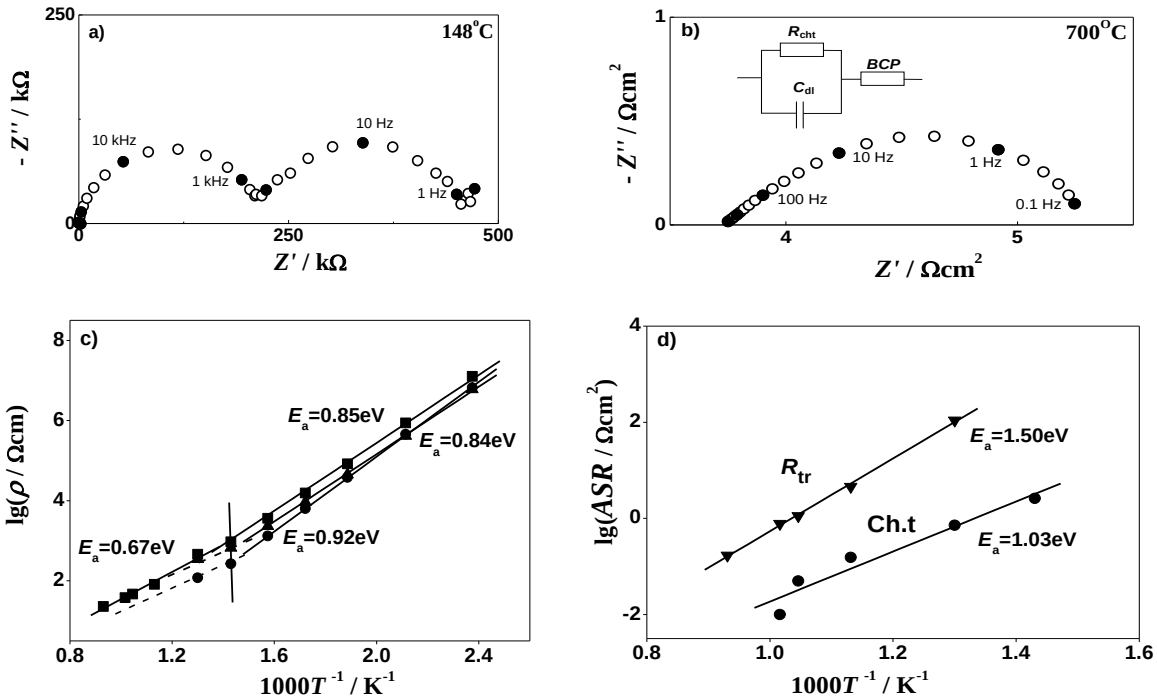

Fig. 2. Impedance measurements of symmetrical LSCF/YDC/LSCF half cell at different temperatures: (a), (b) - complex plane impedance diagrams; (c) - Arrhenius plots of the electrolyte: (▲) bulk; (●) grain boundaries; (■) total; d) - Arrhenius plots of the electrode reaction: (▼) transport; (●) charge transfer.

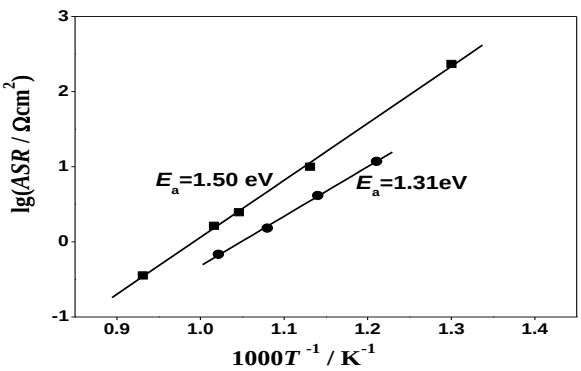

Fig. 3. Arrhenius plots of the polarization resistance for: (■) LSCF electrode; (●) composite LSCF/YDC15 electrode.

performed, preceded by measurements of Pt/BCY15/Pt for optimization of the electrolyte support sintering conditions [8]. The obtained results show that the anode microstructure is an important optimization parameter. At lower sintering temperatures (1100ºC), which ensure sufficient porosity of the anode, both the electrolyte resistance and the polarization resistance are much higher than the parameters measured on half cell with Pt electrodes (Fig. 4). Since the electrolyte support is the same, the deterioration of the half cell performance should be related to the cermet anode. The increase of the sintering temperature above 1350°C brings to significant improvement of the anode compartment electrochemical behaviour

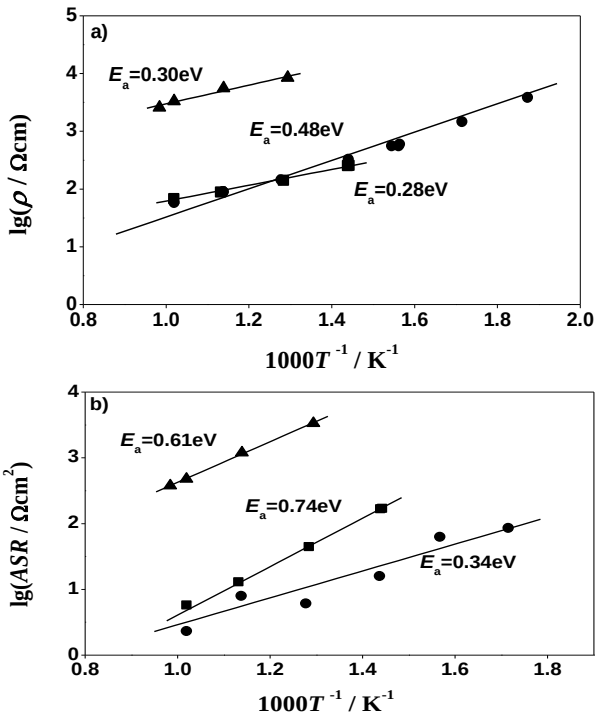

Fig. 4. Measurements of symmetrical half cell BCY15-Ni/BCY15/BCY15-Ni: (a) Arrhenius plots for the electrolyte resistivity, (b) Arrhenius plots for the anode polarization; Sample 1 (▲) - cermet sintered at 1100°C; Sample 2 (■) - cermet sintered at 1350°C; comparative measurements of Pt/BCY15/Pt (●). The electrolyte support for both samples is sintered at 1450°C.

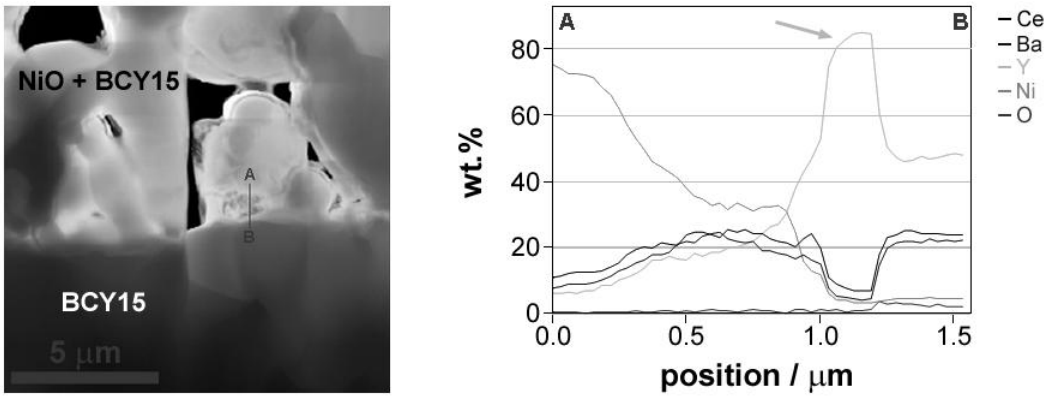

Fig. 5. STEM-HAADF image of anode/electrolyte interface (A-B) and linear composition profile (in wt. %) across this interface.

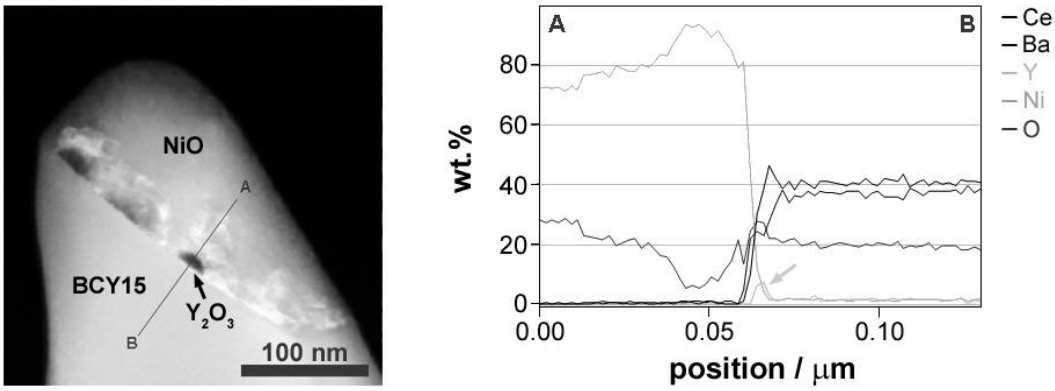

Fig. 6. STEM-HAADF image of BCY15/NiO interface (A-B) and linear composition profile (in wt. %) across this interface

(Fig. 4). STEM-HAADF analysis of the samples sintered at lower temperatures registered precipitation of Y_2O_3 on both electrolyte/electrode (Fig. 5) and BCY/NiO (Fig. 6) interfaces, which can be regarded as an efficient electrical barrier.

At higher sintering temperatures of the anode the system is stabilized towards segregation of Y_2O_3. However, XRD analysis registers small quantity of a new cerium yttrium oxide phase ($Ce_2Y_2O_7$). Although its influence on the electrochemical behaviour of the anode is not so strong (Fig. 4), the deposition of pure BCY/Ni cermet needs further optimization of the volume ratio BCY15/NiO and the sintering temperature. Recent studies showed that the decrease of the NiO content (starting powders ratio: 67,1 vol.% NiO; 32,9 vol.% BCY15) combined with sintering at 1100°C ensures cermet anodes with 40 vol% open porosity. XRD analysis confirms lack of parasitic phases before and after the NiO reduction [9]. Electrochemical testing is in progress.

It was supposed that BCY, which in principle has oxygen vacancies for initialization of the proton conductivity [4], could have also oxygen conductivity. For this purpose measurements of Me/BCY15/Me half cell in oxygen atmosphere were performed. They confirmed the presence of good oxide ion conductivity (Fig. 7). This phenomenon should be studied systematically, since it is important for the central membrane design, as well as for the development of a "monolithic" DMFC design, based on the replacement of YDC15 with BCY15. The first experiments on monolithic design are very promising [8].

Dual membrane fuel cell performance studies

The impedance measurements of half cells Me/YDC15$_{porous}$BCY15$_{porous}$/Me with CM support in both oxygen and hydrogen atmospheres provided important information about the individual conductivity of each one of the two electrolytes in the real ceramic structure. As it could be expected, the porosity increased the resistivity of both electrolytes. Those experiments, however, can not give information about the water vapour formation and transport in the CM, which is an important factor in the optimization of the cell performance.

For this purpose impedance measurements during operation of a model dual membrane fuel cell were performed in especially selected working points and frequency range, which ensured observability of the studied phenomena. The processes related to the water formation and transport should be measured at low frequencies. The impedance notification of water formation and growth could be a combination of capacitive and inductive loops corresponding respectively to the formation and to the spontaneous growth of the new phase. For registration of the second process impedance measurement was performed on dried central membrane after OCV under small current. Those conditions ensure enough "impedance time" for registration of the inductive loop, which disappears after longer exploitation (Fig. 8a, b) when the CM is watered and the clusters form a layer of polarized semiliquid film (the BCY pore walls are hydrophilic). This new phenomenon is described in more details in [10]. For observation of the slowest phenomenon - water permeability in the CM, the frequency range was additionally extended in the low frequency range down to 1 mHz, where a new capacitive semi-circle with diameter increasing with the time was registered (Fig. 8c, d). It can be related to the continuous formation of water which fills the volume of the pores and penetrates towards the periphery of the CM where it can be evacuated.

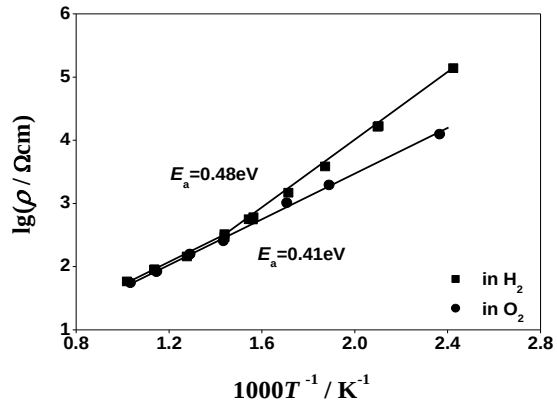

Fig. 7. Arrhenius plots for the electrolyte resistivity of symmetrical half cell Pt/BCY15/Pt measured in wet hydrogen and in oxygen.

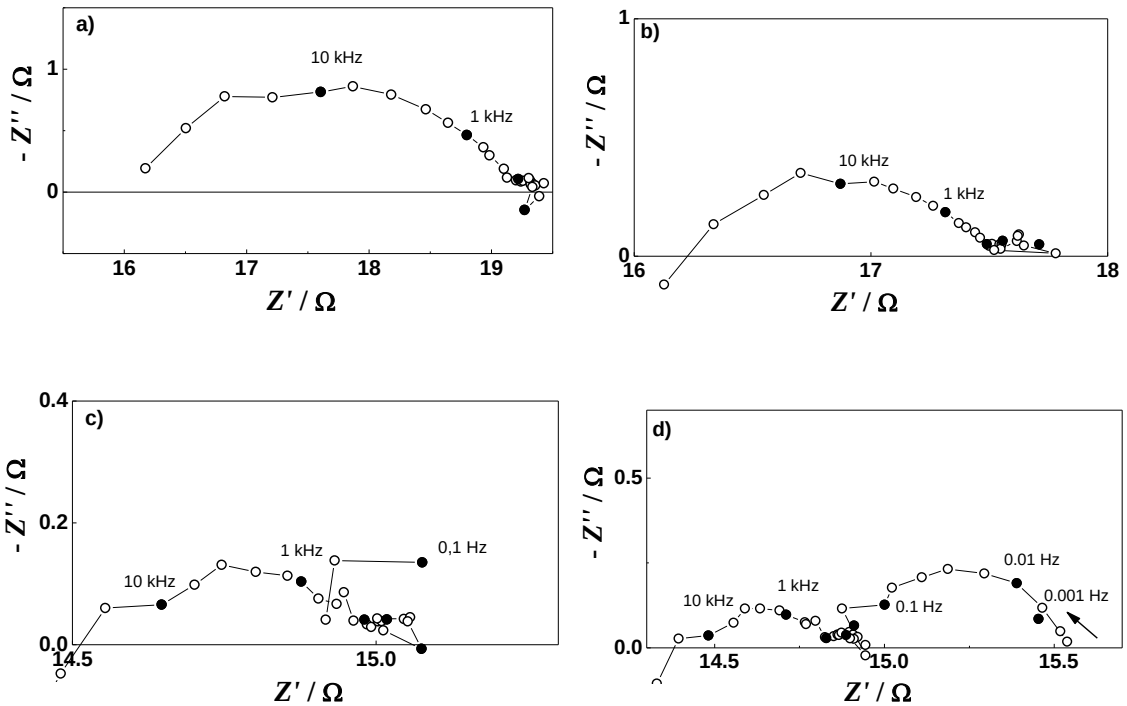

Fig. 8. Complex plane impedance diagrams of monolithic cell Pt/BCY15/BCY15 $_{porous}$/BCY15/Pt measured at 700°C: a) small load after OCV (AC = 0.5 mA, DC = 2 mA), frequency range 1 MHz - 0,1 Hz; b) small load (AC = 0.5 mA, DC = 2 mA) and long time of operation, frequency range 1 MHz - 0,1 Hz; c) bigger load (AC = 0.5 mA, DC = 16 mA), frequency range 1 MHz - 0,1 Hz; d) same load as in c), frequency range 1 MHz - 1 mHz.

It should be noted that the contribution of the water formation and evacuation from the CM in the total resistance of the cell is much smaller than that of the electrolytes, including the CM. Thus the decrease of their thickness is of big importance. Since a chemical reaction is taking place in the central membrane, the principle of Le Chatelier

could be applied for improving water evacuation and cell performance.

CONCLUSIONS

The impedance investigations carried out confirmed the dual membrane fuel cell concept. It was shown that the oxygen ions and the protons, produced at the electrodes move toward the central membrane where they produce water.

The impedance measurements performed on half cells ensured detailed characterization of the cell components – electrolytes (including granular and inter-granular conductivity), electrodes (charge transfer and gas transport), central membrane (mixed conductivity, porosity and presence of water). Mixed (oxide ion and proton) conductivity was registered in the proton conducting electrolyte BCY15. The first steps towards the application of this phenomenon for optimization of the DMFC are in progress. Activation of the cells during operation was also observed, which may be related to the new phenomenon registered and studied for a first time - formation of adsorbed film of water in porous ceramic media at high temperatures. It could be related to a super-critical state of the water supported by strong hemisorption. For further investigations of this phenomenon permittivity and permeability measurements are in progress.

Acknowledgements: *The research leading to these results has received funding from the European Community's Seventh Framework Programme (FP7/2007–2013) under grant agreement No 213389. Powders were fabricated and supplied by Marion Technologies.*

REFERENCES:

1 Patent No 0550696000, March 7ht, 2005: CELLULE DE PILE A COMBUSTIBLE HAUTE TEMPERATURE A CONDUCTION MIXTE ANIONIQUE ET PROTONIQUE, International extension in 2006.

2 A. Thorel, A. Chesnaud, M. Viviani, A. Barbucci, S. Presto, P. Piccardo, Z. Ilhan, D. Vladikova and Z. Stoynov, in *Solid Oxide Fuel Cells 11* (SOFCXI), edited by S.C. Singhal, and H. Yokokawa, The Electrochemical Society Proceedings Series 25, ECS Transactions, Pennington, NJ, p. 753 (2009).

3 D. Vladikova, Z. Stoynov, G. Raikova, A. Thorel, A. Chesnaud, J. Abreu, M. Viviani, A. Barbucci, S. Presto and P. Carpanese, *Electrochim. Acta* **56,** 7955, (2011).

4 D. Vladikova, Z. Stoynov, G. Raikova, in Z. Stoynov, D. Vladikova (Eds.), Portable and Emergency Energy Sources, Marin Drinov Academic Publishing House, Sofia, p. 383, (2006).

5 Z. Stoynov and D. Vladikova, in *Encyclopedia of Electrochemical Power Sources*, edited by U. Garche, Elsevier, p.632, (2009).

6 Z. Stoynov, D. Vladkova, Differential Impedance Analysis, Marin Drinov Academic Publishig House, Sofia, 2005.

7 A. Barbucci, M. Viviani, P. Carpanese, D. Vladikova, Z. Stoynov, *Electrochim Acta* **51,** 1641, (2006).

8 M. Viviani, S. Presto, A. Barbucci, M. Carpanese, R. Amendola, A. Thorel, A. Chesnaud, J. Abreu, R. Costa, Z. Ilhan, S. Ansar, D. Vladikova, Z. Stoynov, 2011 MRS Spring Meeting Symposium J: Proton in Solids, April 25–29, 2011, San Francisco, CA, USA.

9 A. Chesnaud, A. Thorel, J. Valy, D. Vladikova, Z. Stoynov, G. Raikova, in D. Vladikova, Z. Stoynov (Eds.), Proc. Internat. Workshop "Advances and Innovations in SOFCs 2", 11-16 September, 2011, Katarino, Bulgaria, p. 45.

10 S. Presto, A. Barbucci, M. Viviani, Z.Ilhan, S. Ansar, D. Soysal, A. Thorel, J. Abreu, A. Chesnaud, T. Politova, K. Przybylski, J. Prazuch, Z. Zhao, D. Vladikova, Z. Stoynov, in *Solid Oxide Fuel Cells 11* (SOFCXI), edited by S.C. Singhal, and H. Yokokawa, The Electrochemical Society Proceedings Series 25, ECS Transactions, Pennington, NJ, p.773, (2009).

ДВОЙНО-МЕМБРАННА ГОРИВНА КЛЕТКА - ИМПЕДАНСЕН ПОДХОД ЗА ДОКАЗВАНЕ НА КОНЦЕПЦИЯТА

Д. Владикова[1*], З. Стойнов[1], Г. Райкова[1], М. Кръпчанска[1], А. Торел[2], А. Чесно[2]

[1]*Институт по електрохимия и енергийни системи „Акад. Е. Будевски", Българска академия на науките, ул. „Акад. Г. Бончев" бл. 10, 1113 София, България*

[2] *Център по материалознание, Мини-ПариТех, BP 87, 91 003 Еври, Франция*

Постъпила на 20 февруари, 2012 г.; приета на 20 февруари, 2011 г.

(Резюме)

Двойно-мембранната горивна клетка (ДМГК) е нов иновативен дизайн на високо-температурна горивна клетка, в която кислородна секция (катод и йон-проводящ електролит) е свързана с водородна секция (анод и протон-проводящ електролит) посредством пореста централна мембрана (ЦМ) със смесена проводимост, където двата типа йони реагират. Получената вода се отделя през порите на мембраната. Концепцията е доказана на моделна клетка с помощта на техники, базирани на D.C. измервания и импедансна спектроскопия. С цел оптимизиране на трите компонента на ДМГК (кислороден, водороден и ЦМ) по отношение на материалите и технологичните условия за отлагането им, са проведени импеднансни измервания на симетрични полуклетки. Специално внимание е отделено на някои нови методи за изясняване процеса на образуване и отделяне на водата в централната мембрана

Bulgarian Chemical Communications, Volume 44, Number 4 (pp. 371 – 382) 2012

Application of electrochemical impedance spectroscopy for fuel cell characterization: polymer electrolyte fuel cell (pefc) and oxygen reduction reaction in alkaline solution

N. Wagner

German Aerospace Center, Institute for Technical Thermodynamics, Pfaffenwaldring 38-40, D-70569 Stuttgart, Germany

Received February 20, 2012, accepted February 20, 2012

One of the most common method used to characterize the electrochemical performance of fuel cells is recording of current/voltage U(i) curves. Separation of electrochemical and ohmic contributions to the U(i) characteristics requires additional experimental techniques like Electrochemical Impedance Spectroscopy (EIS) or current interrupt method (CI). The application of EIS is an in-situ approach to determine parameters which have proved to be indispensable for the characterization and development of all types of fuel cell electrodes and electrolyte electrode assemblies [1]. In addition to EIS semi-empirical approaches based on simplified mathematical models can be used to fit experimental U(i) curves [2].

By varying the operating conditions of the fuel cell and by simulation of the measured EIS with an appropriate equivalent circuit, it is possible to split the cell impedance into electrode impedances and electrolyte resistance. Integration in the current density domain of the individual impedance elements enables the calculation of the individual overpotentials in the fuel cell (PEFC) and the assignment of voltage loss to the different processes. In case of using a three electrode cell configuration with a reference electrode one can determine directly the corresponding overvoltage. For the evaluation of the measured impedance spectra the porous electrode model of Göhr [3] was used. This porous electrode model includes different impedance contributions like impedance of the interface porous layer/pore, interface porous layer/electrolyte, interface porous layer/bulk, impedance of the porous layer and impedance of the pores filled by electrolyte.

Keywords: Electrochemical Impedance Spectroscopy, Porous Electrode Models, PEFC, AFC, Oxygen Reduction Reaction, Gas Diffusion Electrode, Diffusion

INTRODUCTION

Fuel cells allow an environmentally friendly and highly efficiently conversion of chemical energy to electricity and heat. Therefore, they have a high potential to become important components of an energy-efficient and sustainable economy. The main challenges in the development of fuel cells are cost reduction and long-term durability. Whereas the cost can be significantly reduced by innovative mass production, the knowledge to enhance the life time sufficiently is presently not available.

Low temperature (T<90ºC) fuel cells like Polymer Electrolyte Fuel Cells (PEFC) and Alkaline Fuel Cells (AFC) are promising for pollution-free energy supplying different applications. Alkaline fuel cells are in some respects an interesting alternative to polymer electrolyte membrane fuel cells. In AFC no expensive platinum metal or noble metal alloys are necessary. Nickel (usually Raney-Nickel) can be used for the hydrogen oxidation reaction (catalyst in the anode) and on the cathode silver can be used as catalyst for the oxygen reduction reaction, because the alkaline electrochemical environment in AFC is less corrosive compared to acid fuel cell conditions. In addition, using liquid alkaline solution as electrolyte heat balance and water management is enhanced. However, normally an electrolyte cycle is needed to remove the product water from the cell, but the electrolyte cycle can also be used as a cooling cycle. A major disadvantage is that AFC are typically operated with pure gases, in particular oxygen instead of air.

The life time of fuel cells is a decisive factor for their commercialization. Therefore, the degradation of fuel cell components is under increased investigation and mainly focused on PEFC [4–10]. Although for alkaline fuel cells several studies of degradation processes exist [11–13], they are all focussed on the electrodes, because the electrolyte in AFCs can be easily exchanged. In the case of using the silver GDE in a complete alkaline fuel cell, the high solubility of silver can lead in certain

* To whom all correspondence should be sent:
E-mail: Norbert.Wagner@dlr.de

© 2012 Bulgarian Academy of Sciences, Union of Chemists in Bulgaria

circumstances to a transfer of silver to the anode and a resulting metal deposition associated with a decrease of activity of the anode. Open circuit situations of the cell may lead to oxidation of silver. A known degradation mechanisms of both AFC and PEFC is carbon corrosion of the catalyst support on the cathode which is accelerated by higher temperatures and higher potentials (e.g. at OCV). Shut down and restarting procedures can lead to enhanced degradation too.

Even if the operation and the components of PEFC and AFC are significantly distinct, for the electrochemical characterization one can use the same measuring technique (EIS) and for the evaluation of the experimental data the same porous electrode model. This paper deals with EIS investigation of:

- Polymer Electrolyte Fuel Cell with a solid proton conducting polymer membrane as electrolyte and electrodes impregnated with electrolyte suspension before use
- Silver gas diffusion cathode during oxygen reduction reaction used in Alkaline Fuel Cells with liquid alkaline electrolyte.

EXPERIMENTAL

In this paper two different experimental set-ups are used. In the case of PEFC the cell impedance of the whole fuel cell consisting of anode, proton conducting membrane and cathode is determined during one measurement without using a reference electrode. In the case of AFC, given by the liquid electrolyte a three electrode cell (half-cell) configuration with a reference electrode is applicable, so that each electrode (anode or cathode) can be investigated separately.

Application of EIS for PEFC characterization

The investigated PEFC electrodes were commercial electrodes from EÏTEK (20% Pt/C, 0.4 mg/cm^2, thickness 200 μm) impregnated before use with 1 mg/cm^2 Nafion suspension, Aldrich Chemie and with Nafion® 117 as electrolyte. After pretreatment (activation) of the Nafion membrane with H_2O_2/H_2SO_4, electrodes and membrane have been hot pressed (1.6 MPa, increasing temperature up to 160ºC) for 10 minutes. The resistance of the proton exchange membrane shows a strong dependence on water content. The fuel cell was operated at 80ºC with the hydrogen feeds stream humidified by passage through a bubbling bottle at

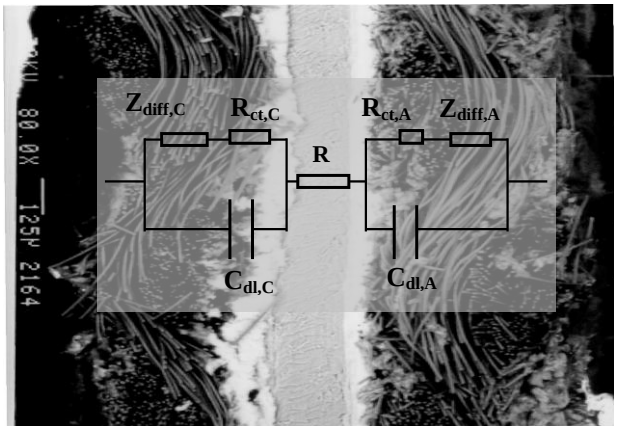

Fig. 1. Common equivalent circuit (EC) used for the simulation of fuel cells

a temperature of 90ºC. The oxygen was not humidified, it was only heated up to 30ºC before it entered the cell. Pure hydrogen and oxygen were used, both at 2.0 bar absolute. The hydrogen flow was „dead end“ whereas the oxygen flow rate was adapted to twice the stoichiometric requirement at each current density. The geometric surface of the electrodes used in the PEFC is 23 cm^2.

The electrochemical characterization of the fuel cells was performed by electrochemical impedance measurements in the frequency range from 10 mHz to 4 MHz (IM6, Zahner-elektrik, Kronach, Germany). Measurements at currents up to 25 A have been carried out in combination with an external electronic load (Power potentiostat PP240 from Zahner-elektrik). Such high currents lead, however, to a limitation in the upper frequency range (<100 kHz), due to the low impedance of the fuel cell at frequencies higher than 10 kHz (at PEFC with 25 cm^2 active surface typically lower than 5ºmΩ) and to a mutual induction artefact [14].

Applying a three electrode cell with one reference electrode is complex for the investigation of electrochemical systems with solid electrolytes. Therefore, the anode and cathode transfer functions have been determined independently without a reference electrode using symmetric gas supply of hydrogen or oxygen on both electrodes of the fuel cell at open circuit potential (OCP). Thus, cathode and anode impedance can be determined directly with two independent experiments and appropriate equivalent circuits are derived to analyze the impedance response of the fuel cell at different current densities. Furthermore, by varying the electrode composition [15] and experimental conditions (temperature, gas composition and humidification) the measured cell impedance under load can be split up into anode impedance, cathode impedance and electrolyte resistance without using reference electrodes [16–17]. A general equivalent

circuit that can be used for the evaluation of measured spectra at fuel cells is shown in Fig.1. Under certain operating conditions (e.g. use of reference electrode) and in function of the fuel cell type one or more impedance elements from Fig. 1 can be omitted.

Results

Impedance spectra are presented as Bode plots, where the logarithm of the impedance magnitude and phase-shift are plotted vs. the logarithm of the frequency. To identify and separate the different diffusion processes, it is useful to represent the measured impedance spectra also as Nyquist diagram (imaginary part vs. real part of the impedance). In the Nyquist diagram one can observe the Nernst-impedance (finite diffusion) as an additional loop at the lowest part of the frequency range, the Warburg-impedance (infinite diffusion) as a straight line with a slope of 1 (real part = imaginary part). In the Bode diagram due to the logarithmical scale of the impedance the difference of the two kinds of diffusion can not be discerned so clearly.

EIS measured on the PEFC (H_2/O_2) in the potential range from OCV (1024 mV) to 600ºmV (Fig.2) show in the Bode representation in the low frequency range of the spectra an exponential potential dependency of the impedance reaching a minimum at 600 mV (9 A). At cell voltages below 600 mV one can observe an increase of the cell impedance (e.g. spectra measured at 317 mV in Fig.1) and an additional phase-shift maximum at 50 mHz. The appearance and the nature of the new impedance contribution can be better seen from the Nyquist representation in Fig.3. From this increase of the cell impedance, one can deduce that at higher load of the cell an additional overvoltage occurs. From the shape of impedance spectra we can identify this additional overvoltage as a diffusion overvoltage. In this case it is a finite diffusion, corresponding to the „Nernst-impedance“ as defined in equation (4) below, for details see [1].

Given the time constant of the mass transport, the impedance related to the diffusion is usually found at the lowest region of the frequency range. Therefore, the impedance has to be measured in a wide frequency range, down to 10 mHz or even lower.

In order to evaluate the measured impedance spectra, the reaction steps can be translated into an appropriate equivalent circuit (EC) which contains various impedance elements representing the involved reaction steps. Starting point is the general EC shown in Fig. 1. For the evaluation of EIS shown in Fig. 2 and Fig. 3 one can use the EC shown inside Fig.4. In Fig.4 EIS spectra measured in the low cell voltage range (high current range) of PEFC are shown, whereas the points represent the measured data and the solid lines the simulated data after fitting the spectra with the corresponding EC.

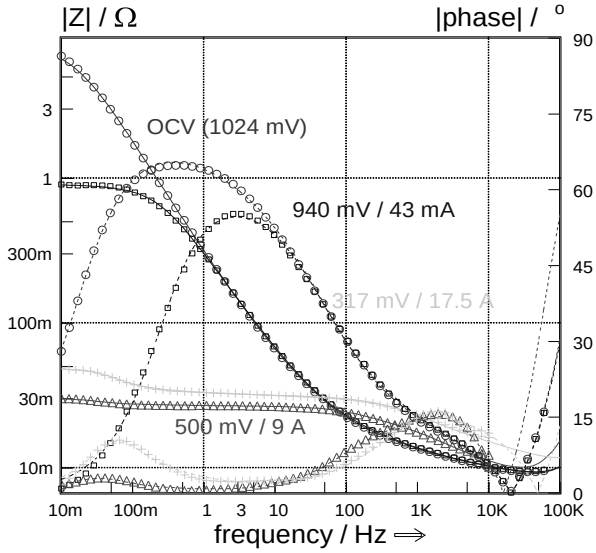

Fig. 2. Bode diagram of selected EIS measured on PEFC, 80°C, at 2 bar absolute, at different cell voltages (currents): (o) 1024 V, (□) 940 mV, (Δ) 500 mV and (+) 317 mV.

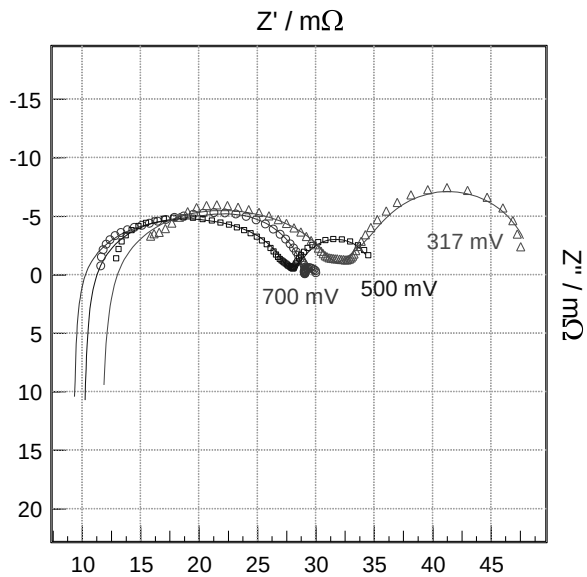

Fig. 3. Nyquist diagram of selected EIS measured on PEFC at low cell voltages, 80°C, at 2 bar absolute, at different cell voltages (currents): (o) 700 mV (5.4 A), (□) 500 mV (12.1 A) and (Δ) 317 mV (17.5 A).

The EC consist of a series resistance (electrolyte or membrane resistance R_{el}) and 3 parallel R/C terms which three different potential depending time constants. In the simulation of the measured

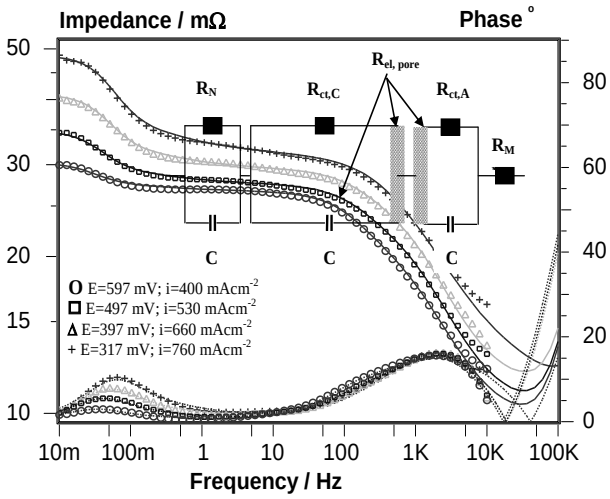

Fig. 4. Bode diagram of EIS measured in the low cell voltage range, at 80°C, at 2 bar absolute, at different cell voltages (currents): (o) 597 V, (□) 497 mV, (Δ) 397 mV and (+) 317 mV with the schematic representation of the used EC for fitting as insert.

impedance spectra the ideal capacitance (C) was replaced by CPE (CPE= constant phase element)due to the porous structure of the electrodes. Due to the fact that the electrodes have a porous structure the model of Göhr [1, 3] was used. Taking into account only the electrolyte resistance of the pores filled by electrolyte ($R_{el,pore}$) and the charge transfer resistance (R_{ct}) at the interface porous layer/pore in the porous electrode than we can use a simplified equation (Equ.1) for each polarization resistance (R_p) of the corresponding porous electrode (anode and cathode):

$$R_{p,A} = \frac{\left(R_{el,pore,A} \cdot R_{ct,A}\right)^{\frac{1}{2}}}{\tanh\left\{\left(\frac{R_{el,pore,A}}{R_{ct,A}}\right)^{\frac{1}{2}}\right\}} \qquad (1)$$

$$R_{p,C} = \frac{\left(R_{el,pore,C} \cdot R_{ct,C}\right)^{\frac{1}{2}}}{\tanh\left\{\left(\frac{R_{el,pore,C}}{R_{ct,C}}\right)^{\frac{1}{2}}\right\}}$$

The impedance elements $R_{el,pore}$ and R_{ct} from equation (1) are part of the used EC from Fig.4 and the numerical values are obtained after a complex nonlinear last square fit of the measured impedance spectra.

For the oxygen reduction reaction (ORR) at the cathode a parallel R/C term for the charge transfer

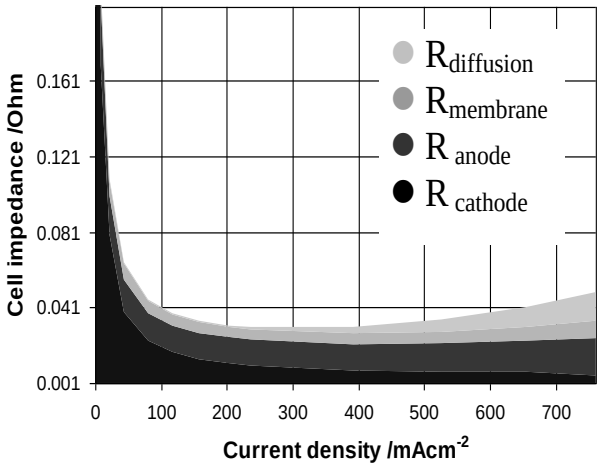

Fig. 5. Current density dependence of different contributions to the overall cell impedance after fitting the measured EIS with the EC from Fig.4.

through the double layer of the cathode ($R_{ct(C)}$ / $CPE_{dl(C)}$) can be used. A second parallel R/C term for the finite diffusion of water with a Nernst-impedance like behaviour ($R_{(N)}$ / $CPE_{(N)}$ and finally for the simulation of the hydrogen oxidation reaction (HOR) at the anode a third parallel R/C term ($R_{ct(A)}$ / $CPE_{dl(A)}$ can be used. This EC was used to determine the influence of electrolyte (milled Nafion powder) content in the electrode on the electrode (cell) performance [18].

In the impedance spectra (e.g. Fig. 4) we can find the contribution of slow reactions at low frequencies (e.g. diffusion, adsorption, and recrystallization) and the contribution of fast reactions at high frequencies (charge transfer reaction of HOR) [19]. The contribution of electrolyte (membrane) resistance R_M is located at the high frequency end of the impedance spectra, where also some parasitic inductive contribution of connecting wire can be found, especially in the case of very low impedance values.

Using the EC from Fig.4 the numerical values of the resistances, as a function of the applied potential (current density) can be obtained with the complex nonlinear least-square fit program and are represented as a function of the current density in Fig.5. For a more detailed representation of the dependence of the different resistances on current density a linear scale from 0 to 0.2 Ω is used in Fig.5. In the low current density region the cell impedance (resistance) is dominated by the charge transfer resistance of the oxygen reduction reaction. At current densities higher than 236ºmAcm^{-2} an additional contribution (diffusion) to the cell impedance is present due to an insufficient

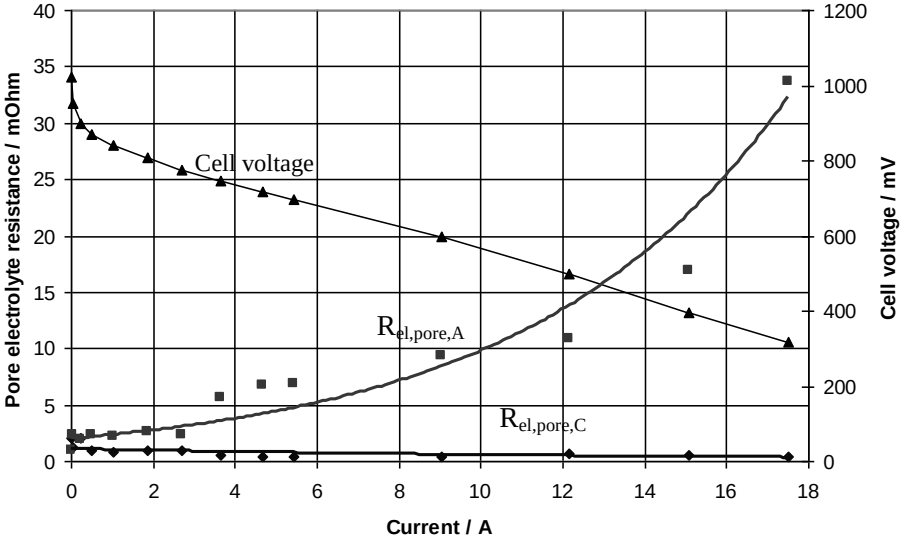

Fig. 6. Current dependence of cell voltage (▲), pore electrolyte resistance of the anode ($R_{el,pore,A}$) (■) and cathode ($R_{el,pore,C}$) (◆).

humidification of the membrane and of the electrolyte component in the anode. The insufficient humidification of the hydrogen feed leads to an increase of the charge transfer resistance of the hydrogen oxidation reaction and also to a strong increase of the pore electrolyte resistance in the anode ($R_{el,pore,A}$ in Fig.6).

The used model (equivalent circuit) for the interpretation of the measured impedance data has to be validated concerning the unambiguous assignment of the impedance elements used in the EC to the electrochemistry of the system by changing some operational conditions like gas composition, partial pressure, concentration, electrode composition, temperature, etc. In the case of PEFC one can also use symmetrical cell configuration or change of the cathode gas supply from pure oxygen to air or changing the anode gas supply from pure hydrogen to CO-containing hydrogen (e.g. H_2 + 100 ppm CO) during constant load of the cell. Another way to validate the used model is to change one of the electrode material or composition, for example using Pt or Pt/Ru anodes for the oxidation of CO-containing hydrogen [20]. During constant load of the cell the anode surface is poisoned and the impedance related to the anode increases due to the decrease of the active anode surface. The impedance of the cathode will remain unaffected from the composition of the anode and in this way one can separate the contribution of the anode and cathode from the cell impedance.

Application of EIS during Oxygen Reduction Reaction in Alkaline Solution

Oxygen reduction electro catalysis is of special importance for fuel cells, metal-air batteries and industrial chlorine-alkali electrolysis as well. Silver is well known as an effective electro catalyst for the reduction of oxygen in alkaline fuel cell cathodes. To enhance his catalytic activity, silver is used in a form with high specific area such as porous electrodes where the silver particles are dispersed in a porous matrix, e.g. PTFE. The porous PTFE-bonded gas-diffusion electrodes can be prepared by a reactive mixing and rolling (RMR) production technique, first described by Winsel [21], and later improved and adapted by other groups [22] or by wet techniques using inks or suspensions. A comprehensive overview on the subject is given in [23]. The electrodes consist of the electrocatalytic active powder (silver, Raney-silver, silver covered with PTFE (Silflon) or silver oxide), the organic binding agent (PTFE), pore forming material (e.g. $NaHCO_3$) and a metal wire gauze to stabilise mechanically the electrode and to collect the current. In gas diffusion electrodes both hydrophobic and hydrophilic pore systems are required. In AFC the hydrophilic system allows the penetration of the electrolyte (alkaline solution) into the electrode and the transport of the ions to or from the reaction zone; in contrast the hydrophobic pore system is required for the transport of the oxygen to the reaction zone. In addition, to give the mechanical stability, the PTFE in the electrodes forms a hydrophobic pore system, whereby a “spider web” of PTFE fibres in and on the electrodes are formed during preparation, as shown

in Fig. 7. Two electrode components Ag and PTFE can clearly be distinguished in Fig. 7. Details of electrode preparation, activation (silver oxide reduction) and experimental set-up are given in [23].

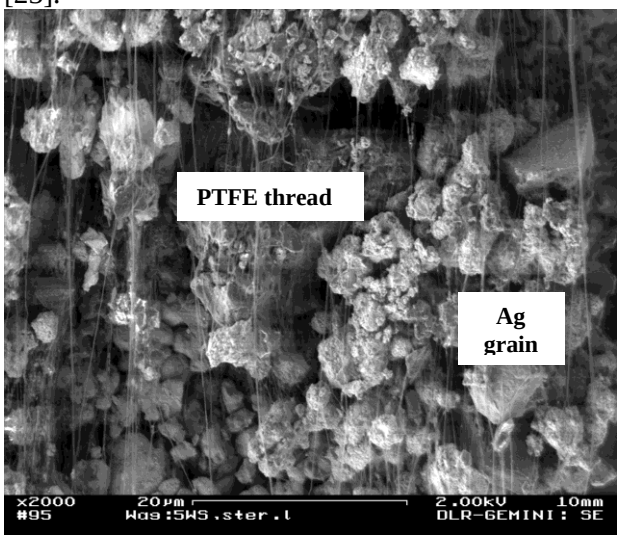

Fig. 7. SEM picture of PTFE bounded silver gas diffusion electrodes (GDE).

Since the electrolyte is a liquid, in contrast to the case of the PEFC the use of a reference electrode (RHE or Hg/HgO) is easily possible and the two electrodes of a fuel cell, anode and cathode can be investigated independent from each other, in half-cell configurations. To indicate the nature of the investigated electrochemical reaction (reduction process) the sign of the current density is negative. Since the kinetics of the oxygen reduction reaction is much slower than the kinetics of the hydrogen oxidation reaction the performance loss of the fuel cell will be determined mainly by the cathode and therefore the oxygen reduction on silver has been investigated by several authors [25–26] with different steady state and potential step techniques on smooth electrodes. The reduction process has been found to follow two reaction pathways [27]: the direct $4e^-$ path and the $2e^-$ path (generally referred to as the sequential path) involving the formation of peroxide as an intermediate product.

To elucidate the reaction mechanism and to obtain the kinetic parameters for oxygen reduction on PTFE-bonded gas-diffusion silver electrodes in alkaline solution the AC impedance method was applied by several investigators [28–29].

The objective in this second part is to obtain the kinetic parameters for oxygen reduction on PTFE-bonded gas-diffusion silver electrodes in alkaline solution by using cyclic voltammetry (CV) and electrochemical impedance spectroscopy.

The experiments were carried out in a polymethylmetacrylate half-cell with two chambers, a gas chamber and an electrolyte chamber, which are kept tightly together by four screws. The gas chamber has inlet and outlet for the gas flow, while the electrolyte chamber has connections for filling and draining the electrolyte. The working electrode (GDE) is placed between these two chambers and fixed with a sealing rubber. The whole assembly is placed in a thermostatic water bath for carrying out experiments at different temperatures.

Results

The working electrodes were circular PTFE-bonded Gas-Diffusion silver Electrodes (GDE) with an apparent geometric surface area of 1 cm^2. The thickness of the electrode was 0.3 mm. These electrodes were produced by the reactive mixing and rolling (RMR) production technique starting from a powder mixture of silver oxide (Ag_2O) and PTFE forming an Ag_2O–GDE. This electrode was integrated in a half-cell and reduced in situ electrochemically to silver. The reduction of the silver oxide (2) electrode was performed galvanostatically by applying a current density of -50ºmAcm^{-2} (referred to geometric surface area) for 1 hour in 10ºN NaOH at 60C. The reduction of silver oxide takes place simultaneously with the oxygen reduction reaction (3):

$$Ag_2O + H_2O + 2e^- \rightarrow 2Ag + 2OH^- \quad \text{with } E^0 = 247 \text{ mV vs. Hg/HgO} \qquad (2)$$

$$O_2 + 4e^- + 2H_2O \rightarrow 4OH^- \quad \text{with } E^0 = 303 \text{ mV vs. Hg/HgO} \qquad (3)$$

The counter electrode was a Pt-foil. The reference electrode was an Hg/HgO electrode (Ingold Messtechnik, Germany). All potentials are referred to the used Hg/HgO reference electrode, unless otherwise stated. Electrolyte solutions were prepared from analytical grade (Merck) reagents.

2.2.1.1. Results from CV measurements. All CV measurements were performed in 10 N NaOH solution at 80°C with scan rates of 1 mV/s in the potential range from OCP to -700 mV vs. Hg/HgO (230 mV vs. RHE) and with 50 mV/s in an extended potential range from OCP to an upper potential of 450 mV and in the reverse scan down to -700 mV and back to the starting potential(OCP).

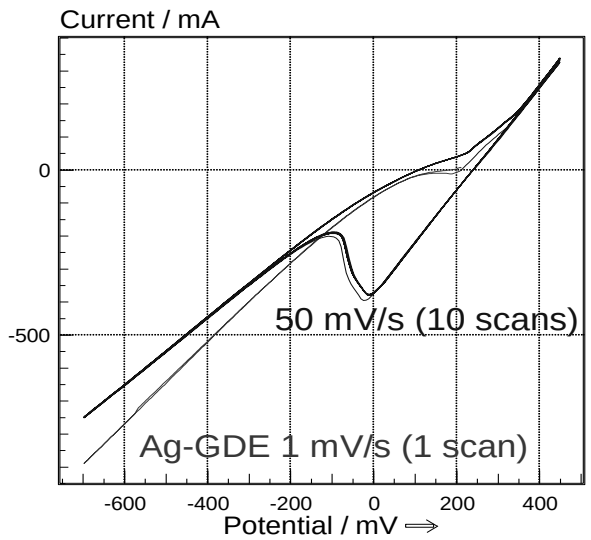

Fig. 8. CV measured during oxygen reduction on Ag-GDE in 10 N NaOH at 80°C with scan rates of 50 mV/s and 1 mV/s.

The Ag_2O reduction peak (Fig.8) appears only in the reverse scan of the spectra recorded up to 450 mV when at potentials higher than OCP the oxidation of silver occurs. This finding suggests that close to OCP both reactions take place: oxidation of silver / reduction of silver oxide and reduction of oxygen.

During CV measurements the electrolyte resistance (R_{el}) was not compensated. Before evaluating the slow CV (1 mV/s) and extracting kinetic relevant parameter first the potentials have to be iR_{el} corrected. The value of R_{el} can be determined from the measured impedance spectra, as shown in the next section. In the CV from Fig.9 uncorrected and iR_{el} corrected potentials referred to the RHE are shown.

Tafel slope and apparent exchange current density can be determined from the Tafel representation of the iR_{el} corrected slow CV from Fig. 9. For more accuracy the current density range was limited in Fig. 10 to the kinetically relevant domain from 0 to -0.1 Acm^{-2}. A Tafel slope of 80 mV/decade and an apparent exchange current density of 4.57 10^{-3} Acm^{-2} was determined.

Results from impedance measurements.

The electrode impedance was measured with an ac voltage signal in the frequency range from 50 mHz to 100 kHz superimposed on the dc polarisation potential or in the case of galvanostatical control of the half-cell on the dc current. The amplitude of ac signal was kept smaller than 10 mV peak-to-peak in order that the current response remains within a linear range.

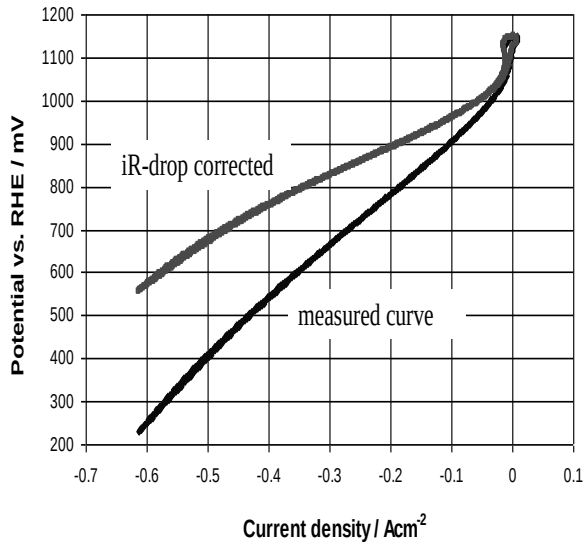

Fig. 9. Uncorrected and iR_{el} corrected data of the CV recorded with 1 mV/s at 80°C during ORR in 10 N NaOH in the potential range from OCP to 230 mV vs. RHE (-700 mV vs. Hg/HgO)

Since the geometric area of the used electrode is 1 cm^2 the measured impedance values correspond to the area-related values.

Impedance spectra have been measured at 80°C, in 10 N NaOH in the low current density range from -5 $mAcm^{-2}$ to -50 $mAcm^{-2}$ (Fig. 11 and Fig. 12).

In order to evaluate the measured impedance spectra and to obtain kinetic data of the oxygen reduction reaction, the reaction steps can be translated into an appropriate equivalent circuit (EC). The evaluation of the measured EIS was performed with a part of EC from Fig. 1 that represents the cathode of the fuel cell, namely the serial combination of Nernst-impedance (diffusion element) and charge transfer resistance connected in parallel with the double layer capacity. These elements are forming the pore's wall surface impedance (Z_q) of the cylindrical-pore model proposed by Göhr. From this model only Z_q and the pore electrolyte (Z_p) impedance (resistance) were considered. The uncompensated electrolyte resistance R_{el} (element 5 from equivalent circuit in Fig.13) is connected in series with the impedance of the porous cathode.

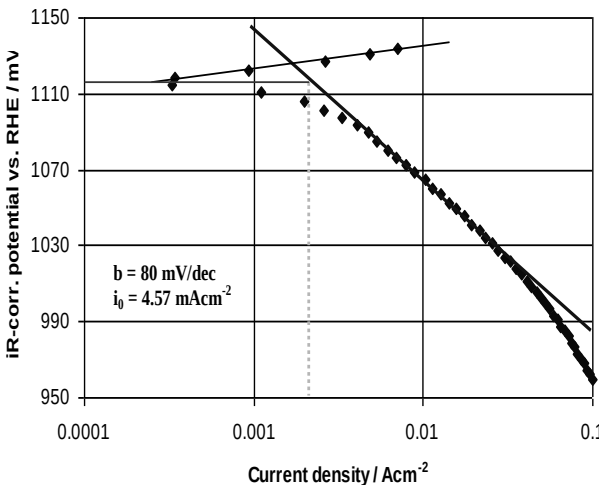

Fig. 10. Tafel-plot of data measured during ORR on Ag-GDE in 10 N NaOH at 80°C.

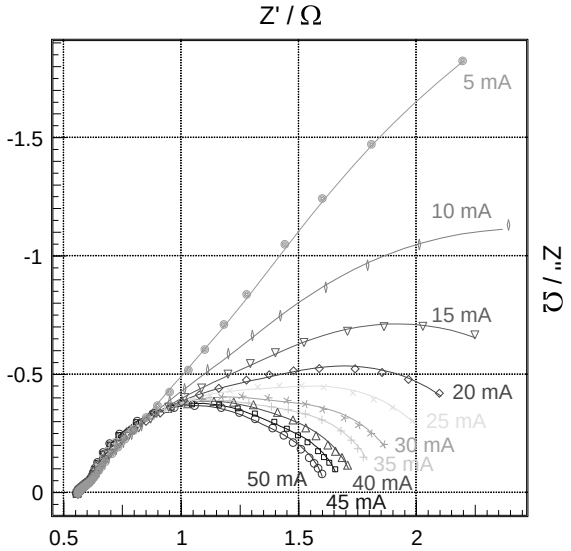

Fig. 12. Nyquist representation of impedance spectra measured in the frequency range from 50 mHz to 10 kHz at different current densities during oxygen reduction reaction on Ag-GDE in 10 N NaOH

The current density dependency of the charge transfer resistance R_{ct} and used EC are given in Fig.13. R_{ct} first increase from 0.883 Ωcm^2 at -5 $mAcm^{-2}$ to 1.485 Ωcm^2 at -10 $mAcm^{-2}$ and than decrease to 0.824 Ωcm^2 at -50 $mAcm^{-2}$. This finding suggests that at low current densities close to open cell potential (OCP) two different reactions take place: ORR and silver oxide reduction. At current densities higher than - 10 $mAcm^{-2}$ the oxygen reduction reaction is predominant.

To extract the kinetic data of the OCR the values of R_{ct} were plotted in function of the current density (Fig.14) assuming a Butler-Volmer behaviour. Extrapolating the straight line to zero current one can calculate from the intercept with the y-axis the

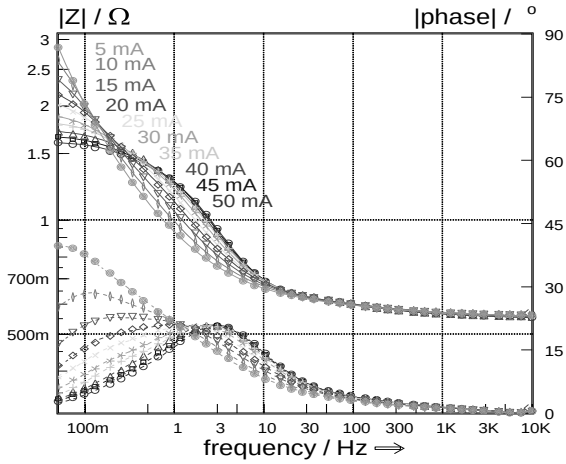

Fig. 11. Bode representation of impedance spectra measured at different current densities during oxygen reduction reaction on Ag-GDE in 10 N NaOH, 80°C.

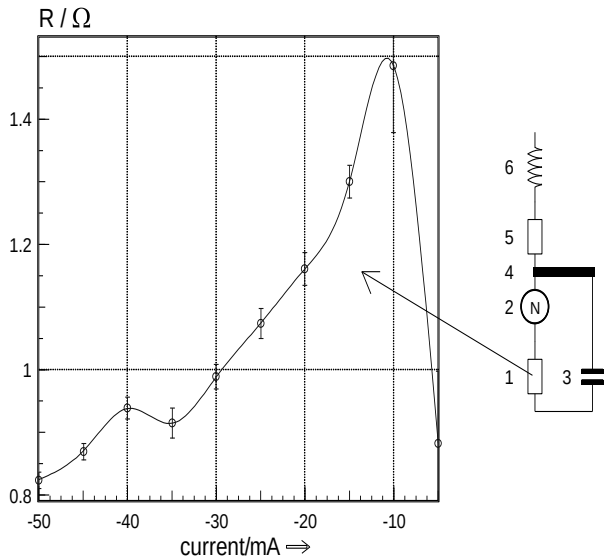

Fig. 13. Current density dependence of the charge transfer resistance (element number 1) during oxygen reduction reaction on Ag-GDE in 10 N NaOH, 80°C.

value of R_{ct} for the OCR without contributions of the silver oxide reduction reaction. The value calculated for R_{ct} is 1.79 Ωcm^2 and with the formula indicated in the graph one can calculate the apparent exchange current density (i_0) of the oxygen reduction reaction. The calculated value for i_0 is 4.2 $mAcm^{-2}$ and is in good agreement with 4.57 $mAcm^{-2}$ calculated from the CV from Fig. 10.

From the current density dependency of the other impedance elements of the EC, in particular the double layer capacity C (Fig. 15) and electrolyte resistance inside the pore (Fig.16) it is found that with increasing current density the electrochemical active surface and pore electrolyte resistance are increasing. One can

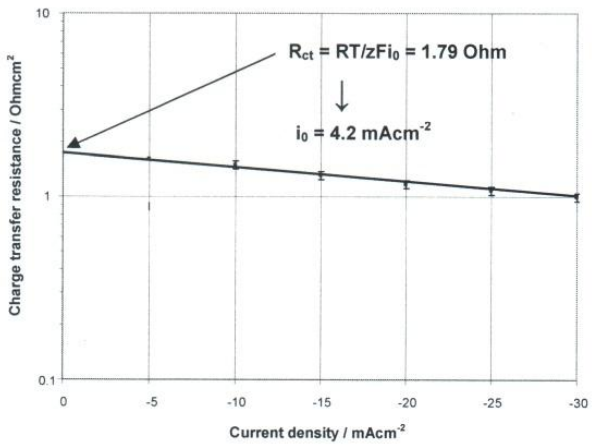

Fig. 14. Low current density dependence of the charge transfer resistance (logarithmical representation) during oxygen reduction reaction on Ag-GDE in 10 N NaOH, 80°C.

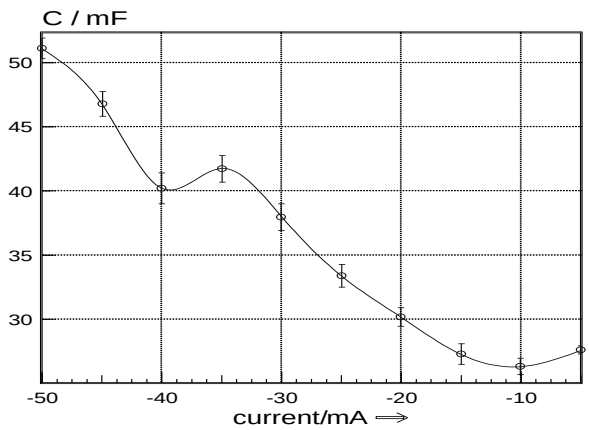

Fig. 15. Current density dependence of the double layer capacity during oxygen reduction reaction on Ag-GDE in 10 N NaOH, 80°C.

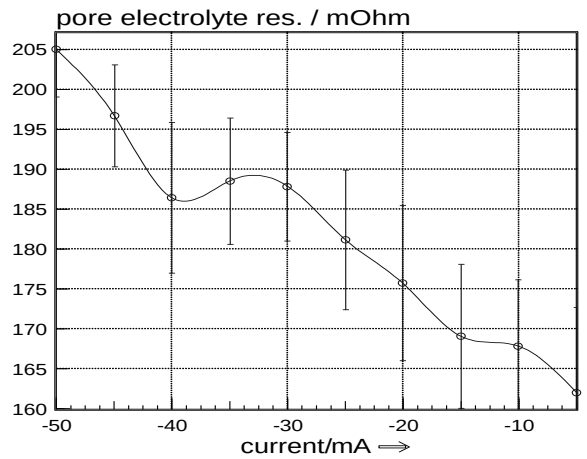

Fig. 16. Current density dependence of the pore electrolyte resistance during oxygen reduction reaction on Ag-GDE in 10 N NaOH, 80°C.

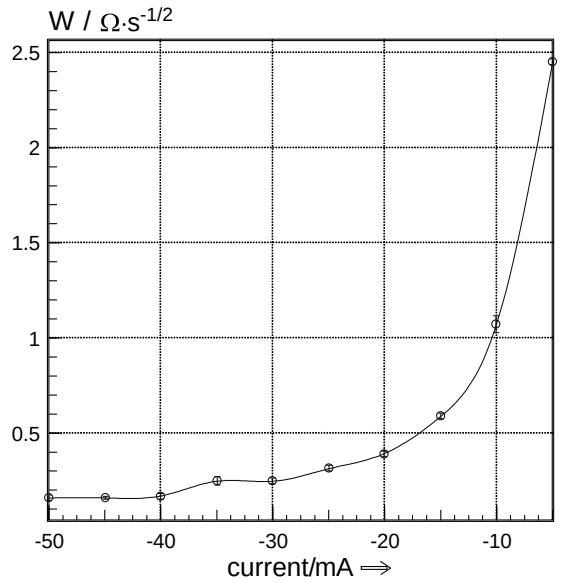

Fig. 17. Current density dependency of the Warburg parameter (W) during oxygen reduction reaction on Ag-GDE in 10 N NaOH, 80°C

conclude that in the investigated current density range from OCP to -50 mAcm^{-2} the reaction zone moves with increasing current density within the porous electrode from electrolyte side to gas side. This assumption is confirmed by the current density dependence of the elements of the Nernst-impedance. The Nernst impedance Z_N contains two parameters:the Warburg parameter W with the unit $\Omega s^{-1/2}$ and a diffusion time constant (k_N), determined by the constant of diffusion (D_k) and diffusion layer thickness (d_N). The Nernst impedance is calculated by equation (4):

$$Z_N = \frac{\nu^2}{z^2} \cdot \frac{R \cdot T}{F^2} \cdot \frac{1}{c_d \cdot \sqrt{D}} \cdot \frac{\tanh\sqrt{\frac{j \cdot \omega \cdot d^2}{D}}}{\sqrt{j \cdot \omega}} \equiv \frac{\mathrm{W}}{\sqrt{j \cdot \omega}} \cdot \tanh\sqrt{\frac{j \cdot \omega}{k_N}} \quad (4)$$

The current density dependence of the Warburg parameter (W) is shown in Fig. 17.

The dependence of diffusion layer thickness (d_N) on current density can be evaluated from the value of diffusion time constant k_N (Fig.18) and is calculated by with equation (5). Increasing the current density up to -50 mAcm^{-2} the diffusion layer thickness decreases from 150 µm to 57 µm.

In this work two different formulas for the transfer functions of the diffusion processes were used. In the inset of Fig. 1 a general impedance element Z_{diff} and in the equivalent circuit from Fig.4 a parallel RC-term (R_N and C) is used.

$$d_N = \sqrt{\frac{D}{k_N}} \quad (5)$$

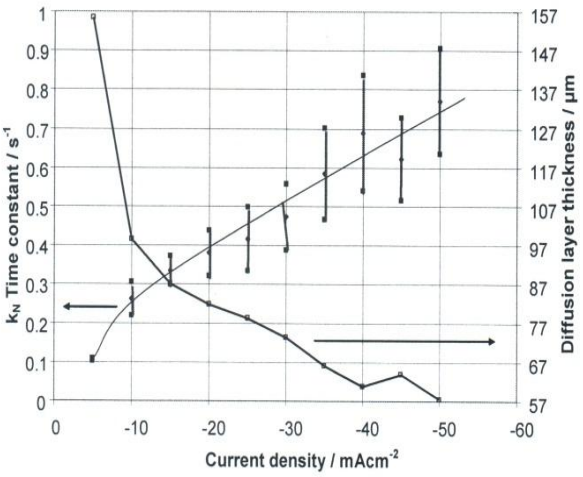

Fig. 18. Current density dependence of the diffusion time constant (2nd parameter of Z_N) and calculated diffusion layer thickness during oxygen reduction reaction on Ag-GDE in 10 N NaOH, 80°C.

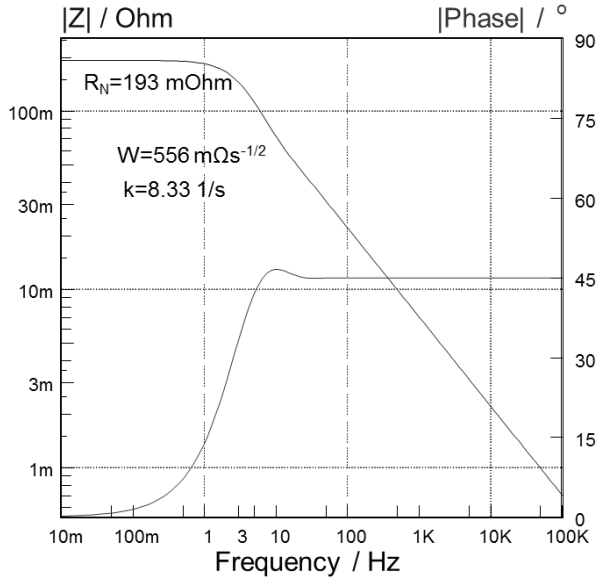

Fig. 19. Bode diagram of simulated impedance spectra of the Nernst impedance Z_N with W=556 mΩs$^{-1/2}$ and k_N=8.33 s^{-1}.

Depending of the boundary condition of the diffusion process we can distinguish between "General Warburg Impedance" element, often called "Nernst diffusion element - Z_N or finite diffusion impedance", with the transfer function given by equation (4), "Special Warburg" diffusion impedance, often called only "Warburg impedance – Z_W or infinite diffusion impedance", with the transfer function given by equation (6).

$$Z_W = \frac{\nu^2}{z^2} \cdot \frac{R \cdot T}{F^2} \cdot \frac{1}{c_d \cdot \sqrt{D}} \cdot \frac{1}{\sqrt{j \cdot \omega}} \equiv \frac{\mathrm{W}}{\sqrt{j \cdot \omega}} \quad (6)$$

A third kind of diffusion impedance is the finite diffusion impedance Z_S (not used in this work) with the transfer function given by equation (7). Z_S describes a diffusion process where the diffusion length is finite due to a phase boundary assumed in a certain distance from the electrode. This kind of diffusion appears in impedance spectra of batteries e.g. Lithium-ion batteries [30]. The high frequency part of the impedance spectra exhibits the same shape like the Warburg impedance (Special Warburg Impedance) whereas the low frequency part is similar to a capacity.

$$Z_S = \frac{\nu^2}{z^2} \cdot \frac{R \cdot T}{F^2} \cdot \frac{1}{c_d \cdot \sqrt{D}} \cdot \frac{\coth\sqrt{\frac{j \cdot \omega \cdot d^2}{D}}}{\sqrt{j \cdot \omega}} \equiv \frac{\mathrm{W}}{\sqrt{j \cdot \omega}} \cdot \coth\sqrt{\frac{j \cdot \omega}{k_S}} \quad (7)$$

In the some cases like used in the equivalent circuit in the inset of Fig.4 one can replace Z_N with a parallel combination of R_N and C. This is only true if the argument of the tanh function in equation (3) $\omega\ d^2 / D >> 3$ so that the equation can be simplified into equation (8):

$$R_N = Z_{N(w=0)} = \frac{\nu^2}{z^2} \cdot \frac{R \cdot T}{F^2} \cdot \frac{1}{c_d \cdot \sqrt{D}} \cdot \frac{1}{\sqrt{j \cdot \omega}} \equiv \frac{\mathrm{W}}{\sqrt{k_N}} \cdot \quad (8)$$

The validation of equation 8 is demonstrated in Fig. 19 by using one value (W=556 mΩs$^{-1/2}$ and k_N=8.33 s^{-1}) of the Nernst impedance from Fig. 13. The low frequency limit of Z_N is identical with R_N calculated with equation (8).

3. CONCLUSION

The evaluation of EIS using the porous electrode model proposed by Göhr is very helpful to understand some important features of fuel cell electrodes and operating conditions. In the case of PEFC it could be shown that insufficient humidification of the anode leads to an increase of performance loss not only due to the well-known increase of the membrane resistance (R_M) but also due to an increase of pore electrolyte resistance inside the anode affecting the electrode composition, in particular the content of solid electrolyte in the anode [18]. An increase of pore electrolyte resistance in the anode ($R_{el,pore,A}$ in Fig.6) increases the potential drop in the anode and contribute to an increase of performance loss of the anode and fuel cell respectively.

In the case of silver gas diffusion electrodes used for the oxygen reduction in alkaline solution it could be shown the movement of reaction zone

inside the GDE and change of diffusion layer thickness with current density in the current density range from 0 to –50 $mAcm^{-2}$.

Acknowledgements: *The oxygen reduction part of this work was funded by the German Ministry of Education and Research (BMBF) under the "klimazwei" research programme (Contract No.: 01 LS 05007).*

REFERENCES:

1. N. Wagner, "Electrochemical power sources – Fuel cells" in *Impedance Spectroscopy: Theory, Experiment, and Applications*, 2nd Edition, Edited by Evgenij Barsoukov and J. Ross Macdonald, John Wiley&Sons, Inc., ISBN: 0-471-64749-7, pp. 497-537, (2005).
2. P. Spinelli, C. Francia, E.P. Ambrosio, M. Lucariello, *J. Power Sources* **178,** 517, (2008).
3. H. Göhr, *Electrochemical Applications* **1**, 2, (1997) (http://www.zahner.de)
4. D.P. Davies, P.L. cAdcock, M. Turpin, S.J. Rowen, *J. Power Sources* **86,** 237, (2000).
5. B. Mattsson, H. Ericson, L.M. Torell, F. Sundfolm, *Electrochim. Acta* **45,** 1405, (2000).
6. A.S. Aricò, A. Stassi, E. Modica, R. Ornelas, I. Gatto, E. Passalacqua, V, Antonucci, *J.Power Sources* **178,** 525, (2008).
7. M. Schulze, M. Lorenz, N. Wagner, E. Gülzow, *FreseniusJ. Anal. Chem.* **365,** 106, (1999).
8. F. N. Büchi, B. Gupta, O. Haas, G.G. Scherer, *Electrochim. Acta* **40,** 345, (1995).
9. E. Gülzow, A. Helmbold, T. Kaz, R. Reißner, M. Schulze, N. Wagner, G. Steinhilber, *J. Power Sources* **86,** 352, (2000).
10. M. Schulze, N. Wagner, T. Kaz, K.A. Friedrich, *Electrochim. Acta* **52,** 2328, (2007).
11. E. Gülzow, M. Schulze, G. Steinhilber, *J. Power Sources* **106,** 126, (2002).
12. Y. Kiros, S. Schwartz, *J. Power Sources* **87,** 101, (2000).
13. N. Wagner, M. Schulze, E. Gülzow, *J. Power Sources* **127,** 264, (2004).
14. F. Richter, C.-A. Schiller, N. Wagner, Current Interrupt Technique-Measuring low impedances at high frequencies, in „Electrochemical Applications, 1/2002", p.1-6, Ed. Zahner-elektrik, Kronach, 2002
15. N. Wagner, T. Kaz, K.A. Friedrich, *Electrochim. Acta* **53,** 7475, (2008).
16. N. Wagner, *J. Appl. Electrochem*. **32**, 859, (2002).
17. X. Yuan, H. Wang, J.C. Sun, J. Zhang, *Int. J. Hydrogen Energy* **32,** 4365, (2007).
18. N. Wagner, T. Kaz, K. A. Friedrich, *Electrochim. Acta* **53,** 7475, (2008).
19. N. Wagner, K.A. Friedrich, Dynamic Operational Conditions. In J. Garche, C. Deyer, P. Moseley, Z. Ogumi, D. Rand and B. Scrosati (Eds.). Encyclopedia of Electrochemical Power Sources, Vol.2, ISBN-978-0-444-52093-7, Amsterdam, Elsevier 2009, pp. 912-930.
20. N. Wagner, M. Schulze, *Electrochim. Acta* **48,** 3899, (2003).
21. A. Winsel, German Patent, DE 3342969, 1985.
22. N. Wagner, German Patent, DE 199 40 015, 2004.
23. I. Moussallem, J. Jörissen, U. Kunz, S. Pinnow, T. Turek, *J. Appl. Electr*ochem. **38,** 1177, (2008).
24. E. Gülzow, N. Wagner and M. Schulze, *Fuel Cells – From Fundamentals to Systems* **3** 67, (2003).
25. P. Fischer, J. Heitbaum, *J. Electroanal. Chem*. **112,** 21, (1980).
26. B.D. Cahan, J.B. Ockerman, R.F. Amlie, P.Rüetschi, *J. Electrochem. Soc*. **107,** 725, (1960).
27. J.P. Hoare, The Electrochemistry of Oxygen, Interscience, New York, 1968
28. K. Mund, *Siemens Forsch.- und Entwickl.- Ber*. **4,** 68, (1975).
29. R. Holze, W. Vielstich, *J. Electrochem. Soc.* **131,** 2298, (1984).
30. M. Chamas, P-E. Lippens, J-C. Jumas, J. Hassoun, S. Panero, B. Scrosati, *Electrochim. Acta* **56,** 6732, (2011).

ПРИЛОЖЕНИЕ НА ЕЛЕКТРОХИМИЧНА ИМПЕДАНСНА СПЕКТРОСКОПИЯ ЗА ОХАРАКТЕРИЗИРАНЕ НА ГОРИВНИ ЕЛЕМЕНТИ: ГОРИВЕН ЕЛЕМЕНТ С ПОЛИМЕРЕН ЕЛЕКТРОЛИТ И РЕАКЦИЯ НА РЕДУКЦИЯ НА КИСЛОРОДА В АЛКАЛЕН РАЗТВОР

Н. Вагнер

Германски аерокосмически център, Институт по техническа термодинамика, Пфафенвалдринг 38-40, D-70569, Щутгарт, Германия

Постъпила на 20 февруари, 2012 г.; приета на 20 февруари, 2012 г.

(Резюме)

Един от най-разпространените методи за охарактеризиране електрохимичните отнасяния на горивни елементи е регистрирането на волтамперните U(i) криви. Разделянето на електрохимичния от омовия принос към волтамперните характеристики изисква допълнителни експериментални техники като електрохимична импедансна спектроскопия (IES) и токово въздействие (CI). Прилагането на EIS е *in-situ* подход за определяне на параметри, които се оказват незаменими за характеризирането и разработването на всички видове електроди и агрегати електрод-електролит за горивни елементи [1]. Освен IES, за напасването на експерименталните U(i) криви могат да се използват полуемпирични подходи, основани на опростени математически модели [2].

Импедансът на горивния елемент може да бъде разделен на електроден импеданс и съпротивление на електролита чрез промяна на работните условия на горивния елемент и симулиране на измерената EIS с подходяща еквивалентна схема. Като се интегрират отделните елементи на импеданса в токовата област, може да се пресметнат отделните свръхнапрежения в горивния елемент и падовете на напрежение да се припишат на различните процеси. При триелектродна конфигурация на клетката със сравнителен електрод, съответното свръхнапрежение може да бъде определено директно. Моделът на порист електрод на Göhr [3] е използван за оценка на измерените импедансни спектри. Моделът на порист електрод включва различни приноси към импеданса като импедансите на граничните повърхности порист слой/пора, порист слой/електролит и порист слой/обемен материал, импедансът на самия порист слой и импедансът на запълнената с електролит пора

Bulgarian Chemical Communications, Volume 44, Number 4 (pp. 383 – 388) 2012

Selected problems of the analysis of impedance and transfer function spectra: a revue paper

P. Zoltowski

Institute of Physical Chemistry of Polish Academy of Sciences, ul. Kasprzaka 44/50, 01224 Warsaw (Poland)

Received February 20, 2012, accepted February 20, 2012

Experimental impedance spectrum (IS), or, more generally, a transfer functions spectrum (TFS) of a system, and especially sets of spectra measured at various values of the system variables provides a wealth of information about the system and the processes taking place there. However, the knowledge of this information in concepts of physical chemistry requires the application of special procedures in the spectra analysis.

In this paper, selected major issues associated with the reliability of TFSs and of their analysis procedures, mainly based on personal experience of the author of this article, are reminded. Mainly, these issues are: problems arising from the fact that actual systems imperfectly meet the requirements for the measurement of TFS (e.g. linearity), the initial visual analysis of TFS, the principles of modelling and the discussion of different types of models (the latter for ISs), and know-how of the fitting of a selected model to the given TFS and criteria of the fit goodness.

Key words: Impedance spectra, Transfer function spectra, Spectra quality, Modeling,Fittings

INTRODUCTION

The transfer functions (TFs), *H*'s, are ratios of a chosen response of a linear system being close to steady state to the perturbing signal (more generally, ratio of generalised force and resulting displacement) or vice versa, or else ratios of two chosen responses of such a system. *H*'s are vector quantities, and they are dependent on the frequency of the signal [1–3]. In a frequency range, H_k is described by its spectrum (TFS), which can be presented as a 3-column matrix where in the first and next columns the successive frequencies and quantities describing the corresponding vector (e.g. in rectangular coordinates, its real and imaginary components) are given, respectively.

H_k is immittance, X_k, in a specific case when: 1/ the signal and response are electric potential, *E*, and current, *I*, and 2/ the system is one-port. Main forms of *X* are impedance, *Z*, and admittance, *Y*, defined as follows, respectively:

$$Z = \delta E / \delta I \quad (1)$$

$$Y = Z^{-1} = \delta I / \delta E \quad (2)$$

where δ denotes small-amplitude function; its presence in these definition is necessary for the general case of nonlinear systems, in order to allow their linearization. For simplicity, below it will be assumed that δ *E* is the signal. In such a case:

$$\delta E = \Delta E \sin(\omega t) \quad (3)$$

$$\delta I = \Delta I \sin(\omega t + \varphi) \quad (4)$$

where Δ, *ω*, *t* and *φ* denote amplitude functions, angular frequency (*ω* = 2π*f*, *f* being frequency in Hz), time and phase shift (angular delay of the response), respectively. In the above equations, Δ's are real functions.

The last two equations can be presented in a more convenient notation:

$$\delta E = \Delta E \exp(st) \quad (5)$$

$$\delta I = \Delta I \exp(st) \quad (6)$$

where Δ*E* and Δ*I* are complex quantities, and *s* denotes imaginary angular frequency (*s* = i*ω*, i being the imaginary unit: i = √–1). For instance, from Eqs. 1, 5 and 6 it follows that:

$$Z = \frac{\Delta E}{\Delta I} \quad (7)$$

Formally, it is unimportant whether IS is measured under control of *E* or *I*. However, from the physico-chemical point of view it can be of real importance. For instance, for passivating metal electrodes the dependence of *I* on *E* is univocal, but the opposite dependence is multi-valued (in fact, the passive state is not a steady state in the thermodynamic sense). However, the most important argument for using the *E* signals is that, in general, *E* directly controls the chemical potentials of main reactants.

* To whom all correspondence should be sent:
E-mail: zoltowski1@o2.pl

© 2012 Bulgarian Academy of Sciences, Union of Chemists in Bulgaria

An experimental immittance spectrum (IS), and especially a set of ISs measured at various values of system variables (e.g. composition of specimen or surroundings, *E*, temperature etc.), can provide a wealth of information on the system under study and the processes taking place there [4, 5]. However, the knowledge of this information in physico-chemical concepts requires the application in spectra analysis of special procedures [6]. The above applies to TFSs, too.

Recently, several monographs on immittance spectroscopy (traditionally called "impedance spectroscopy"), including to some extend also the transfer function spectroscopy, have been published [7–9]. However, the practical problems of applying this method and the know-know of the spectra analysis are treated there a little cursorily.

The aim of the present paper is to remind some important issues related with the reliability of experimental TFSs and procedures of their analysis, mainly basing on the personal experience of the author of the paper. That will be performed for the most part on the example of ISs, as being best recognised.

PROBLEMS RELATED WITH THE LINEARITY AND NUMBER OF PORTS OF AN ACTUAL SYSTEM

As *X* is a quantity characterising a linear system, the ratio of the two Δ functions in Eqs. 3 and 4 cannot depend on Δ of the signal. Otherwise, the measured IS will be distorted by systematic errors [6]. Obviously, for TFS a similar requirement is in force.

In electrodics, typically the 3-electrode measurement cell is used. In such a case, the system under study consists of the working electrode (WE) plus the counter and reference electrodes, and electrolytic solution in between; hence, actually it is not a one-port system. In order to fulfil the respective requirement, the cell must be designed in a way allowing for ascribing the measured *X* only to WE itself. Otherwise, the measured IS will be distorted by systematic errors [6].

INITIAL INSPECTION OF INDIVIDUAL EXPERIMENTAL IMMITTANCE SPECTRA

Prior to beginning the first step of analysis of an experimental IS, i.e. a trial of modelling of the system characterized by this IS, the so-called „wild points", where at individual *f*'s IS is contaminated by exceptionally large noise, should be eliminated. These points can be noticed when IS in question is

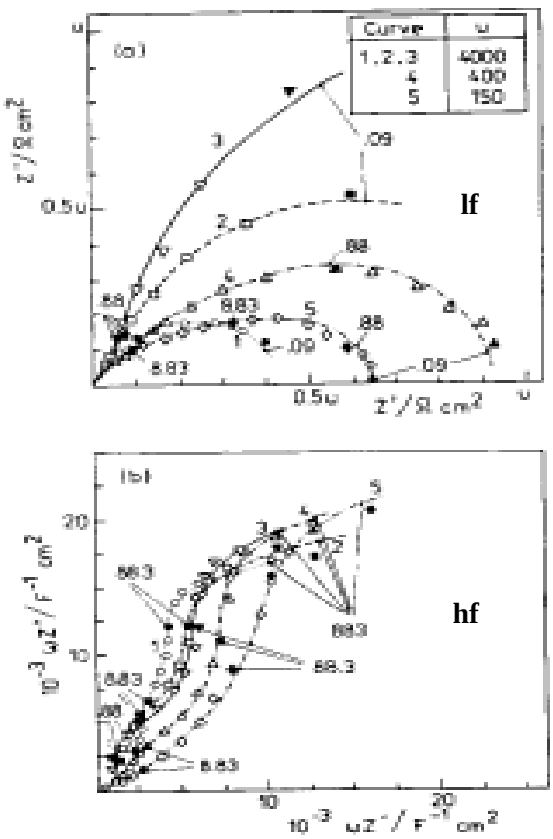

Fig. 1. Example of plots of a set of immittance spectra measured for the same system at several values of some system variable, in various coordinates: (a) and (b) in *Z* and *ωZ* complex plane, respectively. Values close to solid points indicate the respective frequencies in Hz, and lf and hf denote low and high frequency regions, respectively [4]

inspected simultaneously in plots of several different coordinates, e.g. *Z* and *ωZ* (so-called elastance) complex planes (–Im(X_k) vs. Re(X_k)), Bode coordinates (log |*Z*| and *φ* vs. log *f*) etc., because particular coordinates are characterised by differentiated sensitivity or zooming in various frequency ranges. For instance, *Z* and *ωZ* complex planes are especially sensitive in the low (lf) and high frequency (hf) regions, respectively (see Fig. 1). In some coordinates, the wild points will be visible as points breaking the smoothness of the experimental IS curve [4, 6]. By the way, any plot of IS should not be confused with IS itself. For TFS an analogous approach is advisable.

The visual inspection of IS in various plots can help also in the elimination of the frequency range where the given IS seems to be obviously unreliable [4].

MODELS AND THEIR FEATURES

The simplest goal of modelling of an experimental IS is its synthetic description in the whole range of frequencies where it is supposed to be reliable. In other words, the model should provide a computed (theoretical) IS as close to the modelled experimental one as possible, both qualitatively and quantitatively. The model should be possibly simple and of minimal number of parameters, these being independent of frequency. Finally, it should be of a form suitable for estimation of kinetics of processes taking place in the system under study, in further steps of analysis, e.g. a simultaneous analysis of a set of ISs measured at several values of a system variable.

The starting information for formulating a hypothetical model of a selected experimental IS should be drown out from the inspection of its plots in various coordinates. For instance, the plots presented in Fig. 1a (probably two overlapped semicircles in the 1st quadrant a conventional complex plane, i.e. $-\mathrm{Im}H_k$ vs. $\mathrm{Re}H_k$) suggest that in the system in question two RC time constants (τ's) are involved, whilst, in turn, these in Fig. 1b suggest a larger number of time constants, the hf τ resulting from a presence of a constant phase element (CPE) (at hf's apparently straight-line section of a none-zero slope) [4]. It is noteworthy that in ωZ or Y/ω complex planes the curve shapes are richer than in the Z or Y planes, as in the former cases an apparently straight-line section supplements the semicircles or shorter arc sections characteristic for RC electrical circuits (please notice the hf section in Fig. 1b).

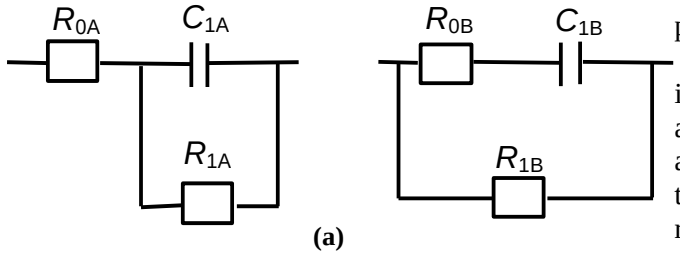

Fig. 2. One time constant RC electrical equivalent circuits used in modelling of an IS characterised in Z conventional complex plane by a one semicircle in the first quadrant.

As models, the so-called electrical equivalent circuits are most frequently used. If in the Z complex plane a given IS is represented by a simple semicircle in the first quadrant, one of the circuits presented in Fig. 2, differing by their topology, can by alternatively applied, as both of them result in an identical IS under condition of proper recalculations of their elements [6,10]. If the system under study is an electrode||electrolytic solution interface, in the case of choice of circuit of Fig. 2a its elements R_{0A}, C_{1A}, and R_{1A} will model the ohmic resistance (mainly of the solution), the interfacial double layer capacitance and the resistance of a simple redox reaction (e.g. $Fe^{+2} \leftrightarrow Fe^{+3} + e$). However, if one will tray to apply this circuit as subcircuit modelling only a Faradaic process with ad-/desorption (e.g. $H_2 \leftrightarrow 2H_{ad} \leftrightarrow 2H^+ + 2e$) taking place at this interface, the physical meaning of its elements will be not so simple [5, 10, 11].

Hence, if the system under study is considered as a "black box" and one know solely its IS, there is no criterion for making the choice of the circuit topology. Accordingly, the topological ambiguity is one of the features of the equivalent circuit models. It results from the fact that the X functions of both above circuits can be transformed to an identical mathematical formula (for further details see below).

Similarly, if in the Z complex plane a given IS is represented by two simple semicircles in the first quadrant, for instance any of the circuits presented in Fig. 3, all of them involving two RC τ's, can be applied, as all of them result in an identical IS under condition of proper recalculations of their elements [4, 6, 10].

The topological ambiguity results from the fact that all equations in Fig. 3 can be transformed to a common formula (for Y it would be quite similar) [4, 6, 8]:

$$Z = \frac{s^2 a_2 + s a_1 + a_0}{s^2 + s b_1 + b_0} \tag{11}$$

where only the definitions of coefficients in particular terms depend on the circuit topology.

However, in spite of the topological ambiguity, in the case of two (or n, $n \geq 2$) RC τ 's circuits another ambiguity appears. It is the solution ambiguity. Namely, for the circuit of a given topology there are n sets of values of its elements resulting in an identical IS [4, 10, 11].

The solution ambiguity results from the fact that, in contrast to the transformation of any formula of the type presented in Fig. 3 (simple reduction to a common denominator) to Eq. 11, the opposite transformation needs the solution of a set of five equations, one of them being a square one. It is similar as the case of solution of a typical square equation, $x^2a + xb + c = 0$. The sole exception is for the circuit of LADDER structure (Fig. 3A), because it corresponds to the case of square equation when the two solutions are identical. In turn, in the case

(A) - LADDER structure (B) - Voigt structure (C) - two subcircuits in parallel

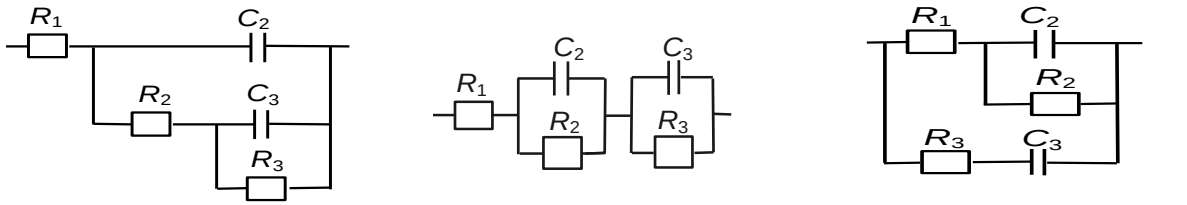

$$Z_{(A)} = R_1 + \cfrac{1}{sC_2 + \cfrac{1}{R_2 + \cfrac{1}{sC_3 + \cfrac{1}{R_3}}}} \quad (8)$$

$$Z_{(B)} = R_1 + \cfrac{1}{\cfrac{1}{R_2} + sC_2} + \cfrac{1}{\cfrac{1}{R_3} + sC_3} \quad (9)$$

$$Z_{(C)} = \cfrac{1}{\cfrac{1}{R_1 + \cfrac{1}{sC_2 + \cfrac{1}{R_2}}} + \cfrac{1}{R_3 + \cfrac{1}{sC_3}}} \quad (10)$$

Fig. 3. Two time constant RC electrical equivalent circuits used in modelling of ISs characterised in *Z* complex plane by two semicircles in the first quadrant, and the respective equations for *Z* in forms closest related with these circuits topology ($Z_R = R$, $Y_C = sC$) [4, 6, 11]

of Voigt structure the two solutions differ only by the subscripts of the two R_jC_j couples in parallel. However, but the case of circuits of LADDER or Voigt structure, the two solutions can result in sets of drastically different values for particular circuit elements [4].

Both above types of ambiguities are important disadvantages of equivalent circuit models. In the literature the topological ambiguity is seldom taken into consideration, whilst the solution ambiguity is quite neglected, in spite that its existence is crucial for the conclusions on the system under study in physico-chemical terms [4, 5, 10, 11].

Free of the above disadvantage is "the generalised mathematical model", formulated by extension of Eq. 11 for modelling the systems characterised by *n* τ's and generalised from *Z* to *X* [10]:

$$X = \frac{\sum_{k=n}^{0} s^k a_k}{s^n + \sum_{k=n-1}^{0} s^k b_k} \quad (12)$$

where *k*'s are integers. Obviously, a_k and b_k coefficients depend also on the detailed meaning of *X* (*Z* or *Y*) [7].

When for the system under study also a CPE should be taken into account (in contrast to e.g. *R* and *C* elements, CPE has two parameters), a model similar to Eq. 12 can be used. However, in such a case both in the numerator and denominator additional terms of *s* at fractional powers (fractal values of *k*) appear, what results in constrains between some coefficients; hence, not all of them are independent [10].

In the general case of *H*'s, i.e. when signals and responses are not restricted to electrical quantities, and the system is not restricted to one-port, relatively simple models, similar to the discussed above for *X*, find no application. Instead, just from the beginning of modelling much more detailed models, taking into account also the system variables, must be used. For instance, one of the various possible TFs of transport of hydrogen (H) throughout a large thin single-phase elastic metal (M) membrane (one-dimensional transport, along the *z* coordinate, $0 < z < L$) in response to a small amplitude H concentration, *c*, signal at the $z = 0$ surface, $\delta c_{z=0}$, close to equilibrium ($c_{0 \le z < L} \approx c_{eq}$) is the ratio of small-amplitude hydrogen flux, δJ, responses at the $z = L$ and $z = 0$ surfaces of the specimen. Under assumptions that 1/ this transport takes place in a self-stressed (as, typically, H atoms expand the original M lattice) M, and 2/ hindrances of the surface processes can be neglected, the following model has been proposed [1]:

$$H_{L/0} = \frac{\Delta J_{z=L}}{\Delta J_{z=0}} \quad (13)$$

$$= \frac{(1 + Ac_{eq})q \sinh^{-1}(qL) - c_{eq}\frac{12A}{q^2L^3}\left[\left(\frac{qL}{2}\right)\coth\left(\frac{qL}{2}\right) - 1\right]}{(1 + Ac_{eq})q \coth(qL) - c_{eq}\frac{12A}{q^2L^3}\left[\left(\frac{qL}{2}\right)\coth\left(\frac{qL}{2}\right) - 1\right]}$$

where $A = \frac{2V^2\overline{Y}}{3RT}$ (14)

$$q = \sqrt{\frac{s}{D\left(1 + Ac_{eq}\right)}} \quad (15)$$

and *V* and $\overline{Y}$ denote partial molar volume of H in M (its not-zero value causes self-stress in M lattice) and bulk elastic modulus of the M-H solid solution, respectively, *R* and *T* gas constant and

temperature, and D diffusion constant of H in the M-H solid.

The main criterion of correctness, or rather usefulness of the chosen hypothetical model for a given TFS is the qualitative and quantitative similarity of its theoretical computed spectrum to the modelled, i.e. experimental TFS. The qualitative similarity is determined by the selected model, while the quantitative similarity is improved in the procedure of fitting of this model by a gradual change of its parameters, i.e. fitting of its theoretical spectrum to the modelled experimental one [6].

ADVICES RELATED TO THE FITTING OF A SELECTED MODEL TO TFS

Typically, the fitting of a selected model to a given experimental TFS is performed by Complex Non-linear Least Squares method (CNLS), by minimising in an iterative procedure the weighted χ^2 function, defined as follows [6]:

$$\chi^2 = \sum_{k=1}^{l} \left[w_k^{'} \left(H_{k_{ex}}^{'} - H_{k_{th}}^{'} \right)^2 + w_k^{''} \left(H_{k_{ex}}^{''} - H_{k_{th}}^{''} \right)^2 \right] \tag{14}$$

where k denotes sequence number of successive experimental points (usually from the highest to the lowest f) up to l ($0 \le k \le l$), H' and H'' are real and imaginary components of H_k, respectively, and the subscripts th and ex denote the theoretical (computed from the model) and experimental quantities, while w' and w'' are respective statistical weights.

As all least squares (NLS) methods, CNLS is based on the assumption that the experimental TFS is contaminated only by random errors, Gaussian in character. Hence, the presence of errors of any other character in the given modelled TFS reduces the reliability of the fitting results.

At a proper convergence of the iterative procedure, χ^2 should gradually decrease down to its so-called "global minimum" value, where the model parameters free (i.e. not fixed at an assumed value) in the given fitting computation attain their so-called "best-fit" estimates. The smaller the value of χ^2, the better is the (statistical) goodness of the fit.

With respect to the choice of weighting system, the assumption that $w' = w'' = 1$ (so-called "unit weights") is worst. If there is no specific premises, the so-called "modulus weights" should be advised [6, 13]:

$$w_k^{'} = w_k^{''} = \frac{1}{\left| H_{k_{ex}} \right|^2} \tag{15}$$

The number of experimental points in the fitted spectrum should be possibly large. On the other hand, the model should be not over-flexible, i.e. the number of its parameters should be possibly small. Both above aspects are taken into account if as the measure of fit goodness, instead of χ^2, the standard deviation of the given fit is considered [6]:

$$\sigma_{\text{fit}} = \sqrt{\frac{\chi^2}{l - nfp}} \tag{16}$$

where nfp denotes the number of model parameters being free in the given fitting. Hence, σ_{fit} can be considered as χ^2 normalised on $(l - nfp)$. Another advantage of σ_{fit}, in comparison with χ^2, is that at the advised weighting system (Eq. 15) it is dimensionless.

The convergence of the CNLS procedure and aptitude for finding the global minimum depends on many factors. For instance, the procedure may stop at a so-called "local minimum", characterised by a large χ^2. In such a case, a change of the staring value of some model's parameter and/or an instantaneous change of its character from free to fixed can be helpful. Both the convergence of procedure and its sensitivity to the starting estimates of parameters is very sensitive to the applied detailed type of model. For instance, the application of the selected equivalent circuit model in its Y form to the given IS recalculated from its Z to Y form may allow for attaining the global minimum, what before those recalculations was not possible. However, the generalised mathematical models (Eq. 12) seem to be by very far the best [12]. Probably, the smaller the degree of nonlinearity of the model with respect to its parameters, the smaller the sensitivity on the aptness of starting estimates and the higher the convergence of the fitting procedure are [6, 12]. On the other hand, the generalised mathematical models are cumbersome to use because the starting estimates of their parameters cannot be proposed directly from the plots of ISs.

Additional important criteria of the choice of optimal model for the given TFS and its fit goodness are the computed relative confidence limits of the best-fit parameter estimates (or individual standard deviations), and magnitude of correlation coefficients of pairs of the best-fit estimates. Very broad confidence limits of a parameter suggest that it is probably redundant in the model. In turn, the magnitude of correlation coefficients of two estimates approaching ± 1 indicates that the respective couple is poorly

independent. However, one should bear in mind that, as in all NLSs, those quantities are computed under the assumption that close to the fitting minimum the model is linear [4, 6].

CONCLUSIONS

Experimental transfer function spectra (TFS) can be considered as reliable only if they were measured at steady state of the system and under experimental conditions assuring its linearity.

An initial inspection of an experimental TFS in plots of various coordinates is necessary, mainly for elimination of "wild points", elimination of the frequency range where the TFS in question seems to be unreliable, and the preliminary estimation of the character and complexity of the system under study.

The character and complexity of the primary proposed hypothetical model for a given TFS should result from the initial inspection of the latter. Its poor fit goodness should result in modification of the previously applied model.

In the case of looking for equivalent electrical circuit models for an immittance spectrum (IS) one should take into account their possible ambiguities: topological and solution.

Free of ambiguities are the generalised mathematical models. Their additional advantages are 1/ high convergence ability in the fitting procedure, and 2/ exceptionally small sensitivity to the selection of staring estimates of the model parameters.

Acknowledgements: *The author would like to express his gratitude to Prof. V. Horvat-Radošević for organising the 9th Internat. Microsymposium on Electrochemical Impedance Analysis at St. Andrew Island in Croatia and encouraging him to give a lecture there, what has finally resulted in the preparation of this article.*

REFERENCES:

1. P. Zoltowski, *Electrochim. Acta* **51,** 1576, (2006).
2. P. Zoltowski, *Electrochim. Acta* **56,** 1498, (2011).
3. P. Zoltowski, *Acta Mater.* **51,** 5489, (2003).
4. P. Zoltowski, *J. Electroanal. Chem*. **260,** 269, (1989).
5. P. Zoltowski, *J. Electroanal. Chem*. **260,** 287, (1989).
6. P. Zoltowski, *Solid State Ionics* **176,** 1979, (2005).
7. A. Lasia, Electrochemical Impedance Spectroscopy and its Applications, in: B.E. Conway, J.O'M. Bockris, R.E. White (Eds.), Modern Aspects of Electrochemistry, vol. 32, Kluwer/Plenum Press, New York, 1999, p. 143.
8. E. Barsoukov, J.R. Macdonald, Impedance Spectroscopy - Theory, Experiment, and Applications, 2nd ed., J. Wiley & Sons, Inc., New Jersey, 2005.
9. M.E. Orazem, B. Tribollet, Electrochemical Impedance Spectroscopy, J. Wiley & Sons, Inc., Hoboken, New Jersey, 2008.
10. P. Zoltowski, *J. Electroanal. Chem*. **275,** 45, (1994).
11. P. Zoltowski, *J. Electroanal. Chem.* **240,** 53, (1988).
12. P. Zoltowski, *J. Electroanal. Chem*. **424,** 173, (1997).
13. P. Zoltowski, *J. Electroanal. Chem*. **178,** 11, (1984).

ИЗБРАНИ ПРОБЛЕМИ НА АНАЛИЗА НА СПЕКТРИТЕ НА ИМПЕДАНСА И ПРЕХОДНАТА ФУНКЦИЯ: ОБЗОР

П. Золтовски

Институт по физикохимия на Полската академия на науките, ул. Каспрзака 44/50, 01224 Варшава, Полша

Постъпила на 20 февруари 2012 г.р приета на 20 февруари 2012 г.

(Резюме)

Експерименталният импедансен спектър (IS), или по-общо, спектърът на преходната функция (TFS) на дадена система и особено множество спектри, снети при различни стойности на системните променливи, дават обилна информация за системата и протичащите в нея процеси. Изразяването на тази информация в термините на физикохимията, обаче, изисква прилагането на специални процедури при анализа на спектрите.

В тази работа се припомнят избрани въпроси, свързани с надеждността на TFS и на процедурите за техния анализ, основани главно на личния опит на автора. Тези въпроси са преди всичко: проблеми, произтичащи от факта, че действителните системи не изпълняват напълно изискванията за измерването на TFS (напр. линейност), първоначалният визуален анализ на TFS, принципите на моделиране и дискусията на различни видове модели (последното за IS), както и ноу-хау за напасването на избрания модел към даден TFS и критерии за качеството на това напасване.

Bulgarian Chemical Communications, Volume 44, Number 4 (pp. 389 – 394) 2012

Impedance investigation of $BaCe_{0.85}Y_{0.15}O_{3-\delta}$ properties for hydrogen conductor in fuel cells

G. Raikova[1]*, M. Krapchanska1, I. Genov[1], G. Caboche[2], L. Combemale[2], A. Thorel[3], A. Chesnaud[3], D. Vladikova[1], Z. Stoynov[1]

[1]*Institute of Electrochemistry and Energy Systems "Acad. E. Budevski" – Bulgarian Academy of Sciences, 10 Acad. G. Bonchev St., Sofia 1113, Bulgaria*

[2]*Institute Carnot de Bourgogne, Université de Bourgogne, BP47870, 21078 Dijon Cedex, France*

[3]*Centre des Matériaux, Mines-ParisTech, BP 87, 91003 Evry Cedex, France*

Received August 10, 2012; accepted October 2, 2012

The influence of the sintering conditions on the electrochemical properties of the proton conducting electrolyte $BaCe_{0.85}Y_{0.15}O_{3-\delta}$ (BCY15) and Ni - based BCY15 cermet anode for application in high temperature proton conducting fuel cell are investigated by electrochemical impedance spectroscopy. The results show that at lower sintering temperatures due to the formation of parasitic Y_2O_3 phase an increase of both the electrolyte and electrode resistances is observed. This effect is strongly reduced by enhancement of the sintering temperature. The obtained BCY15 conductivity ($\sigma = 2.5x10^{-2}$ S/cm at 700°C) is comparable with that of the best proton conducting materials, while the BCY15-Ni cermet (with ASR = 2.5 Ωcm^2 at 700°C) needs further optimization. The results of impedance investigations of BCY15 as proton conducting electrolyte and cermet anode have been applied in development of innovative high temperature dual membrane fuel cell.

Keywords: BCY15, Proton-conducting electrolyte, Anode, Electrochemical impedance spectroscopy

INTRODUCTION

The registration of high temperature proton conductivity in doped Sr and Ba cerates in the late eighties of the last century [1, 2] opened a new niche for optimization of SOFC towards reduction of the operating temperature (500-800°C) due to the higher mobility of protons. High temperature proton conducting fuel cell (PCFC) design eliminates the principal disadvantage of SOFC to form water at the anode side, where it mixes with the fuel, resulting in electromotive force losses. However, PCFC needs the development of an appropriate cathode material and interconnect resistive to the highly corrosive oxygenized water, as well as a counter-flow to sweep water out of the catalytic sites. Acceptor doped perovskites with general formula $AB_{1-x}M_xO_{3-\alpha}$ (A = Ba, Sr; B = Ce, Zr; M = rare earth metal; x - less than the upper limit of solid solution formation) are promising proton conducting systems. Proton conduction increases in the order $BaCeO_3 > SrCeO_3 > SrZrO_3$, while the chemical stability deteriorates in the opposite order [3, 4].

Under humidified hydrogen atmosphere protonic defects are formed by dissociative absorption of water in the presence of oxygen vacancies. Water vapor dissociates into a hydroxide ion which fills an oxide-ion vacancy, and a proton that forms a covalent bond with lattice oxygen, i.e. two proton defects are created stoiciometrically [5], marked according to Kröger-Vink notation as follows:

$$H_2O_{(g)} + V_O^{\bullet\bullet} + O_O^x \rightarrow 2OH_O^{\bullet} \qquad (1)$$

Since the incorporation of water is exothermic [3, 6], the protonic transport is dominating at lower temperatures (under 600°C).

The doping with aliovalent rare earth cations brings to the formation of oxygen vacancies and significantly improves the proton conductivity [3-5, 7]. In the $BaCeO_3$ system, which is considered to be very promising because of the registered high protonic conductivity (0.01 – 0.05 S/cm between 600-800°C [6, 8]), the reaction can be described as:

$$2Ce_{Ce}^x + M_2O_3 + O_O^x \rightarrow 2M'_{Ce} + V_O^{\bullet\bullet} + 2CeO_2 \qquad (2)$$

Proton conductivity in cerates depends on the crystallographic structure, which is a function of temperature and doping concentration. It decreases when transformations to higher symmetry (from orthorhombic to cubic) which bring to equivalent distribution of all oxygen positions and to evenly distributed oxygen ion vacancies take place [3, 7,

9]. In addition to the temperature, gas atmosphere and pressure, including water vapor, is detrimental for proton conductivity.

The disadvantages of SOFC and PCFC connected with the production of water at the electrodes can be avoided in the innovative design of high temperature dual membrane fuel cell, named "IDEAL Cell" after the acronym of a running FP7 project [10]. The "IDEAL Cell" concept [11] is based on a junction between a SOFC cathode/electrolyte part and a PCFC electrolyte/anode part through a mixed oxide ion and proton conducting porous ceramic membrane. Oxygen ions created at the cathode side progress toward the central membrane where they meet the protons created at the anode side, and produce water [12] which is evacuated through the interconnecting porous media. In this way oxygen, hydrogen and water are located in 3 independent chambers (Fig. 1).

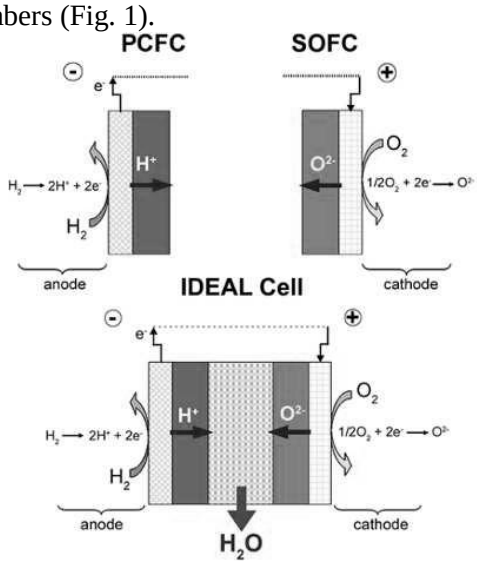

Fig.1. Representation of the PCFC anode/electrolyte couple, the SOFC electrolyte/cathode couple and the IDEAL-Cell concept

This paper presents results for the $BaCe_{0.85}Y_{0.15}O_{3-\delta}$ (BCY15) and Ni-BCY15 cermet conductivities in wet hydrogen. The influence of the different sintering conditions on their electrochemical properties is analyzed by electrochemical impedance spectroscopy for performance optimization in the new dual membrane cell configuration.

EXPERIMENTAL

The BCY15 powders, supplied by Marion Technologies (MT), were fabricated by auto-combustion process starting from metal nitrates and applying urea as reducing agent. Calcinations of the precursor at 1100-1150°C in a carrier gas (helium or argon) for complete CO_2 elimination ensured the production of single phase powder with chemical composition $Ba_{1.04}Ce_{0.82}Y_{0.15}O_{3-\alpha}$, determined by ion coupled plasma analysis with dominating particle size round 200 nm and minor degree of agglomeration.

The BCY15 electrolyte support pellets (diameter/thickness = 20-25/1-1,3 mm) were prepared by cold pressing and sintered in the temperature range from 1100°C to 1450°C for 5 hours at heating rate 300°C h^{-1}.

BCY15/NiO (NOVAMET, HP green NiO-Type A) slurry with composition 28.6 vol.% BCY15 and 71.4 vol.% NiO was deposited by tape-casting and sintered in the temperature range 1100-1350 °C.

For impedance characterization of the BCY15 electrolyte supported Pt/BCY15/Pt symmetrical half cells were prepared. Platinum (Metalor) electrodes were painted and sintered in air following a procedure recommended by the producer.

In order to characterise the changes in the microstructure of the materials, a series of analytical techniques was used: X-Ray Diffraction (XRD) with Energy-dispersive X-ray spectroscopy (EDX), Scanning Electron Microscopy (JEOL JSM 6400F), and Transmission Electron Microscopy (JEOL JEM-2100 TEM) in combination with Ultrathin windowed energy-dispersive X-ray spectrometer (EDS) and Scanning Transmission Electron Microscopy - High Angle Annular Dark Field (STEM - HAADF) on a TECNAL 20F ST microscopy.

The impedance measurements were performed with Solartron 1260 Frequency Response Analyser in a temperature interval of 200 – 700ºC at frequency range from 10 MHz down to 0.1 Hz and density of 5 points/decade. They were done in two modes: potentiostatic and galvanostatic. The half cell measurements were carried out at OCV in working atmosphere wet (3% H_2O) hydrogen.

The impedance data were analyzed by the technique of the Differential Impedance Analysis (DIA) [13, 14]. DIA works with no preliminary working hypotheses, because the information about the model structure is extracted directly from the experimental data. It also identifies frequency dependent behavior, which can be additionally analyzed by the secondary analysis. More information about the secondary DIA can be found in [14, 15]. Before the analysis a calibration procedure for post-experimental elimination of the parasitic components in the impedance diagrams coming from the cell rig was performed [15, 16].

RESULTS AND DISCUSSION

The results from the impedance measurements of dense BCY15 electrolyte (Fig. 2) are generalized in the Arrhenius plots (Fig. 2c). They show that different sintering conditions influence the BCY15 conductivity. The electrolyte sintered at 1300oC has higher resistivity and thus lower conductivity than the electrolyte sintered at 1450oC (Fig. 2).

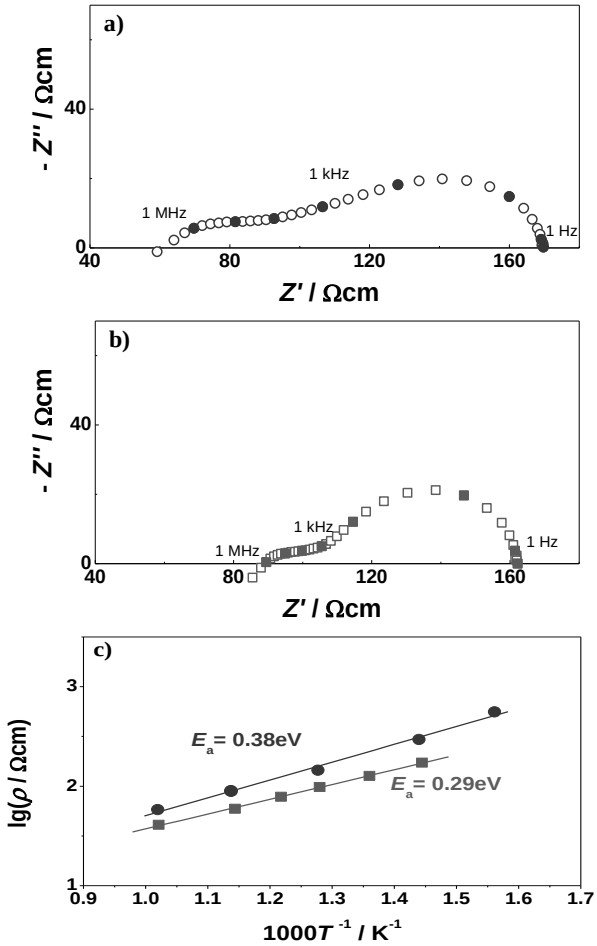

Fig. 2. Complex plane impedance diagrams (a),(b) at 600°C and corresponding Arrhenius plots (c) of Pt/BCY15/Pt sintered at: (•) 1300°C and (■) 1450°C

The change in the conductivity for these samples was explained with observed change in their microstructure. The performed XRD analyses show a presence of parasitic phase (Fig. 3), registered as Y_2O_3 which quantity decreases with the increase of the sintering temperature and thus improves the electrolyte conductivity.

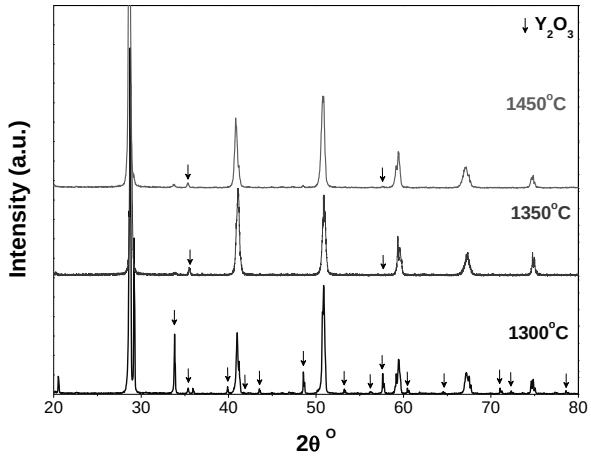

Fig. 3. X-ray diffraction patterns of BCY15 sintered at different temperatures.

Table 1. EDX analysis of dense BCY15 electrolyte

	Ce/Ba	Y/Ba
Theoretical ratio	0.85	0.15
BCY15 electrolyte	0.81	0.15

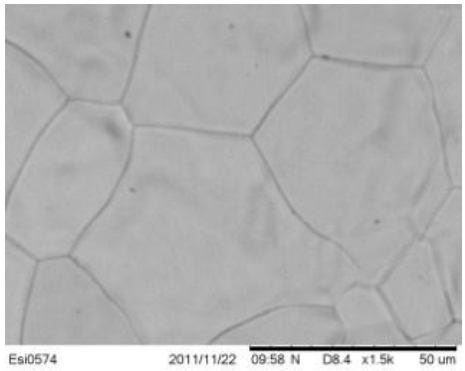

Fig. 4. SEM micrograph of dense BCY15 electrolyte

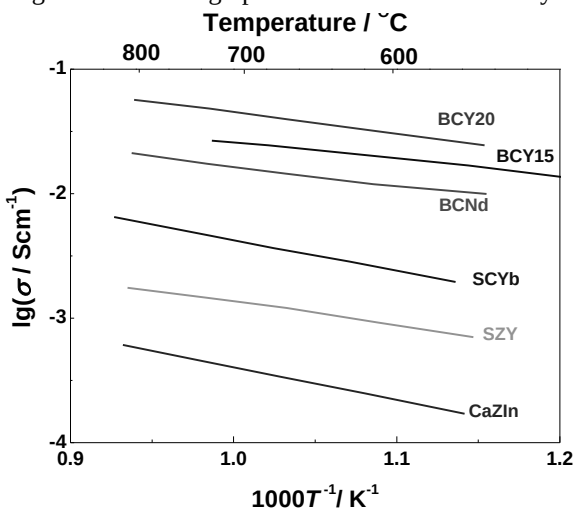

Fig. 5. Comparison of the BCY15 proton conductivity with data from the literature [5]: $BaCe_{0.9}Nd_{0.1}O_{3-\alpha}$ (BCNd); $ScCe_{0.95}Yb_{0.05}O_{3-\alpha}$ (SCYb); $SrZr_{0.95}O_{3-\alpha}$ (SZY); $CaZr_{0.9}In_{0.1}O_{3-\alpha}$ (CaZIn)

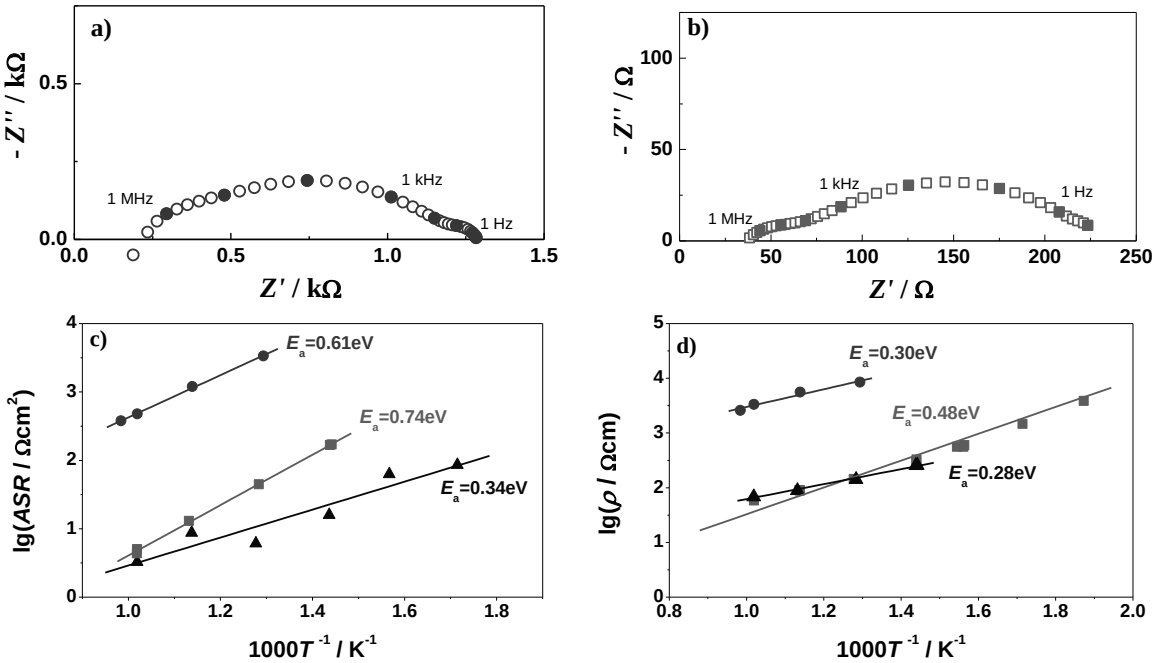

Fig. 6. Complex plane impedance diagrams (a), (b) at 500°C and corresponding Arrhenius plots (c) of the anode polarization obtained from measurements of symmetrical half cell BCY15-Ni/BCY15/BCY15-Ni. The electrolyte support is sintered at 1450°C/4 h; (●) – cermet sintered at 1100°C/2h; (■) – cermet sintered at 1350°C/2h; (▲) comparative measurement of Pt/BCY15/Pt

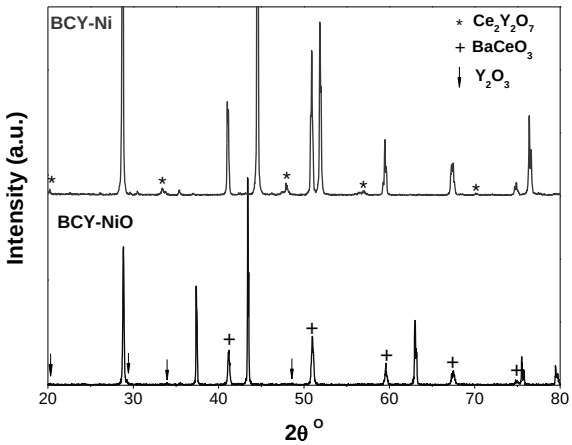

Fig. 7. X-ray diffraction patterns of BCY-NiO cermet layers sintered at 1100°C/5h (before reduction) and 1450°C/5h (after reduction)

The optimized in this way microstructure (grain size 35-50 μm, Fig. 4) and its chemical analysis (Table 1) makes BCY15 dense electrolyte conductivity comparable with that of the best proton conducting materials (Fig. 5).

Table 1. EDX analysis of dense BCY15 electrolyte

	Ce/Ba	Y/Ba
Theoretical ratio	0.85	0.15
BCY15 electrolyte	0.81	0.15

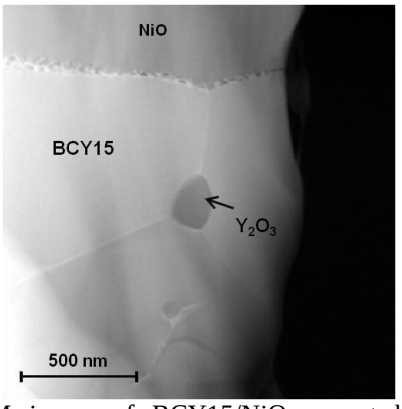

Fig. 8. SEM image of BCY15/NiO cermet before reduction

In order to fulfil its role, the anode composition (BCY15/NiO) should lead to the best compromise between a good mechanical compatibility with the BCY15 electrolyte(already optimized) and a good ionic and electronic conductivity, keeping a highly open porous microstructure (for gas convection) and avoiding eventual reactivity within the composite. The first impedance measurements on electrolyte supported BCY15-Ni/BCY15/BCY15-Ni half cell showed a big increase of the anode polarization and also of the electrolyte resistivity with respect to the results obtained from metal electrodes (Fig. 6). Absence of good lateral electrode conductivity was also registered.

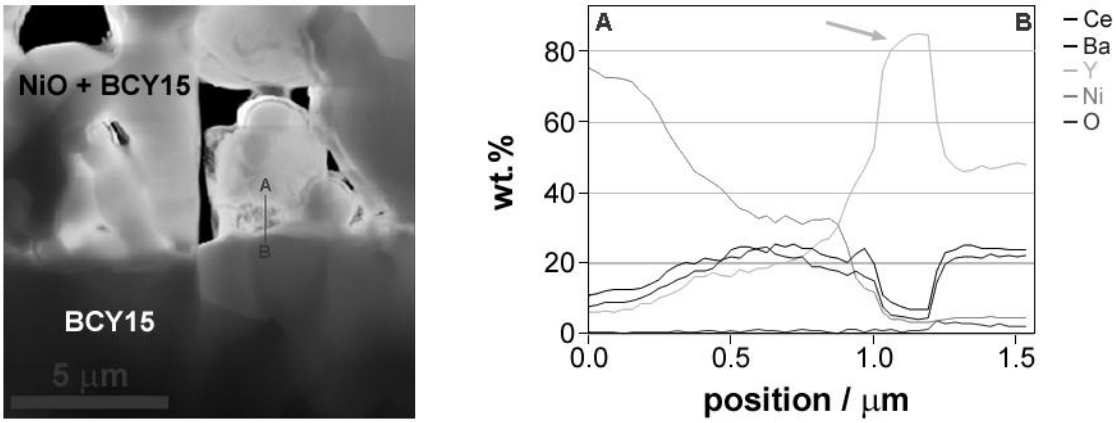

Fig. 9. STEM-HAADF image of the anode-electrolyte interface (left side image); linear composition profile (in wt%) across the interface in direction A→B (right side image)

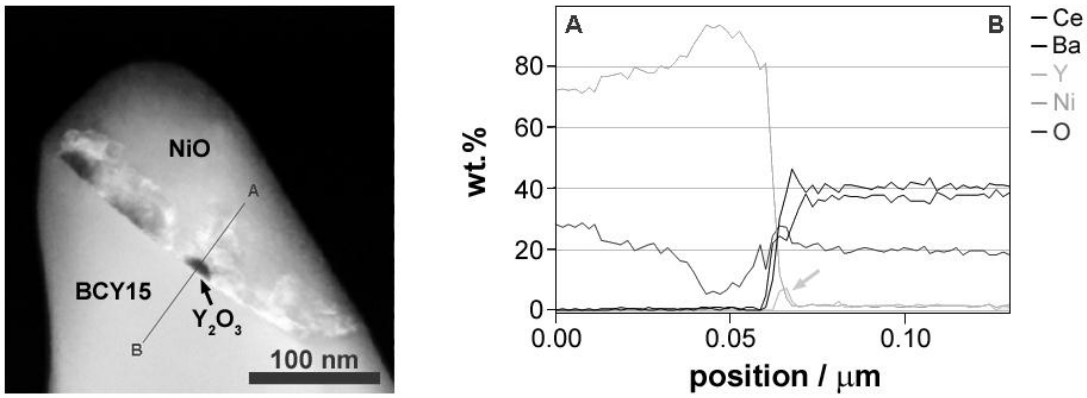

Fig. 10. STEM-HAADF image of the BCY15/NiO interface with Y_2O_3 inclusions (a); linear composition profile (in wt %) across the interface in direction A→B (b)

The microstructural analysis on those anodes (sintered at relatively low temperature - 1100°C for high porosity) indicates that cermet material is not a single-phased system. The appearance of additional peaks reveals the presence of Y_2O_3 and $BaCeO_3$ (Fig. 7).a single-phased system. The appearance of additional peaks reveals the presence of Y2O3 and BaCeO3 (Fig. 7).

Thorough SEM/STEM analytical experiments of the anode BCY15/NiO demonstrated an extensive precipitation of Y_2O_3 particles along the NiO/BCY15 and the anode/BCY15 electrolyte interface. It strongly decreases towards the depth of the electrolyte (Figs. 8, 9, 10).

Thus an efficient electrical barrier between the protonic (BCY) and the electronic (Ni) phases is produced. This phenomenon may be initiated by slight diffusion of Ba toward NiO. As it was expected, the increase of the sintering temperature decreases the quantity of parasitic phases and improves the cermet conductivity (Fig. 6).

After sintering at 1350°C for 2 hours and a reduction treatment at 700°C for 5 hours (in 5 vol.% H_2/95 vol. % Ar atmosphere) an improvement of both the ASR and the resistivity of the electrolyte was observed (Fig. 6). The obtained results for BCY15 electrolyte are already in the range of the values from the measurements of the standard Pt/BCY15/Pt cell (Fig.6d). The performed X-ray diffraction (XRD) shows that NiO is fully reduced to metallic Ni, and the system is stabilized towards segregation of Y2O3 and BaCeO3. In addition small quantity of a new cerium yttrium oxide phase is registered (Fig. 7). Its influence on the electrochemical behavior of the anode is not so strong; however the cermet needs additional optimization.

4. CONCLUSIONS

The results obtained from the impedance measurements of BCY15 for anode compartment (anode/electrolyte) in a PCFC and in a dual membrane fuel cell show that the sintering conditions are an important optimization parameter for both the electrolyte BCY15 and electrode BCY15-Ni cermet. Although the fabricated anode-

electrolyte assembly has acceptable performance ($\sigma_{(BCY15)}$ = 2.5 x 10^{-2} S/cm and $ASR_{(BCY15-Ni)}$ = 2.5 Ωcm^2 at 700°C) further improvement of the cermet's electrochemical behavior is required. It is expected that appropriate combination of the volume ratio BCY15/NiO and sintering temperature will ensure anodes with good mixed conductivity, sufficient porosity and lack of parasitic phases.

Acknowledgements: *The research leading to these results has received funding from the European Community's Seventh Framework Programme (FP7/2007-2013) under grant agreement No 213389. G. Raikova acknowledges also "Science and Business" BG051PO001/3.3-05-001 for the financial support that made possible the publication of this paper.*

REFERENCES

1. H. Iwahara, H. Uchida and K. Ogaki, *J. Electrochem. Soc*. **135,** 529, (1988).
2. H. Iwahara, *Solid State Ionics* **168**, 299, (2004).
3. L. Malavasi, C.A.J. Fisher and M.S. Islam, *Chem. Soc. Rev*. **39**, 4370, (2010).
4. T. Ishihara, N.M. Sammes and O. Yamamoto in *High Temperature Solid Oxide Fuel Cells: Fundamentals, Design and Applications*, edited by S.C. Singhal and K. Kendall, (Elsevier, 2003) pp. 83-117.
5. H. Iwahara, *Solid State Ionics* **86-88**, 9, (1996).
6. A. Bassano**,** V. Buscaglia**,** M. Viviani**,** M. Bassoli**,** M-T . Buscaglia**,** M. Sennour**,** A. Thorel and P. Nanni, *Solid State Ionics* **180**, 168, (2009).
7. N. Bonanos, K.S. Knight and B. Ellis, *Solid State Ionics* **79**, 161, (1955).
8. K.D. Kreuer, *Annu. Rev. Mater. Res*. **33**, 333, (2003).
9. K.S Knight, *Solid State Ionics* **127**, 43, (2000).
10. A.S. Thorel, A. Chesnaud, M. Viviani, A. Barbucci, S. Presto, P. Piccardo, Z. Ilhan, D. E. Vladikova and Z. Stoynov, in Solid Oxide Fuel Cells 11 (SOFCXI), edited by S.C. Singhal, and H. Yokokawa, (The Electrochemical Society Proceedings Series **25**, ECS Transactions, 2009), pp.753–762.
11. Patent N° 0550696000, March 17th, 2005, Cellule de pile a combustible haute temperature a conduction mixte anionique et protonique ; International extension in 2006 Issue 2, Pennington, NJ 753 (2009).
12. D. Vladikova, Z. Stoynov, G. Raikova, A. Thorel, A. Chesnaud, J. Abreu, M. Viviani, A. Barbucci, S. Presto and P. Carpanese, *Electrochim. Acta* **56,** 7955, (2011).
13. Z. Stoynov, D. Vladikova, Differential Impedense Analysis, Marin Drinov Academic Publishing House, Sofia, 2005.
14. Z. Stoynov and D. Vladikova, in Encyclopedia of Electrochemical Power Sources, edited by U. Garche (Elsevier, 2009) pp. 632-642.
15. D. Vladikova, Z. Stoynov, *J. Electroanal. Chem.* **572,** 377, (2004).
16. D. Vladikova, Z. Stoynov, G. Raikova, in Z. Stoynov, D. Vladikova (Eds.), Portable and Emergency Energy Sources, Marin Drinov Academic Publishing House, Sofia, 2006, pp. 383-410.

ИМПЕДАНСНО ИЗСЛЕДВАНЕ НА СВОЙСТВАТА НА $BaCe_{0.85}Y_{0.15}O_{3-\delta}$ ЗА ВОДОРОДЕН ПРОВОДНИК В ГОРИВНИ КЛЕТКИ

Г. Райкова[1*], М. Кръпчанска[1], И. Генов[1], Ж. Кабоч[2], Л. Комбемел[2], А. Торел[3], А. Чесно[3], Д. Владикова[1], З. Стойнов[1]

[1]*Институт по електрохимия и енергийни системи „Акад. Е. Будевски", Българска академия на науките, ул. „Акад. Г. Бончев" бл. 10, 1113 София, България*

[2] *Институт Карно, Бургундски Университет, BP47870, 21078 Дижон, Франция*

[3] *Център по материалознание, Мини-ПариТех, BP 87, 91 003 Еври, Франция*

Постъпила на 10 август, 2012 г.; приета на 2 октомври, 2010 г.

(Резюме)

Чрез електрохимична импедансна спектроскопия е изследвано влиянието на условията на синтеруване върху електрохимичните свойствата на протон- проводящия електролит $BaCe_{0.85}Y_{0.15}O_{2-\delta}$ (BCY15), както и на Ni - базиран BCY15 кермет с приложение като анод във високо-температурна протон проводяща горивна клетка. Резултатите показват, че при по-ниски температури на синтеруване, образуването на паразитна Y_2O_3 фаза води до увеличеване както на съпротивлението на електролита, така и на това на електрода. Този ефект намалява с повишаване температурата на синтеруване. Получената стойност за проводимостта на BCY15 ($\sigma = 2.5\times10^{-2}$ S/см при 700ºC) е сравнима с тази на най-добрите протон-проведящи материали, докато кермета BCY15-Ni (с ASR = 2.5 Ωcm^2 700ºC) се нуждае от допълнителна оптимизация. Проведеното импедансно изследване на протон-проводящия BCY15 като електролит и като кермет за анод е използвано в реализацията на иновативен дизайн на високо температурна двойно-мембранна горивна клетка.

Bulgarian Chemical Communications, Volume 44, Number 3 (pp. 395 – 398) 2012

Electrochemical analysis of solid oxide electrolytes for intermediate temperature fuel cell

A.M. Ionascu [1*], G. Raikova [2], E. Mladenova [2], I. Mercioniu[3]

[1] *University Politehnica of Bucharest, Department of Electrical Engineering, 313 Splaiul Independentei Str., Bucharest, Romania*

[2]*Institute of Electrochemistry and Energy Sources, Bulgarian Academy of Sciences, Acad. G. Bonchev Str., bl.10,1113 Sofia, Bulgaria*

3 National Institute of Materials Physics, 105 bis Atomistilor Str., Magurele, Bucharest, Romania

Received February 20, 2012, revised October 29, 2012

In this paper the electrochemical analysis of new materials, designed to be used as solid electrolytes for intermediate temperature fuel cells (IT-SOFC) was made. The materials are two different composites based on ceria 10YDC + (10%) 150ppm YA and 10ScDC + (10%) 150ppm YA, obtained by sol-gel method and sintered at temperature of 1500 ^{0}C. The electrochemical investigation was performed by Electrochemical Impedance Spectroscopy technique. According of these analyses the composite 10YDC + (10%) 150ppm YA presents better conductivity than 10ScDC + (10%) 150ppm YA. These results were related with morphological investigation, realized by SEM.

Keywords*:* Electrochemical Impedance Spectroscopy, SEM, Y_2O_3, CeO_2, α–Al_2O_3, Sc_2O_3, solid electrolyte, intermediate temperature fuel cells.

INTRODUCTION

In recent years new technologies for production of cheaper and cleaner energy were developed. Among them are also the intermediate temperature fuel cells (IT-SOFC). These cells are constructed of two electrodes (anode and cathode) and solid electrolyte and they operate in the temperature range (600 – 650 ºC) [1].

The problems which designers face regarding these cells are due to the choice of electrolyte, because the electrodes design and the materials used in their production depend on the electrolyte [2]. The electrolyte of these cells must to have the average grain diameter less than 1 μm, absence of porosity, electrical and ionic conductivity as large as possible at the operating cell temperature [1]. Among the electrolytes used for IT-SOFC, the most studied are those based on ceria (CeO_2). They are doped with yttrium trioxide (Y_2O_3), scandium trioxide (Sc_2O_3), Y_2O_3 + Sc_2O_3, gadolinium (Gd), samaria (Sm), etc. [2].

Yttria doped ceria (YDC) with a cubic structure, containing 10 mol % Yttria, is an attractive ceramic used as electrolyte or matrix for electrolyte in IT-SOFC [3]. For obtain a better structure in correlation with good material properties, the introduction of a second phase with good electro-mechanical properties will be beneficiary. Given the properties of low Yttrium doped α-Al_2O_3, mechanical properties, chemical inertness and resistance, high temperature corrosion resistance, good conductivity, high thermal conductivity, in these paper two new electrolytes for IT-SOFC are proposed.

This paper presents a study of the conductivity of two new ceramic composites, based on the combination between the doped ceria and low doped alumina, [(90 %) 10 Y_2O_3: CeO_2 + (10 %) (150 ppm) Y_2O_3: α – Al_2O_3] and [(90 %) 10 Sc_2O_3: CeO_2 + (10 %) (150 ppm) Y_2O_3: α – Al_2O_3], both used as solid electrolyte for IT-SOFC.

Since the electrochemical impedance spectroscopy became a very useful and perspective method for investigating the performance of electrolyte materials, the investigations are based on impedance measurements.

The final results are correlated with morphological investigation realized by scanning electron microscopy (SEM).

* To whom all correspondence should be sent:
E-mail: amionascu@elmat.pub.ro

© 2012 Bulgarian Academy of Sciences, Union of Chemists in Bulgaria

EXPERIMENTS

Materials

Two types of ceramic composite samples based on ceria, denoted by A and B, were used for electrochemical investigation.

The sample A is composed of (10 mol %) Y_2O_3 doped CeO_2 (denoted 10 YDC) and (10 %) (150 ppm) Y_2O_3 doped α – Al_2O_3 (denoted 150 ppm YA).

The sample B is composed of (10 mol %) Sc_2O_3 doped CeO_2 (denoted 10 ScDC) and (10 %) (150 ppm) Y_2O_3 doped α – Al_2O_3 (denoted 150 ppm YA).

Both samples were made by mechanical mixing of two nanopowders, 10 YDC (90 %) and 150 ppm YA (10 %) respectively 10 ScDC (90 %) and 150 ppm YA (10 %), synthesized by sol-gel method. The mixtures (for both samples A and B) were homogenized mechanically, compacted at 3000 kgf and sintered at 1500 ºC for 2 h [4].

The samples present a disk shapes with a diameter of 10 mm and a thickness of 1.2 mm (Fig. 1a).

a. b.

Fig. 1. Samples used for electrochemical investigation: (a) sample before the deposition of the electrodes; (b) sample with silver electrodes.

For electrochemical measurements symmetrical electrolyte supported half cells with Ag electrodes were performed (Fig. 1b). The silver paste for electrodes deposition was painted on both sides of the samples.

Equipments

The impedance measurements were performed with Solartron 1260 Frequency Response Analyser in a temperature interval of 200 – 700ºC at frequency range from 10 MHz down to 0.1 Hz and density of 5 points/decade. For lower temperatures, where the sample resistance is in the MΩ-range, the studies were carried at amplitude 200 mV, which was reduced to 50 mV above 400ºC.

Morphological characterization (grain shape, average grain diameter) of the samples were performed by scanning electron microscopy (SEM). To obtain the SEM images, a scanning electron microscope type TESCAN LYRA 3 XMU was used.

RESULTS AND DISCUSSION

The characterization of the electrolytes behavior was made with Voigt's model structure containing two time constants, i.e. two meshes with *R* and *C* in parallel connection which correspond to the bulk and grain boundary behavior (Fig. 2) [5-8]. Impedance diagrams of samples A and B are shown in Figure 3.

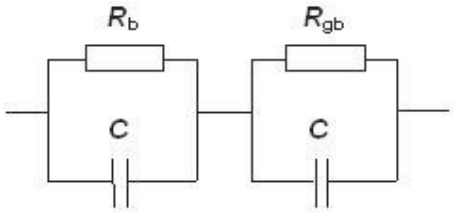

Fig. 2. Equivalent circuit of a two time constant Voigt's model structure.

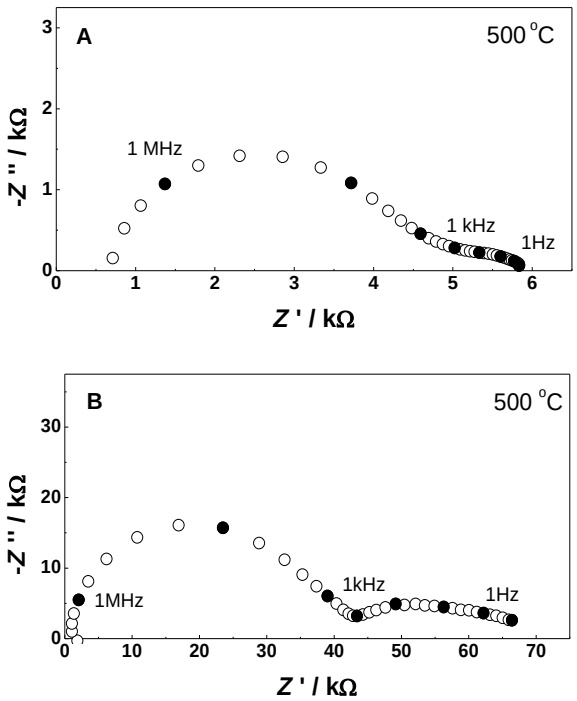

Fig. 3. Complex plane impedance diagrams of samples A and B at 500 ^{0}C temperature.

For the both samples the resistivity is dominated by the grain boundaries. The big arc in the impedance diagrams is an indication for the formation of non-clean grain boundaries. A

possible explanation of these results could be due to the presence of two different phases in the electrolytes with different microstructures (different grains, average diameter, orientation, porosity etc), which determine their higher resistivity.

The resistance values obtained from the impedance measurements for different temperatures were used for the construction of the Arrhenius plots (Fig. 4):

$$\rho = A / T \exp(-E_a / kT) \quad (1)$$

where ρ is the resistivity, A is the pre-exponential term, k is the Boltzmann constant, E_a is the activation energy and T is the temperature in K. The Arrhenius plots for both samples A and B are linear (Fig. 4) and their slopes give the corresponding activation energies Ea (Table 1).

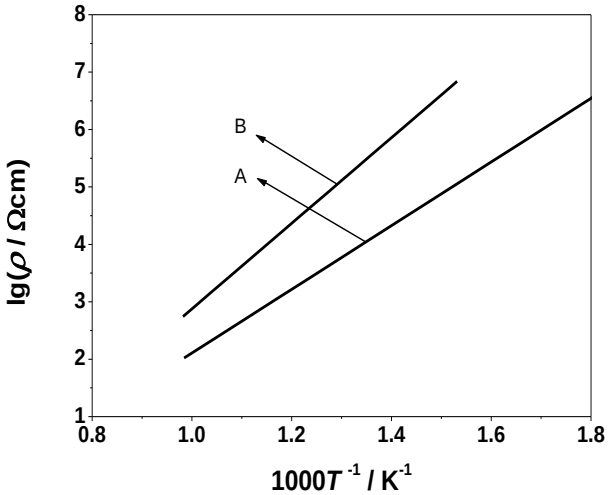

Fig. 4. Arrhenius plots for samples A and B.

Table 1. The conductivities and activation energies of samples A and B.

	σ [S/cm]		E_a [eV]
	600 ^{0}C	**700 ^{0}C**	
Sample A	$1.41 \cdot 10^{-3}$	$3.16 \cdot 10^{-3}$	1.09
Sample B	$1.52 \cdot 10^{-4}$	$6.35 \cdot 10^{-3}$	1.48

A significant difference in the conductivity related to the different dopants is observed. The sample A has lower resistivity and higher conductivity than sample B. On the other hand the values of resistivity decrease with temperature. This is due to the intensification of diffusion of ions which participate in conduction process. However at working temperature of IT-SOFC fuel cells, the difference between the values of conductivity is 13%. From this point of view the sample A present a good value of conductivity ($1.41 \cdot 10^{-3}$ S/cm) at 600 ºC in comparison with the sample B. The values of activation energy and conductivity at 600 ºC and 700 ºC temperatures are tabulated in table 1.

These results are in concordance with the morphological investigation realized by SEM (Figs. 5, 6).

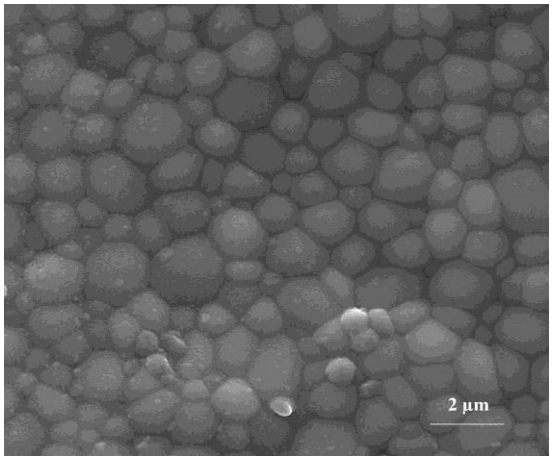

Fig. 5. Scanning electron microscopy for sample A.

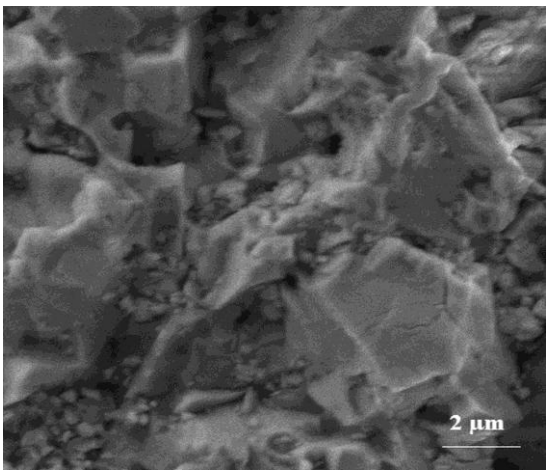

Fig. 6. Scanning electron microscopy for sample B.

For sample A, the 10YDC area contains the spherical grains with the average value of grains diameter 1.18 µm and 3.18 µm for 150 ppm YA area, while for sample B, 10 ScDC area has polyhedral grains with the average grains diameter 1.57 µm and 2.32 µm for 150 ppm YA area.

This investigations show that the microstructure of sample A is much better (small grains, more compact areas, is not so porous) than that of sample B. These results are in concordance with the electrochemical behavior.

The electrochemical behavior of these new electrolytes can be optimized further by using the strong influence of the small variation of doped alumina.

CONCLUSIONS

The results obtained from the electrochemical analysis of the new electrolytes for IT-SOFC, show that, the electrolyte A has a better values (lower resistivity and higher conductivity, $\sigma = 1.41 \cdot 10^{-3}$ S/cm at 600 ^{0}C) than electrolyte B. At working temperatures of IT-SOFC fuel cell the registered difference is about 13% between the values of the conductivity. The electrochemical results are in concordance with the morphological investigation.

Therefore the electrolyte A will be used for future studies. To be used as a solid electrolyte for IT-SOFC, this material requires investigation from point of view of mechanical properties.

Acknowledgment: *The authors would like to thank Prof. Daria Vladikova and Prof. Zdravko Stoynov for assistance and support for the impedance measurements and Dr. Nicoleta Popescu – Pogrion for useful advices.*

A.M. Ionascu acknowledges also the Sectoral Operational Programme Human Resources Development 2007-2013 of the Romanian Ministry of Labour, Family and Social Protection through the Financial Agreement POSDRU/88/1.5/S/60203, who funded her work.

REFERENCES

1. G. Pasciak, K. Prociow,W. Mielkarek, B. Gornicka, B. Mazurek, Solid electrolytes for gas sensors and fuel cells applications, *Journal of the European Ceramic Society* **21**, 1867, (2001).
2. H.He, Y. Huang, J. Regal, M. Boaro, G. M. Vohs, R. J. Gorte, Low temperature fabrication of oxide composites for solid-oxide fuel cells, *J. Am. Ceram. Soc*. **87**, 331, (2004).
3. M. Dudek, J.Molenda, Ceria-ytria-based solid electrolytes intermediate temperature solid oxide fuel cell, *Materials Science-Poland* **24**, 45, (2006).
4. A. M. Vlaicu, I. Mercioniu, B. S. Vasile, C. C. Negrila, C. Logofatu, N. C. Cretu, P. Nita, N. Popescu-Pogrion, Structural and chemical properties of cerium-magnetoplumbite in cerium based IT-SOFC compounds, *Optoelectronics and Advanced Materials-Rapid Communications* **5**, 143, (2011).
5. Z. Stoynov and D. Vladikova, in: Impedance Spectroscopy of Electrochemical Power Sources, *Encyclopedia of Electrochemical Power Sources*, edited by U. Garche, Elsevier, 2009, pp.632-642.
6. Z. Stoynov, D. Vladkova, *Differential Impedance Analysis*, Marin Drinov Academic Publishig House, Sofia, (2005).
7. D. Vladikova, Z. Stoynov, G. Raikova, A. Thorel, A. Chesnaud, J. Abreu, M. Viviani, A. Barbucci, S. Presto and P. Carpanese, Impedance Spectroscopy Studies of Dual Membrane Fuel Cell, *Electrochim. Acta* **56,** 7955, (2011).
8. G. Raikova, D. Vladikova, Z. Stoynov, Differential impedance analysis of the cathode compartment in dual membrane fuel cell, *Bulgarian Chemical Communications* **43**, 134, (2011).

ЕЛЕКТРОХИМИЧЕН АНАЛИЗ НА ТВЪРДО-ОКСИДНИ ЕЛЕКТРОЛИТНИ МАТЕРИАЛИ ЗА ГОРИВНИ КЛЕТКИ, ФУНКЦИОНИРАЩИ ПРИ СРЕДНИ ТЕМПЕРАТУРИ

А.М. Йонашку[1], Г. Райкова[2], Е. Младенова[2], И. Меркьониу[3]

[1]*Политехнически Университет Букорещ, Департамент по електро-инженерство, ул. Сплаиул индепенденей 313, Букорещ, Румъния*

[2]*Институт по електрохимия и енергийни системи-Българска академия на науките, ул. Акад. Г. Бончев, бл.10, София, България*

[3] *Национален институт по физика на материалите, ул. Атомистилор 105, Магуреле, Букорещ, Румъния*

Постъпила на 20 февруари 2012 г., преработена на 29 октомври 2012 г.

(Резюме)

Настоящата статия представя резултати от електрохимичното изследване на нови материали, предназначени да бъдат използвани като твърди електролити за горивни клетки, функциониращи при средни температури (IT-SOFC). Електролитите са съставени от два различни композитни материала, базирани на серий 10YDC + (10%) 150ppm YA и 10ScDC + (10%) 150ppm YA, получени чрез зол-гел метода и синтезирани при температура 1500°C. Материалите са анализирани с техниката на Електрохимичната импедансна спектроскопия. Според анализа композитът 10YDC + (10%) 150ppm YA показва по-добра проводимост от 10ScDC + (10%) 150ppm YA. Тези резултати са свързани с данните от морфологичният им анализ, реализиран чрез СЕМ изследване на материалите.

Bulgarian Chemical Communications, Volume 44, Number 4 (pp. 399 – 406) 2012

Adsorption of o-hydroxybenzoic acid on polymers in supercritical carbon dioxide medium: experimental and modeling

S. Diankov[1]*, P. Subra-Paternault[2], I. Hinkov[1], I. Pentchev[1]

[1] *University of Chemical Technology and Metallurgy – Sofia, Bulgaria*
[2] *Université de Bordeaux, France*

Received: October 17, 2010; accepted: April 26, 2011

In this work we present an experimental set-up used for semi-continuous impregnation per adsorption process of polymers with an organic model component (o-hydroxybenzoic acid – o-HBA) using supercritical CO_2 as solvent and impregnating medium. The aim is to study the effect of the supercritical solvent flow-rate, the pressure and the polymer support on the breakthrough volume and the adsorbed quantity. The regular sampling of the supercritical phase is analyzed by High Performance Liquid Chromatography. It is found that the uptake increases with the pressure and decreases with the supercritical solvent flow-rate. In addition, a 1D model with local equilibrium is developed. The model fits well to the breakthrough curves. The numerically obtained values are in good agreement with the experimental results.

Key words: supercritical carbon dioxide, impregnation, modeling.

INTRODUCTION

During the past several decades, processes carried out in supercritical (SC) media have been widely applied in the chemistry and processing of polymers. The impregnation assisted by SC solvents reveals certain advantages compared to traditional methods. The potential of supercritical fluids (SCF) to replace some traditional toxic solvents results from their specific properties: capacity to dissolve solids, related to their high density; transport capacity, related to the viscosity and diffusion coefficient inciting their excellent penetrability. Therefore, various possibilities for controlled drug delivery systems fabrication were investigated [1-5]. Thus, the amount of the impregnated substance is very important for the posterior application of the product. Especially in pharmaceutics it is required that the product would not be contaminated with residual solvent, hence the interest in using SCF as impregnation media.

EXPERIMENTAL

The experimental setup is presented schematically in Figure 1. It includes three modules: a dissolution module with a reservoir, where the solute is dissolved in supercritical CO_2; an impregnation module with a polymer charged column and a sampling module consisting of a sampling loop. Experiments were performed in two sequential steps: dissolution of the o-HBA in the supercritical CO_2 and impregnation of the solute in the polymer. The inlet side of the column (Top Industries, 10 cm^3) was filled to 60% of the total volume with inert packing (glass beads, 2 *mm*) to ensure better flow distribution before the adsorption section. The adsorption section was filled with a mixture of polymer and glass beads of the same size as the polymer (125 to 250 μm). The method is described in detail in our previous work [6]. Two polymers were used in this study: polymethyl methacrylate - PMMA (Plexidon Spain, 95%) and adsorbent resin Amberlite XAD-7 - AmbXAD7 (Fluka), porosity 55% vol., density between 1.06 and 1.08 g/cm^3, specific surface superior to 400 m^2/g and average pore diameter of 80 Å.

EXPERIMENTAL RESULTS AND DISCUSSION

The reliability of the method was demonstrated by three experiments, using 1 gram of PMMA under the same operating conditions. The CO_2 flow-rate was fixed at 0.67 cm^3/min; the temperature inside the furnace at 40°C and the pressure at 20 MPa. The obtained breakthrough curves are compared in Figure 2. All experimental curves show identical breakthrough time and similar behavior. The average concentration at the plateau (0.175; 0.148 and 0.163 $mg_{(o\text{-}HBA)}/g_{(CO2)}$ for

* To whom all correspondence should be sent:
e-mail: sdiankov@yahoo.com

© 2012 Bulgarian Academy of Sciences, Union of Chemists in Bulgaria

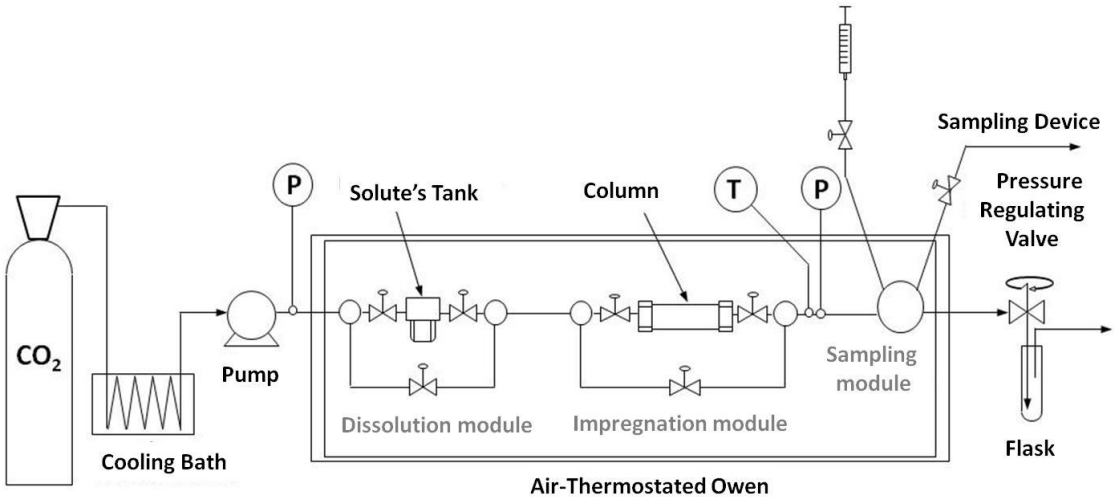

Fig. 1. Experimental setup.

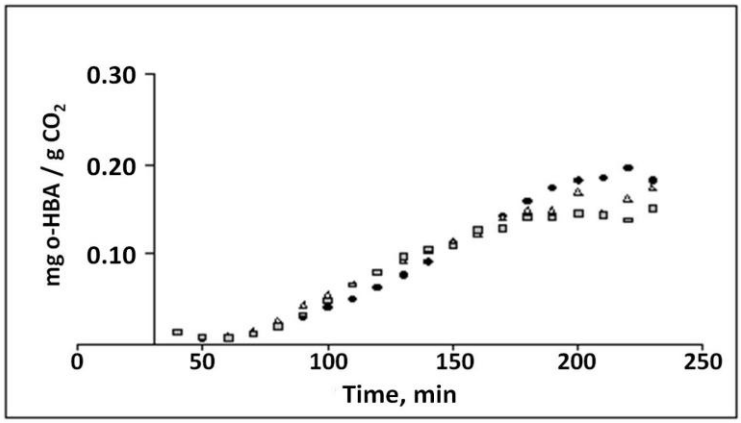

Fig. 2. Three breakthrough curves obtained using CO_2 flow rate = 0.67 cm^3/min; temperature = 40°C and pressure = 20 MPa.

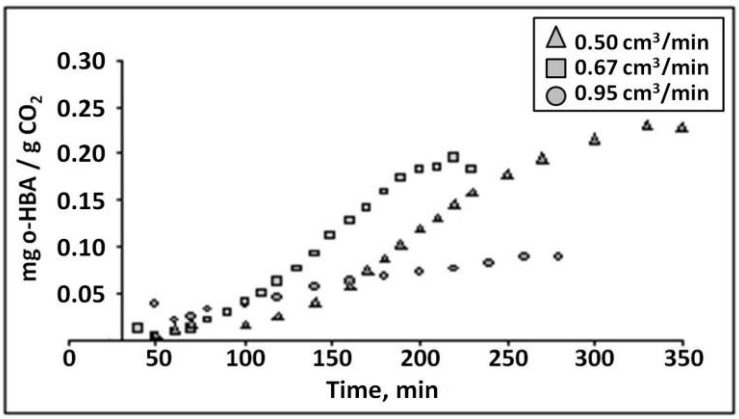

Fig. 3. Breakthrough curves obtained for three CO_2 flow rates; temperature = 40°C and pressure = 20 MPa. The polymer is PMMA.

the three experiments, respectively) was determined as an average of four replicates analysis. The maximum uncertainty is about 17%.

The impregnated amount in the polymer was determined by High Performance Liquid Chromatography (HPLC) analysis. Once the experiment has finished, the polymer support was mixed with methanol in a stirred vessel. Using the calibration curves, we determined the mass of impregnated substance per mass of polymer. These values were then corrected by the non-impregnated quantity of o-HBA dissolved in the CO_2 and

trapped in the column at the end of the experiment. This quantity Q in $mg_{(o\text{-}HBA)}$ was calculated by the following equation:

$$Q = V_{col}.\varepsilon.\rho.C_{feed}$$

where V_{col} is the column volume in cm^3; ε is the ratio of the void volume and the total volume of the column; ρ is the CO_2 density in g/cm^3 and C_{feed} is the feed concentration in $mg_{(o\text{-}HBA)}/g_{(CO2)}$.

Flow-rate influence study

In order to study the influence of CO_2 flow-rate on the impregnated amount we performed three experiments using 0.50; 0.67 and 0.95 cm^3/min. The other operating parameters were fixed: the temperature at 40°C and the pressure at 20 MPa. The support used for this study was PMMA. The breakthrough curves are presented in Figure 3. The supercritical CO_2 flow-rate, the concentrations at the plateau and the impregnated quantities are summarized in Table 1.

The curves obtained using 0.50 and 0.67 cm^3/min flow-rates show a similar trend, however, the breakthrough time (120 and 70 min respectively) and the concentrations at the plateau are different. Increasing the flow-rate to 0.95 cm^3/min leads to significant change in the curve shape. The time necessary to reach the concentration at the plateau is 220 min. The plateau concentration and the impregnated amount decrease upon increasing the flow-rate. From these results we can conclude that the impregnated amount increases proportionally with the feed concentration of the solute. These results confirm our previous observations [7]. Increasing the solvent flow-rate results in decrease of the residence time in the tank. Thus, a lower amount of dissolved substance is impregnated. Hence, in order to increase the impregnated amount in the polymer, it is necessary to use lower flow-rates.

Pressure influence study

In order to study the pressure influence on the impregnated amount, we performed three experiments at 12, 16 and 20 MPa. The CO_2 liquid flow-rate was fixed at 0.5 cm^3/min and the temperature at 40°C. The used support was PMMA. The obtained breakthrough curves are presented in Figure 4. As observed, the curves show similar trend. The breakthrough time remains the same.

However, the time necessary to reach the concentration at the plateau increases upon increasing the pressure. The density of the supercritical CO_2 also increases. This enhances the solvent power and the capacity to dissolve more substances. We should take into consideration that the flow-rate of supercritical solvent containing the solute flow decreases, increasing the pressure.

Table 1. : Flow rate influence. Experimental data.

CO_2 flow rate, cm^3/min		Concentration at the plateau, $mg_{(o\text{-}HBA)}/g_{(CO2)}$	Impregnated Amount $mg_{(o\text{-}HBA)}/g_{(PMMA)}$
Liquid	Supercritical		
0.50	0.59	0.23	16.4
0.67	0.80	0.18	7.0
0.95	1.14	0.09	4.2

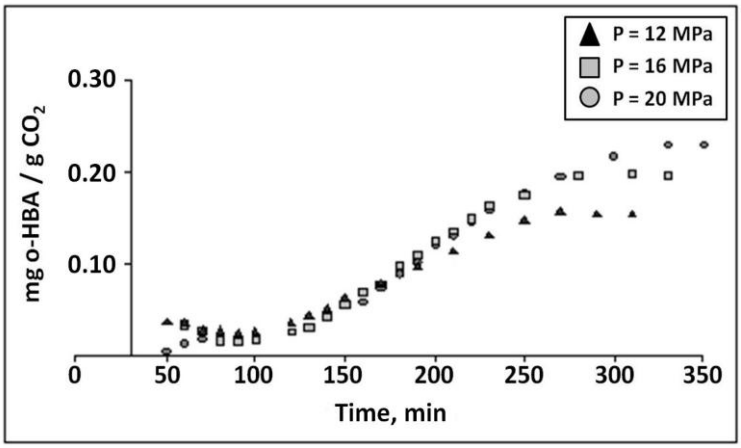

Fig. 4. Breakthrough curves at three pressures; Liquid CO_2 flow rate = 0.5 cm^3/min; temperature = 40°C and pressure P = 20 MPa. The polymer is PMMA.

Table 2. Pressure influence study. Experimental data.

P	Liquid CO_2 density	Supercritical CO_2 density	Supercritical CO_2 flow rate	Concentration at the plateau	Impregnated Amount
MPa	*g/cm³*	*g/cm³*	*cm³/min*	$mg_{(o\text{-}HBA)}/g_{(CO2)}$	$mg_{(o\text{-}HBA)}/g_{(PMMA)}$
12	0.975	0.681	0.79	0.16	7.5
16	0.991	0.792	0.64	0.20	12.7
20	1.013	0.857	0.59	0.23	16.4

Table 3. Support influence. Experimental data.

Pressure *MPa*	Support	Supercritical CO_2 flow rate *cm³/min*	Concentration at the plateau $mg_{(o\text{-}HBA)}/g_{(CO2)}$	Impregnated quantity $mg_{(o\text{-}HBA)}/g_{support}$
16	PMMA	0.64	0.20	12.7
16	AmbXAD7	0.64	0.20	79.6
20	PMMA	0.59	0.23	16.4
20	AmbXAD7	0.59	0.23	90.0

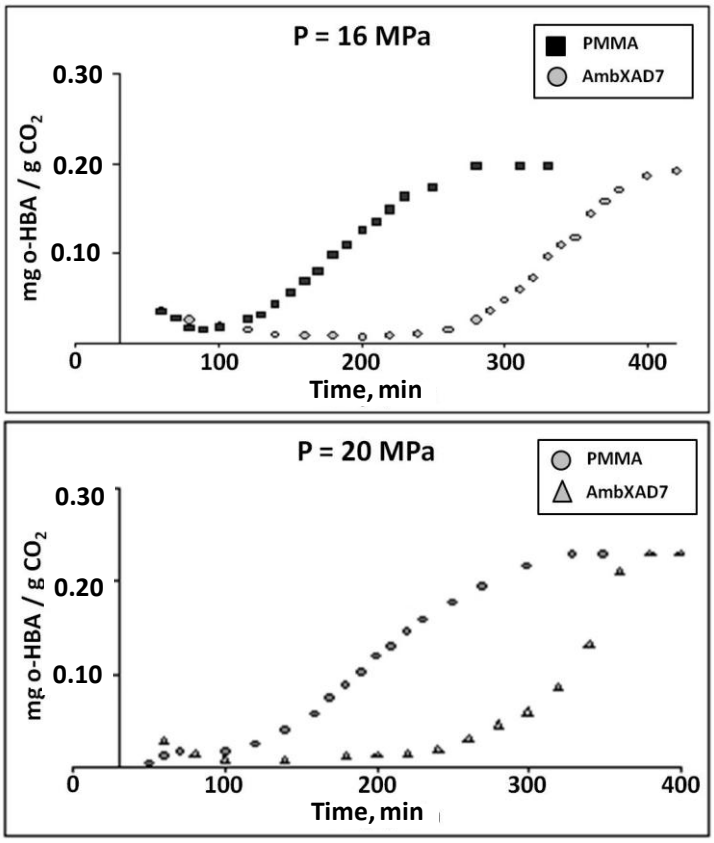

Fig. 5. Breakthrough curves obtained at 16 MPa and 20 MPa, Liquid CO_2 flow rate = 0.5 cm³/min and Temperature = 40°C.

Therefore the residence time in the solute's tank and the column increases. Both effects contribute to higher feed concentration at higher pressure. The experimental data for CO_2 density, flow-rates, concentrations at the plateau and impregnated amount are summarized in Table 2.

Support influence study

For this study we used two polymeric supports: PMMA and AmbXAD7, described above. The operating conditions were: CO_2 liquid flow-rate = 0.5 cm³/min, temperature = 40°C, polymer quantity = 1 gram PMMA or 0.5 gram AmbXAD7. The breakthrough curves obtained at two pressures 16

MPa and 20 MPa are plotted on Figure 5. The experimental data are summarized in Table 3. At 16 MPa the breakthrough time for AmbXAD7 is about three times superior (230-250 min), compared to PMMA (70-90 min). For both experiments, the concentrations at the plateau are identical. Therefore, the adsorbed amount on the AmbXAD7 is considerably higher than on the PMMA. These results show the effect of the porosity and the surface area on the impregnated amount. Therefore, we assume that the polymer porosity does not influence the velocity profile inside the column. At a higher pressure (20 MPa), the breakthrough time for AmbXAD7 is 190-210 min. However, it remains the same for the PMMA. The breakthrough curves and the quantities adsorbed are different, probably because at 20 MPa and 40°C in supercritical CO_2, the PMMA swells and changes its structure.

MODELING

One-dimensional model (1D) with a basic assumption of local equilibrium was developed in this study. The described experimental process is isothermal and the temperature profile would not influence the equilibrium, respectively the concentration profile. Therefore if the variation of the concentration in radial direction is significant, it will be due to the hydrodynamic factors. The bed porosity fluctuations in a small restricted area close to the wall provoke velocity fluctuations. However, they do not affect the overall concentration profile. Experimental observations [7] show a structure modification (swelling) of the polymer during the contact with SC-CO_2. Initially the CO_2 molecules are adsorbed in the polymer volume and this allows posterior penetration and adsorption of dissolved compound. For impregnation processes in SC medium, other authors obtain good results assuming that the polymer loses its porosity. They describe the process as a flow through a flat surface [1]. Based on these assumptions, the equation for the mass transfer through the fixed polymer bed is:

$$\varepsilon\frac{\partial C}{\partial t}+\varepsilon.w_z\frac{\partial C}{\partial z}=\varepsilon.D_{ax}\frac{\partial^2 C}{\partial z^2}-(1-\varepsilon)\frac{\partial q^*}{\partial t} \quad (1)$$

where C is the concentration in the SC phase and the local equilibrium $q^* = f(C)$ is described using the Toth relationship:

$$q^*=q_m\frac{b.C}{\left[1+(b.C)^{\theta}\right]^{\frac{1}{\theta}}} \quad (2)$$

As boundary conditions we assume equality of the mass flow through the interface and flat concentration profile:

$$D_{ax}\left.\frac{\partial C}{\partial z}\right|_{z=0}=w_z\left(C|_{z=0}-C_{feed}\right) \quad (3)$$

$$\left.\frac{\partial C}{\partial t}\right|_{z=L}=0 \quad (4)$$

The initial conditions are:

at $t = 0 \rightarrow C = 0$ for $z > 0$

at $z = 0 \rightarrow C = C_{feed}$ for each t.

where ε is the bed porosity.

When the particle dimension *versus* column diameter ratio is smaller than 0.05 and the number of particle layers in the bed in axial direction is higher than 30, an octahedral arrangement with maximal density of 0.74 could be expected [8]. We estimate a value about 10% greater than the minimal bed porosity: $\varepsilon=0.3$.

W_z is the flow velocity. The flow velocity through the porous bed $W_z = 2.77\times10^{-4}$ *m/s* corresponds to 0.5 *ml/min* experimental flow-rate.

D_{ax} is the axial dispersion coefficient. The relationships proposed by some authors [9-13] cannot be directly applied for our study. Therefore, we determined the axial dispersion coefficient using a breakthrough curve obtained without polymeric support. The pattern and the shape of this curve depend only on the axial dispersion and the dead volume of the column. Then, we calculated the breakthrough curves assuming a linear equilibrium, imposing the linear equilibrium factor equal to zero (no adsorption). Thus we obtained the commonly used model for dispersion in fixed bed [11]. We studied the breakthrough curve response in function of the D_{ax}, all other parameters being already fixed. The best correlation with the experimental data was obtained for $D_{ax} = 1.6\times10^{-6}$ m^2/s. This value is further used in our numerical simulations.

q_m is the maximum substance load and C_{feed} – the feed concentration. These values, experimentally obtained for three pressures (12 MPa, 16 MPa and 20 MPa), are presented in Table 4.

Table 4: Feed concentration and maximal substance load.

	12 *MPa*	16 *MPa*	20 *MPa*
C_{feed} , $mg_{(o\text{-}HBA)}/g_{(CO2)}$	0.156	0.198	0.230
q_m , $mg_{(o\text{-}HBA)}/g_{(PMMA)}$	28.12	28.26	20.66

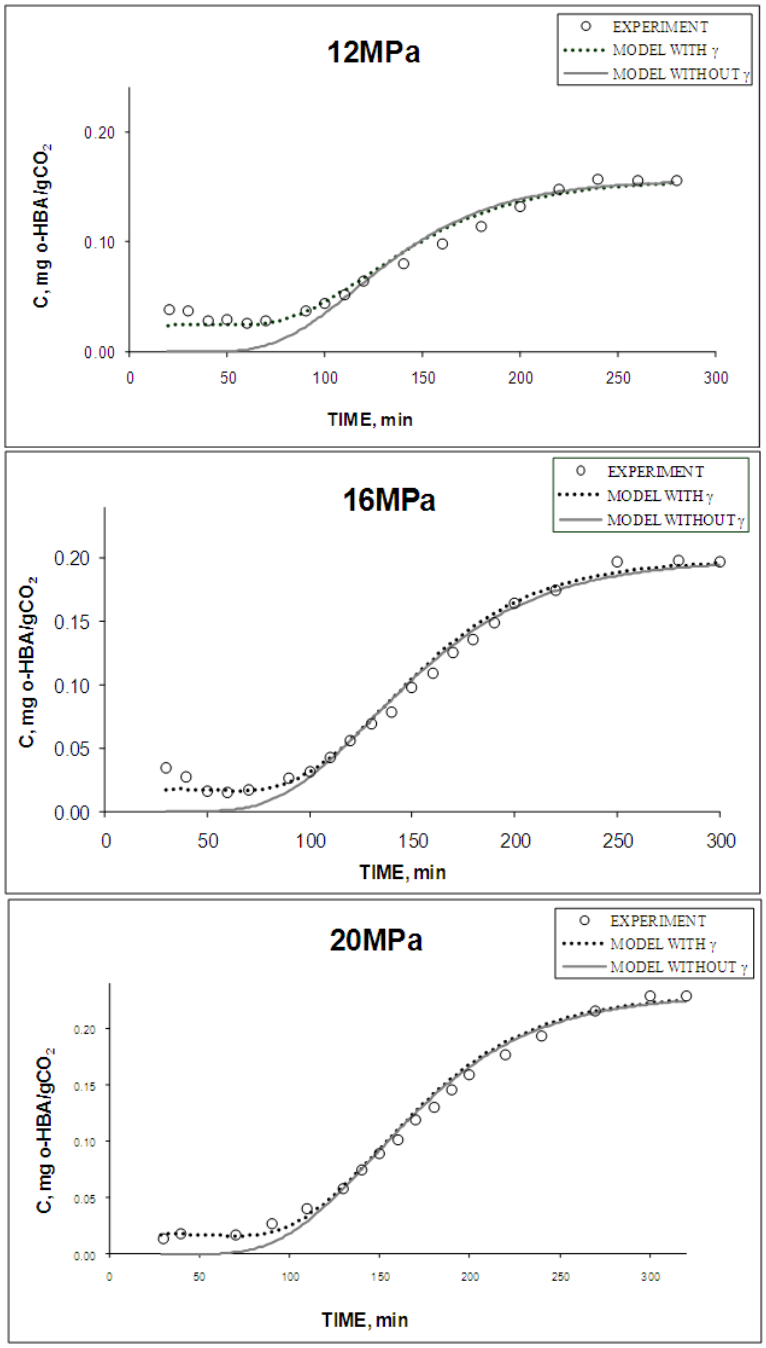

Fig. 6. Comparison of experimental and numerical data.

b and *θ* *are the adsorption parameters*. The numerical method was initially tested assuming linear equilibrium: $q_{ads} = k\,C$. The parameter *k* was adjusted in order to find the best correlation between numerical and experimental data. Next, we introduced the Toth relationship (2) in the equilibrium term. The parameters of the Toth equation were determined in our previous study [7]. However, the kinetic study conditions are different from the equilibrium ones, particularly the two parameters *b* and *θ* contribute directly to the impregnated quantity. For that reason, we considered both parameters adjustable.

For a cylindrical column with fixed bed, the free volume close to the wall is greater than in the centre of the bed. It decreases until stabilization around an average value. That provokes higher velocity of the flow at the wall proximity [14, 15, 16]. The velocity profile strongly depends on the Reynolds number (*Re*). For *Re* > 100 the fluctuations of the flow profile could be neglected. The percentage of the bypass flow close to the wall is proportional to *Re* and the ratio between column and particle diameter (D_{col}/d_{part}) and passes through

$$\varepsilon\frac{C_i^{j+1}-C_i^j}{\tau}+\frac{\varepsilon.w_z.\sigma}{h}\left(C_{i+1}^{j+1}-C_i^{j+1}\right)+\frac{\varepsilon.w_z.(1-\sigma)}{h}\left(C_{i+1}^{j}-C_i^{j}\right)=$$
$$=\frac{\varepsilon.D_{ax}.\sigma}{h^2}\left(C_{i+1}^{j+1}-2.C_i^{j+1}+C_{i-1}^{j+1}\right)+\frac{\varepsilon.D_{ax}.(1-\sigma)}{h^2}\left(C_{i+1}^{j}-2.C_i^{j}+C_{i-1}^{j}\right)-(1-\varepsilon)\frac{\partial q^*}{\partial t}$$

Table 5: Experimental and numerical data for the load.

		Load, $mg_{(o\text{-}HBA)}/g_{(PMMA)}$		
		12*MPa*	16*MPa*	20*MPa*
Experimental		7.5	12.7	16.4
Numerical	with γ	7.4	10.9	16.2
	without γ	7.9	11.5	16.7

a maximum at D_{col}/d_{part} = 10 [16]. For this study, the *Re* number varies from 0.25 to 1.12. At the entry of the column $D_{col}/d_{part} \approx 5.5$ and the velocity profile is expected to be dispersed. Inside the column $D_{col}/d_{part} \approx 45$. Thus, the bypass flow can be neglected and the velocity profile is considered relatively uniform. For reasons of simplicity, we accepted a quasi-uniform profile for the whole column section. Similar hypothesis was proposed by Chern and Chien [17].

The differential equations of the model were approximated by expressing them in finite difference form [18-20]. We used Crank-Nikolson full implicit symmetric scheme with weight coefficient $\sigma=0.5$:

Here τ and h are the time and space steps, respectively.

The experimental and numerical results are compared in Figure 6. We found that the model fits well to the experimental data: breakthrough time, slope and plateau concentration. We observed a small divergence in the initial parts of the curves. We supposed that the residence time in the mass transfer zone and the adsorption capacity of PMMA are not sufficient and small quantity of non adsorbed o-HBA remains in the outlet flow ($\overline{C}_{nonads}$). Therefore, we introduced a correction function γ in the equilibrium term:

$\gamma(t)=\frac{\overline{C}_{nonads}}{\tau^{2.3}}$, using the following boundary condition:

$\gamma|_{t=0}=\overline{C}_{nonads}$ - in the initial moment the correction function is equal to the average of the experimentally measured concentration in the initial period, and decreases rapidly with the time. This function was adjusted so that its contribution becomes negligible before the breakthrough time.

In order to calculate the impregnated amount we first determined the total amount of substance entering in the column. Then Simpson's method was used to calculate the surface area below the breakthrough curve. That corresponds to the amount of non adsorbed substance. The difference between these values is the impregnated substance in the PMMA. The calculated loads were compared to the experimental ones in Table 5. Both numerical values (with and without using the correction function γ) are in good agreement with the experimentally determined quantities.

CONCLUSIONS

Our experimental study shows the effect of three operating parameters both on the dissolving and impregnation process in supercritical CO_2. It was found that lower flow-rates allow increasing of the impregnated amount in the polymer support. Higher pressures lead to increase the time necessary to reach the concentration at the plateau. Finally, we found that the impregnated amount on a porous support is considerably higher, compared to a non porous polymer. A 1D model with a basic assumption of local equilibrium was developed in order to describe and understand the process kinetics. The model fits well to the experimental results – breakthrough curves and total impregnated amount.

REFERENCES

1. O. Guney, A. Akgerman, *AIChE J.*, **48**, 856 (2002).
2. C. Domingo, A. Fanovich, J. Fraile, G. Abraham, J. San Roman, P. Subra, in: *Proc. 8th Meeting on Supercritical Fluids*, **2**, 799 (2002).
3. A. Fanovich, C. Elvira, M. Fernandes, J. San Roman, J. Fraile, C. Domingo, *Chem. Eng. Transactions*, **3**, 551 (2003).
4. C. Magnan, C. Bazan, F. Charbit, J. Joachim, G. Charbit, in: *High Pressure Chemical Engineering*, Ph. Rudolf von Rohr, Ch. Trepp (eds), 1996, p. 509.
5. P.B. Webb, P.C. Marr, A.G. Parsons, H.S. Gidda, S.M. Howdle, *Pure Appl. Chem.*, **72**, 1347 (2004).
6. S. Diankov, P. Subra, I. Pentchev, *Journal of the UCTM*, **37**, 51 (2002).

7. S. Diankov, D. Barth, P. Subra, in: *Proc. 6th International Symposium on Supercritical Fluids*, April 2003, p. 1599.
8. M.A. Goldshtik, Transfer Processes in Granular Layer, (in Russian), Acad. Sci. U.S.S.R., Novosibirsk, 1984.
9. D.J. Gunn, *Chem. Eng. Sci*., **42**, 363 (1987).
10. T. Funazukuri, C. Kong, S. Kagei, *J. Supercrit. Fluids*, **13**, 169 (1998).
11. D. Yu, K. Jackson, T.C. Harmon, *Chem. Eng. Sci*., **54**, 357 (1999).
12. C-S. Tan, D.C. Liou, *Ind. Eng. Chem. Res*., **28**, 1246 (1989).
13. S.M. Ghoreishi, A. Akgerman, *Sep. and Pur. Techn*., **39**, 39 (2004).
14. D. Vortmeyer, K. *Chem. Eng. Sci*., **40,** 2135 (1985).
15. D. Vortmeyer, R.P. Winter, *Chemical Reaction Engineering*, **196,** 49 (1982).
16. D. Vortmeyer, J. Schuster, *Chem. Eng. Sci*., **38,** 1691 (1983).
17. J-M. Chern, Y-W. Chien, *Ind. Eng. Chem. Res*., **40,** 3775 **(**2001).
18. B.M. Berkovskii, E.F. Nogotov, "*Raznostnie Metodi Issledovania Zadatch Teploobmena*", (in Russian), Nauka i Tehnika, Minsk, 1976, pp. 46-49.
19. E.F. Nogotov, B.M. Berkovskii, W.J. Minkowycz, "*Application of Numerical Heat Transfer*", McGraw-Hill Book Comp., 1978.
20. A.A. Samarski, Teoria Raznosnih Shem (in Russian), Nauka, Moskva, 1983, pp.30-35 & 256-260.

АДСОРБЦИЯ НА О-ХИДРОБЕНЗОЕВА КИСЕЛИНА ВЪРХУ ПОЛИМЕРИ В СРЕДА НА СВРЪХКРИТИЧЕН ВЪГЛЕРОДЕН ДИОКСИД: ЕКСПЕРИМЕНТ И МОДЕЛИРАНЕ

С. Дянков[1]*, П. Сюбра-Патерно[2], И. Хинков[1], И. Пенчев[1]

[1] *Химико-технологичен и металургичен университет - София*
[2] *Университет Бордо, Франция*

Постъпила на 17 октомври, 2010 г.; приета на 26 април 2011 г.

(Резюме)

В настоящата работа е представена експериментална инсталация за импрегниране на моделно органично съединение (о-хидробензоева киселина) върху полимери чрез адсорбция в полунепрекъснат режим. Като разтворител и среда за провеждане на процеса е използван свръхкритичен CO_2. Целта е да се изследва влиянието на дебита на свръхкритичния разтворител, на налягането, както и на полимерната подложка върху проскочните криви и адсорбираното количество. Пробите от свръхкритичната фаза са анализирани чрез Високоефективна Течна Хроматография. Установено е, че адсорбираното количество нараства при повишаване на налягането и намалява при увеличаването на дебита на свръхкритичния разтворител. Разработен е 1D математичен модел с локално равновесие, който добре описва проскочните криви. Числено получените стойности показват добро съответствие с експерименталните резултати.

AUTHOR INDEX

Aher H. R., See Y. S. Shelar et al. 172
Aiqing Zhang, See Guangyong Xie et al. 310
Alexandrova R., See Kalfin R. et al. 258
Alova L. G., See Tancheva L. P. et al. 262
Arpadjan S., K. Tsekova, P. Petrova, J. Knutsson, Field sampling, speciation and determination of dissolved iron(II) and iron(III) in waters 299
Ashrafi A.R., H. Shabani, Computing Padmakar-Ivan index of four classes of dendrimers 127
Ashrafi A.R., See Yousefi-Azari H. Et al. … 307
Avdeev G., See Petrova M. et al. 92
Bayar S., See B.A. Fil et al. 201
Bayryamov S. G., See Danalev D. L. et al. 238
Boncukcuoğlu R., See B.A. Fil et al. 201
Belagali S.L., See Divya J. et al. 148
Blaskov V., See Genov K. et al. …….. 144
Boevski I., See Genov K. et al. …. 144
Budinova T., See A.L. Ciripoiu et al. 159
Caboche G., See Raikova G. et al. 389
Chaemchuen S., W. Limsangkass, B. Netiworaraksa, S. Phatanasri , N. Sae-Ma, K. Suriye, Novel catalyst of mixed SiO_2-TiO_2 supported tungsten for metathesis of ethene and 2-butene 87
Chapkanov A. G., B. B. Ivanova, Structural and spectroscopic characterization of 2-amino-3, 5-dibromopyridin 216
Chapkanov A. G., T.A. Dzimbova, B. B. Ivanova , A facile synthesis and IR-LD spectral elucidation of *N*-acetyl amino acid derivatives… ..... .364
Chesnaud A., See Raikova G. et al. … 389
Cholakov G. St., V. B. Toteva, St. D. Janev, St. G. Staykov, K. G. Stanulov, Physical Stability of Detonation Nanodiamonds in Liquid Lubricants… 31
Ciripoiu A.L., B. Tsyntsarski, C. Spataru, B. Petrova, T. Budinova, A. Sarbu, D. Teodosiev, N. Petrov, Carbon materials on the base of inorganic-organic polymer nanocomposite precursors 159
Combemale L., See Raikova G. et al. 389
Danalev D. L., R. N. Raykova, D. A. Marinkova, L. K. Yotova, S. G. Bayryamov, B. H. Hristova, V. S. Stoyanova, Synthesis of new hybrid cell pen-etrating peptides-medical drugs molecules..... 238
Deljur A., F., See Mobinikhaledi A. at al. 122
Deshpande P., S. Vagge, S. Jagtap, R. Khiarnar, S. Kelkar, M. More, Conducting polyanilline based paints on hot dip galvanized low carbon steel for corrosion protection. 318
Detcheva A. K., See Ivanova E. H. et al. 5
Deveci B., See Kilic A. et al. …… 289
Diankov S., P. Subra-Paternault, I. Hinkov, I. Pentchev, Adsorption of o-hydroxybenzoic acid on polymers in supercritical carbon dioxide medium: experimental and modeling. 399
Dincer S., Studies of tautomerism in the azonaphthol derivatives of benzimidazoles 70
Díaz-Cedillo F., See Figueroa-Valverde L. et al. 83
Díaz-Cedillo F., See Figueroa-Valverde L. et al. ….. 139
Divya J., S.L. Belagali, Assessment of urea residues in agricultural soil samples around Mysore, Karnataka, India 148
Dobreva Ek., See Petrova M. et al. 92
Dzimbova T. A., See Pancheva S.S. et al. … 222
Dzimbova T. A., See Chapkanov A. G. et al. 228
Dzimbova T., R. Mavrevski, N. Pencheva, T. Pajpanova, P. Milanov, Computer modelling of ligand-receptor interactions – enkephalin analogues and delta-opioid receptor 242
Dzhonova-Atanasova D. B., See Nakov Sv. Ts. et al. 283
Durgun M., See Kilic A. et al. 289
El-Maghraby A., See Refat M. S.et al. 74
El-Sayed M. Y., See Refat M. S.et al. …… 74
Encheva E. N., See Tancheva L. P. et al. 262
Fil B.A., A. E. Yilmaz, R. Boncukcuoğlu, S. Bayar, Removal of divalent heavy metal ions from aqueous solutions by Dowex HCR-S synthetic resin 201
Figueroa-Valverde L., F. Díaz-Cedillo, El. García-Cervera, A facile synthesis of an indol-dihydrotestosterone succinate derivative 83
Figueroa-Valverde L., F. Díaz-Cedillo, M. López-Ramos, E. García- Cervera, E. Pool-Hernandez, Synthesis and design of a progesterone-alkyne derivative 139
García-Cervera El., See Figueroa-Valverde L. et al. .. 83
García-Cervera E., See Figueroa-Valverde L. et al. . 139
Garcia-Valls R., See Tsibranska I. H. et al. 64
Giamberini M., See Tsibranska I. H. et al. 64
Gharib A., N. N. Pesyan, M. Jahangir, M. Roshani, J. W. Scheeren, Catalytic synthesis of diphenylmethyl ethers (DPME) using Preyssler acid $H_{14}[NaP_5W_{30}O_{110}]$ and silica-supported Preyssler catalysts… 11
Gharib A., M. Jahangir, M. Roshani, A facile synthesis of calix[4]pyrroles using heteropolyacids as green, eco-friendly, reusable and recyclable catalyst..... 113
Gharib A., N. N. Pesyan, M. Jahangir, M. Rosha, J. W. Scheeren, The synthesis of cyclotriveratrylene using heteropolyacids ($H_{3+x}PMo_{12-x}V_xO_{40}$) as recyclable heterogeneous catalysts …. 118
Genov K., V. Blaskov, S. Vassilev, I. Boevski, M. Shipochka, I. Stambolova, Flame AAS Determination of Trace Amounts of Cu, Ni, Co, Cd and Pd in Waters after Preconcentration with 2-Nitroso-1-Naphthol… 144
Genov, G. See Raikova G. et al. … 389
Gentscheva G., A. Petrov, E. Ivanova, I. Havezov, Flame AAS Determination of Trace Amounts of Cu, Ni, Co, Cd and Pd in Waters after Preconcentration with 2-Nitroso-1-Naphthol 52
Georgieva M., See Petrova M. et al. 92
Georgiev T. K., See Hadzhibozheva P. V. et al. 252
Goshev I. G., See Staykova S. Ts. et al. 233

Guangyong Xie, Aiqing Zhang, Efficient approach to the synthesis of ^{i}propylbenzonitriles by selective ammoxidation 310
Guay D., See Tremblay M.-L. et al. 333
Hadzhibozheva P. V., T. K. Georgiev, R. E. Kalfin, A. N. Tolekova, Angiotensin II and Vasopressin effects on motor activity of rat isolated tissue strips from urinary bladder and rectum 252
Hajara Beevi N., See Johnsirani V.,et al. 41
Hamta A., See Mobinikhaledi A. at al. 122
Han S. H., See Y. S. Shelar et al. 172
HariPrasad S., See Venkatesha M. A. at al. 155
Hassanein T.F., B. Koumanova, Binary mixture sorption of basic dyes onto wheat straw 131
Havezov I., See Gentscheva G. et al. 52
Hinkov I., See Diankov S. et al. 399
Horvat-Radošević V., K. Magdić, K. Kvastek, Parametrization of impedance spectra of GC/H_2SO_4 electrode: trials and errors 356
Hoshi M., See Nishikawa S. et al. 314
Hristova B. H., See Danalev D. L. et al. 238
Ionascu A.M., G. Raikova, E. Mladenova, I. Mercioniu, Electrochemical analysis of solid oxide electrolytes for intermediate temperature fuel cell..... 395
Ivanova B. B., See Chapkanov A. G. et al. 216
Ivanova B. B., See Chapkanov A. G. et al. 228
Ivanova E. H., A. K. Detcheva, Green analytical chemistry and its perspectives in Bulgaria 5
Ivanova E., See Gentscheva G. et al. 52
Jagtap S., See Deshpande P. et al. 318
Jahangir M., See Gharib A. et al. 11
Jahangir M., See Gharib A. et al. 113
Jahangir M., See Gharib A. et al. 118
Janev St. D., See Cholakov G. St. et al. 31
Johnsirani V., S. Rajendran, J. Sathiyabama, T. S. Muthumegala, A.Krishnaveni, N. Hajara Beevi, Inhibitive action of malachite green-Zn^{2+} system 41
Jovcheva E. S., See Pancheva S.S. et al. 222
Kalauzka R. H., See Pancheva S.S. et al. 222
Kalfin R., R. Alexandrova, Myocardial preconditioning by short ischemia-reperfusion cycles and levels of the peptide interleukin-8..... 258
Kalfin R., E. Leventieva-Necheva, G. Sgaagli, F. Pessina, Neuropeptids and urinary bladder ischemia-reperfusion injury..... 247
Kalfin R. E., See Hadzhibozheva P. V. et al. 252
Khiarnar R., See Deshpande P. et al. 318
Kelkar S., See Deshpande P. et al. 318
Kilic A., E. Tas, B. Deveci, M. Durgun, Dissymmetrical tetradentate salicylaldimine Cu(II) and Co(II) metal complexes derived 1,8-naphthaline and different salicylaldehyde. 289
Killa H. M. A., See Refat M. S.et al. 74
Klisurov R., See Tancheva L. P. et al. 262
Knutsson, See Arpadjan S. et al. 299
Koleva D. A., K. van Breugel, The integration of EIS parameters and bulk matrix characterization in studying reinforced cement-based materials .. 324
Kolev N. N., See Nakov Sv. Ts. et al. 283
Koumanova B., See Hassanein T.F. et al. 131
Krapchanska M., See Raikova G. et al. 389
Krapchanska M., See Vladikova D. et al. 364
Krishnaveni A., See Johnsirani V. et al. 41
Kuchekar S.R., See Y. S. Shelar et al. 172
Kulevski M. N., See Velev P. N. et al. 164
Kvastek K., See Horvat-Radošević V., et al. 356
Lasia A., See Tremblay M.-L. et al. 333
Leventieva-Necheva E., See Kalfin R. et al. 247
Limsangkass W., See Chaemchuen S. et al. 87
López-Ramos M., See Figueroa-Valverde L. et al. . . 139
Magdić K., See Horvat-Radošević V., et al. 356
Marekov I. N., See Marinova E. M. et al. 57
Marinkova D. A., See Danalev D. L. et al. 238
Marinova E. M., K. A. Seizova, I. R. Totseva, Sv. S. Panayotova, I. N. Marekov, Sv.M. Momchilova, Oxidative changes in some vegetable oils during heating at frying temperature 57
Mavrevski R., See Dzimbova T. et al. 242
Mercioniu I., See Ionascu A.M. et al. 395
Mihaylova B. D., See Staykova S. Ts. et al. 233
Milanov P., See Dzimbova T. et al. 242
Millet P., Electrochemical impedance spectroscopy using exponentially-rising voltage steps. (I) Analysis of a model electrical circuit ..... .338
Millet P., Electrochemical impedance spectroscopy using exponentially-rising voltage steps. (II) Analysis of the hydrogen electro-insertion into palladium foils 346
Miloshev St., See Plachkova-Petrova D. et al. 208
Mladenova E., See Ionascu A.M. et al. 395
Mobinikhaledi A., F. Deljur, A. Hamta, S.M. Shariatzadeh, Copper nitrate catalyzed synthesis and biological activity evaluation of some naphtho[2,3-d]imidazoles..... 122
More M., See Deshpande P. et al. 318
Momchilova Sv. M., See Marinova E. M. et al. 57
Muthumegala T. S., See Johnsirani V. et al. 41
Nakov Sv. Ts., D. B. Dzhonova-Atanasova, N. N. Kolev, Pressure drop of high performance random Intalox Metal Tower Packing 283
Naydenova E. D., See Staykova S. Ts. et al. 233
Nenkova S. K., See Velev P. N. et al. 164
Netiworaraksa B., See Chaemchuen S. et al. 87
Nishikawa S., M. Okimoto, T. Yoshida, M. Hoshi, K. Ohashi, Unexpected formation of novel oxazolidine and tetrahydrooxazine derivatives by condensation of 2-(Hydro-xymethy) or 2-(2-hydroxyethyl) piperidine, and ketones 314
Novakov Ch., See Plachkova-Petrova D. et al. ..... .208
Novoselski M. T., See Tancheva L. P. et al. 262
Ohashi K., See Nishikawa S. et al. 314
Okimoto M., See Nishikawa S. et al. 314
Panayotova Sv. S., See Marinova E. M. et al. 57
Pancheva S. S., R. H. Kalauzka, E. S. Jovcheva, T.A.Dzimbova, E. P. Popgeorgieva, T. I. Pajpanova, Novel cysteic acid S-amides substituted in the sulfonamide function. Synthesis and modifications..... 222

Peev G.A., See Tsibranska I. H. et al. 64
Pencheva N., See Dzimbova T. et al. 242
Pentchev I., See Diankov S. et al. ……..... 399
Petkov V. V., See Tancheva L. P. et al. 262
Petrov N., See A.L. Ciripoiu et al. …….. ..... .159
Petrova B., See A.L. Ciripoiu et al. ……..... 159
Pesyan N. N. See Gharib A. et al. 11
Pesyan N. N., See Gharib A. et al. 118
Petrov A., See Gentscheva G. et al. 52
Plachkova-Petrova D., P. Petrova, St. Miloshev, Ch. Novakov, Optimization of reaction conditions for synthesis of C-tetramethylcalix[4]-resorcin-arene..... 208
Petrova M., M. Georgieva, Ek. Dobreva, G. Avdeev, Electroless deposition of nanodisperse metal coatings on fabrics..……..... 92
Petrova P., See Arpadjan S. et al. ……..……..... 299
Petrova P., See Plachkova-Petrova D. et al. ..... .208
Pajpanova T., See Dzimbova T. et al. ……..…….. 242
Pajpanova T. I., See Pancheva S.S. et al. …..... 222
Pessina F., See Kalfin R. et al. ……..... 247
Phatanasri S., See Chaemchuen S. et al. ……...…... .. 87
Pool-Hernandez E., See Figueroa-Valverde L. et al. 139
Popgeorgieva E. P., See Pancheva S.S. et al. …..... 222
Raikova G., M. Krapchanska, I. Genov, G. Caboche, L. Combemale, A. Thorel, A. Chesnaud, D. Vladikova, Z. Stoynov, Impedance investigation of $BaCe_{0.85}Y_{0.15}O_{3-\delta}$ properties for hydrogen conductor in fuel cells… 389
Raikova G., See Vladikova D. et al. … ..... .364
Raikova G., See Ionascu A.M. et al. …..... 395
Raykova R. N., See Danalev D. L. et al. 238
Rajendran S., See Johnsirani V. et al. ……..... 41
Refat M. S., H. M. A. Killa, A. El-Maghraby, M. Y. El-Sayed, Spectroscopic and thermal studies of perylene charge-transfer complexes … 74
Rosha M., See Gharib A. et al. 118
Roshani M., See Gharib A. et al. 11
Roshani M., See Gharib A. et al. 113
Sae-Ma N., See Chaemchuen S. et al. ..... .87
Sarbu A., See A.L. Ciripoiu et al. 159
Sathiyabama J., See Johnsirani V. et al. ……..... 41
Scheeren J. W. See Gharib A. et al. 11
Scheeren J. W., See Gharib A. et al. 118
Sgaagli G., See Kalfin R. et al. 247
Shabani H., See Ashrafi A.R. et al. 127
Shariatzadeh S.M., See Mobinikhaledi A. at al. 122
Shelar Y. S., H. R. Aher, S.R. Kuchekar, S. H. Han, Extractive spectrophotometric determination of palladium(II) with o-methyl phenyl thiourea from synthetic mixtures 172
Seizova K. A., See Marinova E. M. et al. 57
Shipochka M., See Genov K. et al. …….. 144
Souri M., Comparison between four equations of state in predicting the temperature and density dependencies of the parameters of the average effective pair potential for dense methane 20
Spataru C., See A.L. Ciripoiu et al. 159
Stambolova I., See Genov K. et al. 144
Stancheva S. L., See Tancheva L. P. et al. ……..... .262
Staykova S. Ts., B. D. Mihaylova, I. G. Goshev, D. W. Wesselinova, L. T. Vezenkov, E. D. Naydenova, Antioxidant capacity of new analogs of octreotide…… 233
Stoyanova V. S., See Danalev D. L. et al. 238
Stoynov Z., See Vladikova D. et al. 364
Stoynov Z., See Raikova G. et al. ……..... 389
Subra-Paternault P., See Diankov S. et al. 399
Suriye K., See Chaemchuen S. et al. … 87
Stanulov K. G., See Cholakov G. St. et al. 31
Staykov St. G., See Cholakov G. St. et al. 31
Tancheva L. P., E. N. Encheva, D. S. Tsekova, L. G. Alova, S. L. Stancheva, V. V. Petkov, M. T. Novoselski, R. Klisurov, New L- valine peptide mimetics as potential neuropharma-cological agents..... 262
Tas E., See Kilic A. et al. 289
Teodosiev D., See A.L. Ciripoiu et al. ……..…. 159
Tolekova A. N., See Hadzhibozheva P. V. et al. 252
Thorel A., See Vladikova D. et al. 364
Thorel A., See Raikova G. et al. …….. 389
Toteva V. B., See Cholakov G. St. et al. 31
Totseva I. R., See Marinova E. M. et al. 57
Tremblay M.-L., D. Guay, A. Lasia, Dynamic impedance studies of ethanol oxidation at polycrystalline Pt..... 333
Tsekova D.S., Thaumatin crystallization in hanging drop and in thin layer by vapour diffusion method. 267
Tsekova D. S., See Tancheva L. P. et al. 262
Tsekova K., See Arpadjan S. et al. 299
Tsibranska I. H., B. Tylkowski, G.A. Peev, M. Giamberini, R. Garcia-Valls, Mass transfer kinetics of biologically active compounds from Propolis 64
Tsyntsarski B., See A.L. Ciripoiu et al. 159
Tylkowski B., See Tsibranska I. H. et al. 64
Vagge S., See Deshpande P. et al. ..... .318
van Breugel K., See Koleva D. A. et al. 324
Vassileva P.S., D.K. Voykova, Removal of Mn(II), Fe(III) and Cr(III) from aqueous solutions using Bulgarian clinoptilolite..... 180
Vassilev, S. See Genov K. et al. 144
Velev P. N., S. K. Nenkova, M. N. Kulevski, Polymer composites on the basis of lignocellulose containing copper sulfide for electromagnetic wave protection 164
Venkatesha M. A., S. HariPrasad, A Novel Route for the Synthesis of Six- and Seven- Membered 6-Trimethylsilylspiro[4,n]alk-6-enes 155
Vezenkov L. T., See Staykova S. Ts. et al. 233
Vladikova D., Z. Stoynov, G. Raikova, M. Krapchanska, A. Thorel, A. Chesnaud, Dual membrane fuel cell – impedance approach for proof of concept .. 364
Vladikova D., See Raikova G. et al. 389
Voykova D.K., See Vassileva P.S. et al. 180
Wagner N., Application of electrochemical impedance spectroscopy for fuel cell characterization: polymer electrolyte fuel cell (PEFC) and oxygen reduction reaction in alkaline solution…..... 371
Wesselinova D. W., See Staykova S. Ts. et al. 233

Yilmaz A. E., See B.A. Fil et al. 201
Yoshida T., See Nishikawa S. et al. 314
Yotova L. K., See Danalev D. L. et al. 238
Yousefi-Azari H., A.R. Ashrafi, Computing PI index of micelle-like chiral dendrimers 307
Zoltowski P., Selected problems of the analysis of impedance and transfer function spectra: a revue paper… 383

SUBJECT INDEX

1,8-naphthaline 289
2-amino-3, 5-dibromopyridin 208
2-butene 87
2-nitroso-1-naphthol 52
admixtures ..... .26
adsorption 399
agricultural soil samples 148
alkaline solution..... 371
analysis..... .338, 346, 383
angiotensin II…… 252
antioxidant capacity..... .233
aqueous solutions..... .180, 201
average effective pair potential..... 20
azonaphthol derivatives 70
basic dyes…..... 131
benzimidazoles…… ..... .70
binary mixture……..... 131
biological activity evaluation…..... .122
biologically active compounds……..... .64
calix[4]pyrroles…….. 113
carbon materials..... 159
catalyst…… 87
catalytic synthesis…… 11
Cd……..... …..52
cement-based materials..... 324
characterization..... 371
charge-transfer complexes …….. 74
clinoptilolite…… ..... .180
Co(II)..... 289
Co……..... .52
computer modelling..... 242
condensation..... 314
copper nitrate…… ..... .122
copper sulfide……..... .164
corrosion protection…… ..... .319
Cr(III)……..... ..180
crystallization..... 267
C-tetramethylcalix[4]-resorcinarene..... ..... .208
Cu(II)..... 289
Cu……..... ..…...52
cyclotriveratrylene…… 118
cysteic acid..... 222
delta-opioid receptor..... ..... .242
dendrimers…… ..... ….127
dense methane..... 20
density .... .20
design…… 139
determination…… ..... …...299
detonation…… ..... ….……31
diphenylmethyl ethers 11
dissymmetrical tetradentate..... 289
divalent heavy metal ion..... 201
Dowex HCR-S..... 201
dual membrane fuel cell..... 364
dynamic impedance studies..... ..... .333
EIS parameters..... 324
electrochemical analysis..... 395
electrochemical impedance spectroscopy... .38, 346, 371
electroless deposition..... ..... .92
electromagnetic wave protection… 164
enkephalin analogues.....
equations of state..... 20
ethane…..... …….87
ethanol oxidation..... 333
exponentially-rising voltage steps..... ....338, 346
fabrics..... 92
Fe(III)…….. ..... …...180
field sampling…… ..... ……..299
flame AAS determination…… ..... .52
fuel cell..... ....371, 395
fuel cells……..... ..389
GC/H_2SO_4 electrode..... 356
green analytical chemistry… 5
green, eco-friendly catalyst……..... 113
hanging drop..... ..... .267
heating…… ..... ……57
heterogeneous catalysts..... 118
heteropolyacids…… 113, 118
hybrid cell…… 238
hydrogen conductor… 389
hydrogen electro-insertion..... ..... .346
impedance spectra..... .356
impedance..... ..... .364, 383, 389
indol-dihydrotestosterone succinate derivative..... .83
inhibitive action…… ..... .41
inorganic-organic polymer. 159
Intalox..... 283
integration..... 324
interleukin-8..... 258
i-propylbenzonitriles…..... ...……..310
iron(II)…… ..... …...…..299
iron(III)…… ..... ……..……299
IR-LD spectral elucidation… ..... …..228
ketones..... 314
ligand-receptor interactions..... 242
lignocellulose…..... …...164
liquid lubricants…… ..... ….31
low carbon steel…… 318

l-valine.....262
malachite green….....41
mass transfer kinetics….....64
matrix characterization.......324
medical drugs molecules….....238
medium.....399
metal complexes.....289
metal tower packing.....238
metathesis…….....87
micelle-like chiral dendrimers.....307
mimetics.....262
Mn(II)…….....180
model electrical circuit.....338
modeling.....399
motor activity…….....252
myocardial preconditioning.....258
N-acetyl amino acid derivatives.....228
nanocomposite precursors.....159
nanodiamonds…….....31
nanodisperse metal coatings.....92
naphtho[2,3-d]imidazoles…….....122
neuropeptids…….....247
neuropharma-cological agents.....262
Ni.....52
octreotide.....233
o-hydroxybenzoic acid.....399
o-methyl phenyl thiourea…….....172
oxazolidine.....314
oxidative changes….....57
oxygen reduction.....371
Padmakar-Ivan index…….....127
paints…….....318
palladium foils…….....346
palladium(II)…….....172
Pd…….....52
penetrating peptides…….....238
peptide.....258, 262
perylene …….....74
physical stability…….....31
physico-chemical methods…….....26
PI index.....307
piperidine.....314
polyanilline…….....319
polycrystalline Pt…….....333
polymer composites….....164
polymer electrolyte.....371
polymers.....399
pressure drop.....283
Preyssler acid ….....11
progesterone-alkyne derivative….....139
propolis….....64
rat isolated tissue strips…….....252
reaction.....371
recyclable catalyst….....113, 118
reusable catalyst….....113
salicylaldehyde.....289
salicylaldimine.....289
S-amides.....222
selective ammoxidation….....310
short ischemia-reperfusion cycles.....258
silica-supported Preyssler catalysts 11
SiO_2-TiO_2 supported tungsten…….....87
solid oxide electrolytes 395
sorption.....131
speciation….....299
spectrophotometric determination….....172
spectroscopic characterization.....208
spectroscopic studies 74
sulphonamide.....222
sunflower oil….....26
supercritical carbon dioxide.....399
synthesis….....83, 113, 118. 122, 139
synthetic mixtures….....172
synthetic resin.....201
tautomerism…….....70
temperature.....20, 57, 395
tetrahydrooxazine derivatives.....314
thaumatin 267
thermal studies.....74
thin layer.....267
trace amounts….....52
transfer function spectra.....383
trials and errors.....356
trimethylsilylspiro[4,n]alk-6-enes….....155
urea residues 148
vapour diffusion method.....267
vasopressin effects…….....252
vegetable oils….....26, 57
wheat straw….....131
Zn^{2+}….....41

АВТОРСКИ УКАЗАТЕЛ

Авдеев Г., Виж Петрова М. и др. 98
Аикинг Чанг, Виж Гуангйонг Ксие и др. 313
Александрова Р., Виж Калфин Р. и др. 261
Алова Л. Г., Виж Танчева Л. П. и др. 266
Арпаджян С., К. Цекова, П. Петрова-Кнутсон, Й. Кнутсон, Полево пробовземане, определяне на разтворените химични форми на желязо (II) и желязо (III) във води 306
Ахер Х.Р., Виж Шелар А. С. и др. 179
Ашрафи А. Р., Виж Юсефи-Азари Х., и др. 309
Ашрафи А. Р., Х. Шабани, Пресмятане на индекса Padmakar-Ivan за четири класа дендримери.130
Байрямов, Виж Даналев Д. Л. и др. 241
Баяр С., Виж Фил Б. А. и др. 207
Белагали С. Л., Виж Дивя Дж. и др. 154
Блъсков Вл., Виж Генов Кр. и др. 147
Боевски Ив., Виж Генов Кр. и др. 147
Бонджукджуоолу Р., Виж Фил Б. А. и др. 207
Будинова Т., Виж Чирипою А. Л. и др. 163
Ваг С., Виж Дешпанд 323
Вагнер Н., Приложение на електрохимична импедансна спектроскопия за охарактеризиране на горивни елементи: горивен елемент с полимерен електролит и реакция на редукция на кислорода в алкален разтвор.....382
ван Брьогел К., Виж Колева Д. А. и др.....332
Василев С., Виж Генов Кр. и др. 147
Василева П. С., Д. К. Войкова, Приложение на български клиноптиолит за извличане на Mn(II), Fe(III) и Cr(III) от водни разтвори.....187
Везенков Л. Т., Виж Стайкова С. Ц. и др. 237
Велев П. Н. , С. К. Ненкова, М. Н. Кулевски, Полимерни композити за електро-магнитна вълнова защита на основа на лигноцелулоза съдържаща меден сулфид.....171
Венкатеша М. А., С. Хари Прасад, Нов маршрут за синтез на шест и седем атомни пръстени на 6-треметил-силил-спиро [4,N] алк-6-ени.....158
Веселинова Д. В., Виж Стайкова С. Ц. и др. 237
Владикова Д., Виж Райкова Г. и др. …….....394
Владикова Д., З. Стойнов, Г. Райкова, М. Кръпчанска, А. Торел, А. Чесно, Двойно-мембранна горивна клетка - импедансен подход за доказване на концепцията ……...370
Войкова Д. К., Виж Василева П. С. и др. 187
Гариб А., Н. Н. Песян, М. Джахангир, М. Рошани, Я. В. Схеерен, Синтеза на цикловератрилен с помощта на хетерополи-кисилини ($H_{3+X}PMO_{12-X}V_XO_{40}$) като рециклируеми хетерогенни катализатори.....19
Гариб А., М. Джахангир, М. Рошани, Лесна синтеза на каликс[4]пироли, използвайки “зелени”, екологично съвместими и рециклируеми катализатори…….....…….....11
Гариб А., Н. Н. Песиан, М. Джахангир, М. Рошани, Я. В. Схеерен, Каталитична синтеза на дифенил-метилови етери (DPME) използвайки Preyssler’ова киселина $H_{14}[NaP_5W_{30}O_{110}]$ и Preyssler’ов катализатор върху подложка от силициев диоксид….....19
Гарсиа-Валс Р., Виж Цибранска И. Х. и др. 69
Гарсиа-Сервера Е., Виж Фигероа-Валверде Л. 86
Гарсиа-Сервера Е., Виж Фигероа-Валверде Л. 143
Ге Д., Виж Трамбле М.-Л. и др. 337
Генов И., Виж Райкова Г. и др. …….....394
Генов Кр., Вл. Блъсков, С. Василев, Ив. Боевски, М Шипочка, Ир. Стамболова, Някои физико-химични свойства на клиноптилолит от Бели пласт, Източни Родопи, покрит със сребро чрез спрей пиролиза.....147
Генчева Г., А. Петров, Е. Иванова, И. Хавезов, Пламъково ААС определяне на следи от Cu, Ni, Co, Cd и Pd във води след концентриране с 2-нитрозо-1-нафтол.....56
Георгиев Ц. К., Виж Хаджибожева П. В. и др. 257
Георгиева М., Виж Петрова М. и др. 98
Гошев И. Г., Виж Стайкова С. Ц. и др. 237
Гуангйонг Ксие, Аикинг Чанг, Ефективен подход за синтезиране на изо-пропил-бензонитрили, чрез селективно амоксидиране 313
Даналев Д. Л., Р.Н. Райкова, Д.А. Маринкова, Л.К. Йотова, С.Г. Байрямов, Б.Х. Христова, В.С. Стоянова, Синтез на нови хибридни молекули включващи мембранно проникващи пептиди и лекарствени молекули 241
Девичи Б., Виж Килич А. и др. 298
Делджур Ф., Виж Мобинихаледи А., и др. 126
Дечева А. К., Виж Иванова Е. Х. И др. 10
Дешпанд П., С. Ваг, С. Джагтап, Р. Кхиарнар, С. Келкар, М. Мор, Проводящи бои на полианилинова основа за корозионна защита на поцинкована на горещо нисковъглеродна стомана 323
Джагтап С., Виж Дешпанд 323
Джамберини М., Виж Цибранска И. Х. и др 69
Джахангир М., Виж Гариб А. и др. 19
Джахангир М., Виж Гариб А. и др. 117
Джахангир М., Виж Гариб А. и др. 121
Джонова-Атанасова Д. Б., Виж Наков Св. Ц. и др. 288
Джонсирани В., С. Раджендран, Дж. Сатябама, Т.С. Мутхумегала, А. Кришнавени, Н. Хаджара Бииви, Инхибиращо действие на системата Zn^{2+}-малахитово зелено.....51
Дзимбова Т., Р. Мавревски, Н. Пенчева, Т. Пайпанова, П. Миланов, Компютърно моделиране на взаимодействието лиганд-рецептор–енкефалинови анало-зи и делта-опиоиден рецептор.....246
Дзимбова Т.А., Виж Панчева С. С. и др. 222

Дзимбова, Т. А. Виж Чапкънов А. Г. и др. 228
Диас-Седильо Ф., Виж Фигероа-Валверде Л. 86
Диас-Седильо Ф., Виж Фигероа-Валверде Л. 143
Дивя Дж., С. Л. Белагали, Определяне на остатъчен карбамид в проби от земеделски почви около гр. Майсор, щат Карнатака в Индия..... 154
Динджер С., Изследвания върху тантомерията на азонафтолови производни на бензамидазола 73
Добрева Ек., Виж Петрова М. и др. 98
Дургун М., Виж Килич А. и др. 298
Дянков С., П. Сюбра-Патерно, И. Хинков, И. Пенчев, Адсорбция на о-хидробензоева киселина върху полимери в среда на свръхкритичен въглероден диоксид: експеримент и моделиране 406
Ел-Маграби А., Виж Рефат М.С. и др. ….....82
Ел-Сайед М.И., Виж Рефат М.С. и др. ….....82
Енчева Е. Н., Виж Танчева Л. П. и др. 266
Золтовски П., Избрани проблеми на анализа на спектрите на импеданса и преходната функция: обзор 388
Иванова Б. Б., Виж Чапкънов А. Г. и др. 220
Иванова Б. Б., Виж Чапкънов А. Г. и др. 228
Иванова Е. , Виж Генчева Г. и др. 56
Иванова Е. Х., А. К. Дечева, Зелена аналитична химия и нейните перспективи в България.....10
Йилмаз А. Е., Виж Фил Б. А. и др. 207
Йовчева Е.С., Виж Панчева С. С. и др. 222
Йонашку А.М., Г. Райкова, Е. Младенова, И. Меркьониу, Електрохимичен анализ на твърдо-оксидни електролитни матери-али за горивни клетки, функциониращи при средни температури 398
Йотова Л.К., Виж Даналев Д. Л. и др. 241
Йошида Т., Виж Нишикава Н. и др. 317
Кабоч Ж., Виж Райкова Г. и др. ….....….....394
Калаузка Р.Х., Виж Панчева С. С. и др. 222
Калфин Р. Е., Виж Хаджибожева П. В. и др. 257
Калфин Р., Е. Левентиева-Нечева, Дж. Сгарали, Ф. Песина, Невропептиди и увреждане на пикочния мехур вследствие исхемия и реперфузия 251
Калфин Р., Р. Александрова, Нива на пептида интерлевкин-8 при прекондиция на миокарда посредством кратки цикли на исхемия-реперфузия.....261
Квастек К., Виж Хорват-Радошевич В. и др. 363
Келкар С., Виж Дешпанд 323
Кила Х. М. А., Виж Рефат М. С. и др. ….....82
Килич А., Е. Тас, Б. Девичи, М. Дургун, Асиметрични тетрадентат салицил-алдиминови Cu(II) и Co(II) комплекси, получени от 1,8-нафталин и различни салицилалдехиди 298
Клисуров Р. Ц., Виж Танчева Л. П. и др. 266
Кнутсон Й., Виж Арпаджян С. и др. 306
Колев Д., Виж Наков Св. Ц. и др. ….....288
Колева Д. А., К. ван Брьогел, Изследване на железобетони чрез комплексното приложение на електрохимична импедансна спектроскопия и методи за микроструктурно характеризиране 332
Комбемел Л., Виж Райкова Г. и др. …….....394
Кришнавени А., Виж Джонсирани В., и др. 51
Кръпчанска М., Виж Владикова Д. и др. 370
Кръпчанска М., Виж Райкова Г. и др. ….....394
Кулевски М. Н., Виж Велев П. Н. и др. 171
Куманова Б., Веж Хасанейн Т. Ф. и др. 138
Кучекар С. Р., Виж Шелар А. С. и др. 179
Кхиарнар Р., Виж Дешпанд 324
Лазиа А., Виж Трамбле М.-Л. и др. 337
Левентиева-Нечева Е., Виж Калфин Р. и др. 251
Лимсангкас У., Виж Чемчуен С. и др. 91
Лопес-Рамос М., Виж Фигероа-Валверде Л. 143
Мавревски Р., Виж Дзимбова 246
Магдич К., Виж Хорват-Радошевич В. и др. 363
Мареков И.Н., Виж Маринова Е.М. и др. 63
Маринкова Д. А., Виж Даналев Д. Л. и др. 241
Маринова Е. М., К. А. Сеизова, И. Р. Тоцева, Св. С. Панайотова, И. Н. Мареков, Св. М. Момчилова, Окислителни промени в растителни масла, нагрявани при температура на пържене.....63
Меркьониу И., Виж Йонашку А. М. и др. 398
Мийе П., Електрохимична импедансна спектроскопия с експоненциално нарастващи стъпки на напрежението. (I) Анализ на моделна електрическа схема 345
Мийе П., Електрохимична импедансна спектроскопия с експоненциално нарастващи стъпки на напрежението. (II) Анализ на интеркалацията на водород в палдиеви фолиа 355
Миланов П., Виж Дзимбова Т. и др. 246
Милошев Ст., Виж Плачкова-Петрова Д. и др. 215
Михайлова Б. Д., Виж Стайкова С. Ц. и др. 237
Младенова Е., Виж Йонашку А. М. и др. 398
Мобинихаледи А., Ф. Делджур, А. Хамта, С. М. Шариатзаде, Синтеза на някои нафто[2,3-d] имидаозоли при катализатор от меден нитрат и оценяване на биологичната им активност.....126
Момчилова Св. М., Виж Маринова Е. М. и др. 63
Мор М., Виж Дешпанд 323
Мутхумегала Т.С., Виж Джонсирани В., и др. 51
Найденова Е.Д., Виж Стайкова С. Ц. и др. 237
Наков Св. Ц., Д. Б. Джонова-Атанасова, Н. Н. Колев, Хидравлично съпротивление на високо-ефективния метален Intalox пълнеж за колонни апарати 288
Ненкова С. К., Виж Велев П. Н. и др. 171
Нетовораракса В., Виж Чемчуен С. и др. 91
Николова Кр., М. Перифанова-Немска, Г. Узунова, Откриване на примеси от растителни масла в слънчогледово масло чрез оптични методи..30
Нишикава Н., М. Окимото, Т. Йошида, М. Хоши, К. Онаши, Неочаквано образуване на нови производни на оксазолидин и тетрахидрооксазин при кондензация на 2-(хидроксиметил) или 2-(2-хидроксиетил) пиперидин и кетони 318
Новаков Хр., Виж Плачкова-Петрова Д. и др. 215
Новоселски М. Т., Виж Танчева Л. П. и др. 266
Окимото М., Виж Нишикава Н. и др. 317
Онаши К., Виж Нишикава Н. и др. 317

Пайпанова Т., Виж Дзимбова 246
Пайпанова Т.И., Виж Панчева С. С. и др. 222
Панайотова Св. С., Виж Маринова Е. М. и др. 63
Панчева С.С., Р.Х. Калаузка, Е.С. Йовчева, Т.А. Дзимбова, Е.П. Попгеоргиева,Т. Т.И. Пайпанова, Нови S-амиди на цистеиновата киселина, заместени всулфонамидната група. Синтез и модификации.....222
Пеев Г.А., Виж Цибранска И. Х. и др. 69
Пенчев И., Виж Дянков С. и др. 406
Пенчева Н., Виж Дзимбова 246
Перифанова-Немска М., Виж Николова Кр., и др. .30
Песиан Н. Н., Виж Гариб А. и др. 19
Песина Ф., Виж Калфин Р. и др. 251
Песян Н. Н., Виж Гариб А. и др. 121
Петков В. В., Виж Танчева Л. П. И др. 266
Петров А., Виж Генчева Г. и др. 56
Петров Н., Виж Чирипою А. Л. и др. 163
Петрова Б., Виж Чирипою А. Л. и др. 163
Петрова М., М. Георгиева, Ек. Добрева, Г. Авдеев, Безелектродно отлагане на нанодисперсни метални покрития върху тъкани 98
Петрова П., Виж Плачкова-Петрова Д. и др. 215
Петрова-Кнутсон П., Виж Арпаджян С. и др. 306
Плачкова-Петрова Д., П. Петрова, Ст. Милошев, Хр. Новаков, Оптимизация на реакционните условия за синтез на С-тетраметилкаликс[4]-резорцинарени.....215
Поол-Ернандес Е., Виж Фигероа-Валверде Л. 143
Попгеоргиева Е.П., Виж Панчева С. С. и др. 222
Раджендран С., Виж Джонсирани В., и др. ….....51
Райкова Г., Виж Владикова Д. и др. …….....370
Райкова Г., Виж Йонашку А. М. и др. 398
Райкова Г., М. Кръпчанска, И. Генов, Ж. Кабоч, Л. Комбемел, А. Торел, А. Чесно, Д. Владикова, З. Стойнов, Импедансно изследване на свойствата на $BaCe_{0.85}Y_{0.15}O_{3-\delta}$ за водороден проводник в горивни клетки……394
Райкова Р.Н., Виж Даналев Д. Л. и др. 241
Рефат М.С., Х.М.А. Кила, А. Ел-Маграби, М.И. Ел-Сайед, Спектроскопски и термични изследвания на периленови комплекси с пренос на заряд.....82
Рошани М., Виж Гариб А. и др. 121
Рошани М., Виж Гариб А. и др. 117
Сае-Ма Н., Виж Чемчуен С. и др. 91
Сарбу А., Виж Чирипою А. Л. и др. 163
Сатябама Дж., Виж Джонсирани В., и др. ….....51
Сгарали Дж., Виж Калфин Р. и др. 251
Сеизова К. А., Виж Маринова Е. М. и др. 63
Спатару К., Виж Чирипою А. Л. и др. 163
Стайков Ст. Г., Виж Чолаков Г. Ст. и др. 40
Стайкова С. Ц., Б. Д. Михайлова, И. Г. Гошев, Д. В. Веселинова, Л. Т. Везенков, Е.Д. Найденова, Антиоксидантен капацитет на нови аналози на октреотид.....==.....237
Стамболова Ир., Виж Генов Кр. и др. 147
Станулов К. Г., Виж Чолаков Г. Ст. и др. 40
Станчева С. Л., Виж Танчева Л. П. И др. 266
Стойнов З., Виж Владикова Д. и др. ……..370
Стойнов З., Виж Райкова Г. и др. ……....….394
Стоянова В.С., Виж Даналев Д. Л. и др. 241
Сури М., Сравнение между четири уравнения на състоянието за предсказване на зависимостите на параметрите на средните ефективни потенциали на метан от температурата и плътността….....……..25
Сурие К., Виж Чемчуен С. и др. 91
Схеерен Я. В., Виж Гариб А. и др. 19
Схеерен Я. В., Виж Гариб А. и др. 121
Сюбра-Патерно П., Виж Дянков С. и др. 406
Танчева Л. П., Е. Н. Енчева, Д. С. Цекова, Л. Г. Алова, С. Л. Станчева, В. В. Петков, М. Т. Новоселски, Р. Ц. Клисуров, Нови L-валинови пептидомиметици като потенциални невро-фармакологични агенти 266
Тас Е., Виж Килич А. и др. 298
Теодосиев Д., Виж Чирипою А. Л. и др. 163
Тилковски Б., Виж Цибранска И. Х. и др. 69
Толекова А. Н., Виж Хаджибожева П. В. и др. 257
Торел А., Виж Владикова Д. и др. …….....370
Торел А., Виж Райкова Г. и др. …….....…..…394
Тотева В. Б., Виж Чолаков Г. Ст. и др. 40
Тоцева И. Р., Виж Маринова Е. М. и др. 63
Трамбле М.-Л., Д. Ге, А. Лазиа, Динамично импедансно изследване на окислението на етанол върху поликристална платина 337
Узунова Г., Виж Николова Кр., и др. 30
Фатанасри С., Виж Чемчуен С. и др. 91
Фигероа-Валверде Л., Ф. Диас-Седильо, Е.Гарсиа-Сервера, Лесна синтеза на производно на индол-дихидротестостерон сукцината …….86
Фигероа-Валверде Л., Ф. Диас-Седильо, М. Лопес-Рамос, Е.Гарсиа-Сервера, Е. Поол-Ернандес, Синтиз и дизайн на прогестерон-алкинови производни.....143
Фил Б.А., А.Е. Йилмаз, Р. Бонджукджуоолу, С. Баяр, Отстраняване на двувалентни йони на тежки метали от водни разтвори със синтетична йонообменна смола Dowex HCR-S.....207
Хавезов И., Виж Генчева Г. и др. 56
Хаджара Бииви Н., Виж Джонсирани В., и др. …....51
Хаджибожева П. В., Ц. К. Георгиев, Р. Е. Калфин, А. Н. Толекова, Ефекти на Ангиотензин II и Вазопресин върху съкратителната активност на изолирани тъканни ивици от пикочен мехур и ректум на плъх …….....257
Хамта А., Виж Мобинихаледи А., и др. 126
Хан С.Х., Виж Шелар А. С. и др. 179
Хари Прасад С., Виж Венкатеша М. А. и др. 158
Хасанейн Т.Ф., Б. Куманова, Двукомпонентна адсорбция на основни багрила върху пшеничена слама.....138
Хинков И., Виж Дянков С. и др. 406
Хорват-Радошевич В., К. Магдич, К. Квастек, Определяне параметрите на импедансните спектри на GC/H_2SO_4 електрод: проби и грешки 363
Хоши М., Виж Нишикава Н. и др. 317
Христова, Б.Х., Виж Даналев Д. Л. и др. 241
Цекова К., Виж Арпаджян С. и др. 306
Цекова Д. С., Виж Танчева Л. П. и др. 266
Цекова Д. С., Кристализация на Тауматин във висяща капка и в тънък слой чрез прилагане на парно дифузионния метод.....271

Цибранска И. Х., Б. Тилковски, Г.А. Пеев, М. Джамберини, Р. Гарсиа-Валс, Кинетика на масопренасянето на биологично-активни вещества от прополис.....69
Цинцарски Б., Виж Чирипою А. Л. и др. 163
Чапкънов А. Г., Б. Б. Иванова, Структурно и спектроскопско охарактеризиране на 2-амино-3, 5-дибромопиридин.....220
Чапкънов А. Г., Т. А. Дзимбова, Б. Б. Иванова, Синтез и ИЧ-ЛД спектрално определяне на N-ацетил аминокиселинни производни.....228
Чемчуен С., У. Лимсангкас, В. Нетовораракса, С. Фатанасри , Н. Сае-Ма, К. Сурие, Нов катализатор от волфрам върху SiO_2-TiO_2 за метатеза на етен и 2-бутен.....91
Чесно А., Виж Владикова Д. и др. ……...…..370
Чесно А., Виж Райкова Г. и др. …….....……..….394
Чирипою А. Л., Б. Цинцарски, К. Спатару, Б. Петрова, Т. Будинова, А. Сарбу, Д. Теодосиев, Н. Петров, Въглеродни материали на основата на органо-неорганични полимерни нано-композитни прекурсори 163
Чолаков Г. Ст., В. Б. Тотева, Ст. Д. Янев, Ст. Г. Стайков, К. Г. Станулов, Физическа стабилност на детонационни нанодиаманти в течни смазочни материали …….....40
Шабани Х., Виж и др. Ашрафи А. Р. 130
Шариатзаде С.М., Виж Мобинихаледи А. и др. .. 126
Шелар Я.С., Х.Р. Ахер, С.Р. Кучекар, С.Х. Хан, Екстракционно спектрофотометрично определяне на паладий (II) с о-метил-фенилкарбамид в синтетични среди.....179
Шипочка М., Виж Генов Кр. и др. 147
Юсефи-Азари Х., А.Р. Ашрафи, Изчисляване на PI индекс на мицелоподобни хирални дендримери 309
Янев Ст. Д., Виж Чолаков Г. Ст. и др. 40

ПРЕДМЕТЕН УКАЗАТЕЛ

1,8-нафталин.....298
2- (2-хидроксиетил) пиперидин.....317
2-(хидроксиметил) пиперидин.....317
2-амино-3, 5-дибромопиридин….....….220
2-бутен.....91
2-нитрозо-1-нафтол.....56
6-треметил-силил-спиро [4,N] алк-6-ени.....158
$BaCe_{0.85}Y_{0.15}O_{3-\delta}$.....394
Cu(II) и Co(II) комплекси.....298
C-тетраметилкаликс[4]-резорцинарени.....……215
Dowex HCR-S…….....……207
GC/H_2SO_4 електрод.....363
L-валинови пептидомиметици….....……..266
N-ацетил аминокиселинни производни….....228
Preyssler'ов катализатор 19
Preyssler'ова ниселина 19
S-амиди…….....222
адсорбция.....406
азонафтолови производни.....73
алкален разтвор.....382
анализ на спектри.....388
ангиотензин II…….....257
антиоксидантен капацитет….....237
асиметрични тетрадентат комплекси.....298
без-електродно отлагане.....98
Бензамидазол.....73
биологична активност.....126
биологично-активни вещества.....69
вазопресин…….....257
взаимодействието лиганд-рецептор.....….246
високоефективния метален Intalox пълнеж.....288
висяща капка….....…..271
водни разтвори.....187, 207
водороден проводник.....394
волфрам.....91
индол-дихидротестостерон сукцинат.....86
интеркалацията на водород.....355
въглеродни материали.....163
горивни елементи.....382
горивни клетки.....394, 398
двойно-мембранна горивна клетка.....370
двувалентни йони….....…....207
двукомпонентна адсорбция.....138
делта-опиоиден рецептор…….....…..246
дендримери.....130
детонационни нанодиаманти.....40
дифенил-метилови етери 19
дифузионния метод….....…..271
екологично съвместими катализатори.....117
спектрофотометрично определяне.....179
електромагнитна вълнова защита.....171
електрохимичен анализ.....398
електрохимична импедансна спектроскопия.....
.....332, 345, 355
енкефалинови аналози…….....246
етанол.....337
етен.....91
железобетони.....332
желязо (II).....306
желязо (III).....306
зелена аналитична химия.....10
"зелени" катализатори.....117
земеделски почви.....154
извличане на Mn(II), Fe(III) и Cr(III).....187
изолирани тъканни ивици…….....….….257
изо-пропил-бензонитрили.....313
изчисляване на PI индекс.....309
импеданс.....388
импедансен подход.....370
импедансни спектри.....363
импедансно изследване.....337, 394
индекс Padmakar-Ivan.....130

интерлевкин-8.....261
инхибиращо действие.....51

йонообменна смола….....207
исхемия…….....…...251
исхемия-реперфузия.....261
ИЧ-ЛД спектрално определяне….....228
каликс[4]пироли.....117
катализатор.....91, 126
каталитична синтеза.....19
кетони.....317
кинетика на масопренасянето.....69
клиноптилолит.....147, 187
колонни апарати.....288
компютърно моделиране….....…...246
кондензация.....317
концентриране.....56
корозионна защита.....323
кристализация…….....…...271
лекарствени молекули…….....…...241
лиганд-рецептор.....…..246
лигноцелулоза.....171
проводящи бои.....323
маршрут за синтез.....158
меден нитрат.....126
меден сулфид.....171
мембранно проникващи пептиди….....241
метан.....25
метатеза.....91
микроструктурно характеризиране.....332
миокард.....261
мицелоподобни хирални дендримери.....309
моделиране.....406
моделна електрическа схема.....345
модификации…….....…...222
нанодисперсни метални покрития.....98
напрежение.....345
нафто[2,3-d] имидазоли.....126
невропептиди….....……...251
неврофармакологични агенти.....……...266
нисковъглеродна стомана.....323
окисление.....337
окислителни промени.....63
оксазолидин.....317
октреотид…….....…...237
о-метил-фенилкарбамид.....179
определяне на разтворените химични форми.....306
оптимизация…….....……...215
оптични методи.....30
органо-неорганични прекурсори 163
основни багрила.....138
остатъчен карбамид.....154
откриване на примеси.....30
о-хидробензоева киселина.....406
паладий (II).....179
палдиеви фолиа.....355
параметри.....25
парно дифузионния метод….....…...271
пептиди…….....241, 261
пептидомиметици….....…….266
периленови комплекси.....82
пикочен мехур…….....…...251, 257
пламъково ААС определяне.....56
плътност.....25
подложка.....19
полево пробовземане.....306
полианилинова основа.....323
поликристална платина.....337
полимерен електролит.....382
полимери.....406
полимерни композити.....171
полимерни нанокомпозитни прекурсори.....163
предсказване на зависимости.....25
прекондиция на миокарда.....261
пренос на заряд.....82
преходна функция.....388
проби и грешки.....363
прогестерон-алкинови производни.....143
прополис.....69
пшеничена слама.....138
растителни масла.....30, 63
реакционни условия….....….215
редукция на кислород.....382
ректум на плъх…….....257
реперфузия….....……..251
рециклируеми катализатори.....117, 121
салицилалдехиди.....298
салицилалдиминови комплекси.....298
свръхкритичен въглероден диоксид.....406
селективно амоксидиране.....313
силициев диоксид.....19
синтез…….....……...215, 222, 228, 241
синтеза.....117, 121, 126
синтетични среди.....179
синтиз и дизайн.....143
система Zn^{2+} - малахитово зелено.....51
следи от Cu, Ni, Co, Cd и Pd във води.....56
слънчогледово масло.....30
спектрално определяне…….....228
спектроскопски изследвания.....82
спектроскопско охарактеризиране….....…….220
спрей пиролиза.....147
сребро.....147
средни ефективни потенциали.....25
средни температури.....398
структурно охарактеризиране…….....…220
сулфонамидна група…….....222
съкратителната активност…….....257
тауматин…….....271
тафтомерия.....73
твърдо-оксидни електролитни материали.....398
тежки метали…….....……..207
температура на пържене.....63
температурата.....25
термични изследвания.....82
тетрахидрооксазин.....317
течни смазочни материали.....40
тъкани.....98
тъканни ивици….....…….257
тънък слой…….....……..271
увреждане на пикочния мехур….....251
уравнения на състоянието.....25
физико-химични свойства.....147
физическа стабилност.....40
хетерогенни катализатори.....121
хетеро-поликисилини.....121
хибридни молекули….....…241

хидравлично съпротивление.....288
цикловератрилен.....121
цистеинова киселина….....……222
шест и седем атомни пръстени.....158

BULGARIAN CHEMICAL COMMUNICATIONS

Instructions about Preparation of Manuscripts

General remarks: Manuscripts are submitted in English by e-mail or by mail (in duplicate). The text must be typed double-spaced, on A4 format paper using Times New Roman font size 12, normal character spacing. The manuscript should not exceed 15 pages (about 3500 words), including photographs, tables, drawings, formulae, etc. Authors are requested to use margins of 3 cm on all sides. For mail submission hard copies, made by a clearly legible duplication process, are requested. Manuscripts should be subdivided into labelled sections, e.g. **Introduction, Experimental, Results and Discussion**, *etc*.

The title page comprises headline, author's names and affiliations, abstract and key words.

Attention is drawn to the following:

a) **The title** of the manuscript should reflect concisely the purpose and findings of the work. Abbreviations, symbols, chemical formulas, references and footnotes should be avoided. If indispensable, abbreviations and formulas should be given in parentheses immediately after the respective full form.

b) **The author**'s first and middle name initials, and family name in full should be given, followed by the address (or addresses) of the contributing laboratory (laboratories). **The affiliation** of the author(s) should be listed in detail (no abbreviations!). The author to whom correspondence and/or inquiries should be sent should be indicated by asterisk (*).

The abstract should be self-explanatory and intelligible without any references to the text and containing not more than 250 words. It should be followed by key words (not more than six).

References should be numbered sequentially in the order, in which they are cited in the text. The numbers in the text should be enclosed in brackets [2], [5, 6], [9–12], etc., set on the text line. References, typed with double spacing, are to be listed in numerical order on a separate sheet. All references are to be given in Latin letters. The names of the authors are given without inversion. Titles of journals must be abbreviated according to Chemical Abstracts and given in italics, the volume is typed in bold, the initial page is given and the year in parentheses. Attention is drawn to the following conventions:

a) The names of all authors of a certain publications should be given. The use of "*et al*." in the list of references is not acceptable.

b) Only the initials of the first and middle names should be given.

In the manuscripts, the reference to author(s) of cited works should be made without giving initials, e.g. "Bush and Smith [7] pioneered...". If the reference carries the names of three or more authors it should be quoted as "Bush *et al*. [7]", if Bush is the first author, or as "Bush and co-workers [7]", if Bush is the senior author.

Footnotes should be reduced to a minimum. Each footnote should be typed double-spaced at the bottom of the page, on which its subject is first mentioned.

Tables are numbered with Arabic numerals on the left-hand top. Each table should be referred to in the text. Column headings should be as short as possible but they must define units unambiguously. The units are to be separated from the preceding symbols by a comma or brackets.

Note: The following format should be used when figures, equations, *etc*. are referred to the text (followed by the respective numbers): Fig., Eqns., Table, Scheme.

Schemes and figures. Each manuscript (hard copy) should contain or be accompanied by the respective illustrative material as well as by the respective figure captions in a separate file (sheet). As far as presentation of units is concerned, SI units are to be used. However, some non-SI units are also acceptable, such as °C, ml, l, etc.

The author(s) name(s), the title of the manuscript, the number of drawings, photographs, diagrams, etc., should be written in black pencil on the back of the illustrative material (hard copies) in accordance with the list enclosed. Avoid using more than 6 (12 for reviews, respectively) figures in the manuscript. Since most of the illustrative materials are to be presented as 8-cm wide pictures, attention should be paid that all axis titles, numerals, legend(s) and texts are legible.

The authors are asked to submit **the final text** (after the manuscript has been accepted for publication) in electronic form either by e-mail or mail on a 3.5'' diskette (CD) using a PC Word-processor. The main text, list of references, tables and figure captions should be saved in separate files

(as *.rtf or *.doc) with clearly identifiable file names. It is essential that the name and version of the word-processing program and the format of the text files is clearly indicated. It is recommended that the pictures are presented in *.tif, *.jpg, *.cdr or *.bmp format, the equations are written using "Equation Editor" and chemical reaction schemes are written using ISIS Draw or ChemDraw programme.

The authors are required to submit the final text with a list of three individuals and their e-mail addresses that can be considered by the Editors as potential reviewers. Please, note that the reviewers should be outside the authors' own institution or organization. The Editorial Board of the journal is not obliged to accept these proposals.

Instructions about Preparation of Manuscripts can be found at: http://bcc.bas.bg

EXAMPLES FOR PRESENTATION OF REFERENCES

REFERENCES

1. D. S. Newsome, *Catal. Rev.–Sci. Eng.*, **21**, 275 (1980).
2. C.-H. Lin, C.-Y. Hsu, *J. Chem. Soc. Chem. Commun.*, 1479 (1992).
3. R. G. Parr, W. Yang, Density Functional Theory of Atoms and Molecules, Oxford Univ. Press, New York, 1989.
4. V. Ponec, G. C. Bond, Catalysis by Metals and Alloys (Stud. Surf. Sci. Catal., vol. 95), Elsevier, Amsterdam, 1995.
5. G. Kadinov, S. Todorova, A. Palazov, in: New Frontiers in Catalysis (Proc. 10th Int. Congr. Catal., Budapest, 1992), L. Guczi, F. Solymosi, P. Tetenyi (eds.), Akademiai Kiado, Budapest, 1993, Part C, p. 2817.
6. G. L. C. Maire, F. Garin, in: Catalysis. Science and Technology, J. R. Anderson, M. Boudart (eds), vol. 6, Springer-Verlag, Berlin, 1984, p. 161.
7. D. Pocknell, *GB Patent* 2 207 355 (1949).
8. G. Angelov, PhD Thesis, UCTM, Sofia, 2001.
9. JCPDS International Center for Diffraction Data, Power Diffraction File, Swarthmore, PA, 1991.
10. CA **127**, 184 762q (1998).
11. P. Hou, H. Wise, *J. Catal.*, in press.
12. M. Sinev, private communication.
13. http://www.chemweb.com/alchem/articles/1051611477211.html.

CONTENTS

Sv. Ts. Nakov, D. B. Dzhonova-Atanasova, N. N. Kolev, Pressure drop of high performance random Intalox Metal Tower Packing ……..... 283
A. Kilic, E. Tas, B. Deveci, M. Durgun, Dissymmetrical tetradentate salicylaldimine Cu(II) and Co(II) metal complexes derived 1,8-naphthaline and different salicylaldehyde..... 289
S. Arpadjan, K. Tsekova, P. Petrova, J. Knutsson, Field sampling, speciation and determination of dissolved iron(II) and iron(III) in waters ……...….. 299
H. Yousefi-Azari, A.R. Ashrafi, Computing PI index of micelle-like chiral dendrimers 307
Guangyong Xie, Aiqing Zhang, Efficient approach to the synthesis of *i*-propylbenzonitriles by selective ammoxidation …….……. 310
S. Nishikawa, M. Okimoto, T. Yoshida, M. Hoshi, K. Ohashi, Unexpected formation of novel oxazolidine and tetrahydrooxazine derivatives by condensation of 2-(Hydroxymethy) or 2-(2-hydroxyethyl) piperidine, and ketones ……..…… 314
P. Deshpande, S. Vagge, S. Jagtap, R. Khiarnar, S. Kelkar, M. More, Conducting polyanilline based paints on hot dip galvanized low carbon steel for corrosion protection. 318
D. A. Koleva, K. van Breugel, The integration of EIS parameters and bulk matrix characterization in studying reinforced cement-based materials …… 324
M.-L. Tremblay, D. Guay, A. Lasia, Dynamic impedance studies of ethanol oxidation at polycrystalline Pt…… 333
P. Millet, Electrochemical impedance spectroscopy using exponentially-rising voltage steps. (I) Analysis of a model electrical circuit …….……... 338
P. Millet, Electrochemical impedance spectroscopy using exponentially-rising voltage steps. (II) Analysis of the hydrogen electro-insertion into palladium foils …….. 346
V. Horvat-Radošević, K. Magdić, K. Kvastek, Parametrization of impedance spectra of GC/H_2SO_4 electrode: trials and errors …….....…….. 356
D. Vladikova, Z. Stoynov, G. Raikova, M. Krapchanska, A. Thorel, A. Chesnaud, Dual membrane fuel cell – impedance approach for proof of concept …….…. 364
N. Wagner, Application of electrochemical impedance spectroscopy for fuel cell characterization: polymer electrolyte fuel cell (PEFC) and oxygen reduction reaction in alkaline solution…… 371
P. Zoltowski, Selected problems of the analysis of impedance and transfer function spectra: a revue paper…… 383
G. Raikova, M. Krapchanska, I. Genov, G. Caboche, L. Combemale, A. Thorel, A. Chesnaud, D. Vladikova, Z. Stoynov, Impedance investigation of $BaCe_{0.85}Y_{0.15}O_{3-\delta}$ properties for hydrogen conductor in fuel cells…….…….…. 389
A.M. Ionascu, G. Raikova, E. Mladenova, I. Mercioniu, Electrochemical analysis of solid oxide electrolytes for intermediate temperature fuel cell..... 395
S. Diankov, P. Subra-Paternault, I. Hinkov, I. Pentchev, Adsorption of o-hydroxybenzoic acid on polymers in supercritical carbon dioxide medium: experimental and modeling..... 399
AUTHOR INDEX……... 407
SUBJECT INDEX..... 410
AUTHORS INDEX (IN BULGARIAN)…….... 412
SUBJECT INDEX (IN BULGARIAN)…… 415
INSTRUCTIONS TO THE AUTHORS…….…….…. 418

СЪДЪРЖАНИЕ

Св. Ц. Наков, Д. Б. Джонова-Атанасова, Н. Н. Колев, Хидравлично съпротивление на високоефективния метален Intalox пълнеж за колонни апарати …….. 288

А. Килич, Е. Тас, Б. Девичи, М. Дургун, Асиметрични тетрадентат салицилалдиминови Cu(II) и Co(II) комплекси, получени от 1,8-нафталин и различни салицилалдехиди..... 298

С. Арпаджян, К. Цекова, П. Петрова-Кнутсон, Й. Кнутсон, Полево пробовземане, определяне на разтворените химични форми на желязо (II) и желязо (III) във води... 306

Х. Юсефи-Азари, А.Р. Ашрафи, Изчисляване на PI индекс на мицелоподобни хирални дендримери……..... 309

Гуангйонг Ксие, Аикинг Чанг, Ефективен подход за синтезиране на изо-пропил-бензонитрили, чрез селективно амоксидиране…….....……. 313

Н. Нишикава, М. Окимото, Т. Йошида, М. Хоши, К. Онаши, Неочаквано образуване на нови производни на оксазолидин и тетрахидрооксазин при кондензация на 2-(хидроксиметил) или 2- (2-хидроксиетил) пиперидин и кетони ……..…… 317

П. Дешпанд, С. Ваг, С. Джагтап, Р. Кхиарнар, С. Келкар, М. Мор, , Проводящи бои на полианилинова основа за корозионна защита на поцинкована на горещо нисковъглеродна стомана……. 323

Д. А. Колева, К. ван Брьогел, Изследване на железобетони чрез комплексното приложение на електрохимична импедансна спектроскопия и методи за микроструктурно характеризиране …….…… 332

М.-Л. Трамбле, Д. Ге, А.Лазиа, Динамично импедансно изследване на окислението на етанол върху поликристална платина …… 337

П. Мийе, Електрохимична импедансна спектроскопия с експоненциално нарастващи стъпки на напрежението. (I) Анализ на моделна електрическа схема …… 345

П. Мийе, Електрохимична импедансна спектроскопия с експоненциално нарастващи стъпки на напрежението. (II) Анализ на интеркалацията на водород в палдиеви фолиа……. 355

В. Хорват-Радошевич, К. Магдич, К. Квастек, Определяне параметрите на импедансните спектри на GC/H_2SO_4 електрод: проби и грешки …….. 363

Д. Владикова, З. Стойнов, Г. Райкова, М. Кръпчанска, А. Торел, А. Чесно, Двойно-мембранна горивна клетка - импедансен подход за доказване на концепцията …… 370

Н. Вагнер, Приложение на електрохимична импедансна спектроскопия за охарактеризиране на горивни елементи: горивен елемент с полимерен електролит и реакция на редукция на кислорода в алкален разтвор ……..…….. 382

П. Золтовски, Избрани проблеми на анализа на спектрите на импеданса и преходната функция: обзор…….…… 388

Г. Райкова, М. Кръпчанска, И. Генов, Ж. Кабоч, Л. Комбемел, А. Торел, А. Чесно, Д. Владикова, З. Стойнов, Импедансно изследване на свойствата на $BaCe_{0.85}Y_{0.15}O_{3-\delta}$ за водороден проводник в горивни клетки…….... 394

А.М. Йонашку, Г. Райкова, Е. Младенова, И. Меркьониу, Електрохимичен анализ на твърдо-оксидни електролитни материали за горивни клетки, функциониращи при средни температури..... 398

С. Дянков, П. Сюбра-Патерно, И. Хинков, И. Пенчев, Адсорбция на о-хидробензоева киселина върху полимери в среда на свръхкритичен въглероден диоксид: експеримент и моделиране..... 406

Авторски указател на английски..... 407

Предметен указател на английски……..……..……... 410

Авторски указател на български..... 412

Предметен указател на български…….....……...…… 415

Инструкция за авторите..... 418